

Tutorial : 2-D and 3-D electrical imaging surveys

By

Dr. M.H.Loke

Copyright (1996-2010)

email : mhloke@tm.net.my

drmhloke@yahoo.com

(All rights reserved)

(Revision date : 27th January 2010)

Copyright and disclaimer notice

The author, M.H.Loke, retains the copyright to this set of notes. Users may print a copy of the notes, but may not alter the contents in any way. The copyright notices must be retained. For public distribution, prior approval by the author is required.

It is hoped that the information provided will prove useful for those carrying out 2-D and 3-D field surveys, but the author will not assume responsibility for any damage or loss caused by any errors in the information provided. If you find any errors, please inform me by email and I will make every effort to correct it in the next edition.

You can download the programs mentioned in the text (RES2DMOD, RES2DINV, RES3DMOD, RES3DINV) from the following Web site

www.geoelectrical.com

M.H.Loke
January 2010

Table of Contents

1	Introduction to resistivity surveys.....	1
1.1	Basic resistivity theory.....	1
1.2	Electrical properties of earth materials.....	5
1.3	1-D resistivity surveys and inversions – applications, limitations and pitfalls.....	6
1.4	Basic Inverse Theory.....	12
1.5	2-D model discretization methods.....	14
2	2-D electrical surveys – Data acquisition, presentation and arrays.....	16
2.1	Introduction.....	16
2.2	Field survey method - instrumentation and measurement procedure.....	16
2.3	Available field instruments.....	19
2.4	Pseudosection data plotting method.....	22
2.5	A comparison of the different electrode arrays.....	24
2.5.1	The Frechet derivative for a homogeneous half-space.....	24
2.5.2	A 1-D view of the sensitivity function - depth of investigation.....	25
2.5.3	A 2-D view of the sensitivity function.....	28
2.5.4	Wenner array.....	29
2.5.5	Dipole-dipole array.....	29
2.5.6	Wenner-Schlumberger array.....	33
2.5.7	Pole-pole array.....	35
2.5.8	Pole-dipole array.....	36
2.5.9	Multiple gradient array.....	38
2.5.10	High-resolution electrical surveys with overlapping data levels.....	41
2.5.11	Summary of array types.....	42
2.5.12	Use of the sensitivity values for multi-channel measurements or streamers.....	43
3	A 2-D forward modeling program.....	45
3.1	Finite-difference and finite-element methods.....	45
3.2	Using the forward modeling program RES2DMOD.....	46
3.3	Forward modeling exercises.....	47
4	A 2-D inversion program.....	49
4.1	Introduction.....	49
4.2	Pre-inversion and post-inversion methods to remove bad data points.....	49
4.3	Selecting the proper inversion settings.....	52
4.4	Using the model sensitivity and uncertainty values.....	61
4.5	Methods to handle topography.....	65
4.6	Incorporating information from borehole logs and seismic surveys.....	67
4.7	Model refinement.....	71
4.8	Model resolution and automatic array optimization methods.....	75
4.8.1	Concept of model resolution.....	75
4.8.2	A heuristic explanation of model resolution – through a glass darkly.....	75
4.8.3	Examples of model resolution with standard arrays.....	76
4.8.4	Array optimization methods.....	77
4.8.5	DOI versus model resolution?.....	80
4.9	Pitfalls in 2-D resistivity surveys and inversion.....	81
5	IP inversion.....	87
5.1	Introduction.....	87
5.2	The IP effect.....	87
5.3	IP data types.....	89

6	Cross-borehole imaging.....	92
6.1	Introduction	92
6.2	Electrode configurations for cross-borehole surveys	92
6.2.1	Two electrodes array – the pole-pole.....	92
6.2.2	Three electrodes array – the pole-bipole.....	94
6.2.3	Four electrodes array – the bipole-bipole	96
6.3	Single borehole surveys.....	99
7	2-D field examples	101
7.1	Introduction	101
7.2	Landslide - Cangkat Jering, Malaysia	101
7.3	Old Tar Works - U.K.....	101
7.4	Holes in clay layer - U.S.A.....	102
7.5	Time-lapse water infiltration survey - U.K.	104
7.6	Pumping test, U.K.	106
7.7	Wenner Gamma array survey - Nigeria.....	107
7.8	Mobile underwater survey - Belgium.....	108
7.9	Floating electrodes survey – U.S.A.....	109
7.10	Oil Sands, Canada	110
8	3-D electrical imaging surveys	112
8.1	Introduction to 3-D surveys.....	112
8.2	Array types for 3-D surveys	112
8.2.1	The pole-pole array.....	112
8.2.2	The pole-dipole array.....	115
8.2.3	The dipole-dipole, Wenner and Schlumberger arrays	115
8.2.4	Summary of array types.....	117
8.3	3-D roll-along techniques.....	120
8.4	A 3-D forward modeling program.....	122
8.5	3-D inversion algorithms and 3-D data sets	124
8.6	A 3-D inversion program.....	125
8.7	Banding effects in 3-D inversion models	126
8.8	The use of long electrodes in 3-D surveys	129
8.9	Examples of 3-D field surveys	131
8.9.1	Birmingham field test survey - U.K.....	131
8.9.2	Sludge deposit - Sweden.....	132
8.9.3	Copper Hill - Australia	133
8.9.4	Athabasca Basin – Canada.....	136
	Acknowledgments.....	139
	References.....	140

List of Figures

Figure	Caption	Page Number
1.1	The flow of current from a point current source and the resulting potential distribution.	3
1.2	The potential distribution caused by a pair of current electrodes 1 meter apart with a current of 1 ampere and a homogeneous half-space with resistivity of 1 Ω -m.	3
1.3	A conventional array with four electrodes to measure the subsurface resistivity.	4
1.4	Common arrays used in resistivity surveys and their geometric factors.	4
1.5	The resistivity of rocks, soils and minerals.	6
1.6	The three different models used in the interpretation of resistivity measurements.	7
1.7	A typical 1-D model used in the interpretation of resistivity sounding data for the Wenner array.	7
1.8	A 2-D two-layer model with a low resistivity prism in the upper layer.	10
1.9	Apparent resistivity curves for a 2-D model with a lateral inhomogeneity.	11
1.10	The different models for the subsurface used in the interpretation of data from 2-D electrical imaging surveys.	15
2.1	The arrangement of electrodes for a 2-D electrical survey and the sequence of measurements used to build up a pseudosection.	17
2.2	The use of the roll-along method to extend the area covered by a survey.	18
2.3	Sketch of the ABEM Lund Imaging System.	20
2.4	The Aarhus Pulled Array System.	22
2.5	The Geometrics OhmMapper system using capacitive coupled electrodes.	22
2.6	Schematic diagram of a possible mobile underwater survey system.	22
2.7	The apparent resistivity pseudosections from 2-D imaging surveys with different arrays over a rectangular prism.	23
2.8	The parameters in the sensitivity function calculation at a point (x,y,z) within a half-space.	26
2.9	A plot of the 1-D sensitivity function.	26
2.10	2-D sensitivity sections for the Wenner array.	30
2.11	2-D sensitivity sections for the dipole-dipole array.	32
2.12	Two possible different arrangements for a dipole-dipole array measurement.	33
2.13	2-D sensitivity sections for the Wenner-Schlumberger array.	34
2.14	A comparison of the (i) electrode arrangement and (ii) pseudosection data pattern for the Wenner and Wenner-Schlumberger arrays.	35
2.15	The pole-pole array 2-D sensitivity section.	36
2.16	The forward and reverse pole-dipole arrays.	37
2.17	The pole-dipole array 2-D sensitivity sections.	37
2.18	Sensitivity sections for the gradient array.	39
2.19	(a) Example of multiple gradient array data set and inversion model. (b) Profile plot using exact pseudodepths. (c) Profile plot using approximate pseudodepths.	40

2.20	The apparent resistivity pseudosection for the dipole–dipole array using overlapping data levels over a rectangular prism.	42
2.21	Cumulative sensitivity sections for different measurement configurations using (a) a dipole-dipole sequence, (b) a moving gradient array and (c) an expanding Wenner-Schlumberger array.	44
3.1	The output from the RES2DMOD software for the SINGLE_BLOCK.MOD 2-D model file.	46
4.1	An example of a field data set with a few bad data points.	50
4.2	Selecting the menu option to remove bad data points manually.	51
4.3	Error distribution bar chart from a trial inversion of the Grundfor Line 1 data set with five bad data points.	52
4.4	Different options to modify the inversion process.	53
4.5	Example of inversion results using the l_2 -norm smooth inversion and l_1 -norm blocky inversion model constrains.	54
4.6	The different options for the Jacobian matrix calculation.	55
4.7	Different methods to subdivide the subsurface into rectangular prisms in a 2-D model.	56
4.8	The options to change the thickness of the model layers.	57
4.9	The options under the ‘Change Settings’ menu selection.	59
4.10	The dialog box to limit the model resistivity values.	60
4.11	Landfill survey example (Wenner array).	63
4.12	Landfill survey depth of investigation determination.	64
4.13	Beach survey example in Denmark.	64
4.14	Different methods to incorporate topography into a 2-D inversion model.	66
4.15	Fixing the resistivity of rectangular and triangular regions of the inversion model.	69
4.16	The inversion model cells with fixed regions.	70
4.17	Example of an inversion model with specified sharp boundaries.	70
4.18	The effect of cell size on the model misfit for near surface inhomogeneities.	71
4.19	Synthetic model (c) used to generate test apparent resistivity data for the pole-dipole (a) and Wenner (b) arrays.	72
4.20	The effect of cell size on the pole-dipole array inversion model.	73
4.21	Example of the use of narrower model cells with the Wenner-Schlumberger array.	74
4.22	Example of reduction of near-surface 'ripples' in inversion model.	74
4.23	Model resolution sections for the (a) Wenner, (b) Wenner-Schlumberger and (c) simple dipole-dipole array (d) dipole-dipole array with overlapping data levels.	77
4.24	(a) Model resolution section for comprehensive data set. (b) Model resolution section for optimized data set generated by the ‘Compare R’ method.	78
4.25	Test inversion model for the different arrays.	79
4.26	Inversion results with the (a) Wenner array, (b) Wenner-Schlumberger array, (c) simple dipole-dipole array and (d) dipole-dipole array with overlapping data levels.	80
4.27	Inversions models with the (a) optimized data set with 4462 data points and (b) a truncated optimized data set with 413 data points.	80

4.28	Comparison between the (a) model resolution and (b) DOI index sections for the Landfill data set.	81
4.29	An example of 3-D effects on a 2-D survey.	83
4.30	The 2-D sensitivity sections for the pole-dipole array with a dipole length of 1 meter and with (a) $n=6$, (b) $n=12$ and (c) $n=18$.	85
4.31	Example of apparent resistivity pseudosection with pole-dipole array with large ' n ' values.	86
5.1	The IP values for some rocks and minerals.	88
5.2	The Cole-Cole model.	88
6.1	The possible arrangements of the electrodes for the pole-pole array in the cross-borehole survey and the 2-D sensitivity sections.	93
6.2	A schematic diagram of two electrodes below the surface.	94
6.3	The 2-D sensitivity pattern for various arrangements with the pole-bipole array.	95
6.4	The 2-D sensitivity patterns for various arrangements of the bipole-bipole array.	96
6.5	Possible measurement sequences using the bipole-bipole array.	98
6.6	Several possible bipole-bipole configurations with a single borehole.	100
6.7	A pole-bipole survey with a single borehole.	100
7.1	Landslide field example, Malaysia.	101
7.2	Industrial pollution example, U.K.	102
7.3	Mapping of holes in a clay layer, U.S.A.	103
7.4	Water infiltration mapping, U.K.	104
7.5	Time-lapse sections from the infiltration study.	105
7.6	Hoveringham pumping test, U.K.	106
7.7	Percentage relative change in the subsurface resistivity values for the Hoveringham pumping test. To highlight the changes in the subsurface resistivity, the changes in the model resistivity are shown.	106
7.8	Use of Archie's Law for the Hoveringham pumping test.	107
7.9	Groundwater survey, Nigeria.	108
7.10	Underwater riverbed survey, Belgium.	109
7.11	Thames River (CT, USA) survey with floating electrodes.	110
7.12	Survey to map oil sands, Alberta, Canada.	111
8.1	One possible arrangement of the electrodes for a 3-D survey.	113
8.2	Two possible measurement sequences for a 3-D survey.	113
8.3	3-D sensitivity plots for the pole-pole array.	114
8.4	3-D sensitivity plots for the pole-dipole array with $n=1$ in the form of horizontal slices through the earth at different depths. The C1 electrode is the leftmost white cross.	116
8.5	3-D sensitivity plots for the pole-dipole array with $n=4$ in the form of horizontal slices through the earth at different depths.	116
8.6	3-D sensitivity plots for the dipole-dipole array with $n=1$ in the form of horizontal slices through the earth at different depths. The C2 electrode is the leftmost white cross.	118
8.7	3-D sensitivity plots for the dipole-dipole array with $n=4$ in the form of horizontal slices through the earth at different depths. The C2 electrode is the leftmost white cross.	118
8.8	The 3-D sensitivity plots for the Wenner alpha array at different depths.	119
8.9	The 3-D sensitivity plots for the Wenner-Schlumberger array with the	119

	n=4 at different depths.	
8.10	The 3-D sensitivity plots for the Wenner gamma array at different depths.	120
8.11	Using the roll-along method to survey a 10 by 10 grid with a multi-electrode system with 50 nodes.	121
8.12	A 3-D model with 4 rectangular prisms in a 15 by 15 survey grid.	123
8.13	The models used in 3-D inversion.	125
8.14	Inversion models for the Vetlanda landfill survey data set. (a) Using standard inversion settings. (b) With a higher damping factor for the topmost layer. (c) Using diagonal roughness filter in the horizontal (<i>x-y</i>) directions. (d) Using diagonal roughness filters in the vertical (<i>x-z</i> and <i>y-z</i>) directions as well. (e) Using the roughness filter in all directions.	127
8.15	Figure 8.15. Types of 3-D roughness filters. (a) With components in the <i>x</i> - and <i>y</i> - directions only for the horizontal filter. (b) With components in the diagonal directions in the <i>x-y</i> plane for the horizontal filter. (c) Applying the roughness filter with the corner model cells as well. Only two (out of eight) corner cells are shown.	128
8.16	Figure 8.16. Inversion models for the Vetlanda landfill survey data set using model cells of equal lengths in the <i>x</i> - and <i>y</i> - directions. (a) Using standard inversion settings. (b) With a higher damping factor for the topmost layer. (c) Using diagonal roughness filter in the horizontal (<i>x-y</i>) directions. (d) Using diagonal roughness filters in the vertical (<i>x-z</i> and <i>y-z</i>) directions as well.	129
8.17	Synthetic model for long electrodes survey.	130
8.18	Comparison of inversion models using point electrodes with and without long electrodes.	131
8.19	(a) Arrangement of electrodes in the Birmingham 3-D field survey. (b) Horizontal and (c) vertical cross-sections of the model obtained from the inversion of the Birmingham field survey data set. The location of observed tree roots on the ground surface are also shown.	132
8.20	The 3-D model obtained from the inversion of the Lernacken Sludge deposit survey data set displayed as horizontal slices through the earth.	133
8.21	A 3-D view of the model obtained from the inversion of the Lernacken Sludge deposit survey data set displayed with the Slicer/Dicer program.	134
8.22	Geological map of the Copper Hill area	135
8.23	Electrodes layout used for the 3-D survey of the Copper Hill area.	135
8.24	The IP model obtained from the inversion of the Copper Hill survey data set.	136
8.25	Location of uranium mines in the Athabasca basin, Saskatchewan.	137
8.26	Geological model of uranium deposit.	137
8.27	Example of inversion model from the Midwest deposit area showing the resistivity at a depth of about 200 meters.	138

List of Tables

Table	Caption	Page Number
1.1	1-D inversion examples using the RES1D.EXE program.	11
2.1	The median depth of investigation (z_e) for the different arrays.	28
3.1	Forward modeling examples.	48
4.1	Example method to remove bad data points.	52
4.2	Tests with different inversion options.	61
4.3	Tests with different topographic modeling options.	68
4.4	Tests with the option to fix the model resistivity.	70
5.1	Tests with 2-D IP inversion.	92
6.1	A few borehole inversion tests.	99
8.1	3-D forward modeling examples.	123
8.2	3-D inversion examples.	127

1 Introduction to resistivity surveys

1.1 Basic resistivity theory

The purpose of electrical surveys is to determine the subsurface resistivity distribution by making measurements on the ground surface. From these measurements, the true resistivity of the subsurface can be estimated. The ground resistivity is related to various geological parameters such as the mineral and fluid content, porosity and degree of water saturation in the rock. Electrical resistivity surveys have been used for many decades in hydrogeological, mining and geotechnical investigations. More recently, it has been used for environmental surveys.

The fundamental physical law used in resistivity surveys is Ohm's Law that governs the flow of current in the ground. The equation for Ohm's Law in vector form for current flow in a continuous medium is given by

$$\mathbf{J} = \sigma \mathbf{E} \quad (1.1)$$

where σ is the conductivity of the medium, \mathbf{J} is the current density and \mathbf{E} is the electric field intensity. In practice, what is measured is the electric field potential. We note that in geophysical surveys the medium resistivity ρ , which is equal to the reciprocal of the conductivity ($\rho=1/\sigma$), is more commonly used. The relationship between the electric potential and the field intensity is given by

$$\mathbf{E} = -\nabla\Phi \quad (1.2)$$

Combining equations (1.1) and (1.2), we get

$$\mathbf{J} = -\sigma\nabla\Phi \quad (1.3)$$

In almost all surveys, the current sources are in the form of point sources. In this case, over an elemental volume ΔV surrounding the a current source I , located at (x_s, y_s, z_s) the relationship between the current density and the current (Dey and Morrison 1979a) is given by

$$\nabla \cdot \mathbf{J} = \left(\frac{I}{\Delta V} \right) \delta(x - x_s) \delta(y - y_s) \delta(z - z_s) \quad (1.4)$$

where δ is the Dirac delta function. Equation (3) can then be rewritten as

$$-\nabla \cdot [\sigma(x, y, z) \nabla \phi(x, y, z)] = \left(\frac{I}{\Delta V} \right) \delta(x - x_s) \delta(y - y_s) \delta(z - z_s) \quad (1.5)$$

This is the basic equation that gives the potential distribution in the ground due to a point current source. A large number of techniques have been developed to solve this equation. This is the "forward" modeling problem, i.e. to determine the potential that would be observed over a given subsurface structure. Fully analytical methods have been used for simple cases, such as a sphere in a homogenous medium or a vertical fault between two areas each with a constant resistivity. For an arbitrary resistivity distribution, numerical techniques are more commonly used. For the 1-D case, where the subsurface is restricted to a number of horizontal layers, the linear filter method is commonly used (Koefoed 1979). For 2-D and 3-D cases, the finite-difference and finite-element methods are the most versatile. In Chapter 2, we will look at the use of a forward modeling computer program for 2-D structures.

The more complicated cases will be examined in the later sections. First, we start with the simplest case with a homogeneous subsurface and a single point current source on the ground surface (Figure 1.1). In this case, the current flows radially away from the source, and the potential varies inversely with distance from the current source. The equipotential surfaces have a hemisphere shape, and the current flow is perpendicular to the equipotential surface. The potential in this case is given by

$$\phi = \frac{\rho I}{2\pi r} \quad (1.6)$$

where r is the distance of a point in the medium (including the ground surface) from the electrode. In practice, all resistivity surveys use at least two current electrodes, a positive current and a negative current source. Figure 1.2 show the potential distribution caused by a pair of electrodes. The potential values have a symmetrical pattern about the vertical plane at the mid-point between the two electrodes. The potential value in the medium from such a pair is given by

$$\phi = \frac{\rho I}{2\pi} \left(\frac{1}{r_{C1}} - \frac{1}{r_{C2}} \right) \quad (1.7)$$

where r_{C1} and r_{C2} are distances of the point from the first and second current electrodes.

In practically all surveys, the potential difference between two points (normally on the ground surface) is measured. A typical arrangement with 4 electrodes is shown in Figure 1.3. The potential difference is then given by

$$\Delta\phi = \frac{\rho I}{2\pi} \left(\frac{1}{r_{C1P1}} - \frac{1}{r_{C2P1}} - \frac{1}{r_{C1P2}} + \frac{1}{r_{C2P2}} \right) \quad (1.8)$$

The above equation gives the potential that would be measured over a homogenous half space with a 4 electrodes array.

Actual field surveys are invariably conducted over an inhomogenous medium where the subsurface resistivity has a 3-D distribution. The resistivity measurements are still made by injecting current into the ground through the two current electrodes (C1 and C2 in Figure 1.3), and measuring the resulting voltage difference at two potential electrodes (P1 and P2). From the current (I) and potential ($\Delta\phi$) values, an apparent resistivity (ρ_a) value is calculated.

$$\rho_a = k \frac{\Delta\phi}{I} \quad (1.9)$$

where

$$k = \frac{2\pi}{\left(\frac{1}{r_{C1P1}} - \frac{1}{r_{C2P1}} - \frac{1}{r_{C1P2}} + \frac{1}{r_{C2P2}} \right)}$$

k is a geometric factor that depends on the arrangement of the four electrodes. Resistivity measuring instruments normally give a resistance value, $R = \Delta\phi/I$, so in practice the apparent resistivity value is calculated by

$$\rho_a = k R \quad (1.10)$$

The calculated resistivity value is not the true resistivity of the subsurface, but an “apparent” value that is the resistivity of a homogeneous ground that will give the same resistance value for the same electrode arrangement. The relationship between the “apparent” resistivity and the “true” resistivity is a complex relationship. To determine the true subsurface resistivity from the apparent resistivity values is the “inversion” problem. Methods to carry out such an inversion will be discussed in more detail at the end of this chapter.

Figure 1.4 shows the common arrays used in resistivity surveys together with their geometric factors. In a later section, we will examine the advantages and disadvantages of some of these arrays.

There are two more electrical based methods that are closely related to the resistivity method. They are the Induced Polarization (IP) method, and the Spectral Induced Polarization (SIP) (also known as Complex Resistivity (CR)) method. Both methods require measuring instruments that are more sensitive than the normal resistivity method, as well as significantly higher currents. IP surveys are comparatively more common, particularly in mineral exploration surveys. It is able to detect conductive minerals of very low concentrations that might otherwise be missed by resistivity or EM surveys. Commercial SIP surveys are comparatively rare, although it is a popular research subject. Both IP and SIP surveys use alternating currents (in the frequency domain) of much higher frequencies than standard resistivity surveys. Electromagnetic coupling is a serious problem in both methods. To minimize the electromagnetic coupling, the dipole-dipole (or pole-dipole) array is commonly used.

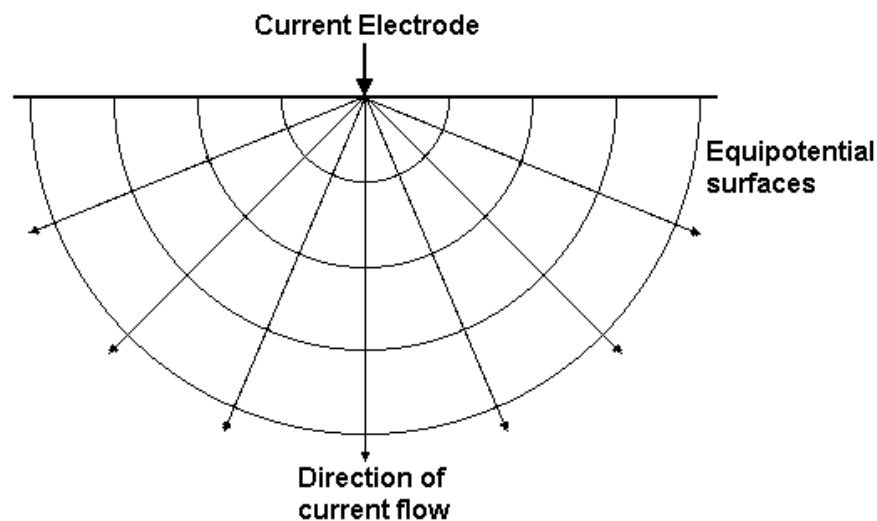


Figure 1.1. The flow of current from a point current source and the resulting potential distribution.

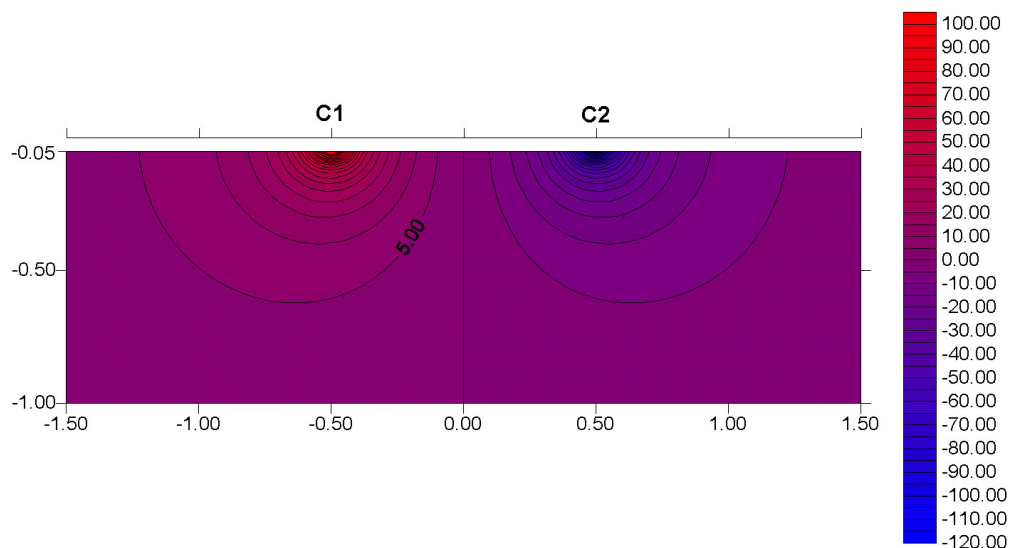


Figure 1.2. The potential distribution caused by a pair of current electrodes. The electrodes are 1 meter apart with a current of 1 ampere and a homogeneous half-space with resistivity of $1 \Omega \cdot \text{m}$.

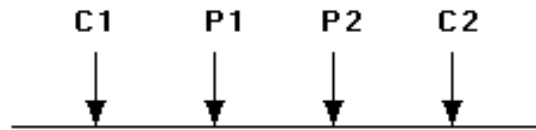


Figure 1.3. A conventional array with four electrodes to measure the subsurface resistivity.

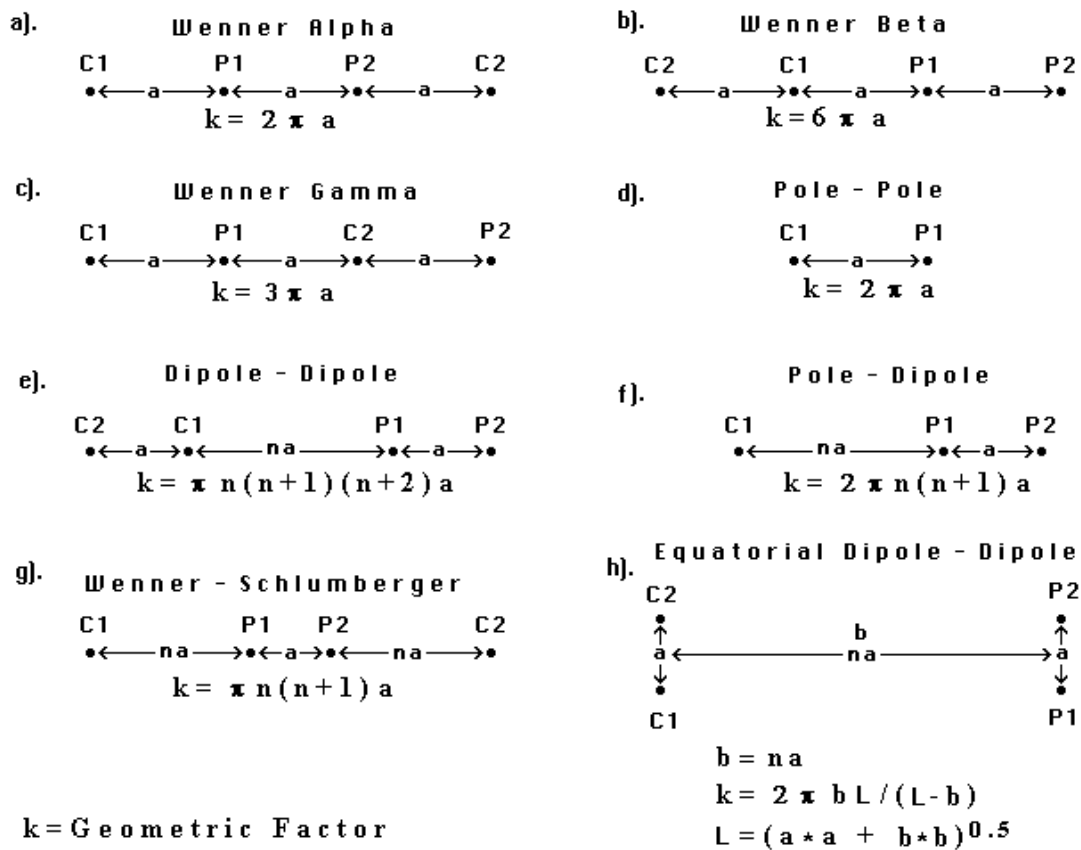


Figure 1.4. Common arrays used in resistivity surveys and their geometric factors. Note that the dipole-dipole, pole-dipole and Wenner-Schlumberger arrays have two parameters, the dipole length “a” and the dipole separation factor “n”. While the “n” factor is commonly an integer value, non-integer values can also be used.

1.2 Electrical properties of earth materials

Electric current flows in earth materials at shallow depths through two main methods. They are electronic conduction and electrolytic conduction. In electronic conduction, the current flow is via free electrons, such as in metals. In electrolytic conduction, the current flow is via the movement of ions in groundwater. In environmental and engineering surveys, electrolytic conduction is probably the more common mechanism. Electronic conduction is important when conductive minerals are present, such as metal sulfides and graphite in mineral surveys.

The resistivity of common rocks, soil materials and chemicals (Keller and Frischknecht 1966, Daniels and Alberty 1966, Telford et al. 1990) is shown in Figure 1.5. Igneous and metamorphic rocks typically have high resistivity values. The resistivity of these rocks is greatly dependent on the degree of fracturing, and the percentage of the fractures filled with ground water. Thus a given rock type can have a large range of resistivity, from about 1000 to 10 million $\Omega\cdot\text{m}$, depending on whether it is wet or dry. This characteristic is useful in the detection of fracture zones and other weathering features, such as in engineering and groundwater surveys.

Sedimentary rocks, which are usually more porous and have higher water content, normally have lower resistivity values compared to igneous and metamorphic rocks. The resistivity values range from 10 to about 10000 $\Omega\cdot\text{m}$, with most values below 1000 $\Omega\cdot\text{m}$. The resistivity values are largely dependent on the porosity of the rocks, and the salinity of the contained water.

Unconsolidated sediments generally have even lower resistivity values than sedimentary rocks, with values ranging from about 10 to less than 1000 $\Omega\cdot\text{m}$. The resistivity value is dependent on the porosity (assuming all the pores are saturated) as well as the clay content. Clayey soil normally has a lower resistivity value than sandy soil. However, note the overlap in the resistivity values of the different classes of rocks and soils. This is because the resistivity of a particular rock or soil sample depends on a number of factors such as the porosity, the degree of water saturation and the concentration of dissolved salts.

The resistivity of groundwater varies from 10 to 100 $\Omega\cdot\text{m}$, depending on the concentration of dissolved salts. Note the low resistivity (about 0.2 $\Omega\cdot\text{m}$) of seawater due to the relatively high salt content. This makes the resistivity method an ideal technique for mapping the saline and fresh water interface in coastal areas. One simple equation that gives the relationship between the resistivity of a porous rock and the fluid saturation factor is Archie's Law. It is applicable for certain types of rocks and sediments, particularly those that have a low clay content. The electrical conduction is assumed to be through the fluids filling the pores of the rock. Archie's Law is given by

$$\rho = a\rho_w\phi^{-m} \quad (1.11)$$

where ρ is the rock resistivity, ρ_w is fluid resistivity, ϕ is the fraction of the rock filled with the fluid, while a and m are two empirical parameters (Keller and Frischknecht 1966). For most rocks, a is about 1 while m is about 2. For sediments with a significant clay content, other more complex equations have been proposed (Olivar *et al.* 1990).

The resistivities of several types of ores are also shown. Metallic sulfides (such as pyrrhotite, galena and pyrite) have typically low resistivity values of less than 1 $\Omega\cdot\text{m}$. Note that the resistivity value of a particular ore body can differ greatly from the resistivity of the individual crystals. Other factors, such as the nature of the ore body (massive or disseminated) have a significant effect. Note that graphitic slate have a low resistivity value, similar to the metallic sulfides, which can give rise to problems in mineral surveys. Most oxides, such as hematite, do not have a significantly low resistivity value. One exception is magnetite.

The resistivity values of several industrial contaminants are also given in Figure 1.5. Metals, such as iron, have extremely low resistivity values. Chemicals that are strong electrolytes, such as potassium chloride and sodium chloride, can greatly reduce the resistivity of ground water to less than $1 \Omega \cdot m$ even at fairly low concentrations. The effect of weak electrolytes, such as acetic acid, is comparatively smaller. Hydrocarbons, such as xylene ($6.998 \times 10^{16} \Omega \cdot m$), typically have very high resistivity values. However, in practice the percentage of hydrocarbons in a rock or soil is usually quite small, and might not have a significant effect on the bulk resistivity. However when the concentration of the hydrocarbon is high, such as the commercial oil sands deposits in Canada, the resistivity method has proved to be a useful exploration method for such deposits (see section 7.10 for an example).

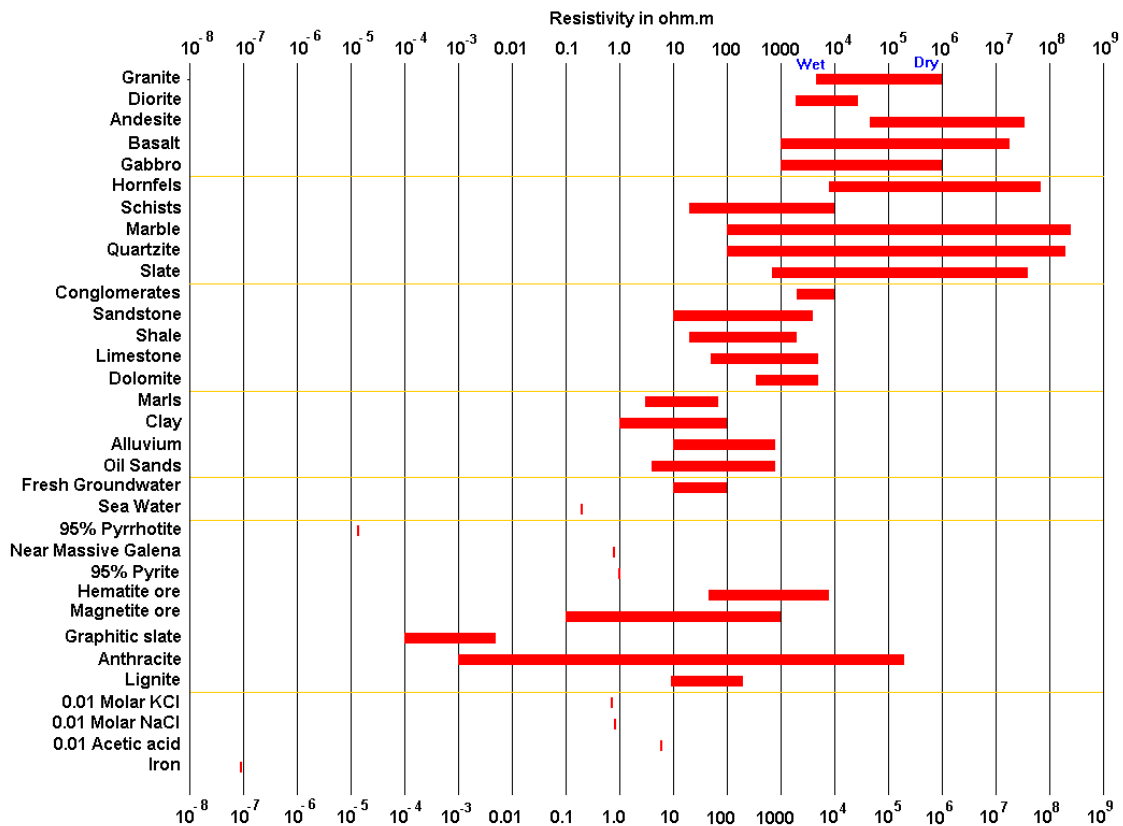


Figure 1.5. The resistivity of rocks, soils and minerals.

1.3 1-D resistivity surveys and inversions – applications, limitations and pitfalls

The resistivity method has its origin in the 1920's due to the work of the Schlumberger brothers. For approximately the next 60 years, for quantitative interpretation, conventional sounding surveys (Koefoed 1979) were normally used. In this method, the center point of the electrode array remains fixed, but the spacing between the electrodes is increased to obtain more information about the deeper sections of the subsurface.

The measured apparent resistivity values are normally plotted on a log-log graph paper. To interpret the data from such a survey, it is normally assumed that the subsurface consists of horizontal layers. In this case, the subsurface resistivity changes only with depth, but does not change in the horizontal direction. A one-dimensional model of the subsurface is used to interpret the measurements (Figure 1.6a). Figure 1.7 shows an example of the data from a sounding survey and a possible interpretation model. This method has given useful

results for geological situations (such the water-table) where the one-dimensional model is approximately true.

The software provided, RES1D.EXE, is a simple inversion and forward modeling program for 1-D models that consists of horizontal layers. Besides normal resistivity surveys, the program will enable you to model IP as well as SIP data. In the software package, several files with extensions of DAT are example data files with resistivity sounding data. Files with the MOD extension are model files that can be used to generate synthetic data for the inversion part of the program. As a first try, read in the file WENNER3.DAT that contains the Wenner array sounding data for a simple 3-layer model.

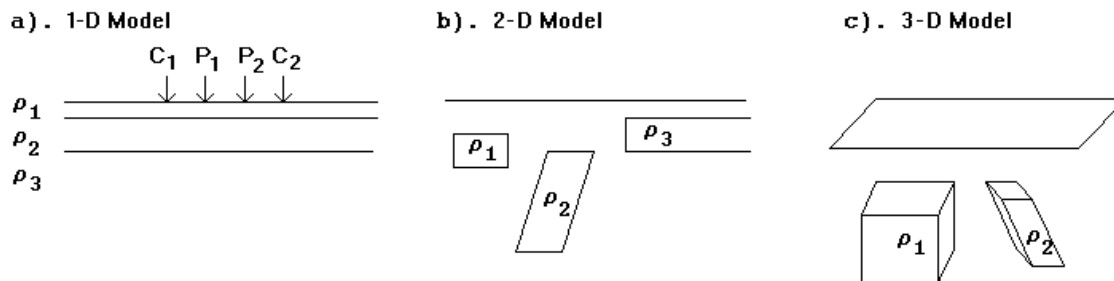


Figure 1.6. The three different models used in the interpretation of resistivity measurements.

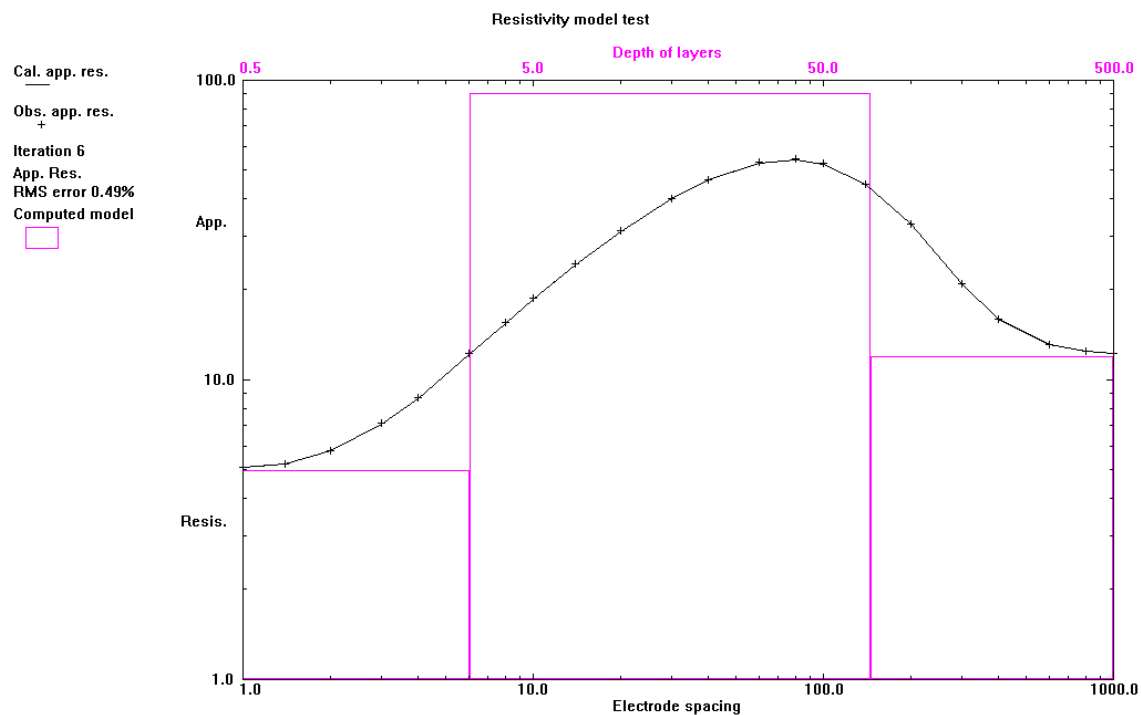


Figure 1.7. A typical 1-D model used in the interpretation of resistivity sounding data for the Wenner array.

The greatest limitation of the resistivity sounding method is that it does not take into account lateral changes in the layer resistivity. Such changes are probably the rule rather than the exception. The failure to include the effect of such lateral changes can result in errors in the interpreted layer resistivity and/or thickness. As an example, Figure 1.8 shows a 2-D model where the main structure is a two-layer model with a resistivity of $10 \Omega\cdot\text{m}$ and a thickness of 5 meters for the upper layer, while the lower layer has a resistivity of $100 \Omega\cdot\text{m}$. To the left of the center point of the survey line, a low resistivity prism of $1 \Omega\cdot\text{m}$ is added in the upper layer to simulate a lateral inhomogeneity. The 2-D model has 144 electrodes that are 1 meter apart. The apparent resistivity pseudosections for the Wenner and Schlumberger array are also shown. For the Schlumberger array, the spacing between the potential electrodes is fixed at 1.0 meter for the apparent resistivity values shown in the pseudosection. The sounding curves that are obtained with conventional Wenner and Schlumberger array sounding surveys with the mid-point at the center of the line are shown in Figure 1.9. In the 2-D model, the low resistivity rectangular prism extends from 5.5 to 18.5 meters to the left of the sounding mid-point. The ideal sounding curves for both arrays for a two-layer model (i.e. without the low resistivity prism) are also shown for comparison. For the Wenner array, the low resistivity prism causes the apparent resistivity values in the sounding curve (Figure 1.9a) to be too low for spacing values of 2 to 9 meters and for spacings larger than 15 meters. At spacings between 9 to 15 meters, the second potential electrode P2 crosses over the low resistivity prism. This causes the apparent resistivity values to approach the two-layer model sounding curve. If the apparent resistivity values from this model are interpreted using a conventional 1-D model, the resulting model could be misleading. In this case, the sounding data will most likely be interpreted as a three-layer model.

The effect of the low resistivity prism on the Schlumberger array sounding curve is slightly different. The apparent resistivity values measured with a spacing of 1 meter between the central potential electrodes are shown by black crosses in Figure 1.9b. For electrode spacings (which is defined as half the total length of the array for the Schlumberger array) of less than 15 meters, the apparent resistivity values are less than that of the two-layer sounding curve. For spacings greater than 17 meters, the apparent resistivity values tend to be too high. This is probably because the low resistivity prism lies to the right of the C2 electrode (i.e. outside the array) for spacings of less than 15 meters. For spacings of greater than 17 meters, it lies between the P2 and C2 electrodes. Again, if the data is interpreted using a 1-D model, the results could be misleading. One method that has been frequently recommended to “remove” the effect of lateral variations with the Schlumberger array is by shifting curve segments measured with different spacings between the central potential electrodes. The apparent resistivity values measured with a spacing of 3 meters between the potential electrodes are also shown in Figure 1.9b. The difference in the sounding curves with the spacings of 1 meter and 3 meters between the potential electrodes is small, particularly for large electrode spacings. Thus any shifting in the curve segments would not remove the distortion in the sounding curve due to the low resistivity prism. The method of shifting the curve segments is probably more applicable if the inhomogeneity lies between the central potential electrodes, and probably ineffective if the inhomogeneity is beyond the largest potential electrodes spacing used (which is the case in Figure 1.8). However, note that the effect of the prism on the Schlumberger array sounding curve is smaller at the larger electrode spacings compared with the Wenner array (Figure 1.9). The main reason is probably the larger distance between the P2 and C2 electrodes in the Schlumberger array.

A more reliable method to reduce the effect of lateral variations on the sounding data is the offset Wenner method (Barker 1978). It makes use of the property that the effect of an inhomogeneity on the apparent resistivity value is of opposite sign if it lies between the two

potential electrodes or if it is between a potential and a current electrode. For the example shown in Figure 1.8, if the low resistivity body lies in between a current and potential electrode (the P2 and C2 electrodes in this case), the measured apparent resistivity value would be lower. If the low resistivity body lies in between the P1 and P2 electrodes, it will cause the apparent resistivity value to be higher. The reason for this phenomenon can be found in the sensitivity pattern for the Wenner array (see Figure 2.10a). By taking measurements with different positions for the mid-point of the array, the effect of the low resistivity body can be reduced.

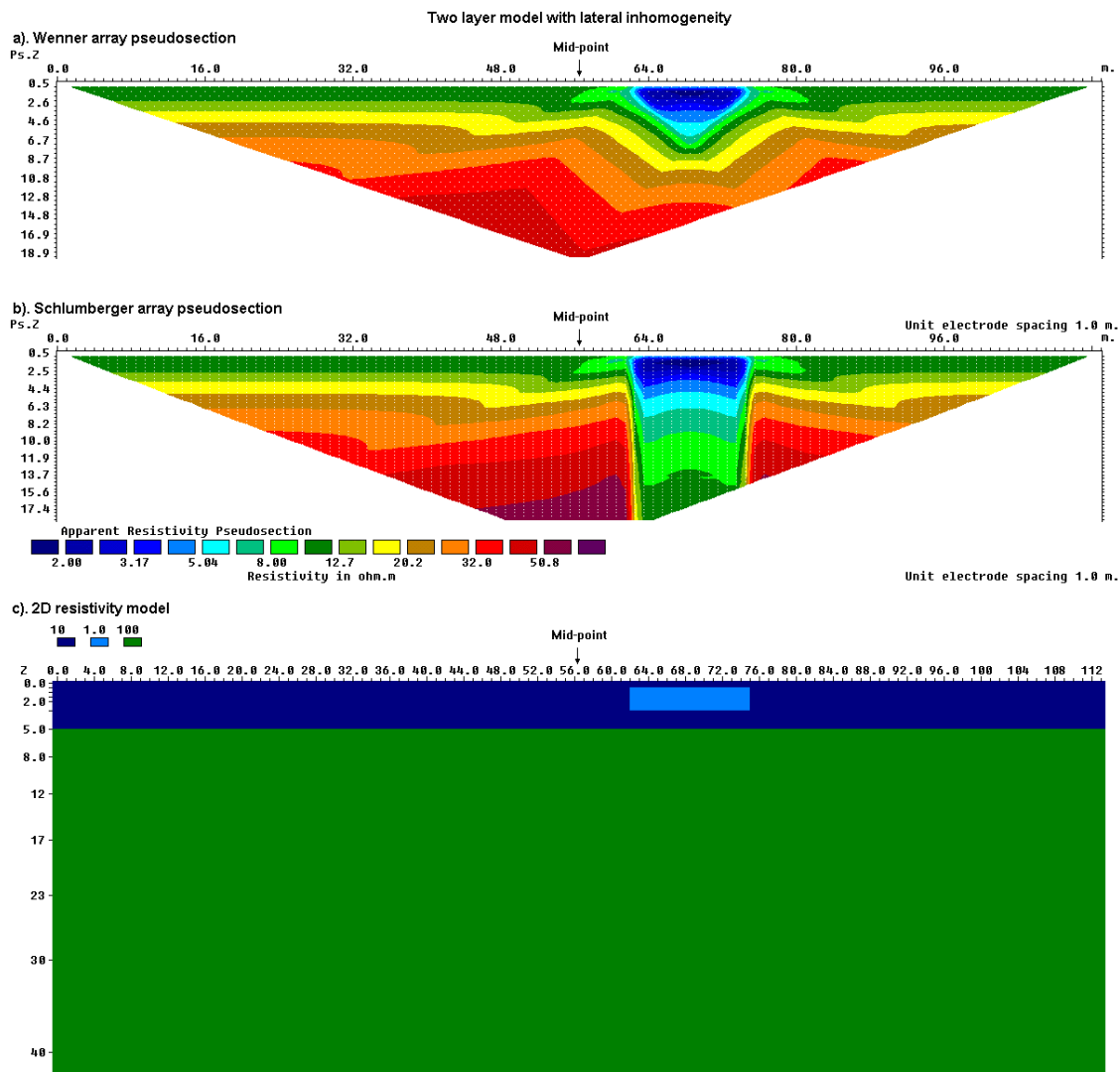


Figure 1.8. A 2-D two-layer model with a low resistivity prism in the upper layer. The calculated apparent resistivity pseudosections for the (a) Wenner and (b) Schlumberger arrays. (c) The 2D model. The mid-point for a conventional sounding survey is also shown.

Another classical survey technique is the profiling method. In this case, the spacing between the electrodes remains fixed, but the entire array is moved along a straight line. This gives some information about lateral changes in the subsurface resistivity, but it cannot detect vertical changes in the resistivity. Interpretation of data from profiling surveys is mainly qualitative.

The most severe limitation of the resistivity sounding method is that horizontal (or lateral) changes in the subsurface resistivity are commonly found. The ideal situation shown in Figure 1.6a is rarely found in practice. As shown by the examples in Figures 1.8 and 1.9, lateral changes in the subsurface resistivity will cause changes in the apparent resistivity values that might be, and frequently are, misinterpreted as changes with depth in the subsurface resistivity. In many engineering and environmental studies, the subsurface geology is very complex where the resistivity can change rapidly over short distances. The 1-D resistivity sounding method would not be sufficiently accurate for such situations.

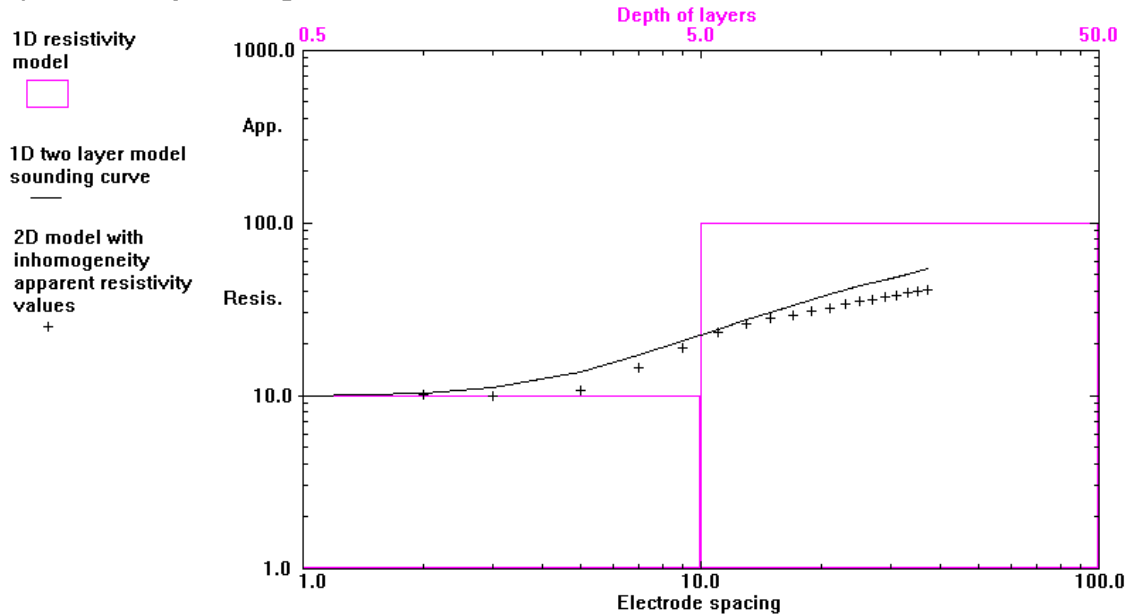
To use the RES1D.EXE program for the exercises in the table below, as well as the other programs that we shall use in the later sections, follows the usual sequence used by Windows XP/Vista. Click the ‘Start’ button, followed by ‘Programs’ and the look for the RES1D folder in the list of installed programs. Alternatively, you can create a shortcut icon on the Windows Desktop.

Exercise 1.1 : 1-D inversion examples using the RES1D.EXE program.

Data set and purpose	Things to try
WENNER3.DAT – A simple synthetic data file for a 3 layer model.	(1). Read in the file, and then run the “Carry out inversion” step.
WENN_LATERAL.DAT and SCHL_LATER.DAT – Wenner and Schlumberger array sounding data shown in Figure 1.9 that are extracted from the 2-D pseudosections.	(1). Read in the files, and then invert the data sets. (2). Compare the results with the true two-layer model (that has resistivities of 10 Ω -m and 100 Ω -m for the first and second layers, and thickness of 5 meters for the first layer).
WENOFFSET.DAT – A field data set collected using the offset Wenner method.	(1). Read in the files, and then invert the data set.
IPTESTM.DAT – A 1-D sounding data file with IP measurements as well to round things up.	(1). Read in the files, and then invert the data set.

To obtain a more accurate subsurface model than is possible with a simple 1-D model, a more complex model must be used. In a 2-D model (Figure 1.6b), the resistivity values are allowed to vary in one horizontal direction (usually referred to as the x direction) but assumed to be constant in the other horizontal (the y) direction. This approximation is reasonable for survey lines that are perpendicular to the strike of an elongated structure. The most realistic model would be a fully 3-D model (Figure 1.6c) where the resistivity values are allowed to change in all 3 directions. The use of 2-D and 3-D surveys and interpretation techniques will be examined in detail in the following chapters.

a). Wenner array sounding curve



b). Schlumberger array sounding curve

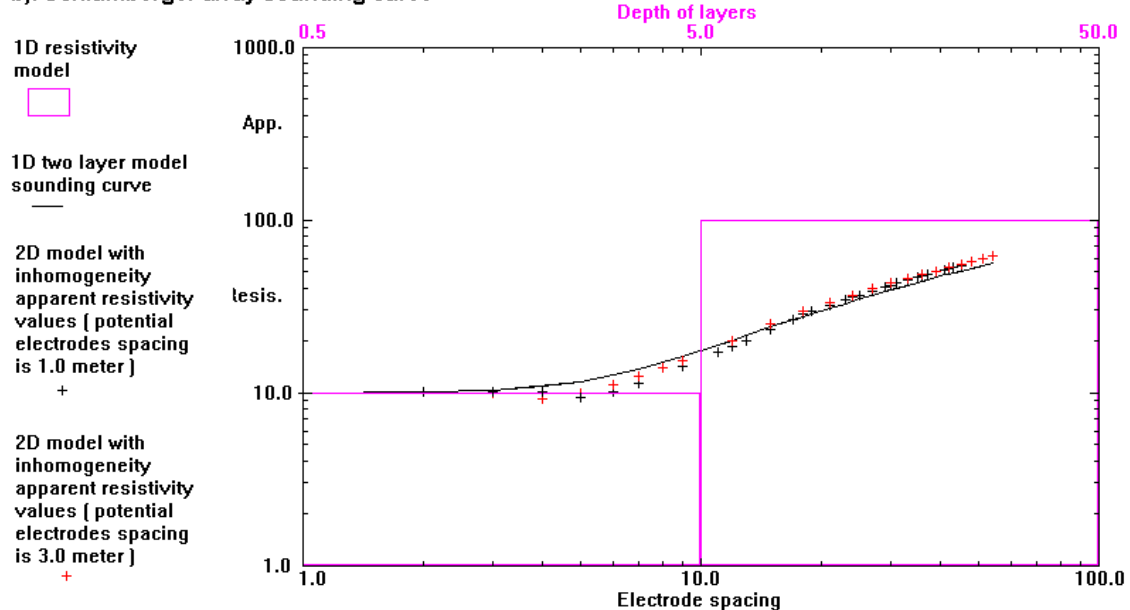


Figure 1.9. Apparent resistivity sounding curves for a 2-D model with a lateral inhomogeneity. (a) The apparent resistivity curve extracted from the 2D pseudosection for the Wenner array. The sounding curve for a two-layer model without the low resistivity prism is also shown by the black line curve. (b) The apparent resistivity curves extracted from the 2-D pseudosection for the Schlumberger array with a spacing of 1.0 meter (black crosses) and 3.0 meters (red crosses) between the potential electrodes. The sounding curve for a two-layer model without the low resistivity prism is also shown.

1.4 Basic Inverse Theory

In geophysical inversion, we seek to find a *model* that gives a response that is similar to the actual measured values. The model is an idealized mathematical representation of a section of the earth. The model has a set of *model parameters* that are the physical quantities we want to estimate from the observed *data*. The *model response* is the synthetic data that can be calculated from the mathematical relationships defining the model for a given set of model parameters. All inversion methods essentially try to determine a model for the subsurface whose response agrees with the measured data subject to certain restrictions and within acceptable limits. In the cell-based method used by the RES2DINV and RES3DINV programs, the model parameters are the resistivity values of the model cells, while the data is the measured apparent resistivity values. The mathematical link between the model parameters and the model response for the 2-D and 3-D resistivity models is provided by the finite-difference (Dey and Morrison 1979a, 1979b) or finite-element methods (Silvester and Ferrari 1990).

In all optimization methods, an initial model is modified in an iterative manner so that the difference between the model response and the observed data values is reduced. The set of observed data can be written as a column vector \mathbf{y} given by

$$\mathbf{y} = \text{col}(y_1, y_2, \dots, y_m) \quad (1.12)$$

where m is the number of measurements. The model response \mathbf{f} can be written in a similar form.

$$\mathbf{f} = \text{col}(f_1, f_2, \dots, f_m) \quad (1.13)$$

For resistivity problems, it is a common practice to use the logarithm of the apparent resistivity values for the observed data and model response, and the logarithm of the model values as the model parameters. The model parameters can be represented by the following vector

$$\mathbf{q} = \text{col}(q_1, q_2, \dots, q_n) \quad (1.14)$$

where n is the number of model parameters. The difference between the observed data and the model response is given by the discrepancy vector \mathbf{g} that is defined by

$$\mathbf{g} = \mathbf{y} - \mathbf{f} \quad (1.15)$$

In the least-squares optimization method, the initial model is modified such that the sum of squares error E of the difference between the model response and the observed data values is minimized.

$$E = \mathbf{g}^T \mathbf{g} = \sum_{i=1}^n g_i^2 \quad (1.16)$$

To reduce the above error value, the following Gauss-Newton equation is used to determine the change in the model parameters that should reduce the sum of squares error (Lines and Treitel 1984).

$$\mathbf{J}^T \mathbf{J} \Delta \mathbf{q}_i = \mathbf{J}^T \mathbf{g} \quad (1.17)$$

where $\Delta \mathbf{q}$ is the model parameter change vector, and \mathbf{J} is the Jacobian matrix (of size m by n) of partial derivatives. The elements of the Jacobian matrix are given by

$$J_{ij} = \frac{\partial f_i}{\partial q_j} \quad (1.18)$$

that is the change in the i th model response due to a change in the j th model parameter. After calculating the parameter change vector, a new model is obtained by

$$\mathbf{q}_{k+1} = \mathbf{q}_k + \Delta \mathbf{q}_k \quad (1.19)$$

In practice, the simple least-squares equation (1.17) is rarely used by itself in geophysical inversion. In some situations the matrix product $\mathbf{J}^T \mathbf{J}$ might be singular, and thus

the least-squares equation does not have a solution for $\Delta\mathbf{q}$. Another common problem is that the matrix product $\mathbf{J}^T\mathbf{J}$ is nearly singular. This can occur if a poor initial model that is very different from the optimum model is used. The parameter change vector calculated using equation (1.17) can have components that are too large such that the new model calculated with (1.19) might have values that are not realistic. One common method to avoid this problem is the Marquardt-Levenberg modification (Lines and Treitel 1984) to the Gauss-Newton equation that is given by

$$(\mathbf{J}^T\mathbf{J} + \lambda\mathbf{I})\Delta\mathbf{q}_k = \mathbf{J}^T\mathbf{g} \quad (1.20)$$

where \mathbf{I} is the identity matrix. The factor λ is known as the Marquardt or damping factor, and this method is also known as the ridge regression method (Inman 1975) or damped least-squares method. The damping factor effectively constrains the range of values that the components of parameter change vector can $\Delta\mathbf{q}$ take. While the Gauss-Newton method in equation (1.17) attempts to minimize the sum of squares of the discrepancy vector only, the Marquardt-Levenberg method also minimizes a combination of the magnitude of the discrepancy vector and the parameter change vector. This method has been successfully used in the inversion of resistivity sounding data where the model consists of a small number of layers. For example, it was used in the inversion of the resistivity sounding example in Figure 1.7 with three layers (i.e. five model parameters). However when the number of model parameters is large, such as in 2D and 3D inversion models that consist of a large number of small cells, the model produced by this method can have an erratic resistivity distribution with spurious high or low resistivity zones (Constable *et al.* 1987). To overcome this problem, the Gauss-Newton least-squares equation is further modified so as to minimize the spatial variations in the model parameters (i.e. the model resistivity values change in a smooth or gradual manner). This smoothness-constrained least-squares method (Ellis and Oldenburg 1994a) has the following mathematical form.

$$(\mathbf{J}^T\mathbf{J} + \lambda\mathbf{F})\Delta\mathbf{q}_k = \mathbf{J}^T\mathbf{g} - \lambda\mathbf{F}\mathbf{q}_k, \quad (1.21)$$

where $\mathbf{F} = \alpha_x\mathbf{C}_x^T\mathbf{C}_x + \alpha_y\mathbf{C}_y^T\mathbf{C}_y + \alpha_z\mathbf{C}_z^T\mathbf{C}_z$

and \mathbf{C}_x , \mathbf{C}_y and \mathbf{C}_z are the smoothing matrices in the x -, y - and z -directions. α_x , α_y and α_z are the relative weights given to the smoothness filters in the x -, y - and z -directions. One common form of the smoothing matrix is the first-order difference matrix (please refer to the paper by deGroot-Hedlin and Constable, 1990 for the details) that is given by

$$\mathbf{C} = \begin{bmatrix} -1 & 1 & 0 & 0 & \dots & \dots & \dots & 0 \\ 0 & -1 & 1 & 0 & \dots & \dots & \dots & 0 \\ 0 & 0 & -1 & 1 & 0 & \dots & \dots & 0 \\ & & & \dots & & & & \\ & & & & \dots & & & \\ & & & & & \dots & & \\ & & & & & & \dots & \\ & & & & & & & \dots \\ & & & & & & & \mathbf{0} \end{bmatrix} \quad (1.22)$$

Equation 1.21 also tries to minimize the *square* of the spatial changes, or roughness, of the model resistivity values. It is in fact an l_2 norm smoothness-constrained optimization method. This tends to produce a model with a smooth variation of resistivity values. This approach is acceptable if the actual subsurface resistivity varies in a smooth or gradational manner. In some cases, the subsurface geology consists of a number of regions that are

internally almost homogeneous but with sharp boundaries between different regions. For such cases, the inversion formulation in (1.21) can be modified so that it minimizes the *absolute* changes in the model resistivity values (Claerbout and Muir 1973). This can sometimes give significantly better results. Technically this is referred to as an l_1 norm smoothness-constrained optimization method, or more commonly known as the blocky inversion method. A number of techniques can be used for such a modification. One simple method to implement an l_1 norm based optimization method using the standard least-squares formulation is the iteratively reweighted least-squares method (Wolke and Schwetlick, 1988). The optimization equation in (1.21) is modified to

$$(\mathbf{J}^T \mathbf{J} + \lambda \mathbf{F}_R) \Delta \mathbf{q}_k = \mathbf{J}^T \mathbf{R}_d \mathbf{g} - \lambda \mathbf{F}_R \mathbf{q}_k, \quad (1.23)$$

with $\mathbf{F}_R = \alpha_x \mathbf{C}_x^T \mathbf{R}_m \mathbf{C}_x + \alpha_y \mathbf{C}_y^T \mathbf{R}_m \mathbf{C}_y + \alpha_z \mathbf{C}_z^T \mathbf{R}_m \mathbf{C}_z$

where \mathbf{R}_d and \mathbf{R}_m are weighting matrices introduced so that different elements of the data misfit and model roughness vectors are given equal weights in the inversion process.

Equation (1.23) provides a general method that can be further modified if necessary to include known information about the subsurface geology. As an example, if it is known that the variations in the subsurface resistivity are likely to be confined to a limited zone, the damping factor values can be modified (Ellis and Oldenburg 1994a) such that greater changes are allowed in that zone.

1.5 2-D model discretization methods

In the previous section, we have seen that the least-squares method is used to calculate certain physical characteristics of the subsurface (the “model parameters”) from the apparent resistivity measurements. The “model parameters” are set by the way we slice and dice the subsurface into different regions. Figure 1.10 shows various possibilities that can be used. The method most commonly used in 2-D (and 3-D) interpretation is a purely cell based model where the subsurface is subdivided into rectangular cells. The positions of the cells are fixed and only the resistivities of cells are allowed to vary during the inversion process. The model parameters is the resistivity of each cell. In the example shown in Figure 1.10, the model parameters are the seventy-two cell resistivity values ρ_1 to ρ_{72} .

A radically different approach is a boundary based inversion method. This method subdivides the subsurface into different regions. The resistivity is assumed to be homogenous within each region. The resistivity is allowed to change in an arbitrary manner across the boundaries, and thus it useful in areas with abrupt transitions in the geology. The resistivity of each region and the depths to the boundaries are changed by the least-squares optimization method so that the calculated apparent resistivity values match the observed values. The “model parameters” for the example shown in Figure 1.10 are the two resistivity values (ρ_1 and ρ_2) and the depths at five points (z_1 to z_5) along the boundary that gives a total of seven parameters. While this method works well for synthetic data from numerical models, for many field data sets it can lead to unstable results with highly oscillating boundaries (Olayinka and Yaramanci, 2000). Its greatest limitation is probably the assumption of a constant resistivity within each region. In particular, lateral changes in the resistivity near the surface have a very large effect on the measured apparent resistivity values. Since this model does not take into account such lateral changes, they are often mistakenly modeled as changes in the depths of the boundaries.

More recent efforts have been in combining the cell based and boundary based inversion methods (Smith et al., 1999). One such method is the laterally constrained

inversion method (Auken and Christiansen, 2004). In this method, lateral changes (but not vertical changes) are allowed in each region (Figure 1.10c), and abrupt transitions across the boundaries are also allowed. The “model parameters” for the example in Figure 1.10 are then the twenty-four resistivity values (ρ_1 and ρ_{24}) and the depths at thirteen points (z_1 to z_{13}) along the boundary giving a total of thirty-seven parameters. Information from other sources, such as borehole or seismic data, can be used to provide an initial estimate of the depth to the boundary. A common situation is when the depth information is available at only one borehole. In this case, the initial boundary is usually set a constant depth. The inversion method then adjusts the depths at a number of points along the boundary during the inversion process. A smoothness-constraint is applied to minimize changes in the depths between adjacent points on the same boundary (Smith et al., 1999). This method works particularly well where the subsurface consists of several sedimentary zones.

A further generalization of this concept is to allow both vertical and lateral changes within each region (as in a pure cell based model) while also allowing sharp changes across the boundaries (Figure 1.10d). The model shown in Figure 1.10d has seventy-two resistivity values and five depth values, giving a total of seventy-seven model parameters. This type of discretization is particularly useful where near-surface inhomogeneities that occur at different depths within the top layer have a large effect on the measured apparent resistivity values. The model cells used so far has rectangular shapes (Figures 1.10a, 1.10c and 1.10d). This is partly due to the use of the finite-difference method in calculating the model apparent resistivity values. A slight disadvantage is that the boundary is approximated by a series of rectangular steps. Figure 1.10e shows a possible variation using the finite-element method with trapezoidal cells where the edges of the cells adjacent to the boundary are adjusted so as to conform to the true shape of the boundary.

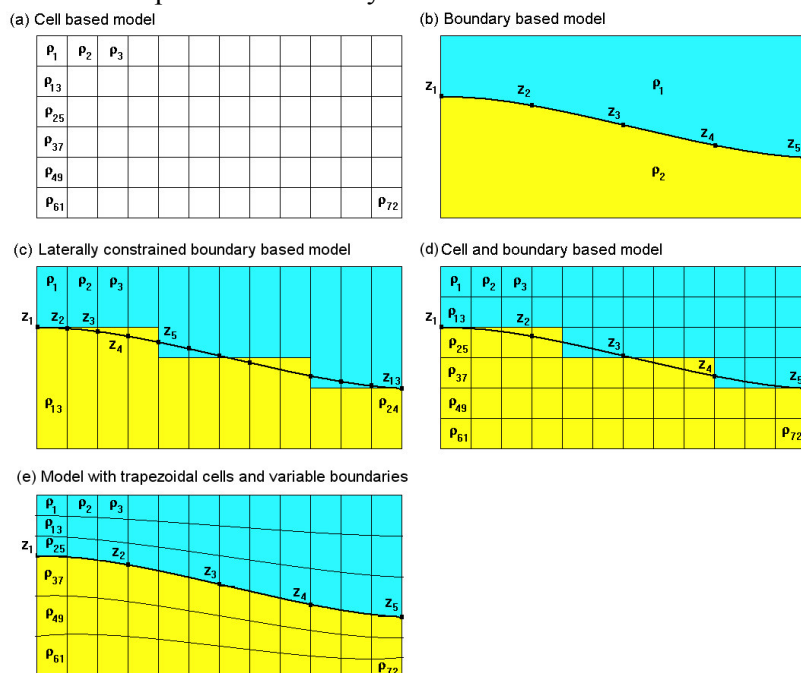


Figure 1.10. The different models for the subsurface used in the interpretation of data from 2-D electrical imaging surveys. (a) A purely cell based model. (b) A purely boundary based model. (c) The laterally constrained model. (d) A combined cell based and boundary based model with rectangular cells, and (e) with boundary conforming trapezoidal cells.

2 2-D electrical surveys – Data acquisition, presentation and arrays

2.1 Introduction

We have seen that the greatest limitation of the resistivity sounding method is that it does not take into account horizontal changes in the subsurface resistivity. A more accurate model of the subsurface is a two-dimensional (2-D) model where the resistivity changes in the vertical direction, as well as in the horizontal direction along the survey line. In this case, it is assumed that resistivity does not change in the direction that is perpendicular to the survey line. In many situations, particularly for surveys over elongated geological bodies, this is a reasonable assumption. In theory, a 3-D resistivity survey and interpretation model should be even more accurate. However, at the present time, 2-D surveys are the most practical economic compromise between obtaining very accurate results and keeping the survey costs down (Dahlin 1996). Typical 1-D resistivity sounding surveys usually involve about 10 to 20 readings, while 2-D imaging surveys involve about 100 to 1000 measurements. In comparison, a 3-D survey might involve several thousand measurements.

The cost of a typical 2-D survey could be several times the cost of a 1-D sounding survey, and is probably comparable with a seismic refraction survey. In many geological situations, 2-D electrical imaging surveys can give useful results that are complementary to the information obtained by other geophysical methods. For example, seismic methods can map undulating interfaces well, but will have difficulty (without using advanced data processing techniques) in mapping discrete bodies such as boulders, cavities and pollution plumes. Ground radar surveys can provide more detailed pictures but have very limited depth penetration in areas with conductive unconsolidated sediments, such as clayey soils. Two-dimensional electrical surveys can be used in conjunction with seismic or GPR surveys as they provide complementary information about the subsurface.

2.2 Field survey method - instrumentation and measurement procedure

Two-dimensional electrical imaging/tomography surveys are usually carried out using a large number of electrodes, 25 or more, connected to a multi-core cable (Griffiths and Barker 1993). A resistivity meter system with an internal microprocessor controlled circuitry together with an electronic switching unit is commonly used to automatically select the relevant four electrodes for each measurement (Figure 2.1). At present, field techniques and equipment to carry out 2-D resistivity surveys are fairly well developed. The necessary field equipment is commercially available from a number of companies. These systems typically costs from about US\$15,000 upwards. Some institutions have even constructed “home-made” manually operated switching units at a nominal cost by using a seismic cable as the multi-core cable!

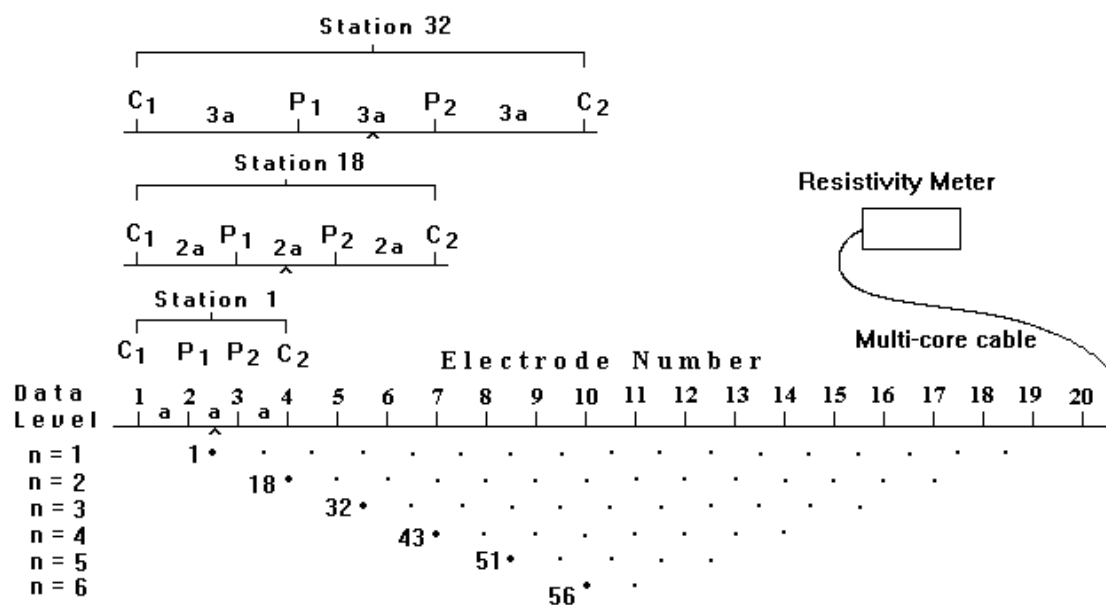
Figure 2.1 shows the typical setup for a 2-D survey with a number of electrodes along a straight line attached to a multi-core cable. Normally a constant spacing between adjacent electrodes is used. The multi-core cable is attached to an integrated resistivity meter system that includes an electronic switching unit. The sequence of measurements to take, the type of array used and other survey parameters (such the current to use) is normally transferred to an internal microprocessor system within the resistivity meter from a personal computer. After reading the control file, the control program then automatically selects the appropriate electrodes for each measurement.

In a typical survey, most of the fieldwork is in laying out the cable and electrodes. After that, the measurements are taken automatically and stored in the resistivity meter system. Most of the survey time is spent waiting for the resistivity meter to complete the set

of measurements!

To obtain a good 2-D picture of the subsurface, the coverage of the measurements must be 2-D as well. As an example, Figure 2.1 shows a possible sequence of measurements for the Wenner electrode array for a system with 20 electrodes. In this example, the spacing between adjacent electrodes is “ a ”. The first step is to make all the possible measurements with the Wenner array with an electrode spacing of “ $1a$ ”. For the first measurement, electrodes number 1, 2, 3 and 4 are used. Notice that electrode 1 is used as the first current electrode C1, electrode 2 as the first potential electrode P1, electrode 3 as the second potential electrode P2 and electrode 4 as the second current electrode C2. For the second measurement, electrodes number 2, 3, 4 and 5 are used for C1, P1, P2 and C2 respectively. This is repeated down the line of electrodes until electrodes 17, 18, 19 and 20 are used for the last measurement with “ $1a$ ” spacing. For a system with 20 electrodes, note that there are 17 ($20 - 3$) possible measurements with “ $1a$ ” spacing for the Wenner array.

After completing the sequence of measurements with “ $1a$ ” spacing, the next sequence of measurements with “ $2a$ ” electrode spacing is made. First electrodes 1, 3, 5 and 7 are used for the first measurement. The electrodes are chosen so that the spacing between adjacent electrodes is “ $2a$ ”. For the second measurement, electrodes 2, 4, 6 and 8 are used. This process is repeated down the line until electrodes 14, 16, 18 and 20 are used for the last measurement with spacing “ $2a$ ”. For a system with 20 electrodes, note that there are 14 ($20 - 2 \times 3$) possible measurements with “ $2a$ ” spacing.



Sequence of measurements to build up a pseudosection

Figure 2.1. The arrangement of electrodes for a 2-D electrical survey and the sequence of measurements used to build up a pseudosection.

The same process is repeated for measurements with “ $3a$ ”, “ $4a$ ”, “ $5a$ ” and “ $6a$ ” spacings. To get the best results, the measurements in a field survey should be carried out in a systematic manner so that, as far as possible, all the possible measurements are made. This will affect the quality of the interpretation model obtained from the inversion of the apparent resistivity measurements (Dahlin and Loke 1998).

2.3 Available field instruments

Over the last 15 years, there has been a steady growth in the number of commercial companies that offer systems for resistivity imaging surveys. The ones that I have come across are listed below in alphabetical order together with the web site address where available.

Manufacturer	Instrument Type		
	Static	Dynamic	IP
Abem Instruments, Sweden (www.abem.se)	x		Y
Advanced Geophysical Instruments, USA (www.agiusa.com)	x		Y
Campus Geophysical Instruments, UK	x		Y
Geofyzika., Czech Republic (www.geofyzika.com)	x		
GF Instruments, Czech Republic (www.gfinstruments.cz)	x		Y
Geometrics, USA (www.geometrics.com)		x	
Geolog, Germany (www.geolog2000.de)	x		
IDS Scintrex, Canada (www.ids-detection.com)	x		Y
Iris Instruments, France (www.iris-instruments.com)	x	x	Y
OYO, Japan	x		
Pasi Geophysics, Italy (www.pasigeophysics.com)	x		Y
MAE srl, Italy (www.mae-srl.it)	x		Y

Most of the above manufacturers have sub-agents in different countries, and there are probably a few others that I have not come across. A few academic and research institutions have designed their own systems, for example the British Geological Survey have built an electrostatic based mobile system.

The instrument type can be divided into two broad categories, static and dynamic systems. Most instruments are of the static type where many electrodes are connected to a multi-electrode cable and planted into the ground during the survey. A typical static system is the Abem Lund system shown in Figure 2.3. One common configuration is a split spread type of cable connection to the switching unit at the center to reduce the individual cable length and weight. The weight of a cable roll is directly proportional to the number of nodes and the spacing between the nodes! A common spacing used for most engineering and environmental surveys is 5 meters. Most systems come with a minimum of 28 nodes, with some system having up to 128 nodes or more! The Lund system is a little unusual in that there are 4 individual cables. Most systems use a 2 cables arrangement. The static systems can be further divided into two sub-categories depending on the arrangement for the switching of the electrodes. Most of the systems house the switches in a single unit and uses a cable with many individual wires connected to each node. Typical examples are the Abem Lund and Campus Geopulse systems. Another arrangement is to have a small switching unit at each electrode and a cable with the minimum number of wires. One early example is the Campus MRT system (Griffiths and Turnbull, 1985). More recent examples are the PASI and Iris Syscal systems.

There have been two new and interesting developments in the resistivity meter systems. One is the addition of I.P. capability. However, the usefulness of the I.P. data from most multi-electrode systems is of limited use. Most systems use a battery power source that cannot deliver enough current (usually less than 1 ampere) for reliable I.P. signals, so the I.P.

data is often extremely noisy.

The second new development is multi-channel measuring systems. In such a system, a number of potential measurements can be simultaneously made for a single pair of current electrodes. This could significantly reduce the survey time. With certain array configurations, a single 2-D survey line could involve thousands of measurements. The major part of the survey time is waiting for a single channel instrument to complete the measurements that could take more than several hours! The IP and multi-channel capability are relatively new developments, so you will need to check the manufacturer's web site to get the latest information.

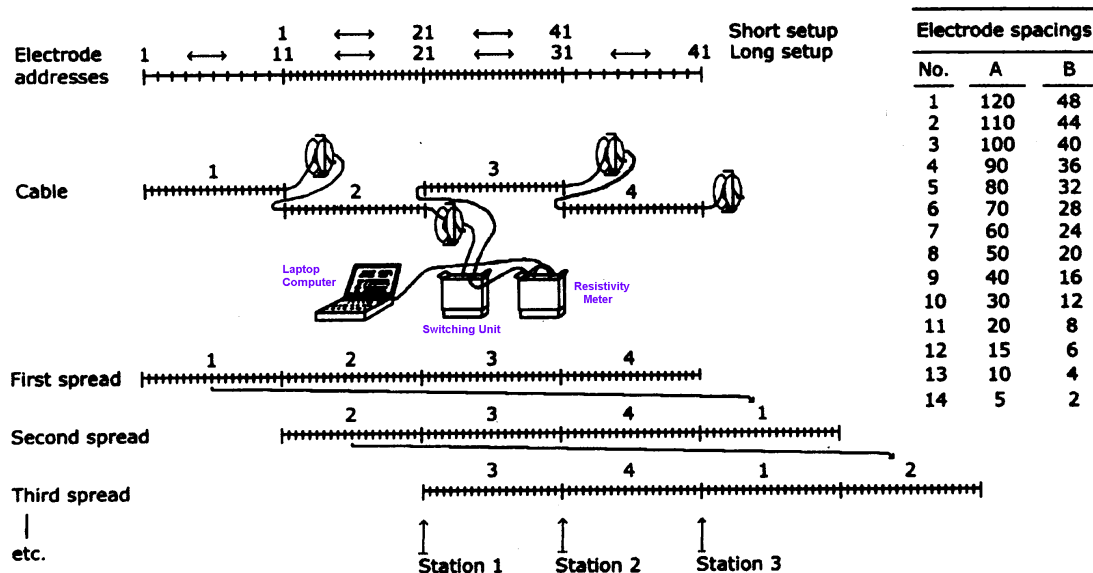


Figure 2.3. Sketch outline of the ABEM Lund Imaging System. Each mark on the cables indicates an electrode position (Dahlin 1996). The cables are placed along a single line (the sideways shift in the figure is only for clarity). This figure also shows the principle of moving cables when using the roll-along technique. The total layout length depends on the spacing between the nodes, but is usually between 160 meters and 800 meters.

Static systems use a large number of nodes to get a wide data coverage. In contrast, dynamic systems use a small number of nodes but move the entire system to obtain a wide coverage. An example of such a system designed by Aarhus University in Denmark (Sorenson 1996) is shown in Figure 2.4. A 100 meters cable with nine heavy cylindrical electrodes is pulled by a small vehicle. Two of the electrodes are used as current electrodes, while six of them are used for the potential measurements and one is used as a ground electrode. This system relies on the current being injected into the ground by direct contact, so it can only be used in open ground, such as farmlands in Northern Europe. A Wenner-Schlumberger type of arrangement (Figure 1.4) is used but with non-integer “ n ” values for some of the measurements. Another mobile system that does not require direct contact with the ground but uses capacitive coupling (Gerard and Tabbagh 1991, Shima *et al.* 1996, Panissod *et al.* 1998) to induce the flow of current in the ground. This system can be used in areas that are paved, such as roads and city areas. One such system shown in Figure 2.5 is the Geometrics OhmMapper system where a cable with 4 to 6 electrodes attached to a measuring unit is pulled by a single operator. The dipole-dipole type of arrangement is used but with non-integer “ n ” values for some measurements.

One of main problems faced by mobile systems on land to get sufficient current to flow into the ground. Direct contact systems such as the Aarhus Pulled Array System can only be used in areas with open ground. The capacitive coupling type does not require direct ground contact and thus can be used in many areas where normal resistivity surveying systems cannot be used (for example in built-up areas) but has the problem of a more limited depth of penetration due to the limited amount of current that can be induced into the ground compared to direct contact systems. An underwater environment provides an almost ideal situation for a direct contact type of mobile system since there is no problem in obtaining good electrode contact! Figure 2.6 shows a possible arrangement for an underwater mobile surveying system where a cable with a number of nodes is pulled along the river/lake/sea bottom by a boat. Two of the nodes are used as current electrodes, while the rest are used as potential electrodes. An example of such an underwater survey is described in section 7.9. If this system is coupled with a multi-channel resistivity meter, the survey can be carried out very rapidly. Shallow seismic reflection surveys are frequently used in rivers/lakes/marine environments for engineering site surveys. A mobile resistivity survey might be a useful addition in some situations, such as in seismically opaque areas. In theory, both surveys can be carried out simultaneously to reduce costs.

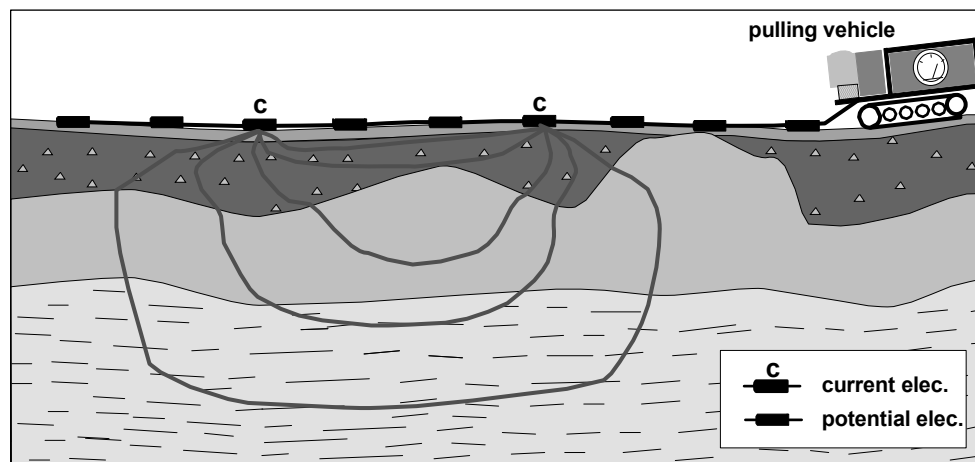


Figure 2.4. The Aarhus Pulled Array System. The system shown has two current (C) electrodes and six potential electrodes (Christensen and Sørensen 1998, Bernstone and Dahlin 1999).

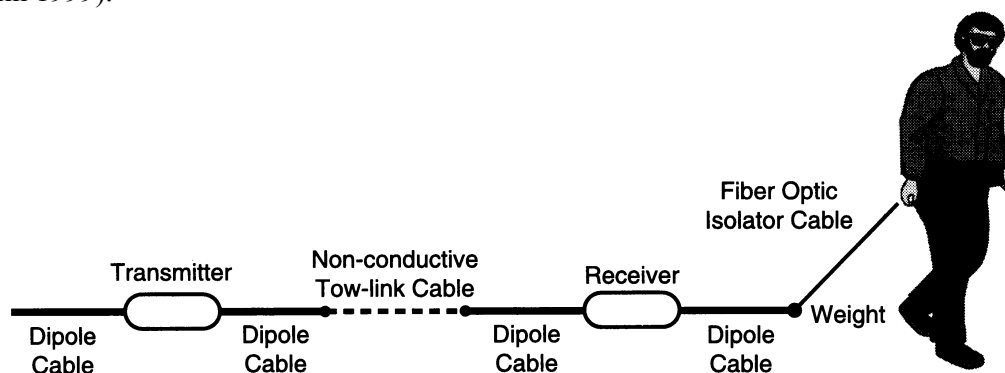


Figure 2.5. The Geometrics OhmMapper system using capacitive coupled electrodes. (Courtesy of Geometrics Inc.)

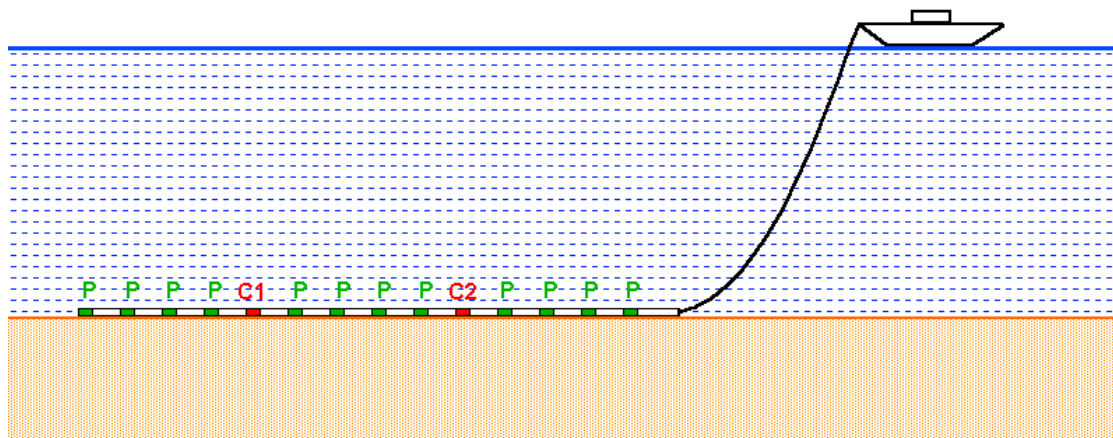


Figure 2.6. Schematic diagram of a possible mobile underwater survey system. The cable has two fixed current electrodes and a number of potential electrodes so that measurements can be made at different spacings. The above arrangement uses the Wenner-Schlumberger type of configuration. Other configurations, such as the gradient array, can also be used.

2.4 Pseudosection data plotting method

To plot the data from a 2-D imaging survey, the pseudosection contouring method is normally used. In this case, the horizontal location of the point is placed at the mid-point of the set of electrodes used to make that measurement. The vertical location of the plotting point is placed at a distance that is proportional to the separation between the electrodes. For IP surveys using the dipole-dipole array, one common method is to place the plotting point at the intersection of two lines starting from the mid-point of the C1-C2 and P1-P2 dipole pairs with a 45° angle to the horizontal. It is important to emphasize that this is merely a plotting convention, and it does not imply that the depth of investigation is given by the point of intersection of the two 45° angle lines (it certainly does not imply the current flow or isopotential lines have a 45° angle with the surface). Surprisingly, this is still a common misconception, particularly in North America!

Another method is to place the vertical position of the plotting point at the median depth of investigation (Edwards 1977), or pseudodepth, of the electrode array used. This pseudodepth value is based on the sensitivity values or Frechet derivative for a homogeneous half space. Since it appears to have some mathematical basis, this method that is used in plotting the pseudosections in the later part of these lecture notes. The pseudosection plot obtained by contouring the apparent resistivity values is a convenient means to display the data.

The pseudosection gives a very approximate picture of the true subsurface resistivity distribution. However the pseudosection gives a distorted picture of the subsurface because the shapes of the contours depend on the type of array used as well as the true subsurface resistivity (Figure 2.7). The pseudosection is useful as a means to present the measured apparent resistivity values in a pictorial form, and as an initial guide for further quantitative interpretation. One common mistake made is to try to use the pseudosection as a final picture of the true subsurface resistivity. As Figure 2.7 shows, different arrays used to map the same region can give rise to very different contour shapes in the pseudosection plot. Figure 2.7 also gives you an idea of the data coverage that can be obtained with different arrays. Note that the pole-pole array gives the widest horizontal coverage, while the coverage obtained by the Wenner array decreases much more rapidly with increasing electrode spacing.

One useful practical application of the pseudosection plot is for picking out bad

apparent resistivity measurements. Such bad measurements usually stand out as points with unusually high or low values.

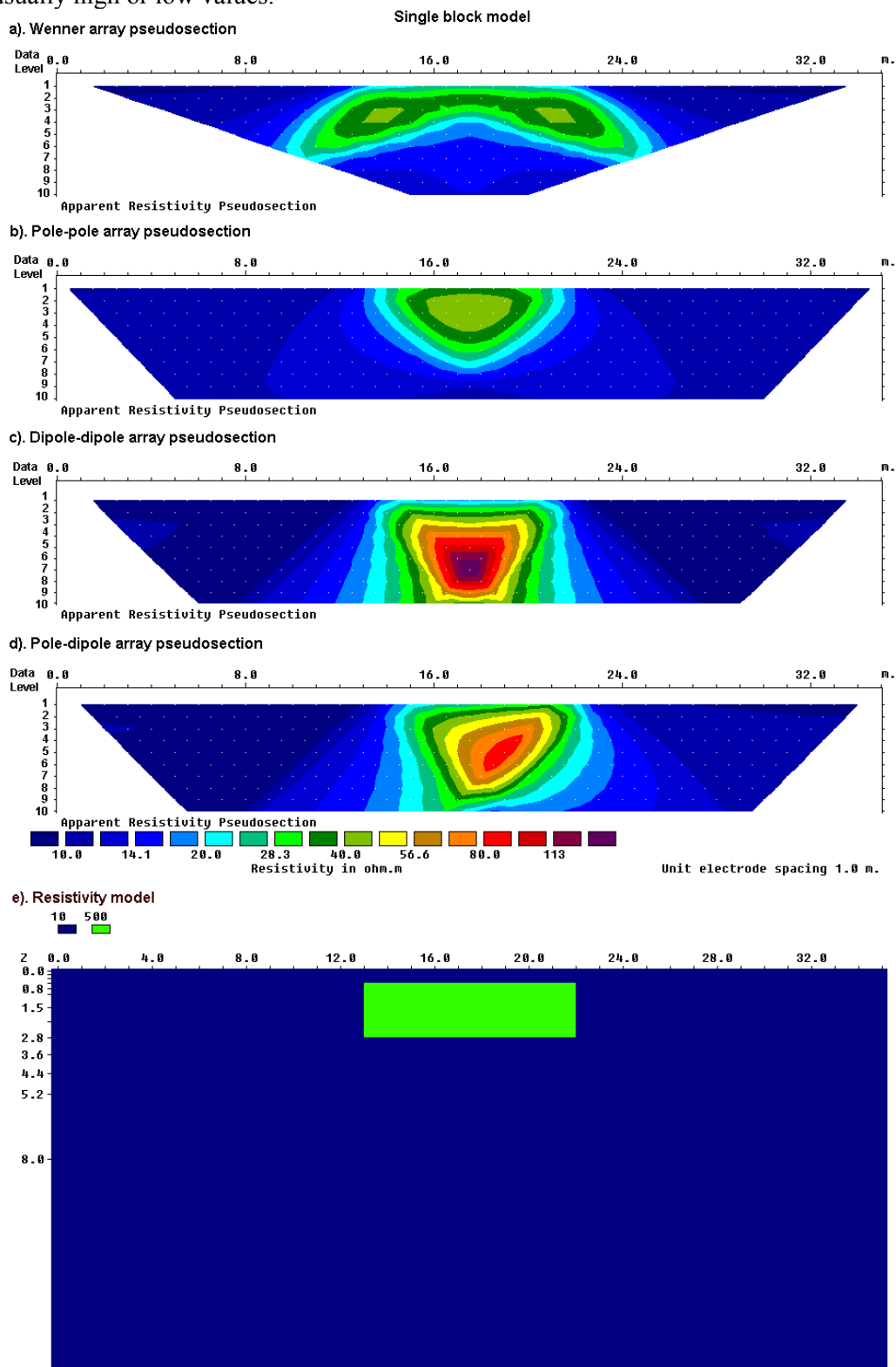


Figure 2.7. The apparent resistivity pseudosections from 2-D imaging surveys with different arrays over a rectangular prism.

2.5 A comparison of the different electrode arrays

As shown earlier in Figure 2.7, the shape of the contours in the pseudosection produced by the different arrays over the same structure can be very different. The arrays most commonly used for resistivity surveys were shown in Figure 1.4. The choice of the “best” array for a field survey depends on the type of structure to be mapped, the sensitivity of the resistivity meter and the background noise level. In practice, the arrays that are most commonly used for 2-D imaging surveys are the (a) Wenner, (b) dipole-dipole (c) Wenner-Schlumberger (d) pole-pole and (d) pole-dipole. Among the characteristics of an array that should be considered are (i) the depth of investigation, (ii) the sensitivity of the array to vertical and horizontal changes in the subsurface resistivity, (iii) the horizontal data coverage and (iv) the signal strength.

2.5.1 The Frechet derivative for a homogeneous half-space

The first two characteristics can be determined from the sensitivity function of the array for a homogeneous earth model. The sensitivity function basically tells us the degree to which a change in the resistivity of a section of the subsurface will influence the potential measured by the array. The higher the value of the sensitivity function, the greater is the influence of the subsurface region on the measurement. Mathematically, the sensitivity function is given by the Frechet derivative (McGillivray and Oldenburg 1990). Consider the simplest possible array configuration shown in Figure 2.8 with just one current located at the origin $(0,0,0)$ and one potential electrode located at $(a,0,0)$, i.e. both electrodes are on the ground surface and they are “ a ” meters apart. We inject 1 ampere of current into the ground through the C1 current electrode that results in a potential ϕ observed at the potential P1 electrode. Suppose we were to change the resistivity within a small volume of the ground located at (x,y,z) by a small amount, say $\delta\rho$. What would be the corresponding change in the potential, $\delta\phi$, measured at P1? It can be shown (Loke and Barker 1995) that this is given by

$$\delta\phi = \frac{\delta\rho}{\rho^2} \int_V \nabla\phi \cdot \nabla\phi' d\tau \quad (2.1)$$

where the change in the resistivity has a constant value in a small volume element $d\tau$ and zero elsewhere. The parameter ϕ' is the potential resulting from a current electrode located at the position of the P1 potential electrode. For the special case of a homogeneous half-space, the potential ϕ at a point in the half-space due to a unit current source on the surface has a relatively simple form, which is

$$\phi = \frac{\rho}{2\pi(x^2 + y^2 + z^2)^{0.5}}, \text{ and similarly} \quad (2.2)$$

$$\phi' = \frac{\rho}{2\pi[(x-a)^2 + y^2 + z^2]^{0.5}}$$

After differentiating the above equations to obtain the divergence, and substituting into (2.1) we get

$$\frac{\delta\phi}{\delta\rho} = \int_V \frac{1}{4\pi^2} \cdot \frac{x(x-a) + y^2 + z^2}{[x^2 + y^2 + z^2]^{1.5} [(x-a)^2 + y^2 + z^2]^{1.5}} dx dy dz \quad (2.3)$$

The 3-D Frechet derivative is then given by the term within the integral, i.e.

$$F_{3D}(x, y, z) = \frac{1}{4\pi^2} \cdot \frac{x(x-a) + y^2 + z^2}{[x^2 + y^2 + z^2]^{1.5} [(x-a)^2 + y^2 + z^2]^{1.5}} \quad (2.4)$$

This gives the Frechet derivative or sensitivity function for the pole-pole array consisting of just one current and one potential electrode. To obtain the Frechet derivative for a general four electrodes array, we need to just add up the contributions from the four current-potential pairs, just as we have done earlier for the potential in equation (1.8).

2.5.2 A 1-D view of the sensitivity function - depth of investigation

In resistivity sounding surveys, it is well known as the separation between the electrodes is increased, the array senses the resistivity of increasingly deeper layers. One common question is – What is a depth of investigation of an array? One quantitative means to put a numerical value for the depth of investigation is by using the sensitivity function or Frechet derivative of the array. In resistivity sounding surveys, the subsurface is assumed to consist of horizontal layers. What we want to determine is the change in the potential as measured by the array on the surface if the resistivity of a thin horizontal is changed. For a horizontal layer, the x and y limits of the layer extends from $-\infty$ to $+\infty$. Thus the sensitivity function for a thin horizontal layer is obtained by integrating the 3D sensitivity function given in equation (2.4) in the x and y directions, i.e.

$$F_{1D}(z) = \frac{1}{4\pi^2} \int_{-\infty}^{+\infty} \int_{-\infty}^{+\infty} \frac{x(x-a) + y^2 + z^2}{[x^2 + y^2 + z^2]^{1.5} [(x-a)^2 + y^2 + z^2]^{1.5}} dx dz$$

The above equation has a simple analytical solution (Roy and Apparao 1971), which is given by

$$F_{1D}(z) = \frac{2}{\pi} \cdot \frac{z}{(a^2 + 4z^2)^{1.5}} \quad (2.5)$$

The above function is also known as the depth investigation characteristic and has been used by many authors to determine the properties of various arrays in resistivity sounding surveys (Edwards 1977, Barker 1991, Merrick 1997). Figure 2.9a shows a plot of this function. Note that it starts from zero and then increases to a maximum value at a depth of about $0.35a$ and then decreases asymptotically to zero. Some authors have used the maximum point as the depth of investigation of the array. However, Edwards (1977) and Barker (1991) have shown that a more robust estimate is the "median depth of investigation". It is the depth above which the area under the curve is equal to half the total area under the curve. In layman's terms, the upper section of the earth above the "median depth of investigation" has the same influence on the measured potential as the lower section. This tells us roughly how deep we can see with an array. This depth does not depend on the measured apparent resistivity or the resistivity of the homogeneous earth model. It should be noted that the depths are strictly only valid for a homogeneous earth model, but they are probably good enough for planning field surveys. If there are large resistivity contrasts near the surface, the actual depth of investigation could be somewhat different.

The sensitivity function for other arrays can be determine by adding up the contributions from the appropriate four pairs of current-potential electrodes. Figure 2.9b shows the sensitivity function plot for the Wenner (alpha) array. Note that the curve around the maximum is narrower for the Wenner array compared with the pole-pole array. This implies that the Wenner array has a better vertical resolution than the pole-pole array.

Table 2.1 gives the median depth of investigation for the different arrays. To determine the maximum depth mapped by a particular survey, multiply the maximum “ a ” electrode spacing, or maximum array length “ L ”, by the appropriate depth factor given in

Table 2. For example, if the maximum electrode “ a ” spacing used by the Wenner array is 100 meters (or maximum L 300 meters), then the maximum depth mapped is about 51 meters. For the dipole-dipole, pole-dipole and Wenner-Schlumberger arrays, the “ n ” factor (Figure 1.4) must also be taken into consideration. For the arrays with four active electrodes (such as the dipole-dipole, Wenner and Wenner-Schlumberger arrays), it is probably easier to use the total array length “ L ”. As an example, if a dipole-dipole survey uses a maximum value of 10 meters for “ a ” and a corresponding maximum value of 6 for n , then the maximum “ L ” value is 80 meters. This gives a maximum depth of investigation of 80×0.216 or about 17 meters.

Table 2.1 also includes the geometric factor for the various arrays for an “ a ” spacing of 1.0 metre. The inverse of the geometric factor gives an indication of the voltage that would be measured between the P1 and P2 potential electrodes. The ratio of this potential compared to the Wenner alpha array is also given, for example a value of 0.01 means that the potential is 1% of the potential measured by the Wenner alpha array with the same “ a ” spacing.

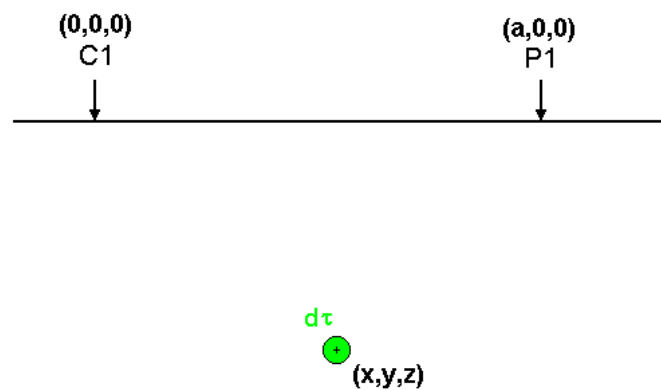


Figure 2.8. The parameters for the sensitivity function calculation at a point (x,y,z) within a half-space. A pole-pole array with the current electrode at the origin and the potential electrode “ a ” meters away is shown.

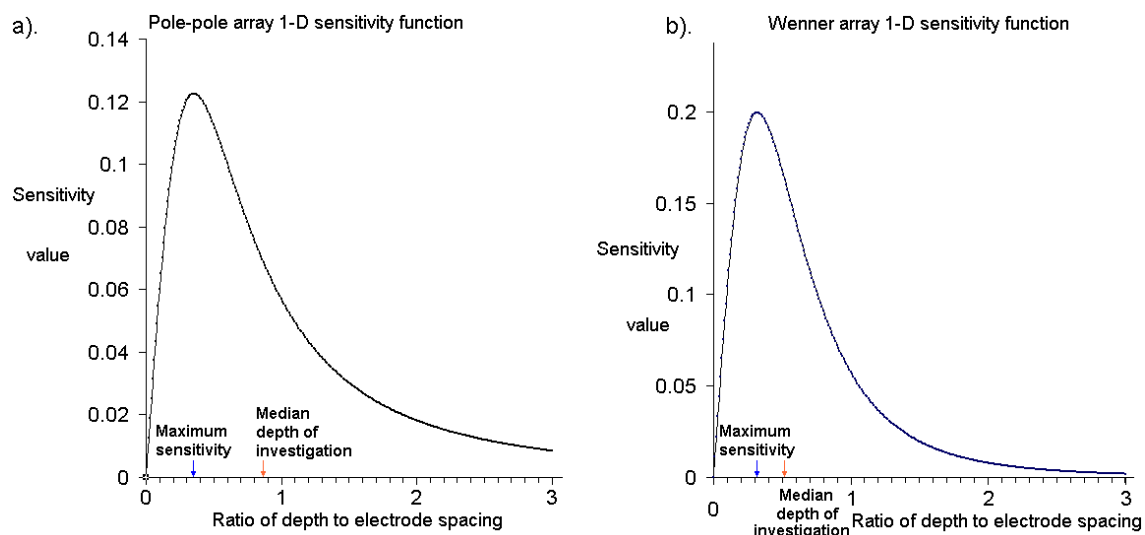


Figure 2.9. A plot of the 1-D sensitivity function. (a) The sensitivity function for the pole-pole array. Note that the median depth of investigation (red arrow) is more than twice the depth of maximum sensitivity (blue arrow). (b) The sensitivity function and median depth of investigation for the Wenner array.

Table 2.1. The median depth of investigation (z_e) for the different arrays (after Edwards 1977). L is the total length of the array. Note identical values of z_e/a for the Wenner-Schlumberger and pole-dipole arrays. Please refer to Figure 1.4 for the arrangement of the electrodes for the different arrays. The geometric factor is for an "a" value of 1.0 meter. For the pole-dipole array, the array length ' L ' only takes into account the active electrodes C1, P1 and P2 (i.e. it does not take into account the remote C2 electrode).

	z_e/a	z_e/L	Geometric Factor	Inverse Geometric Factor (Ratio)
Wenner Alpha	0.519	0.173	6.2832	0.15915 (1.0000)
Wenner Beta	0.416	0.139	18.850	0.05305 (0.3333)
Wenner Gamma	0.594	0.198	9.4248	0.10610 (0.6667)
Dipole-dipole n = 1	0.416	0.139	18.850	0.05305 (0.3333)
n = 2	0.697	0.174	75.398	0.01326 (0.0833)
n = 3	0.962	0.192	188.50	0.00531 (0.0333)
n = 4	1.220	0.203	376.99	0.00265 (0.0166)
n = 5	1.476	0.211	659.73	0.00152 (0.0096)
n = 6	1.730	0.216	1055.6	0.00095 (0.0060)
n = 7	1.983	0.220	1583.4	0.00063 (0.0040)
n = 8	2.236	0.224	2261.9	0.00044 (0.0028)
Equatorial dipole-dipole				
n = 1	0.451	0.319	21.452	0.04662 (0.2929)
n = 2	0.809	0.362	119.03	0.00840 (0.0528)
n = 3	1.180	0.373	367.31	0.00272 (0.0171)
n = 4	1.556	0.377	841.75	0.00119 (0.0075)
Wenner - Schlumberger				
n = 1	0.519	0.173	6.2832	0.15915 (1.0000)
n = 2	0.925	0.186	18.850	0.05305 (0.3333)
n = 3	1.318	0.189	37.699	0.02653 (0.1667)
n = 4	1.706	0.190	62.832	0.01592 (0.1000)
n = 5	2.093	0.190	94.248	0.01061 (0.0667)
n = 6	2.478	0.191	131.95	0.00758 (0.0476)
n = 7	2.863	0.191	175.93	0.00568 (0.0357)
n = 8	3.247	0.191	226.19	0.00442 (0.0278)
n = 9	3.632	0.191	282.74	0.00354 (0.0222)
n = 10	4.015	0.191	345.58	0.00289 (0.0182)
Pole-dipole n = 1	0.519	0.296	12.566	0.07958 (0.5000)
n = 2	0.925	0.308	37.699	0.02653 (0.1667)
n = 3	1.318	0.330	75.398	0.01326 (0.0833)
n = 4	1.706	0.341	125.66	0.00796 (0.0500)
n = 5	2.093	0.349	188.50	0.00531 (0.0334)
n = 6	2.478	0.354	263.89	0.00379 (0.0238)
n = 7	2.863	0.358	351.86	0.00284 (0.0178)
n = 8	3.247	0.361	452.39	0.00221 (0.0139)
Pole-Pole	0.867		6.28319	0.15915 (1.0000)

2.5.3 A 2-D view of the sensitivity function

The plot of the 1-D sensitivity function in Figure 2.9 suggests that the sensitivity of an array to the topmost layer is very small. The plot actually gives the *net* contribution calculated by summing up the contribution for all x - and y -values at the same depth, and it hides a multitude of effects. The *net* contribution for the topmost strip is small only if the ground is completely homogeneous. If it is not homogeneous, the results can be very different.

To study the suitability of the different arrays for 2-D surveys, we need to go one step beyond the simple 1-D sensitivity function, i.e. the 2-D sensitivity function. In this case, for a particular (x,z) location, we add up the contribution from all points for y -values ranging from $+\infty$ to $-\infty$. This involves the integration of the 3-D sensitivity function in equation (2.4) with respect to y , which is

$$F_{2D}(x, z) = \frac{1}{4\pi^2} \int_{-\infty}^{+\infty} \frac{x(x-a) + y^2 + z^2}{[x^2 + y^2 + z^2]^{1.5} [(x-a)^2 + y^2 + z^2]^{1.5}} dy$$

This integral has an analytic solution (Loke and Barker 1995) that is given in terms of elliptic integrals. The complete solution is

$$F_{2D}(x, z) = \frac{2}{\alpha\beta^2} \left[\frac{\alpha^2 E(k) - \beta^2 K(k)}{(\alpha^2 - \beta^2)} - \frac{\gamma[(\alpha^2 + \beta^2)E(k) - 2\beta^2 K(k)]}{(\alpha^2 - \beta^2)^2} \right] \quad (2.6)$$

where

$$k = \frac{(\alpha^2 - \beta^2)^{0.5}}{\alpha}$$

for $x > 0.5a$,

$$\alpha^2 = x^2 + z^2, \beta^2 = (x-a)^2 + z^2, \gamma = xa$$

and for $x < 0.5a$,

$$\beta^2 = x^2 + z^2, \alpha^2 = (x-a)^2 + z^2, \gamma = a(x-a)$$

and for $x = 0.5a$,

$$F_{2D}(x, z) = \pi \left[\frac{1}{2\alpha^3} - \frac{3a^2}{16\alpha^5} \right], \text{ with } \alpha = 0.25a^2 + z^2$$

As an example, Figure 2.10a shows the contour pattern for the sensitivity function of the Wenner array. The sensitivity function shows the degree to which a change in the resistivity of a section of the subsurface will influence the potential measured by the array. The higher the value of the sensitivity function, the greater is the influence of the subsurface region on the measurement. Note that for all the three arrays, the highest sensitivity values are found near the electrodes. At larger distances from the electrodes, the contour patterns are different for the different arrays. The difference in the contour pattern of the sensitivity function plot helps to explain the response of the different arrays to different types of structures.

In the following plots of the sensitivity sections, the distance between the first electrode and the last electrode (for example the C1 and C2 in the case of the Wenner alpha array in Figure 2.10a) is normalized to 1.0 meter. To avoid the singularities at the electrodes, the sensitivity values are shown from a depth of 0.025 meter downwards to 1.0 meter. In all the sensitivity section diagrams, the location of the plotting point used in the pseudosection is marked by a small black cross.

2.5.4 Wenner array

This is a robust array that was popularized by the pioneering work carried by The University of Birmingham research group (Griffiths and Turnbull 1985; Griffiths, Turnbull and Olayinka 1990). Many of the early 2-D surveys were carried out with this array. The "normal" Wenner array is technically the Wenner Alpha array. For a four-electrode array, there are three possible permutations of the positions of the electrodes (Carpenter and Habberjam 1956). In Figure 2.10a, the sensitivity plot for the Wenner Alpha array has almost horizontal contours beneath the center of the array. Because of this property, the Wenner array is relatively sensitive to vertical changes in the subsurface resistivity below the center of the array. However, it is less sensitive to horizontal changes in the subsurface resistivity. In general, the Wenner is good in resolving vertical changes (i.e. horizontal structures), but relatively poor in detecting horizontal changes (i.e. narrow vertical structures). In Table 2.1, the median depth of investigation for the Wenner Alpha array is approximately 0.5 times the "a" spacing used. Compared to other arrays, the Wenner Alpha array has a moderate depth of investigation. The signal strength is inversely proportional to the geometric factor used to calculate the apparent resistivity value for the array (Table 2.1). The geometric factor for the Wenner array is $2\pi a$. This is smaller than the geometric factor for other arrays. Among the common arrays, the Wenner array has the strongest signal strength. This can be an important factor if the survey is carried in areas with high background noise. One disadvantage of this array for 2-D surveys is the relatively poor horizontal coverage as the electrode spacing is increased (Figure 2.7). This could be a problem if you use a system with a relatively small number of electrodes.

Note that the sensitivity section shows large negative values near the surface between the C1 and P1 electrodes, as well as between the C2 and P2 electrodes. This means that if a small body with a higher resistivity than the background medium is placed in these negative zones, the measured apparent resistivity value will decrease. This phenomenon is also known as an "anomaly inversion". In comparison, if the high resistivity body is placed between the P1 and P2 electrodes where there are large positive sensitivity values, the measured apparent resistivity will increase. This is the basis of the offset Wenner method by Barker (1992) to reduce the effects of lateral variations in resistivity sounding surveys.

The other two permutations of the Wenner array are the Wenner Beta and the Wenner Gamma arrays. The Wenner Beta array is in fact a special case of the dipole-dipole array where the spacings between the electrodes are the same. Thus this array will be discussed in the following section under the dipole-dipole array. The Wenner Gamma array has a relatively unusual arrangement where the current and potential electrodes are interleaved. The sensitivity section shows that the deepest regions mapped by this array are below the two outer electrodes (C1 and P2 in Figure 2.10c), and not below the center of the array.

2.5.5 Dipole-dipole array

This array has been, and is still, widely used in resistivity and IP surveys because of the low EM coupling between the current and potential circuits. The arrangement of the electrodes is shown in Figure 1.4. The spacing between the current electrodes pair, C2-C1, is given as "a" which is the same as the distance between the potential electrodes pair P1-P2. This array has another factor marked as "n" in Figure 1.4. This is the ratio of the distance between the C1 and P1 electrodes to the C2-C1 (or P1-P2) dipole length "a". For surveys with this array, the "a" spacing is initially kept fixed at the smallest unit electrode spacing and the "n" factor is increased from 1 to 2 to 3 until up to about 6 in order to increase the depth of investigation.

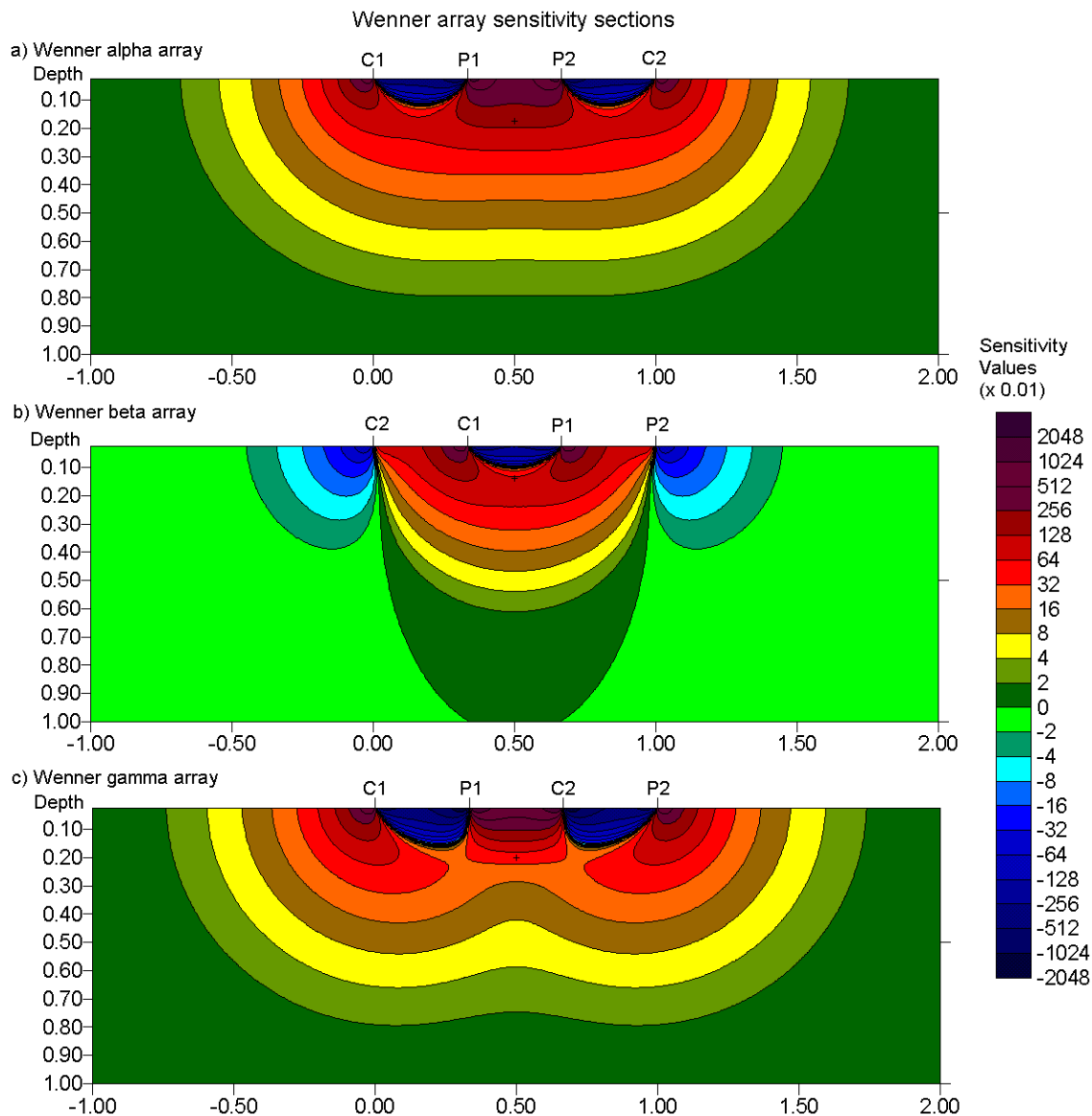


Figure 2.10. 2-D sensitivity sections for the Wenner array. The sensitivity sections for the (a) alpha, (b) beta and (c) gamma configurations.

Figure 2.11 shows the sensitivity sections for this array for " n " values ranging from 1 to 6. The largest sensitivity values are generally located between the C2-C1 dipole pair, as well as between the P1-P2 pair. This means that this array is most sensitive to resistivity changes below the electrodes in each dipole pair. As the " n " factor is increased, the high sensitivity values become increasingly more concentrated beneath the C1-C2 and P1-P2 dipoles, while the sensitivity values beneath the center of the array between the C1-P1 electrodes decreases. For " n " values of greater than 2, the sensitivity values at the pseudosection plotting becomes negligible. The sensitivity contour pattern becomes almost vertical for " n " values greater than 2. Thus the dipole-dipole array is very sensitive to horizontal changes in resistivity, but relatively insensitive to vertical changes in the resistivity. Thus it is good in mapping vertical structures, such as dykes and cavities, but relatively poor in mapping horizontal structures such as sills or sedimentary layers. The median depth of investigation of this array depends on both the " a " spacing and the " n "

factor (Table 2.1). In general, this array has a shallower depth of investigation compared to the Wenner array, for example at $n=1$ the depth of investigation is $0.416a$ compared to $0.512a$ for the Wenner Alpha array. Due to the almost vertical pattern of the sensitivity contours, the depth of investigation (which is a 1-D horizontal average of the sensitivity values) is not particularly meaningful for the dipole-dipole array for " n " values greater than 2. From experience with synthetic modeling and field data, the median depth of investigation might underestimate the depth of structures sensed by this array by about 20% to 30% for the large " n " factors. For 2-D surveys, this array has better horizontal data coverage than the Wenner (Figure 2.7). This can be an important advantage when the number of nodes available with the multi-electrode system is small.

One possible disadvantage of this array is the very low signal strength for large values of the " n " factor. The voltage is inversely proportional to the *cube* of the " n " factor. For the same current, the voltage measured by the resistivity meter drops by about 56 times when " n " is increased from 1 to 6 (Table 2.1). One method to overcome this problem is to increase the " a " spacing between the C1-C2 (and P1-P2) dipole pair to reduce the drop in the potential when the overall length of the array is increased to increase the depth of investigation. Figure 2.12 shows two different arrangements for the dipole-dipole array with the same array length but with different " a " and " n " factors. The signal strength of the array with the smaller " n " factor is about 28 times stronger than the one with the larger " n " factor.

To use this array effectively, the resistivity meter should have comparatively high sensitivity and very good noise rejection circuitry, and there should be good contact between the electrodes and the ground. With the proper field equipment and survey techniques, this array has been successfully used in many areas to detect structures such as cavities where the good horizontal resolution of this array is a major advantage.

The plotting location of the corresponding data point (based on the median depth of investigation) used in drawing the apparent resistivity pseudosection is also shown in Figure 2.11. Note that the pseudosection plotting point falls in an area with very low sensitivity values for " n " values of 4 and above. For the dipole-dipole array, the regions with the high sensitivity values are concentrated below the C1-C2 electrodes pair and below the P1-P2 electrodes pair. In effect, the dipole-dipole array gives minimal information about the resistivity of the region surrounding the plotting point, and the distribution of the data points in the pseudosection plot does not reflect the subsurface area mapped by the apparent resistivity measurements. Note that if the data point is plotted at the point of intersection of the two 45° angle lines drawn from the center of the two dipoles, it would be located at a depth of 0.7 units in Figure 2.11d (compared with 0.19 units given by the median depth of investigation method) where the sensitivity values are almost zero!

Loke and Barker (1996a) used an inversion model where the arrangement of the model blocks directly follows the arrangement of the pseudosection plotting points. This approach gives satisfactory results for the Wenner and Wenner-Schlumberger arrays where the pseudosection point falls in an area with high sensitivity values (Figures 2.10a and 2.13). However, it is not suitable for arrays such as the dipole-dipole and pole-dipole where the pseudosection point falls in an area with very low sensitivity values. The RES2DINV program uses a more sophisticated method to generate the inversion model where the arrangement of the model blocks is not tightly bound to the pseudosection.

A final minor note. In most textbooks, the electrodes for this array are arranged in a C1-C2-P1-P2 order that will in fact give a negative geometric factor. The arrangement assumed in these notes is the C2-C1-P1-P2 arrangement.

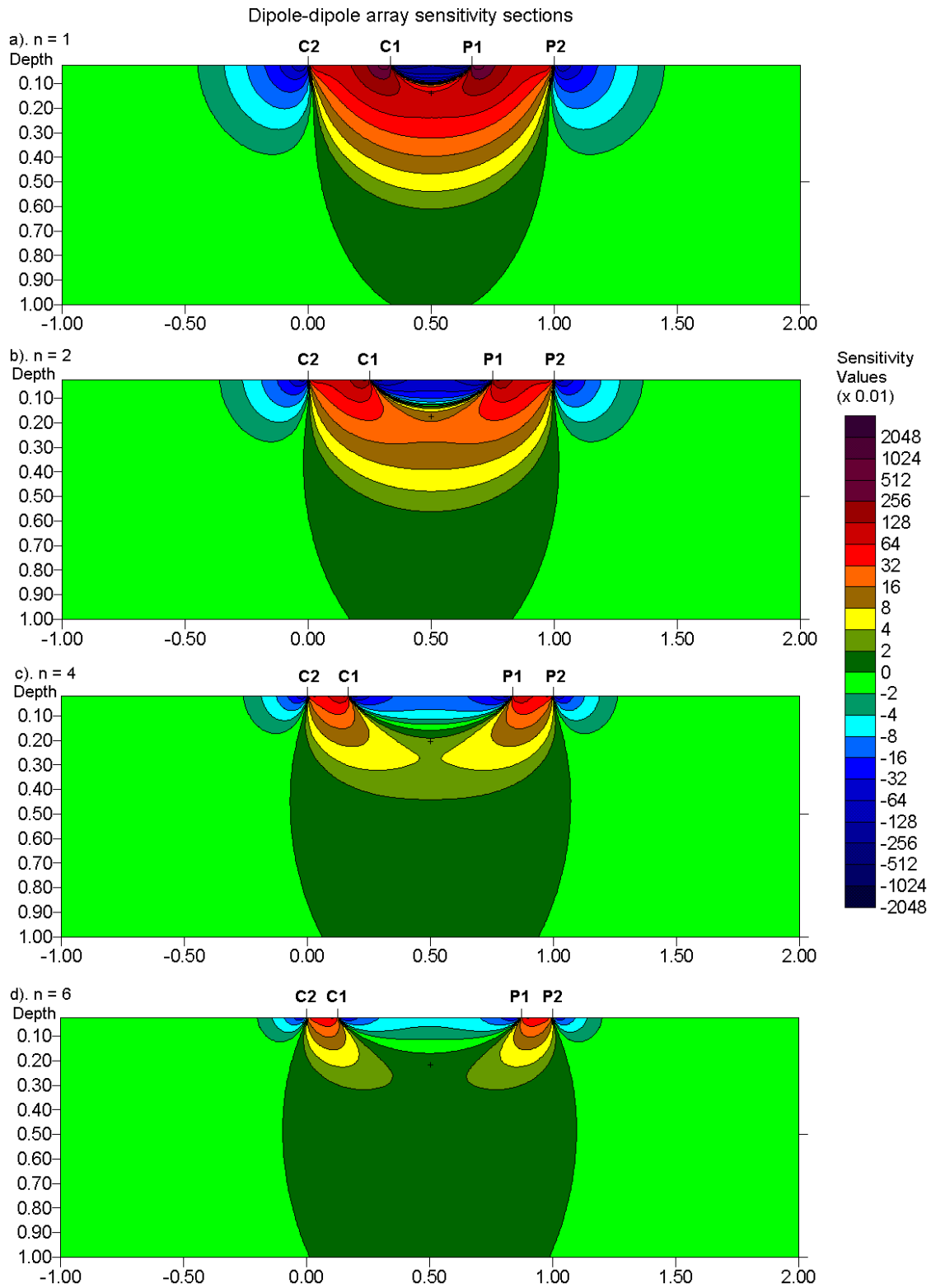


Figure 2.11. 2-D sensitivity sections for the dipole-dipole array. The sections with (a) $n=1$, (b) $n=2$, (c) $n=4$ and (d) $n=6$.

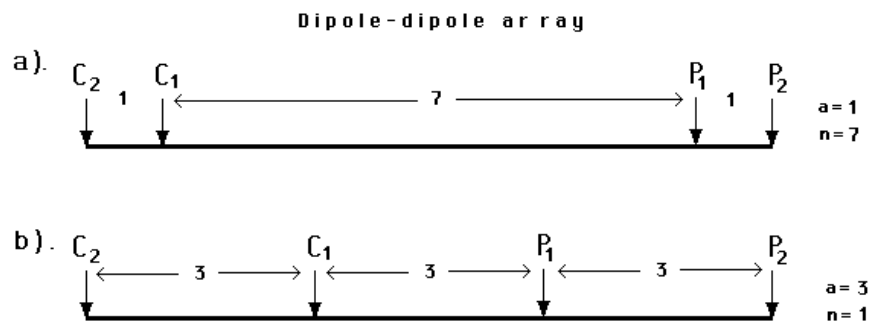


Figure 2.12. Two possible different arrangements for a dipole-dipole array measurement. The two arrangements have the same array length but different “ a ” and “ n ” factors resulting in very different signal strengths.

2.5.6 Wenner-Schlumberger array

This is a new hybrid between the Wenner and Schlumberger arrays (Pazdirek and Blaha 1996) arising out of more recent work with electrical imaging surveys. The classical Schlumberger array is one of the most commonly used arrays for resistivity sounding surveys. A digitized form of this array so that it can be used on a system with the electrodes arranged with a constant spacing is shown in Figure 2.14b. The “ n ” factor for this array is the ratio of the distance between the C1-P1 (or P2-C2) electrodes to the spacing between the P1-P2 potential pair. Note that the Wenner array is a special case of this array where the “ n ” factor is equals to 1.

Figure 2.13 shows the sensitivity pattern for this array as the “ n ” factor is increased from 1 (Wenner array) to 6 (the classical Schlumberger array). The area of highest positive sensitivity below the center of the array becomes more concentrated beneath central P1-P2 electrodes as the “ n ” factor is increased. Near the location of the plotting point at the median depth of investigation, the sensitivity contours has a slight vertical curvature below the center of the array. At $n=6$, the high positive sensitivity lobe beneath the P1-P2 electrodes becomes more separated from the high positive sensitivity values near the C1 and C2 electrodes. This means that this array is moderately sensitive to both horizontal (for low “ n ” values) and vertical structures (for high “ n ” values). In areas where both types of geological structures are expected, this array might be a good compromise between the Wenner and the dipole-dipole array. The median depth of investigation for this array is about 10% larger than that for the Wenner array for the same distance between the outer (C1 and C2) electrodes for “ n ” values greater than 3. The signal strength for this array is approximately inversely proportional to the square of the “ n ” value. The signal strength is weaker than that for the Wenner array, but it is higher than the dipole-dipole array and twice that of the pole-dipole.

Figure 2.14 shows the pattern of the data points in the pseudosections for the Wenner and Wenner-Schlumberger arrays. The Wenner-Schlumberger array has a slightly better horizontal coverage compared with the Wenner array. For the Wenner array each deeper data level has 3 data points less than the previous data level, while for the Wenner-Schlumberger array there is a loss of 2 data points with each deeper data level. The horizontal data coverage is slightly wider than the Wenner array, but narrower than that obtained with the dipole-dipole array.

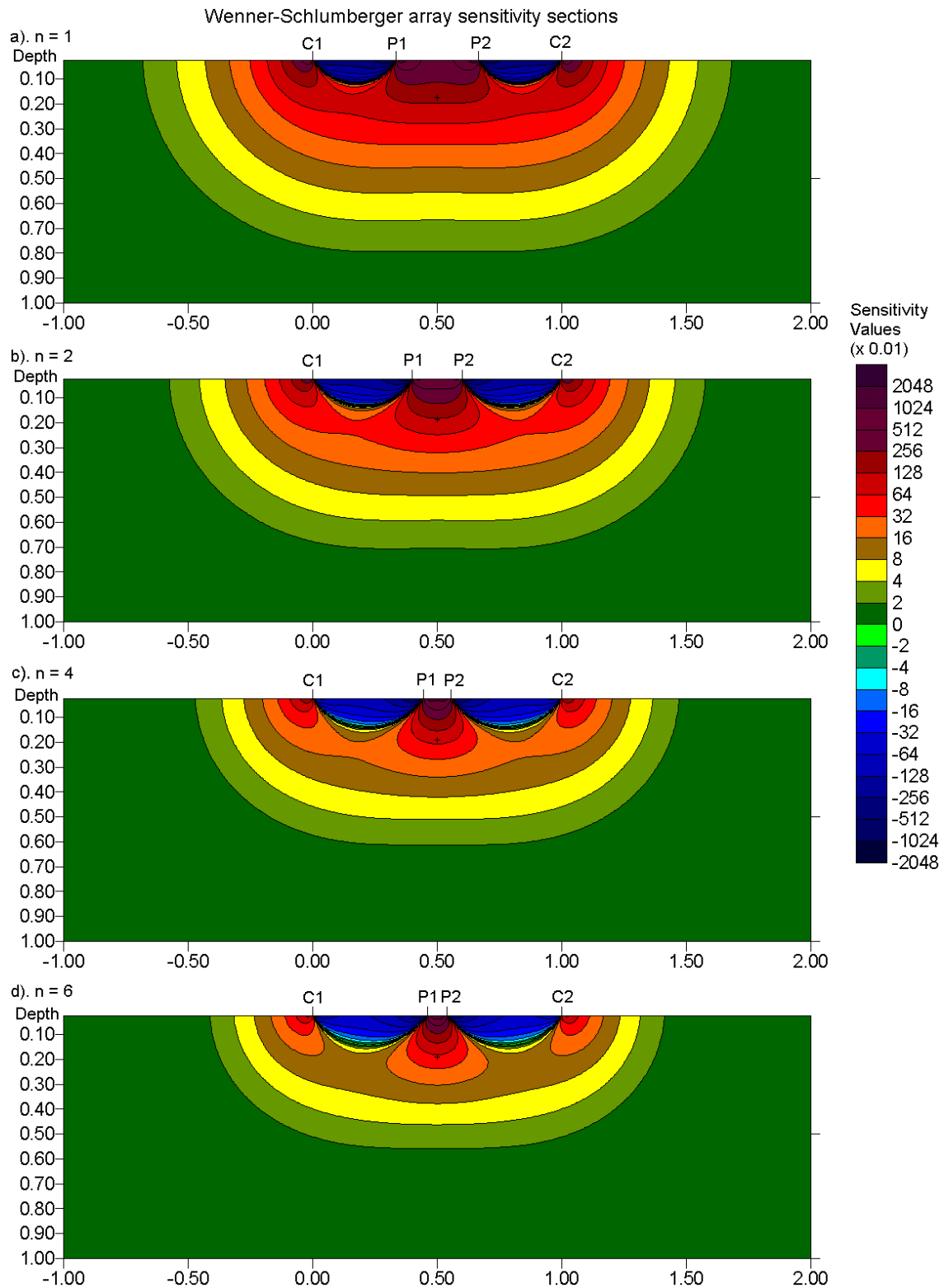


Figure 2.13. 2-D sensitivity sections for the Wenner-Schlumberger array. The sensitivity sections with (a) $n=1$, (b) $n=2$, (c) $n=4$ and (d) $n=6$.

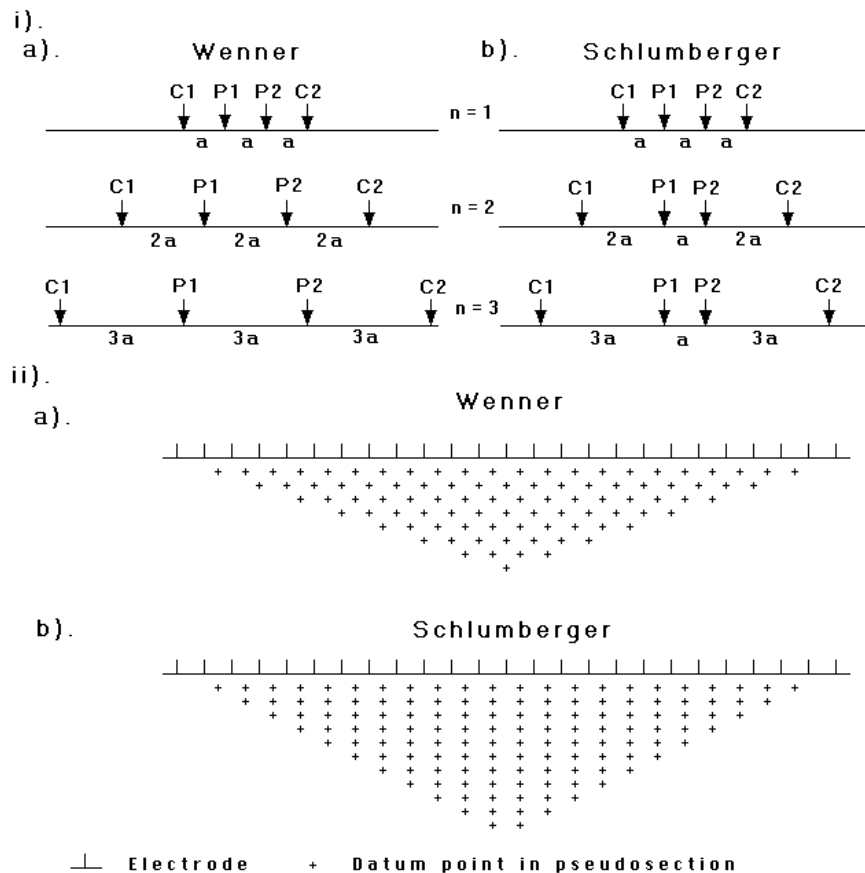


Figure 2.14. A comparison of the (i) electrode arrangement and (ii) pseudosection data pattern for the Wenner and Wenner-Schlumberger arrays.

2.5.7 Pole-pole array

This array is not as commonly used as the Wenner, dipole-dipole and Schlumberger arrays. In practice the ideal pole-pole array, with only one current and one potential electrode (Figure 1.4d), does not exist. To approximate the pole-pole array, the second current and potential electrodes (C2 and P2) must be placed at a distance that is more than 20 times the maximum separation between C1 and P1 electrodes used in the survey. The effect of the C2 (and similarly for the P2) electrode is approximately proportional to the ratio of the C1-P1 distance to the C2-P1 distance. If the effects of the C2 and P2 electrodes are not taken into account, the distance of these electrodes from the survey line must be at least 20 times the largest C1-P1 spacing used to ensure that the error is less than 5%. In surveys where the inter-electrode spacing along the survey line is more than a few meters, there might be practical problems in finding suitable locations for the C2 and P2 electrodes to satisfy this requirement. Another disadvantage of this array is that because of the large distance between the P1 and P2 electrodes, it is can pick up a large amount of telluric noise that can severely degrade the quality of the measurements. Thus this array is mainly used in surveys where relatively small electrode spacings (less than a few meters) are used. It is popular in some applications such as archaeological surveys where small electrode spacings are used. It has also been used for 3-D surveys (Li and Oldenburg 1992).

This array has the widest horizontal coverage and the deepest depth of investigation. However, it has the poorest resolution, which is reflected by the comparatively large spacing between the contours in the sensitivity function plot (Figure 2.15).

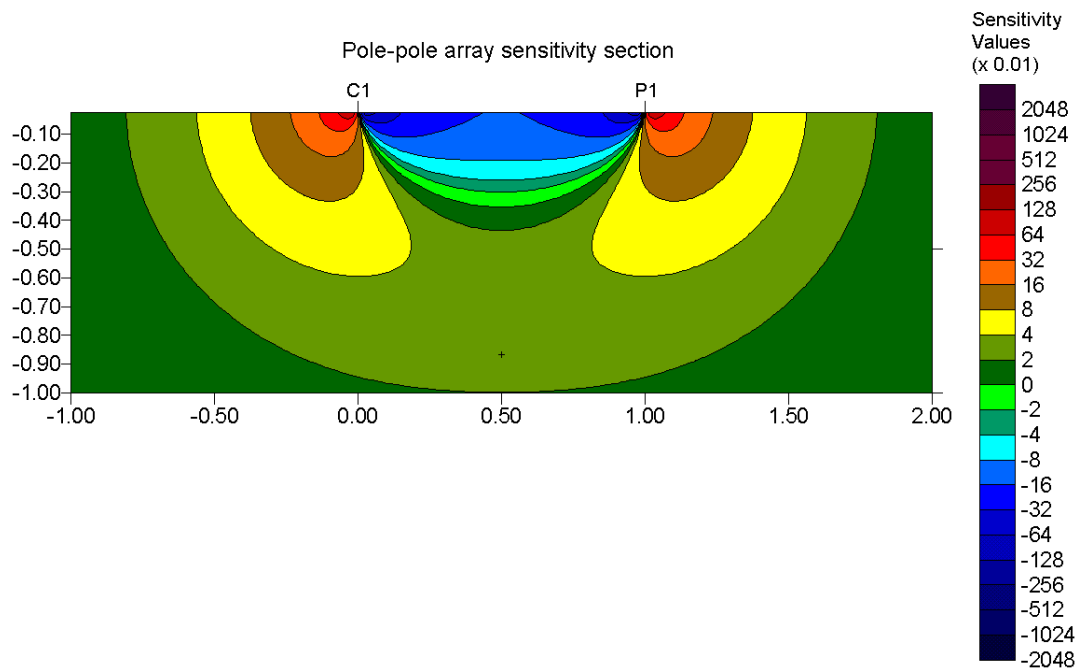


Figure 2.15. The pole-pole array 2-D sensitivity section.

2.5.8 Pole-dipole array

The pole-dipole array also has relatively good horizontal coverage, but it has a significantly higher signal strength compared with the dipole-dipole array and it is not as sensitive to telluric noise as the pole-pole array. Unlike the other common arrays, the pole-dipole array is an asymmetrical array (Figure 1.4f). Over symmetrical structures the apparent resistivity anomalies in the pseudosection are asymmetrical (Figure 2.7d). In some situations, the asymmetry in the measured apparent resistivity values could influence the model obtained after inversion. One method to eliminate the effect of this asymmetry is to repeat the measurements with the electrodes arranged in the reverse manner (Figure 2.16b). By combining the measurements with the “forward” and “reverse” pole-dipole arrays, any bias in the model due to the asymmetrical nature of this array would be removed. This procedure will double the number of data points and consequently the survey time, but it is not a severe problem with multi-channel systems.

The sensitivity section shows that area with the greatest sensitivity lies beneath P1-P2 dipole pair, particularly for large “ n ” factors. For “ n ” values of 4 and higher, the high positive sensitive lobe beneath the P1-P2 dipole becomes increasingly vertical. Thus, similar to the dipole-dipole array, this array is probably more sensitive to vertical structures. Note also the zone with negative sensitivity values between the C1 and P1 electrodes, as well as the smaller zone of high positive values to the left of the C1 electrode.

The pole-dipole array requires a remote electrode, the C2 electrode, which must be placed sufficiently far from the survey line. For the pole-dipole array, the effect of the C2 electrode is approximately proportional to the *square* of ratio of the C1-P1 distance to the C2-P1 distance. Thus the pole-dipole array is less affected by the C2 remote electrode compared to the pole-pole array. If the distance of the C2 electrode is more than 5 times the largest C1-P1 distance used, the error caused by neglecting the effect of the C2 electrode is less than 5% (the exact error also depends on the location of the P2 electrode for the particular measurement and the subsurface resistivity distribution).

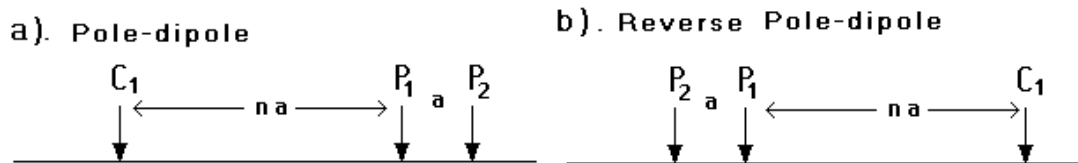


Figure 2.16. The forward and reverse pole-dipole arrays.

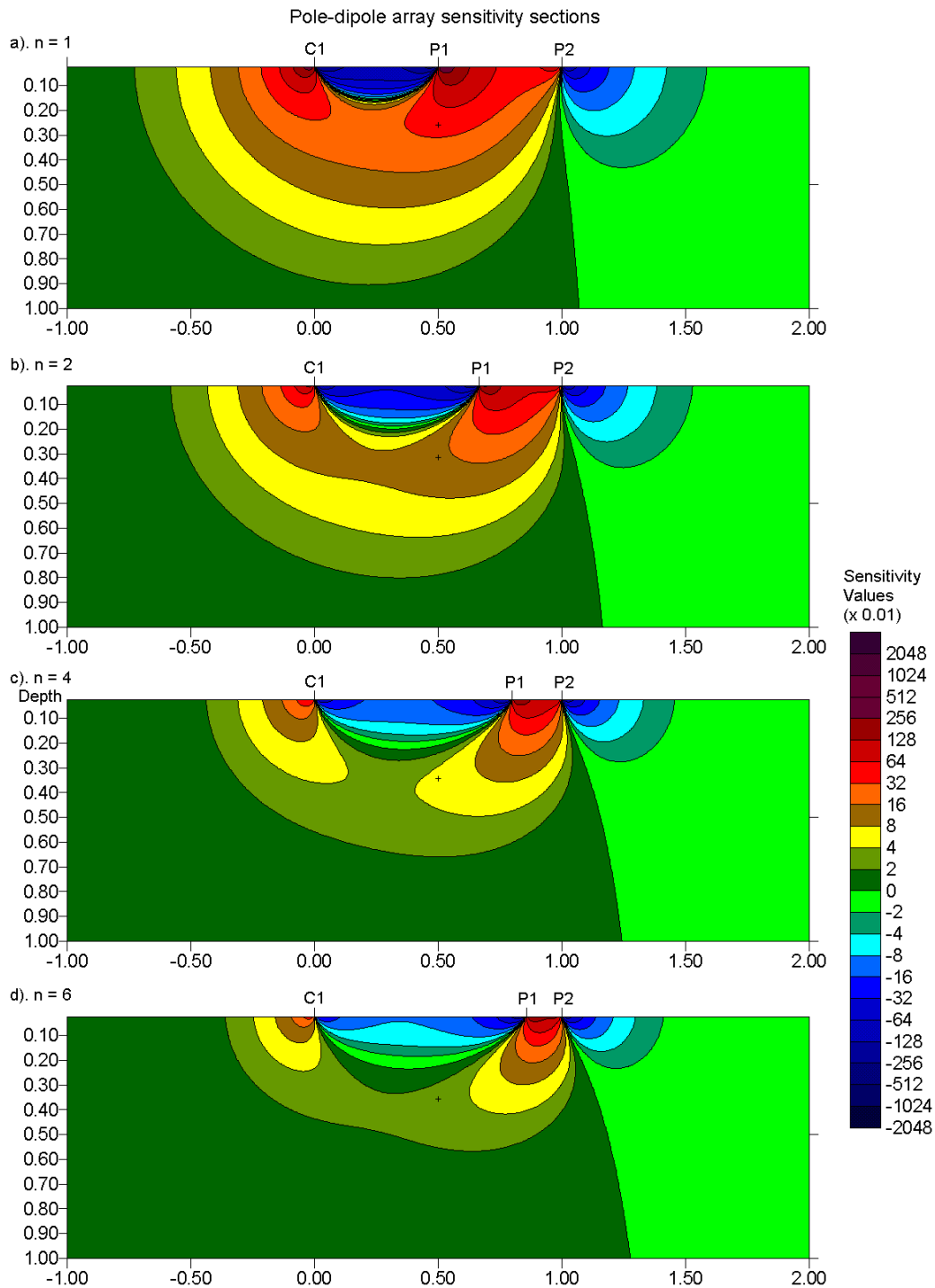


Figure 2.17. The pole-dipole array 2-D sensitivity sections. The sensitivity sections with (a) $n=1$, (b) $n=2$, (c) $n=4$ and (d) $n=6$.

Due to its good horizontal coverage, this is an attractive array for multi-electrode resistivity meter systems with a relatively small number of nodes. The signal strength is lower compared with the Wenner and Wenner-Schlumberger arrays but higher than the dipole-dipole array. For IP surveys, the higher signal strength (compared with the dipole-dipole array) combined with the lower EM coupling (compared with the Wenner and Wenner-Schlumberger arrays) due to the separation of the circuitry of the current and potential electrodes makes this array an attractive alternative.

The signal strength for the pole-dipole array decreases with the *square* of the “ n ” factor. While this effect is not as severe as the dipole-dipole array, it is usually not advisable to use “ n ” values of greater than 8 to 10. Beyond this, the “ a ” spacing between the P1-P2 dipole pair should be increased to obtain a stronger signal strength. The ratio of the depth of investigation to the array length does not increase significantly for ‘ n ’ values beyond 4 or 5 (Table 2.1). Thus to increase the depth of investigation, it is better to increase the ‘ a ’ spacing rather than to keep increasing the ‘ n ’ value when it reaches 5. There is another interesting effect when the ‘ n ’ factor is increased that is frequently not appreciated, and leads to an interesting pitfall in field surveys. This is discussed in section 4.9.

2.5.9 Multiple gradient array

This is a relatively new array developed primarily for multi-channel resistivity meter systems (Dahlin and Zhou 2006). A multi-channel system can make several measurements simultaneously with the potential electrode pairs at different location but with the same positions of the current electrodes. The dipole-dipole and pole-dipole arrays are the obvious arrays that are suitable for such measurements. However, the dipole-dipole arrays is relatively sensitive to noise while the pole-dipole array requires a remote electrode at a sufficiently large distance from the survey line. For some surveys, an ‘alpha’ type of electrode arrangement with the potential electrodes located between the current electrodes is desirable. One possibility is the ‘reverse’ Schlumberger array with the current electrodes at the centre and the potential electrodes as the outer electrodes. However, this arrangement will be more sensitive to telluric noise due to the large distance between the potential electrodes. The current electrodes in the traditional gradient array are fixed at the end of the line, while measurements are made with the potential electrodes at different positions along the line.

In the multiple gradient array, different sets of measurements are made with the current electrodes at different locations. As an example, for a system with 32 electrodes, one set of measurements can be made with the current electrodes at nodes 1 and 32. Next, another series of measurements are made with the current electrodes at nodes 1 and 16, as well as another with the current electrodes at 16 and 32. A similar set of measurements can be made with the C1-C2 electrodes at 1-8, 8-16, 16-24 and 2-32. This can be repeated using smaller distances between the current electrodes. The sensitivity sections with the same positions of the C1-C2 current electrodes, but with the potential dipole P1-P2 being moved from the center to one end of the array is shown in Figure 2.18. Not surprisingly, the sensitivity contour pattern slowly changes from a Wenner-Schlumberger pattern (Figure 2.13) towards the pole-dipole pattern (Figure 2.17) as the potential dipole moves closer to the current electrode one end of the array. The results obtained by this array is comparable to those obtained by the dipole-dipole and pole-dipole arrays (Dahlin and Zhou 2004) while it has more favourable noise characteristics (Zhou and Dahlin 2003).

One interesting minor problem associated with this array is the plotting method for the pseudosection and profiles. The vertical position can be easily determined by using the median depth of investigation which can be numerically determined. The main issue is the horizontal position of the plotting point.

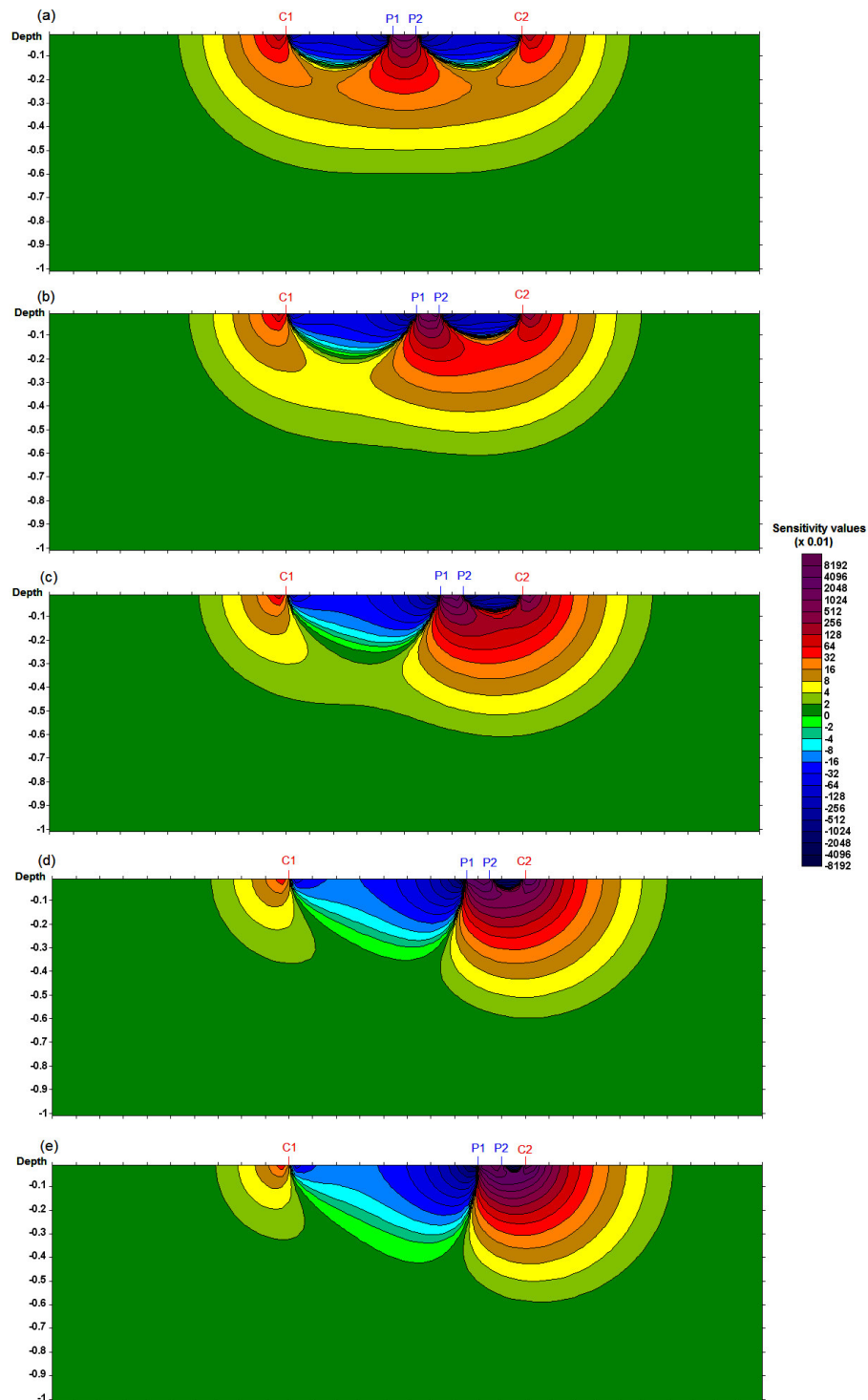


Figure 2.18. Sensitivity sections for the gradient array. The current electrodes are fixed at $x=0$ and 1.0 meters, and the distance between the potential electrodes is 0.1 m. The position of the P1-P2 potential electrodes at (a) 0.45 and 0.55 m., (b) 0.55 and 0.65 m., (c) 0.65 and 0.75 m, (d) 0.75 and 0.85 m. and (e) 0.80 and 0.90 m.

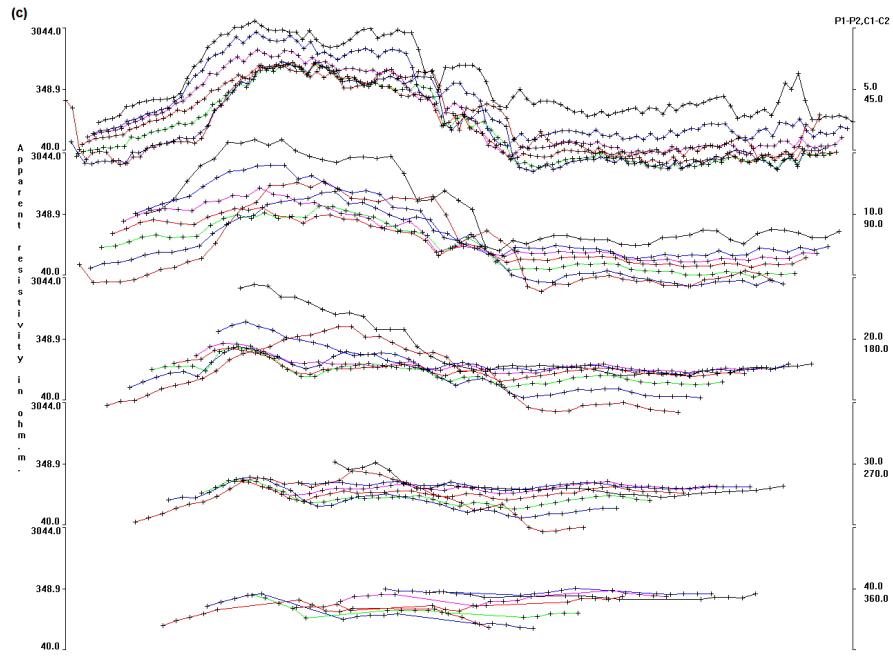
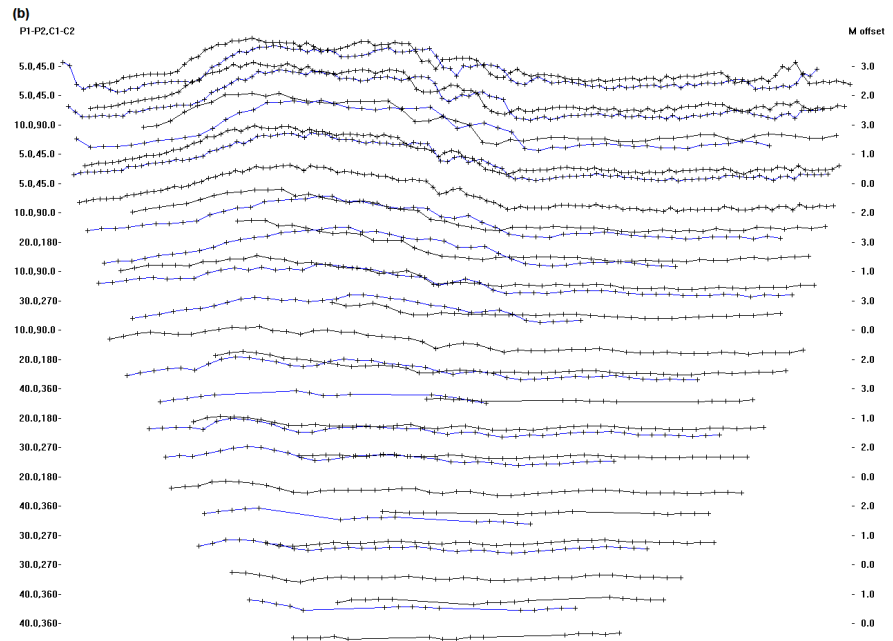
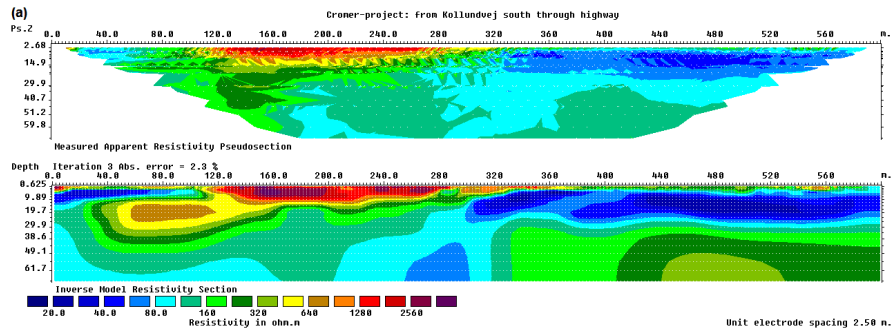


Figure 2.19. (a) Example of multiple gradient array data set and inversion model. (b) Profile plot using exact pseudodepths. (c) Profile plot using approximate pseudodepths.

Two possibilities are using the average of the locations of all the four electrodes (C1-P1-P2-C2), or just the midpoint of the P1-P2 electrodes (Dahlin and Zhou, 2006). However, for some data sets, both methods might result in a situation where two data points measured with different array configurations end up at the same plotting location. There might be no single method that works satisfactory in all cases. The RES2DINV program has two options for plotting the data as profiles are shown in Figure 2.19. The profile plot is commonly used to pick out outliers in the data.

2.5.10 High-resolution electrical surveys with overlapping data levels

In seismic reflection surveys, the common depth point method is frequently used to improve the quality of the signals from subsurface reflectors. A similar technique can be used to improve the data quality for resistivity/IP surveys, particularly in noisy areas. This is by using overlapping data levels with different combinations of “**a**” and “**n**” values for the Wenner-Schlumberger, dipole-dipole and pole-dipole arrays.

To simplify matters, let us consider the case for the Wenner-Schlumberger array with an inter-electrode spacing of 1 meter along the survey line. A high-resolution Wenner-Schlumberger survey will start with the “**a**” spacing (which is the distance between the P1-P2 potential dipole) equals to 1 meter and repeat the measurements with “**n**” values of 1, 2, 3 and 4. Next the “**a**” spacing is increased to 2 meter, and measurements with “**n**” equals to 1, 2, 3 and 4 are made. This process is repeated for all possible values of the “**a**” spacing. To be on the safe side, the data set should contain all the possible data points for the Wenner array. The number of data points produced by such a survey is more than twice that obtained with a normal Wenner array survey. Thus the price of better horizontal data coverage and resolution is an increase in the field survey time.

A Wenner array with “**a**” equals to 2 meters (Figure 2.14) will have a total array length of 6 meters and a median depth of investigation of about 1.04 meters. In comparison, a measurement made with “**a**” equals to 1 meter and “**n**” equals to 2 using the Wenner-Schlumberger array will have a total array length of 5 meters and a slightly smaller depth of investigation of 0.93 meter (Figure 2.14). While the depth of investigation of the two arrangements are similar, the section of the subsurface mapped by the two arrays will be slightly different due to the different sensitivity patterns (Figures 2.13a and 2.13b). So the two measurements will give slightly different information about the subsurface. A measurement with “**a**” equals to 1 meter and “**n**” equals to 3 (Figure 2.14) will have a depth of investigation of 1.32 meters. If all the 3 combinations are used, the data set will have measurements with pseudodepths of 0.93, 1.02 and 1.32 metres. This results in a pseudosection with overlapping data levels.

A similar “high-resolution” survey technique can also be used with the dipole-dipole and pole-dipole arrays by combining measurements with different “**a**” and “**n**” values to give overlapping data levels. In particular, this technique might be useful for the dipole-dipole array since the signal strength decreases rapidly with increasing “**n**” values (section 2.5.5). A typical high-resolution dipole-dipole survey might use the following arrangement; start with a dipole of “**1a**” and “**n**” values of 1, 2, 3, 4, 5; followed by a dipole of “**2a**” and “**n**” values of 1, 2, 3, 4, 5; and if necessary another series of measurements with a dipole of “**3a**” and “**n**” values of 1, 2, 3, 4, 5. Measurements with the higher “**n**” values of over 4 would have higher noise levels. However, by having such redundant measurements using the overlapping data levels, the effect of the more noisy data points will be reduced. Figure 2.20 shows the apparent resistivity pseudosection for single prism model using this arrangement. This arrangement has been widely used for IP surveys with the dipole-dipole array (Edwards 1977).

In theory, it should be possible to combine measurements made with different arrays to take advantage of the different properties of the various arrays. Although this is not a common practice, it could conceivably give useful results in some situations. The RES2DINV program supports the use of such mixed data sets.

Besides the standard arrays discussed, there is now interest in automatically computer generated optimized arrays. This is discussed later in section 4.8.

2.5.11 Summary of array types

The Wenner array is an attractive choice for a survey carried out in a noisy area (due to its high signal strength) and also if good vertical resolution is required. The dipole-dipole array might be a more suitable choice if good horizontal resolution and data coverage is important (assuming your resistivity meter is sufficiently sensitive and there is good ground contact). The Wenner-Schlumberger array (with overlapping data levels) is a reasonable all-round alternative if both good and vertical resolutions are needed, particularly if good signal strength is also required. If you have a system with a limited number of electrodes, the pole-dipole array with measurements in both the forward and reverse directions might be a viable choice. For surveys with small electrode spacings and require a good horizontal coverage, the pole-pole array might be a suitable choice. For multi-channel arrays, the possible arrays are the multiple gradient, the dipole-dipole and pole-dipole arrays.

The papers by Dahlin and Zhou (2004) and Zhou and Dahlin (2003) has interesting discussions on the properties of different arrays.

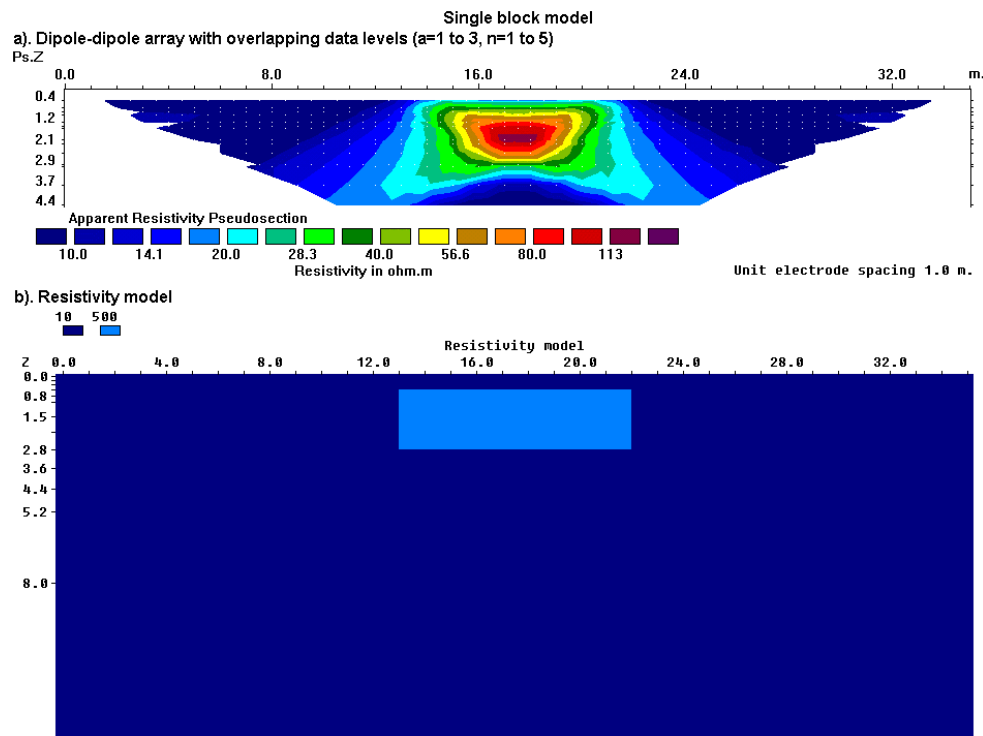


Figure 2.20. The apparent resistivity pseudosection for the dipole-dipole array using overlapping data levels over a rectangular prism. Values of 1 to 3 meters are used for the dipole length ‘ a ’, and the dipole separation factor ‘ n ’ varies from 1 to 5. Compare this with Figure 2.7c for the same model but with ‘ a ’ fixed at 1 meter, and ‘ n ’ varying from 1 to 10. In practice, a ‘ n ’ value greater than 8 would result in very noisy apparent resistivity values.

2.5.12 Use of the sensitivity values for multi-channel measurements or streamers

Here we will look at one example of the use of the sensitivity values. The problem faced is as follows.

- a). We have a multi-channel resistivity meter that can make 8 measurements at a single time.
- b). The cable used (possibly in the form of a streamer for mobile surveys on land or in water covered areas) has 10 nodes. Two of the nodes are fixed as the current electrodes, while the potential measurements are made using any 2 of the remaining 8 nodes.
- c). We want to get the most information possible in terms of depth and a uniform horizontal coverage below the streamer for a single set of 8 measurements.

To study the characteristics of the array configurations, we add up the sensitivity values for all the 8 measurements. The formula used for the cumulative sensitivity, F_I , is

$$F_I = \frac{1}{8} \sum_{i=1}^{i=8} |F_{2Di}(x, z)| \quad (2.7)$$

Note that the absolute value of the sensitivity value is used, since negative sensitivity values also give information about the subsurface. This is also to avoid a situation where the negative sensitivity value for one measurement cancels out the positive value for another measurement.

Figure 2.21a shows a dipole-dipole array based measurement sequence. The two current electrodes are set at one end of the line and the potential measurements are made using successive pairs of the potential nodes. Note the area with the highest cumulative sensitivity is around the first 4 electrodes. The area of deepest penetration is between the second and third electrodes, i.e. between the current dipole and the first potential electrode.

The second configuration places the current electrodes at the ends of the line (Figure 2.21b). Almost all the measurements are made using a fixed separation of one unit electrode spacing between the potential electrodes. The potential dipole is moved from one end of the survey line to the other end, i.e. a gradient array type of arrangement. One advantage of this configuration over the dipole-dipole arrangement is the larger voltage (i.e. lower noise level) measured by the potential electrodes. The cumulative sensitivity section shows a more uniform pattern compared to that produced by the dipole-dipole configuration. The depth of investigation is slightly deeper below current electrodes, and slightly less below the center of the line.

The third configuration also places the current electrodes at the ends of the lines, but keeps the center of the potential dipoles at or near the center of the line. The first 4 measurements use a symmetrical Wenner-Schlumberger arrangement and increase the separation between the potential electrodes until they reach next to the current electrodes. The second set of 4 measurements uses separations of 2 and 3 times the unit spacing for the potential dipole pair but with a mid-point slightly to one side of the center of the line. The cumulative sensitivity pattern has an even more uniform pattern below the line compared with the gradient array configuration.

To get an idea of the relative depths of investigation for the 3 configurations, we use the light blue contour (with a value of 8 units) as a guide. The expanding Wenner-Schlumberger configuration has the deepest depth with high sensitivity values while the dipole-dipole configuration appears to have the shallowest. Note the current electrodes for dipole-dipole array is limited to the left end of the line, and for this reason the region with the deepest depth of investigation is skewed towards the left.

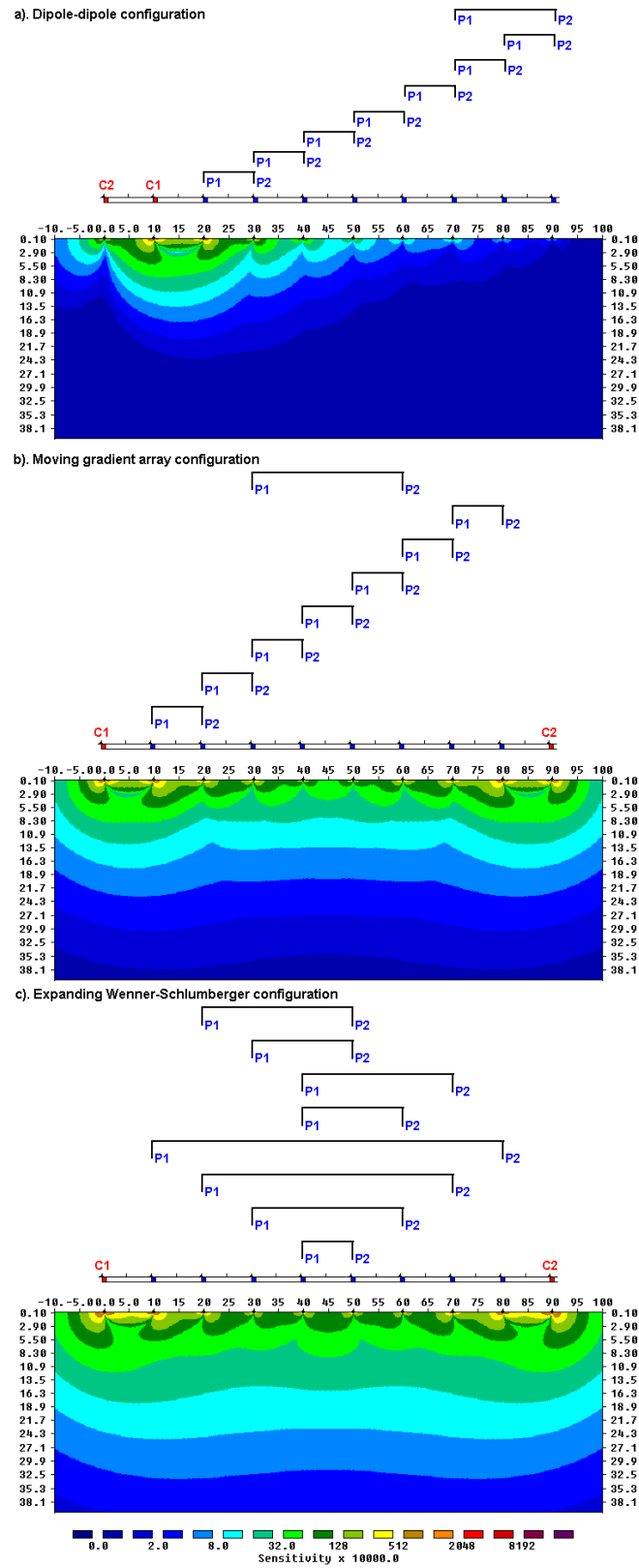


Figure 2.21. Cumulative sensitivity sections for different measurement configurations using (a) a dipole-dipole sequence, (b) a moving gradient array and (c) an expanding Wenner-Schlumberger array.

3 A 2-D forward modeling program

3.1 Finite-difference and finite-element methods

In the forward modeling problem, the subsurface resistivity distribution is specified and the purpose is to calculate the apparent resistivity that would be measured by a survey over such a structure. A forward modeling subroutine is in fact also an integral part of any inversion program since it is necessary to calculate the theoretical apparent resistivity values for the model produced by the inversion routine to see whether it agrees with the measured values. There are three main methods to calculate the apparent resistivity values for a specified model. They are (i) analytical methods, (ii) boundary element methods and (iii) the finite-difference and finite-element methods. Analytical methods are probably the most accurate methods, but they are restricted to relative simple geometries (such as a sphere or cylinder). Boundary element methods are more flexible, but the number of regions with different resistivity values that is allowed is somewhat limited (usually less than 10). In engineering and environmental surveys the subsurface can have an arbitrary resistivity distribution, so the finite-difference and finite-element methods are usually the only viable choice. These methods can subdivide the subsurface into thousands of cells with different resistivity values. However, the analytical and boundary element methods are useful independent methods that can be used to check the accuracy of the finite-difference and finite-element methods.

In the RES2DMOD software, the user can choose the finite-difference or the finite-element method. The subsurface is subdivided into a large number of rectangular cells (Figure 3.1) and the user can specify the resistivity value of each cell. The finite-difference method is based on a method described by Dey and Morrison (1979a), but with a modification by Loke (1994) to correct for a minor inconsistency in the Dey and Morrison discretization by area method. The finite-element method uses the standard first-order triangular elements (Silvester and Ferrari 1990).

While our main interest is in the inversion of field data, the forward modeling program is also useful, particularly in the planning stage of the survey. In the previous chapter we have seen that different arrays can have sensitivity sections that are radically different. In theory, from the sensitivity sections we can get an idea of the type of array that will give a reasonably good response over a particular class of structures (for example a vertical fracture zone). However, there is no substitute for a hands-on direct calculation of the expected apparent resistivity pseudosection. Before carrying out a field survey, some information about the shape and size of expected targets is frequently known. By trying different arrays digitally on the computer screen, we can avoid using an array that is unsuitable for the detection of the structures of interest. We can also have an idea of a suitable spacing between adjacent electrodes to use, and the maximum electrode separation needed.

In the program, the subsurface is divided into a large number of small rectangular cells. This program is largely intended for teaching about the use of the 2-D electrical imaging method. Hopefully, it will assist the user in choosing the appropriate array for different geological situations or surveys. The arrays supported by this program are the Wenner (Alpha, Beta and Gamma configurations), Wenner-Schlumberger, pole-pole, inline dipole-dipole, pole-dipole and equatorial dipole-dipole (Edwards 1977). Each type of array has its advantages and disadvantages. This program will hopefully help you in choosing the "best" array for a particular survey area after carefully balancing factors such as the cost, depth of investigation, resolution and practicality.

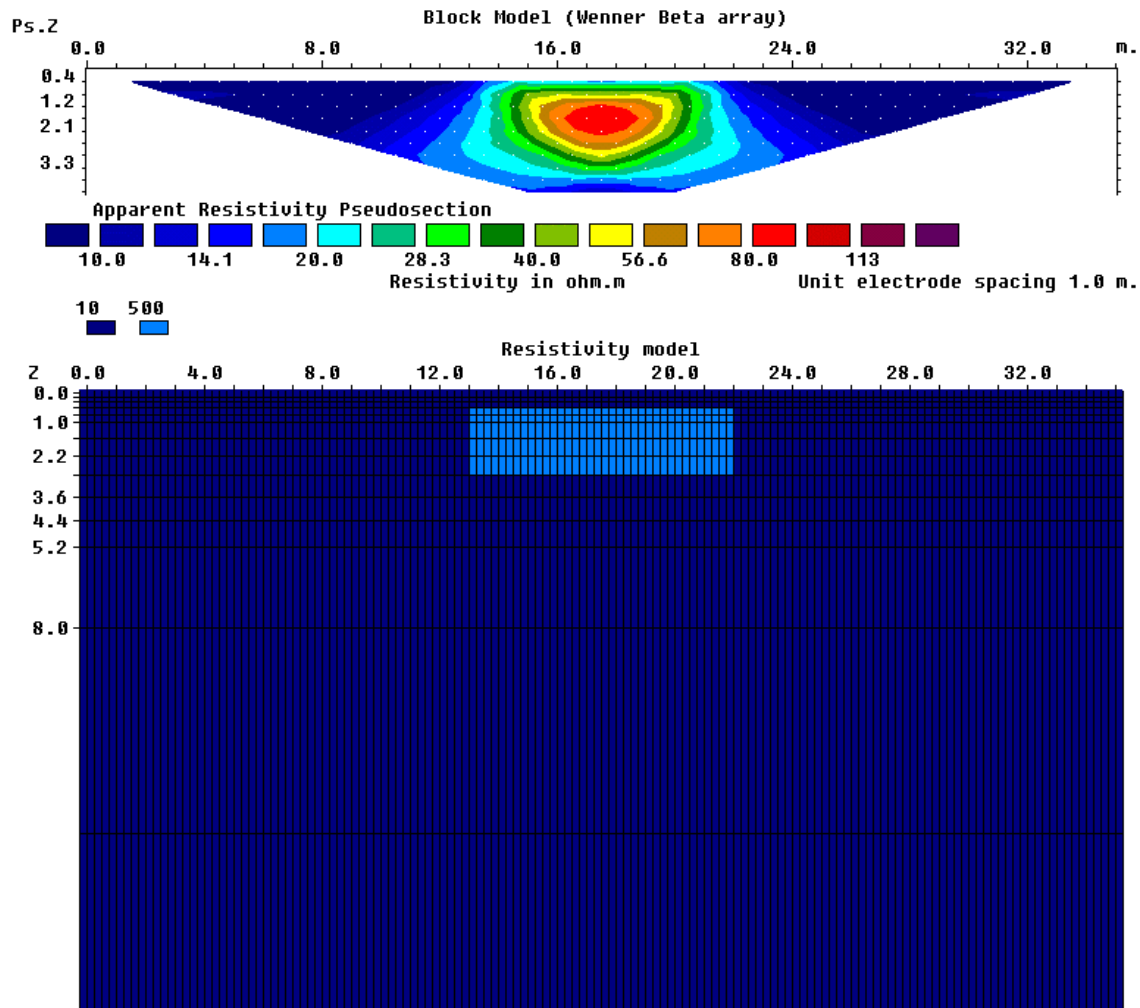


Figure 3.1. The output from the RES2DMOD software for the SINGLE_BLOCK.MOD 2-D model file. The individual cells in the model are shown in the lower figure, while the upper figure shows the pseudosection for the Wenner Beta (dipole-dipole with $n=1$) array.

3.2 Using the forward modeling program RES2DMOD

The program requires the resistivity model values to be typed in separately in a text file. The model data format, and other details about the use of this program, can be found in the RES2DMOD.PDF manual file. In this course, we will use several model files that are already present in the program package to take a look at the shapes of the contours in the pseudosections for different geological structures. By playing around with this program, you can get a feel of the effects of array type over the amplitude, size and shape of the contours in the pseudosection.

After starting up the RES2DMOD program, click the ‘File’ menu option on the main menu bar. Next select the “Read data file with forward model” suboption to read in one of the example input model files provided. The files with the forward model have a MOD extension. As an example, read in the file SINGLE_BLOCK.MOD that has a simple model with a rectangular prism. After reading in this file, select the “Edit/Display Model” option followed by the “Edit model” suboption to take a look at the model. This will show you the actual cells that make up the model.

The program also allows you to change the model interactively using the left and right

mouse buttons. To change a single cell, click it with the left mouse button. Then move the cursor to one of the color boxes in the legend above the model, and click the resistivity value you want. Press the F1 key to get information about the keys used by the program to edit the model. Note that clicking the cells with the mouse buttons will only change the resistivity of the cells displayed on the screen, but will not change the resistivity of the buffer cells towards the left, right and bottom edges of the mesh. To change the resistivity of the buffer cells, you need to use the “[“, “]” and “D” keys.

Next select the “Model Computation” option to calculate the potential values for this model. The calculations will probably only take a few seconds, after which you should go back to “Edit/Display Model” option. In this option, select the “Edit model” sub-option again to see the apparent resistivity pseudosection for this model. The program will ask you to select the type of contour intervals you wish to use. For most resistivity pseudosections choose the ‘Logarithmic contour intervals’, while for I.P. pseudosections choose the linear contour intervals.

To change the type of array, use the “Change Settings” sub-option. Select another array, such as the pole-pole or dipole-dipole, and see what happens to the shape of the contours in the pseudosection.

3.3 Forward modeling exercises

Here we will try out a few model files that are provided to get a feel of what pseudosections look like, and the effect of different choices on the results. The RES2DMOD program also has an option to save the calculated apparent resistivity values into the format used by the RES2DINV inversion program. You might like to save some of the results from this exercise into this format to use with the RES2DINV program later on. This is useful in studying the model resolution that can be obtained over different structures using various arrays.

Exercise 3.1. Forward modeling examples.

Model file and purpose	Things to try
<p>BLOCK_ONE.MOD To see the effect of selecting the array type on the shape of the contours in the pseudosection. The model is a simple rectangular prism.</p>	<p>(1). The default array type is the Wenner Alpha. Run the ‘Model computation’ option to get things started. Next use the ‘Edit model’ option to take a look at the pseudosection. Compare the shape of the anomaly in the pseudosection with the actual shape of the prism. What is the maximum apparent resistivity value (compare it with the prism resistivity of 100 Ω-m)?</p> <p>(2). Next change the array type to Wenner Beta, and take a look at the shape of the contours. Also, what is the maximum apparent resistivity value? Repeat with the Wenner Gamma array. Among the 3 versions of the Wenner array, which do you think is the ‘best’?</p> <p>(4). Next try the inline dipole-dipole. What is the maximum ‘n’ value you need to use in order to fully map this prism? For a current of 10mA, what would the voltage be for this ‘n’ value when the dipole length is 1 meter? The program also allows you to change the ‘a’ dipole length. Try changing it to 2 and see what happens.</p> <p>(5). To complete things, try out the other arrays, such as the pole-pole, pole-dipole, equatorial dipole-dipole and Wenner-Schlumberger.</p> <p>(6). Edit the model using the ‘Edit Model’ option. Try increasing the thickness and/or width of the prism and see what happens to the anomaly in the pseudosection. Also try changing the resistivity of the prism to 500 Ω-m.</p>

<p>BLOCK_TWO2.MOD In this case, we have two prisms at a mean depth of 1 meter, and 2 meters apart. The two prisms are identical and at the same depth. We will try different arrays to which ones are more likely to be able to resolve the prisms in the pseudosection.</p>	<p>(1). The default array type is the Wenner Alpha. Run the ‘Model computation’ option to get things started. (2). Next, take a look at the pseudosection. Is it possible to separate the highs due to each prism? (3). Try the whole range of arrays, i.e. the 3 different versions of the Wenner, pole-dipole, dipole-dipole, Schlumberger etc. Which arrays are more likely to be able to resolve the two prisms?</p>
<p>BLOCKS_UP.MOD Now we have two prisms, one on top of another. Is it possible to tell them apart?</p>	<p>(1). The default array type is the Wenner Alpha. Run the ‘Model computation’ option to get things started. (2). Next, take a look at the pseudosection. Is it possible to separate the highs due to each prism? (3). Try the whole range of arrays, i.e. the 3 different versions of the Wenner, pole-dipole, dipole-dipole, Schlumberger etc. Which arrays are more likely to be able to resolve the two prisms?</p>
<p>THICK_DIKE.MOD This model has a wide low resistivity dike in high resistivity bedrock.</p>	<p>(1). The default array type is the Wenner Beta. Calculate the potentials and take a look at the pseudosection. Is it possible to infer the existence of the dike from the pseudosection? (2). Change to the Wenner Alpha, and see what happens. (3). Try other arrays such as the Wenner Gamma, Wenner-Schlumberger and pole-dipole. Which arrays show a significant low resistivity anomaly?</p>
<p>THIN_DIKE.MOD This model has a thin dike in high resistivity bedrock. This is a more difficult target than the thick dike.</p>	<p>(1). The default array type is the Wenner Beta. Calculate the potentials and take a look at the pseudosection. Is it possible to infer the existence of the dike for the pseudosection? (2). Change to the Wenner Alpha, and see what happens. (3). Try other arrays such as the Wenner Gamma, Wenner-Schlumberger and pole-dipole. Which arrays show a significant low resistivity anomaly?</p>
<p>MODEILIP.MOD An I.P. model just to round things up.</p>	<p>(1). The default array type is the dipole-dipole, which is probably the most commonly used array for I.P. surveys. Calculate the potential values, and take a look at the pseudosections. (2). Another array that is sometimes used for I.P. surveys is the pole-dipole that has the advantage of a stronger signal strength. Check the pseudosections obtained with this array.</p>

Now that we had some experience in creating pseudosections, it is time to have a look the inversion program RES2DINV that will do the reverse, i.e. creating a model from the pseudosection.

4 A 2-D inversion program

4.1 Introduction

After the field survey, the resistance measurements are usually reduced to apparent resistivity values. Practically all commercial multi-electrode systems come with the computer software to carry out this conversion. In this section, we will look at the steps involved in converting the apparent resistivity values into a resistivity model section that can be used for geological interpretation. I will assume that the data is already in the RES2DINV format. The conversion program is provided together with many commercial systems. So far, the ones that have the conversion program include Abem, AGI, Campus, Geofysika, Geometrics, Iris, OYO, Pasi and Scintrex. If your equipment manufacturer is not on the list, please contact them about the conversion software. The data format used by the RES2DINV program is described in detail in the RES2DINV.PDF manual provided with the program. Please refer to the manual for the details.

In the next section, we will look at two methods to handle bad data points. Such bad data points should be removed before a final interpretation is made.

Due to the large variety of data sets collected over various geological environments, no single inversion method will give the optimum results in all cases. Thus the RES2DINV program has a number of settings that can be changed by the user to obtain results that are closer to the known geology. The various options are also discussed in the following sections.

4.2 Pre-inversion and post-inversion methods to remove bad data points

To get a good model, the data must be of equally good quality. Bad data points fall into two broad categories, i.e. “systematic” and “random” noise. Systematic noise is usually caused by some sort of failure during the survey such that the reading does not represent a true resistivity measurement. Examples include breaks in the cable, very poor ground contact at an electrode such that sufficient current cannot be injected into the ground, forgetting to attach the clip to the electrode, connecting the cables in the wrong direction etc. Systematic noise is fairly easy to detect in a data set as it is usually present in limited number of readings, and the bad values usually stick out like sore thumbs. Random noise include effects such telluric currents that affects all the readings, and the noise can cause the readings to be lower or higher than the equivalent noise-free readings. This noise is usually more common with arrays such as the dipole-dipole and pole-dipole that have very large geometric factors, and thus very small potentials for the same current compared to other arrays such as the Wenner. It is also common with the pole-pole array due to the large distance between the P1 electrode and the remote (and fixed) P2 electrode. This array tends to pick up a large amount of telluric noise due to the large distance between the two potential electrodes.

As a general rule, before carrying out the inversion of a data set, you should first take a look at the data as a pseudosection plot (Figure 4.1a) as well as a profile plot (Figure 4.1b). The bad data points with “systematic” noise show up as spots with unusually low or high values (Figure 4.1a). In profile form, they stand out from the rest and can be easily removed manually for the data set. In the RES2DINV program, choose the ‘Edit data’ on the top menu bar followed by the ‘Exterminate bad data points’ option (Figure 4.2). The bad data points can be removed by clicking them with the mouse.

When the noise is of a more random nature, the noisy data points are not as obvious, so it might not be practical to remove them manually. Also, manually picking out the bad data points becomes impractical if there are a large number of bad data points, particularly if the data set contains more than a thousand data points. In some cases, it is not possible to display the data as pseudosections or profiles, such as in 3D data sets. RES2DINV (and

RES3DINV) has a general technique to remove the bad data points with minimal input from the user, and can be used for practically any array and any distribution of the data points. The main disadvantage of the method is the larger amount of computer time needed. In this method, a preliminary inversion of the data set is first carried with all the data points. After carrying out the trial inversion, switch to the 'Display' window in RES2DINV, and read in the INV file containing the inversion results. After that, select the 'RMS error statistics' option that displays the distribution of the percentage difference between the logarithms of the measured and calculated apparent resistivity values. The error distribution is shown in the form of a bar chart, such as in Figure 4.3. Normally, the highest bar is the one with the smallest errors, and the heights of the bars should decrease gradually with increasing error values. The bad data points, caused by problems such as poor ground contact at a small number of electrodes, should have significantly higher errors than the "good" data points.

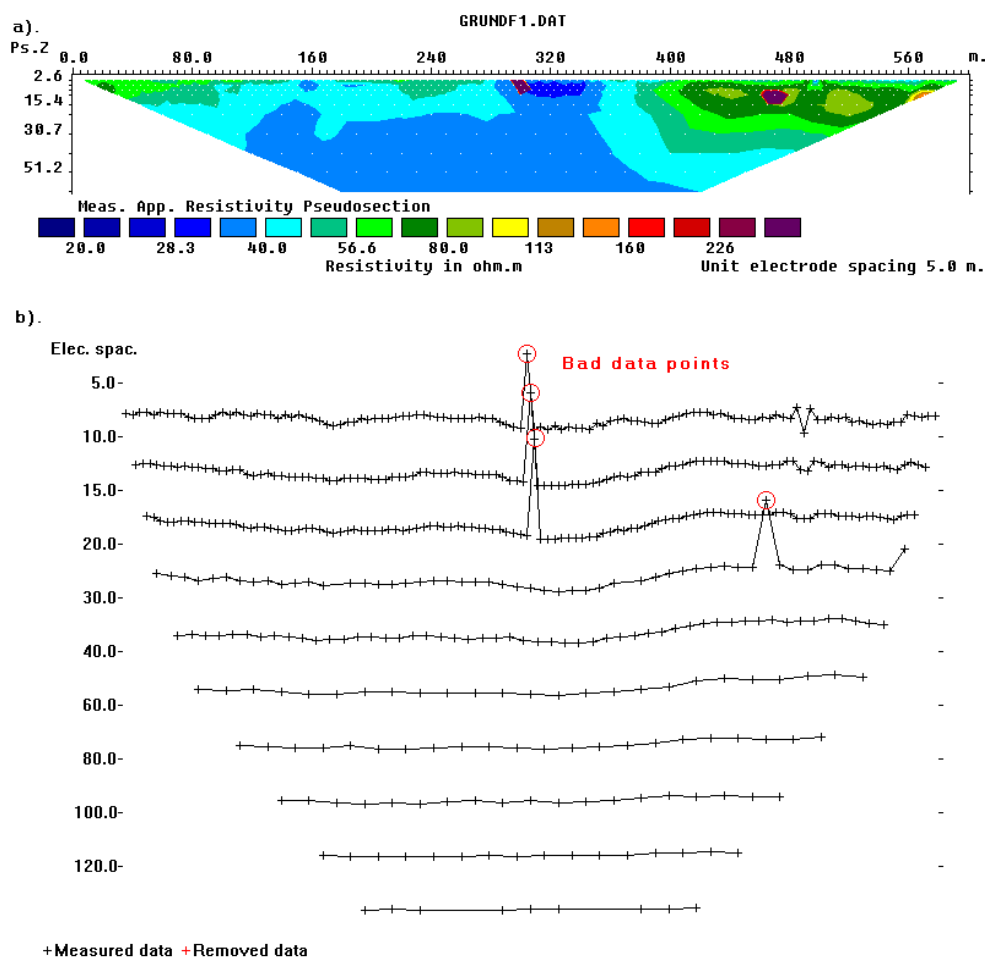


Figure 4.1. An example of a field data set with a few bad data points. The most obvious bad datum points are located below the 300 meters and 470 meters marks. The apparent resistivity data in (a) pseudosection form and in (b) profile form.

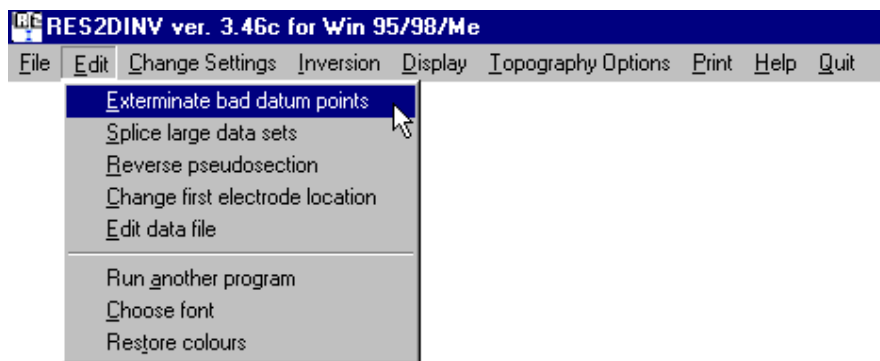


Figure 4.2. Selecting the menu option to remove bad data points manually.

Figure 4.3 shows the error distribution bar chart for the data set shown in Figure 4.1 in that has a few bad data points. In the bar chart, almost all the data points have errors of 20 percent or less. The bad data points show up data points with errors of 60 percent and above, which can be easily removed from the data set by moving the green cursor line to the left of the 60% error bar. In this way the 5 bad data points are removed from this data set. For some data sets, the error distribution might show a more complicated pattern. As a general rule, data points with errors of 100 percent and above can usually be removed.

Exercise 4.1 : Methods to remove bad data points

Data set and purpose	Things to try
GRUNDF1.DAT – An example of a field data set with bad data points.	<p>(1) Use the 'File' and then the 'Read data file' options to read in this data file. Go to the 'Display' windows, and then the 'Display data and model sections' option. The bad data points should be quite obvious.</p> <p>(2) Next, leave the 'Display' window, and then choose 'Edit data' on the top menu bar followed by the 'Exterminate bad data points' option. Pick out the bad data points. After that save the edited data in a file. Read in this edited data file, and then go back to the 'Display' window and check the pseudosection again.</p> <p>(3) After that, leave the 'Display' window, and then run an inversion of the data set using the 'Inversion' and then the 'Least-squares inversion' menu options.</p> <p>(4) After the inversion has finished, go the 'Display' window to take a look at the model. After that choose the 'Edit data' and then the 'RMS error statistics' options. Take a look at the bar chart. Is it possible to remove more bad data points?</p> <p>(5). Try running an inversion of the data set without first manually removing the bad data points. Then use the 'RMS error statistics' option to remove them. Does this get rid of the bad data points also?</p>

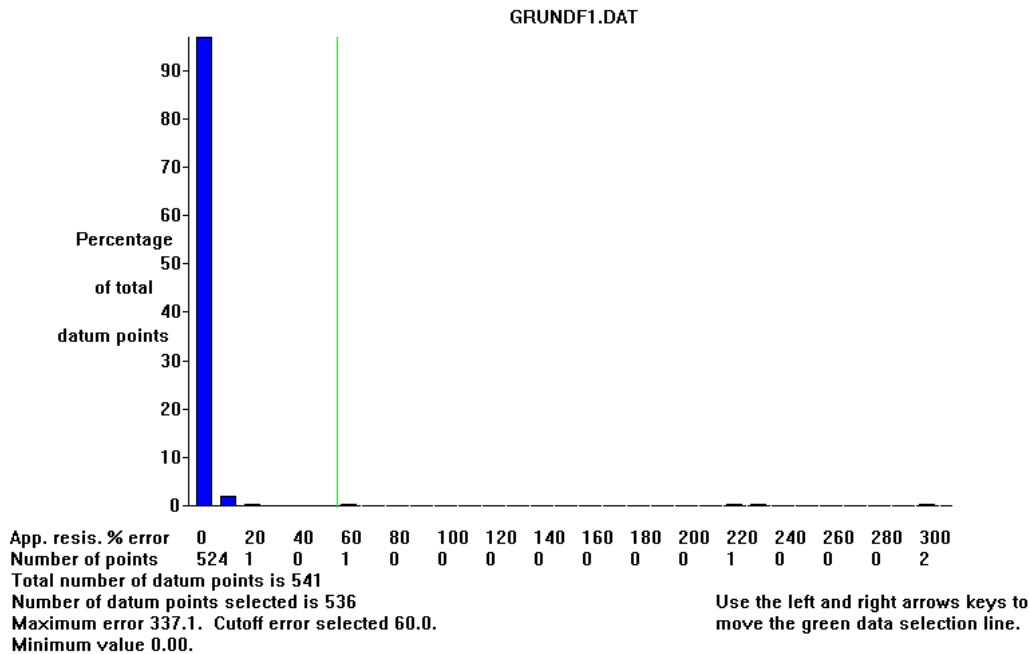


Figure 4.3. Error distribution bar chart from a trial inversion of the Grundfor Line 1 data set with five bad data points.

4.3 Selecting the proper inversion settings

Many professionals carrying out resistivity imaging surveys will likely to be field engineers, geologists or geophysicists who might not familiar with geophysical inversion theory. The RES2DINV program is designed to operate, as far as possible, in an automatic and robust manner with minimal input from the user. It has a set of default parameters that guides the inversion process. In most cases the default parameters give reasonable results. This section describes some of the parameters the user can modify to fine-tune the inversion process. In the program, the different options are divided into six major groups. The groups are placed under the ‘Change Settings’ or ‘Inversion’ choices on the main menu bar. The groups are ‘INVERSION METHODS’, ‘MODEL DISCRETIZATION’ and ‘MODEL SENSITIVITY OPTIONS’ under the ‘Inversion’ menu choice; and ‘INVERSION DAMPING PARAMETERS’, ‘MESH PARAMETERS’ and ‘INVERSION PROGRESS’ under the ‘Change Settings’ menu choice. Here, we will look at a few of the more important settings that can be changed.

a). INVERSION METHODS

The problem of non-uniqueness is well known in the inversion of resistivity sounding and other geophysical data. For the same measured data set, there is wide range of models that can give rise to the same calculated apparent resistivity values. To narrow down the range of possible models, normally some assumptions are made concerning the nature of the subsurface that can be incorporated into the inversion subroutine. In almost all surveys, something is known about the geology of the subsurface, for example whether the subsurface bodies are expected to have gradational or sharp boundaries.

The default smoothness-constrained inversion formulation used by the RES2DINV program is given by (please refer to section 1.4 for the details)

$$(\mathbf{J}^T \mathbf{J} + \lambda \mathbf{F}) \Delta \mathbf{q} = \mathbf{J}^T \mathbf{g} \quad (4.1)$$

This formulation constrains the *change* in the model resistivity values, $\Delta \mathbf{q}$, to be smooth but does not guarantee that the resistivity values change in a smooth manner (Oldenburg, pers.

comm.). However, this formulation has been quite popular and used by a number of researchers (deGroot-Hedlin and Constable 1990, Sasaki 1992).

The first option ‘Include smoothing of model resistivity’ uses a formulation that will apply the smoothness constrain directly on the model resistivity values. This formulation is given by

$$(\mathbf{J}^T \mathbf{J} + \lambda \mathbf{F}) \Delta \mathbf{q} = \mathbf{J}^T \mathbf{g} - \lambda \mathbf{F} \mathbf{q}, \quad (4.2)$$

so that the model resistivity values, \mathbf{q} , changes in a smooth manner. The next option ‘Use combined inversion method’ attempts to combined the smoothness-constrained method as given in (4.1) with the Marquardt-Levenberg as given in (1.20). However, the result obtained by this combination has not been very impressive and will not be examined.

The ‘Select robust inversion’ option has proved to be much more useful. It modifies the formulation in (4.2) so that different elements of the model parameter change and data misfit vectors have the same magnitudes. It is given by

$$(\mathbf{J}^T \mathbf{J} + \lambda \mathbf{F}_R) \Delta \mathbf{q}_k = \mathbf{J}^T \mathbf{R}_d \mathbf{g} - \lambda \mathbf{F}_R \mathbf{q}_k. \quad (4.3)$$

The details are described in section 1.4. This method is also known as an l_1 -norm or robust or blocky inversion method, whereas the conventional smoothness-constrained least-squares method as given in equation (4.2) is an l_2 -norm inversion method. The l_2 -norm inversion method gives optimal results where the subsurface geology exhibits a smooth variation, such as the diffusion boundary of a chemical plume. However, in cases where the subsurface consists of bodies that internally homogeneous with sharp boundaries (such as an igneous dyke), this method tends to smear out the boundaries. The l_1 -norm or blocky optimisation method tends to produce models that are piecewise constant (Ellis and Oldenburg 1994a). This might be more consistent with the known geology in some situations.

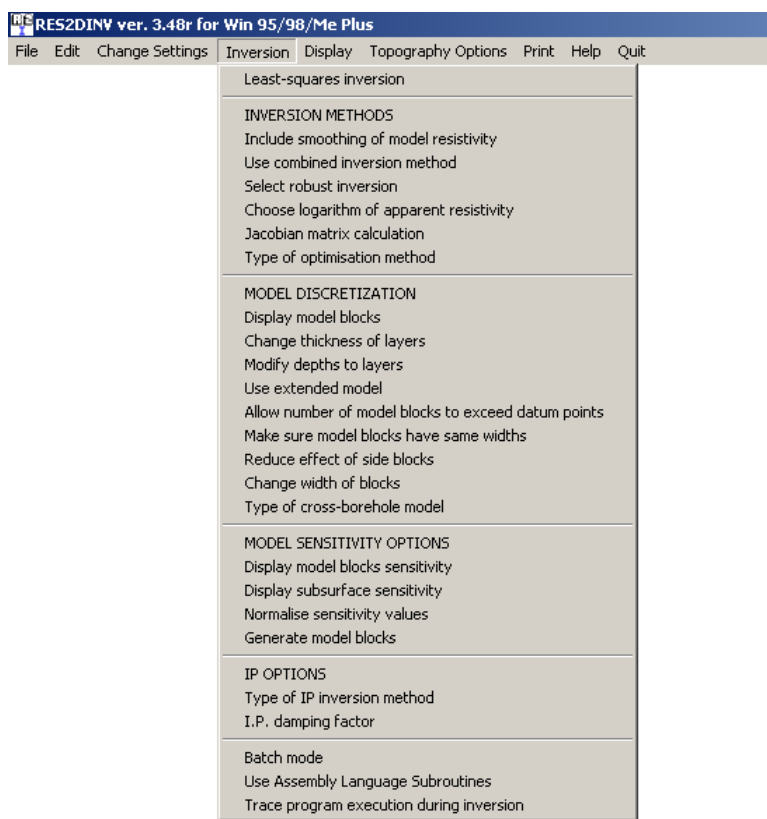


Figure 4.4. Different options to modify the inversion process.

Figure 4.5 shows the inversion results for data from a synthetic model with sharp boundaries. In this case, the robust inversion method gives significantly better results since the true model consists of three homogenous regions with sharp boundaries. Many synthetic test models are of a similar nature with sharp boundaries, so not surprisingly, results obtained with the l_2 -norm smooth inversion method are not optimal for such data sets (Olayinka and Yaramanci 2000).

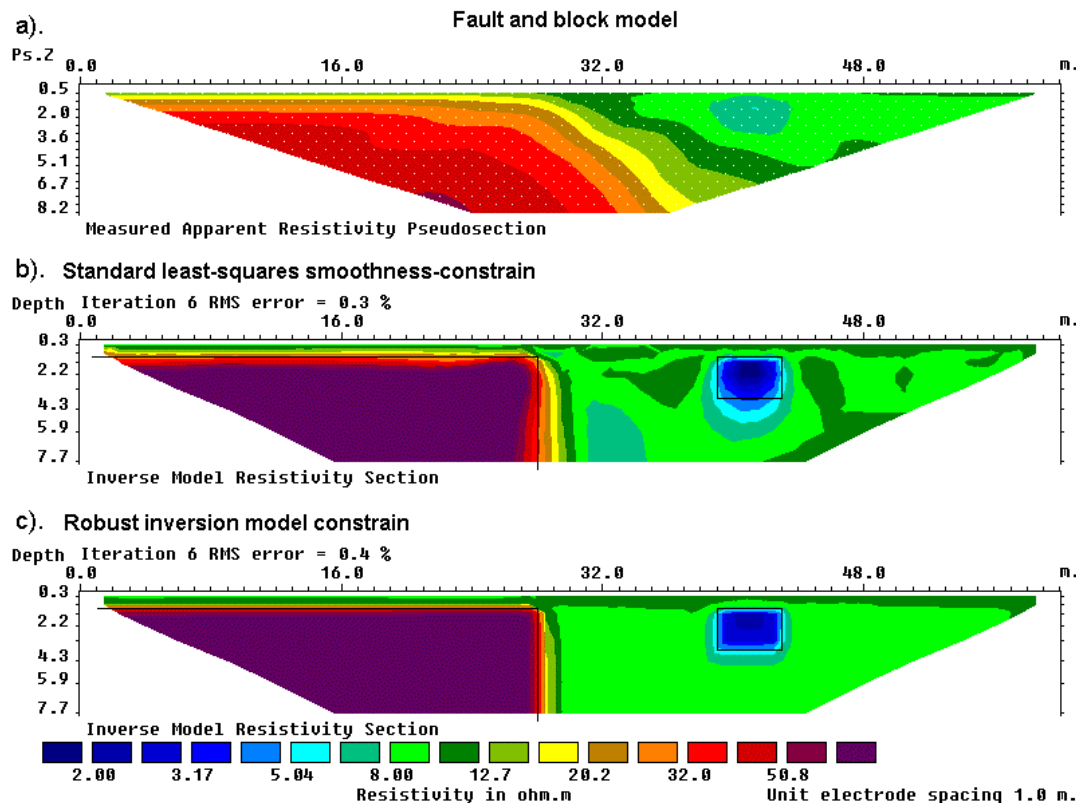


Figure 4.5. Example of inversion results using the l_2 -norm smooth inversion and l_1 -norm blocky inversion model constrains. (a) Apparent resistivity pseudosection (Wenner array) for a synthetic test model with a faulted block (100 Ω -m) in the bottom-left side and a small rectangular block (2 Ω -m) on the right side with a surrounding medium of 10 Ω -m. The inversion models produced by (b) the conventional least-squares smoothness-constrained or l_2 -norm inversion method and (c) the robust or l_1 -norm inversion method.

Resistivity values have a logarithmic range, possibly ranging from less than 1 to over 1000 Ω -m in a single data set. By using the logarithm of the resistivity values as the parameters in the inversion process, the numerical range of the parameters can be reduced to a linear range. However, in some situations, it is not possible to make use of the logarithm if there are negative or zero values. This does not usually occur for normal surface surveys with the standard arrays, but could occur in borehole surveys or if non-standard arrays are used. The program also allows the use to use the apparent resistivity value directly as the inversion parameter in the “Choose logarithm of apparent resistivity” option.

The setting ‘Jacobian matrix calculation’ provides three options on the method used by the program to determine the Jacobian matrix values (please refer to equation 1.18 to see what is the Jacobian matrix). The first version of the RES2DINV program was written in the days of the 80386 computers, so reducing the computer time was a high priority. The quasi-

Newton method (Loke and Barker, 1996a) was used to minimize the computer time. In the quasi-Newton method, the Jacobian matrix for a homogenous earth model (which can be calculated analytically) was used for the first iteration and an updating method was used to estimate the Jacobian matrix value for subsequent iterations. This method avoids a direct calculation of the Jacobian matrix. This is the first option shown in Figure 4.6. This method is fast and works well with low resistivity contrasts, and it is probably useful in providing an approximate model for cases with larger contrasts (Loke and Dahlin 2002). Subsequent improvements in computer technology and software algorithms have significantly reduced the time taken to directly calculate the Jacobian matrix for non-homogeneous models using the finite-difference or finite-element methods. The user can choose to recalculate the Jacobian matrix in every iteration. In theory, this should give the most accurate results. As a compromise between speed and accuracy, a third option is provided where the Jacobian matrix is recalculated in the first few iterations (where the largest changes occur), and estimated for the later iterations. This is the default option used by the RES2DINV program.

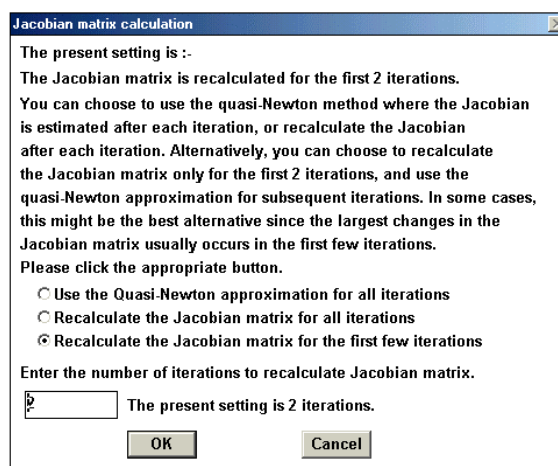


Figure 4.6. The different options for the Jacobian matrix calculation.

The last setting ‘Type of optimization method’ provides two numerical methods to solve the least-squares equation (as in equations 4.1 to 4.3). The default method, particularly when the number of model parameters n is small, is the standard (or complete) Gauss-Newton method where a direct method (Golub and van Loan 1989) is used to solve the equation. This method produces an exact solution but as the time taken is proportional to n^3 , it could take a very long time for large data set with over 5000 model cells. An alternative method, the incomplete Gauss-Newton method, can be used for such cases. In the incomplete Gauss-Newton method, an approximate solution of the least method is determined by using an iterative method (Golub and van Loan 1989). The final solution obtained with this method has a difference of about 1 to 2 percent compared to the complete Gauss-Newton method solution. By sacrificing a small amount of accuracy in the solution to the least-squares equation, the computer time required could be reduced by a factor of 5 to 10 times for very large models.

b). MODEL DISCRETIZATION

This set of options control the way the program subdivides the subsurface into rectangular cells. By default, the program uses a heuristic algorithm partly based on the position of the data points to generate the size and position of the model blocks. In the original algorithm by Loke and Barker (1996a), the model blocks were arranged in exactly the same manner as the data points in the pseudosection. This works well for the relatively

simple pseudosections measured at that time, but this model discretization method will break down for pseudosections with overlapping data levels (Figure 2.18) or if there are significant missing data points (holes) in the pseudosection. The RES2DINV program uses a more sophisticated algorithm to subdivide the subsurface where the distribution of the model blocks is loosely tied to the data points in the pseudosection.

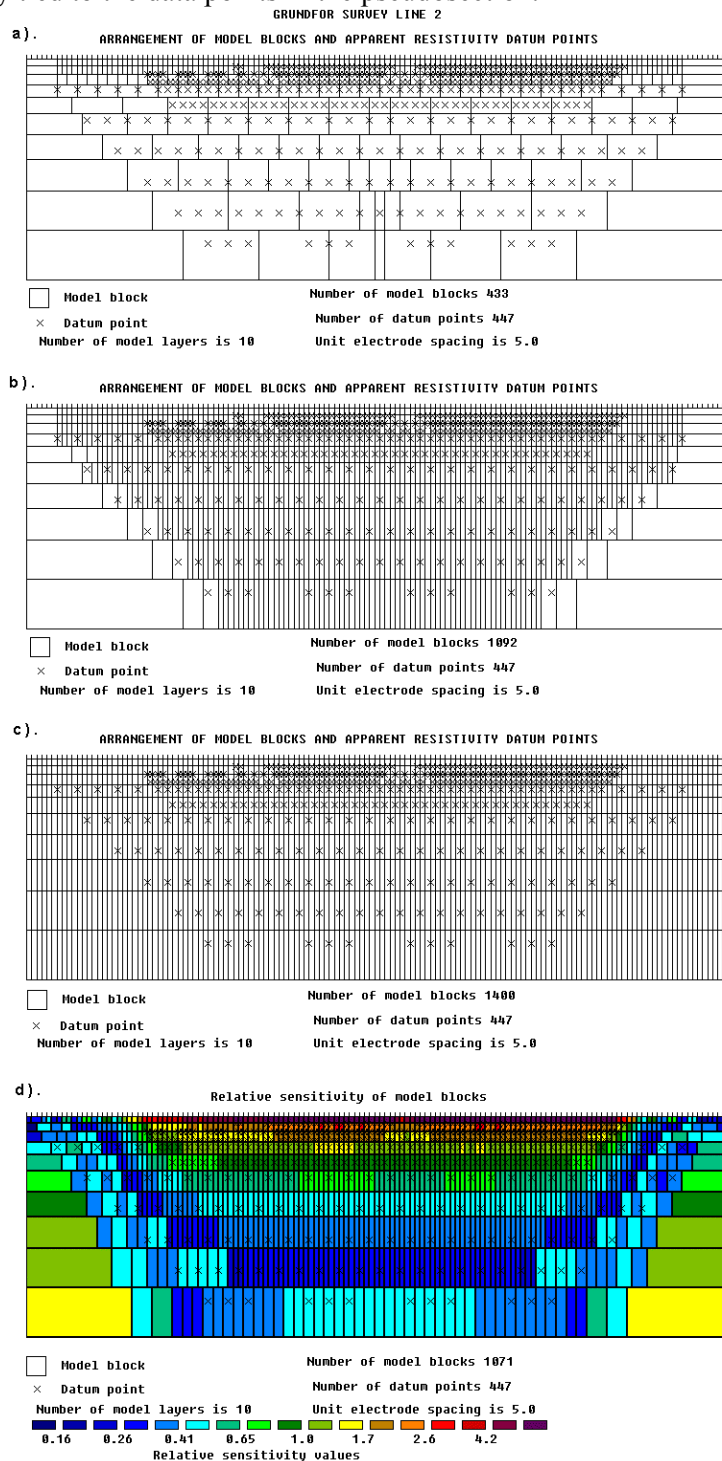


Figure 4.7. Different methods to subdivide the subsurface into rectangular prisms in a 2-D model. Models obtained with (a) the default algorithm, (b) by allowing the number of model cells to exceed the number of data points, (c) a model which extends to the edges of the

survey line and (d) using the sensitivity values for a homogeneous earth model.

In the default algorithm used, the depth to the deepest layer in the model is set to be about the same as the largest depth of investigation of the data points, and the number of model cells does not exceed the number of data points. The thickness of each deeper layer is increased to reflect the decreasing resolution of the resistivity method with increasing depth. In general, this produces a model where the thickness of the layers increases with depth, and with thicker cells at the sides and in the deeper layers (Figure 4.6a). For most cases, this gives an acceptable compromise. The distribution of the data points in the pseudosection is used as a rough guide in allocating the model cells, but the model section does not rigidly follow the pseudosection. However, the user can change the width and thickness of the cells using a variety of options.

After reading a data file, clicking the ‘Display model blocks’ option will show the distribution of the model cells currently used by the program, such as in Figure 4.7a. Clicking the ‘Change thickness of layers’ option will bring up the following dialog box.

Figure 4.8. The options to change the thickness of the model layers.

Firstly, you can choose a model where the layer thickness increases moderately (10%) or greatly (25%) with depth. If these two options are still not satisfactory, you can choose the ‘User defined model’ where you need to set the thickness of first layer and the factor to increase the thickness with depth. In this dialog box, you can also allow the program to use a model where the number of model cells exceeds the number of data points. This is useful to avoid having a model with very wide cells near the bottom for data sets with very sparse data sets. Figure 4.7b shows such an example with this option enabled.

The program will set the model layers until it reaches the maximum pseudodepth of the data points. If you need even deeper layers, the last setting ‘Factor to increase model depth range’ forces the program to add more layers. For example, if you choose a value of 1.25 for this factor, the program will add layers until a depth that is 25% greater than the

maximum pseudodepth in the data set.

The ‘Modify depth to layers’ option allows you to set the depth to each layer individually. This is useful if you want a layer boundary to coincide exactly with a known geological boundary.

In ‘Use extended model’ option, model cells of uniform thickness right up to the left and right edges of the survey line are used (Figure 4.7c). This is probably an extreme case. As the number of model parameters increase, the computer time needed to carry out the inversion also increases. This can be an important consideration for very large data sets with several hundred electrodes. The ‘Make sure model blocks have same widths’ option is probably more useful. It uses a base model such as in Figure 4.7b, but avoids thicker cells at the sides. It ensures that the cells at the sides to have the equal widths.

The ‘Reduce effect of side blocks’ option affects the calculation of the Jacobian matrix values for the model cells located at the sides and bottom of the model section. Normally, for a cell located at the side, the contributions by all the mesh elements associated with the model cell are added up right to the edge of the mesh. This gives a greater weight to the side cell compared to the interior cells. In some cases, particularly when the robust inversion option is used, this can result in unusually a high or low resistivity value for the side cell. This option leaves out the contribution of the mesh elements outside the limits of the survey line to the Jacobian matrix values for the side cells.

The last two options, ‘Change width of blocks’ and ‘Type of cross-borehole model’, are only used for certain special cases, and will not be described here. Please refer to the RES2DINV.PDF manual for the details.

c). **MODEL SENSITIVITY OPTIONS**

This set of options relate to the model sensitivity (Jacobian matrix) values. The ‘Display model blocks sensitivity’ option will display the sum of the absolute values of the sensitivity values associated with the model cell. Figure 4.7d shows an example. Note the blocks at the sides and bottom has greater sensitivity values due to the larger sizes. To avoid this effect, the ‘Display subsurface sensitivity’ option divides the subsurface into cells of equal size and shows the sensitivity values. This is useful to get an idea of the regions of the subsurface “scanned” by the survey configuration used.

All the techniques used to subdivide the subsurface described in the earlier section are based on heuristic algorithms. Figure 4.7d shows the block distribution generated by a more quantitative approach based the sensitivity values of the model cells. This method is selected by the ‘Generate model block’ option. This technique takes into account the information contained in the data set concerning the resistivity of the subsurface for a homogeneous earth model. It tries to ensure that the data sensitivity of any cell does not become too small (in which case the data set does not have much information about the resistivity of the cell).

The next set of inversion options are grouped below the ‘Change Settings’ choice on the main menu bar. Clicking this will bring up the list of options shown in Figure 4.9.

d). **INVERSION DAMPING PARAMETERS**

This set of options is related to the damping factor λ used in the least-squares equations (4.1) to (4.3). By default, the program uses a value of 0.16 for the initial damping factor value for the first iteration. The damping factor is decreased by about half after each iteration. However, to avoid instability in the model values due to a damping factor value that is too small, a minimum limit of 0.015 is used by the program.

The ‘Damping factors’ option allows you to set the initial damping factor and the minimum limit. If the data set appears to be very noisy, and unusually high or low model resistivity values are obtained with the default values, try using larger values for the damping

factors.

Since the model resolution decreases with depth, the program increases the damping factor value by about 5% for each deeper layer. You can change this factor using the “Change damping factor with depth’ option. Instead of automatically decreasing the damping factor by half after each iteration, the ‘Optimize damping factor’ option allows the program to look for an optimum damping factor. The time taken per iteration will be more, but fewer iterations might be needed for the program to converge.

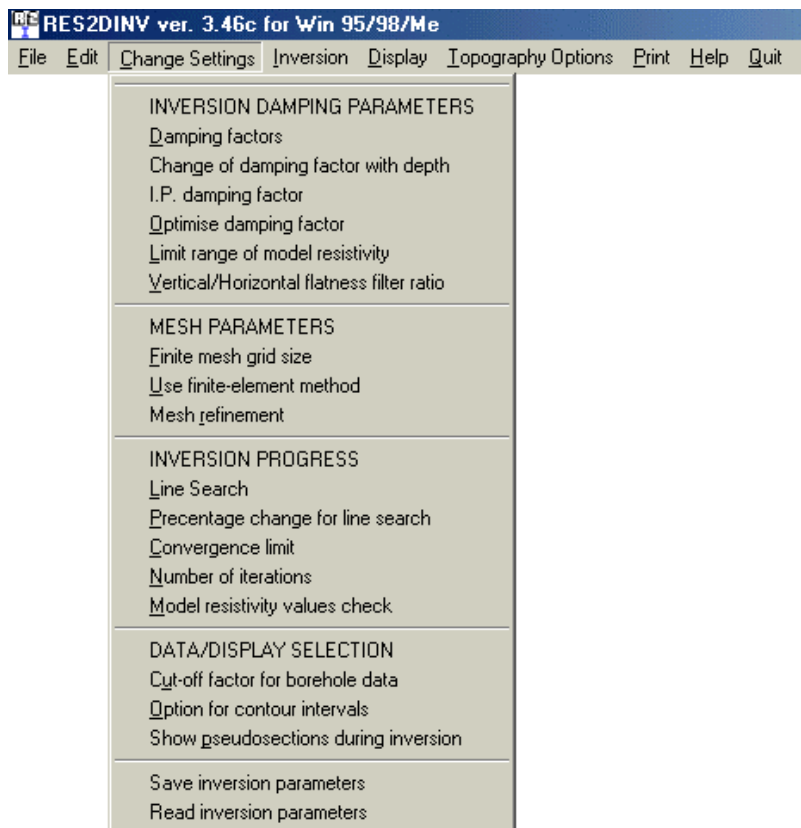


Figure 4.9. The options under the ‘Change Settings’ menu selection.

The ‘Limit range of model resistivity values’ option is intended for cases where the default settings (without limits) produces a model with resistivity values that are too high or too low. Selecting this option will bring up the dialog box shown in Figure 4.10. In this example, the upper limit for is 20 times the average model resistivity value for the previous iteration while the lower limit is 0.05 times (i.e. 1/20 times). The program uses “soft” limits that allow the actual resistivity model values to exceed the limits to a certain degree. However, this option will avoid extremely small or large model resistivity values that are physically unrealistic.

The ‘Vertical/Horizontal flatness filter ratio’ option allows the user to fine-tune the smoothness-constrain to emphasize vertical or horizontal structures in the inversion model. Some geological bodies have a predominantly horizontal orientation (for example sedimentary layers and sills) while others might have a vertical orientation (such as dykes and faults). This information can be incorporated into the inversion process by setting the relative weights given to the horizontal and vertical flatness filters. If for example the structure has a predominantly vertical orientation, such as a dyke, the vertical flatness filter is given a greater weight than the horizontal filter.

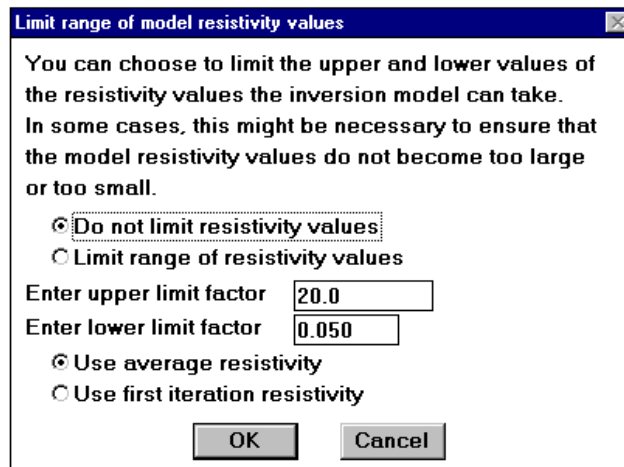


Figure 4.10. The dialog box to limit the model resistivity values.

e). **MESH PARAMETERS**

This set of options controls the finite-element or finite-difference mesh used by the forward modeling subroutine. The ‘Finite mesh grid size’ option changes the mesh size in the *horizontal* direction, while the ‘Mesh refinement’ option changes the mesh settings in the *vertical* direction. Using a finer mesh normally increases the accuracy of the forward modeling subroutine, particularly if very large resistivity contrasts are present.

Exercise 4.2 : Tests with different inversion options

Data set and purpose	Things to try
GRUNDFOR.DAT – An example of a field data with smooth variation of the resistivity values. The purpose is to see the effect of the different model discretizations. The purpose of this field survey was to map the soil lithology (Christensen and Sorenson 1994).	<p>(1). Read in the data set using the ‘File’ and then carry out the inversion with the default model discretization. You can take a look at the way the subsurface is divided into cells by selecting the ‘Display model blocks’ option.</p> <p>(2). Now choose the option to ‘Allow number of model blocks to exceed data points’, and run the inversion again. Make sure to use a different name for the inversion results file, for example GRUNFOR2.INV. Check out the arrangement of the cells again using the ‘Display model blocks’ option.</p> <p>(3). Now we will reduce the width of the side cells as well. Select the ‘Make sure model blocks have same widths’ option, and check out the arrangement of the cells. Next run the inversion again.</p> <p>(4). Finally we will use an arrangement with even more model cells. Select the ‘Use extended model’ option, and then run the inversion.</p> <p>As the number of model cells increase, the computer time increases. Which do you think is the best compromise between getting a finer model and reducing the computer time?</p>
BLOCK_ONE.DAT – A synthetic test model. To show advantage of robust l_1 norm	<p>(1). After reading in the data file, choose the ‘Include smoothing of model resistivity’ option to ensure inversion model is smooth. Run the inversion and see what you get.</p>

inversion for models with sharp boundaries.	You might like to display the inversion model in the form of blocks rather than contours. This shows up the smearing out of the boundaries better. Compare the maximum and minimum model resistivity values with the true values. (2). Next select the ‘Select robust inversion’ option, and the enable both the robust model and data constrains. Check out the resulting inversion model.
ODARSLOV.DAT – A field data set with a vertical dike.	(1). To get the best results, enable both the option to “Allow number of model blocks to exceed datum points”. Make sure the option ‘Include smoothing of model resistivity’ is on to get a maximally smooth model. (2). Next use the robust inversion method. You should see a dramatic change in the model. (3). One of the undesirable side effects of the robust inversion option is the model resistivity values at the bottom-left and bottom-right corners can take extreme values. To reduce this effect, select the ‘Reduce effect of side blocks’ option, and then run the inversion again.

4.4 Using the model sensitivity and uncertainty values

The depth of investigation and sensitivity sections described in section 2.5 gives an idea of the depth of the regions sensed by a single electrode configuration. A 2-D survey typically has hundreds of data points collected with electrodes at different locations and spacings. A question that frequently arises in 2-D interpretation is as follows. What are the regions of the subsurface sensed by the survey, and what is the reliability of the results? The first question can be easily determined, but at present there is no simple answer to the second.

The “Display blocks sensitivity” option under the “Inversion” menu will show a plot of the sensitivity of the cells used in the inversion model. The sensitivity value is a measure of the amount of information about the resistivity of a model block cell in the measured data set. The higher the sensitivity value, the more reliable is the model resistivity value. In general, the cells near the surface usually have higher sensitivity values because the sensitivity function has very large values near the electrodes. The cells at the sides and bottom can also have high sensitivity values due to the much larger size of these cells that are extended to the edges of the finite-difference or finite-element mesh (the program has an option to reduce this effect which might produce artifacts at the edges of the model). If you had carried out an inversion of the data set before calling this option, the program will make use of the Jacobian matrix of the last iteration. Otherwise, it will calculate the Jacobian matrix for a homogenous earth model. Figure 4.7d shows an example of a plot of the sensitivity section for a model.

Figure 4.11b shows the model section obtained from the inversion of a data set for a survey to map leakage of pollutants from a landfill site (Niederleithinger, 1994). The model sensitivity section in Figure 4.11c shows high sensitivity values near the surface with decreasing values with depth. This is to be expected as the near surface materials have a larger influence on the measured apparent resistivity values.

In order to assess the accuracy of the inversion model, an estimate of the reliability of the model values is required. One possible approach is by using the model covariance matrix (Menke 1984). This is commonly used for models that consist of a small number of parameters (such as the 1-D model in Figure 1.7). Figure 4.11d shows the model uncertainty values obtained from the covariance matrix method as described by Alumbaugh and Newman

(2000) where the smoothness constraint is included in the model uncertainty estimate. In this way, the model uncertainty values are less sensitive to size of the model cells. However, the uncertainty values are only meaningful if the subsurface resistivity varies in a smooth manner, as assumed by the smoothness constraint. If the subsurface resistivity does not vary in a smooth manner, this method is likely to underestimate the actual uncertainty. Figure 4.11e shows the maximum and minimum resistivity values of each cell at the limits of the model uncertainty range. Features that are common to both model sections can be considered more reliable.

A different approach is to empirically determine the depth of investigation of the data set is by carrying out at least two inversions of the data set using different constraints. Oldenburg and Li (1999) used the following least-squares formulation to carry out the 2-D inversion.

$$(\mathbf{J}^T \mathbf{J} + \lambda \mathbf{F}_R) \Delta \mathbf{q}_k = \mathbf{J}^T \mathbf{R}_d \mathbf{g} - \lambda \mathbf{F}_R (\mathbf{q}_k - \mathbf{q}_o), \quad (4.4)$$

with $\mathbf{F}_R = \alpha_s + \alpha_x \mathbf{C}_x^T \mathbf{R}_m \mathbf{C}_x + \alpha_z \mathbf{C}_z^T \mathbf{R}_m \mathbf{C}_z$.

\mathbf{q}_o is a homogeneous half-space reference model and α_s is an additional “self” damping factor that has a value of about 0.0001 to 0.01 times the α_x and α_z damping factors. In the proposed method, two inversions are carried out using different resistivity values for the reference model. Typically, the second reference model has a resistivity of 10 to 100 times the first reference model. From the model resistivity values, the following depth of investigation (DOI) index is calculated.

$$R(x, z) = \frac{m_1(x, z) - m_2(x, z)}{m_{1r} - m_{2r}} \quad (4.5)$$

m_{1r} and m_{2r} are the resistivity of first and second reference models, $m_1(x, z)$ and $m_2(x, z)$ are model cell resistivity obtained from the first and second inversions. R will approach a value of zero where the inversion will produce the same cell resistivity regardless of the reference model resistivity. In such areas, the cell resistivity is well constrained by the data. In areas where the data do not have much information about the cell resistivity, R will approach a value of one as the cell resistivity will be similar to the reference resistivity. Thus the model resistivity in areas where R has small values are considered to be “reliable”, while in areas with high R values are not reliable.

The model used to calculate the DOI index use cells that extend to the edges of the survey line, and a depth range of about three to five times the median depth of investigation of the largest array spacing used. This ensures that data has minimal information about the resistivity of the cells near the bottom of the model, i.e. in theory the bottom cells have DOI values of almost 1.0.

Figure 4.12a shows the inversion model of the landfill survey data set with a depth range of about 3.5 times the maximum pseudodepth in the apparent resistivity pseudosection in Figure 4.11a. The resistivity of the reference model used is obtained from the average of the logarithms of the apparent resistivity values. Figure 4.12b shows the DOI plot calculated after carrying out a second inversion using a reference model with 100 times the resistivity of the first reference model. Oldenburg and Li (1999) recommended using a value of 0.1 as the cut-off limit for the effective depth of investigation of the data set. The depth to the contour with a DOI value of 0.1 is about 28 m. along most of the survey line. This is close to the maximum median depth of investigation of about 25 m. for this data set. There are shallower regions with high DOI value, particularly below the 50 m. mark. This is probably partly due to the low resistivity plume that limits the amount of current flowing into the deeper sections below it. The resistivity method uses the electrical current as a probing tool, and where the current flow is limited, the amount of information provided is less. Note the regions with high

DOI values at the sides of the section. This is to be expected as the sides of the survey line have less data points compared to the center.

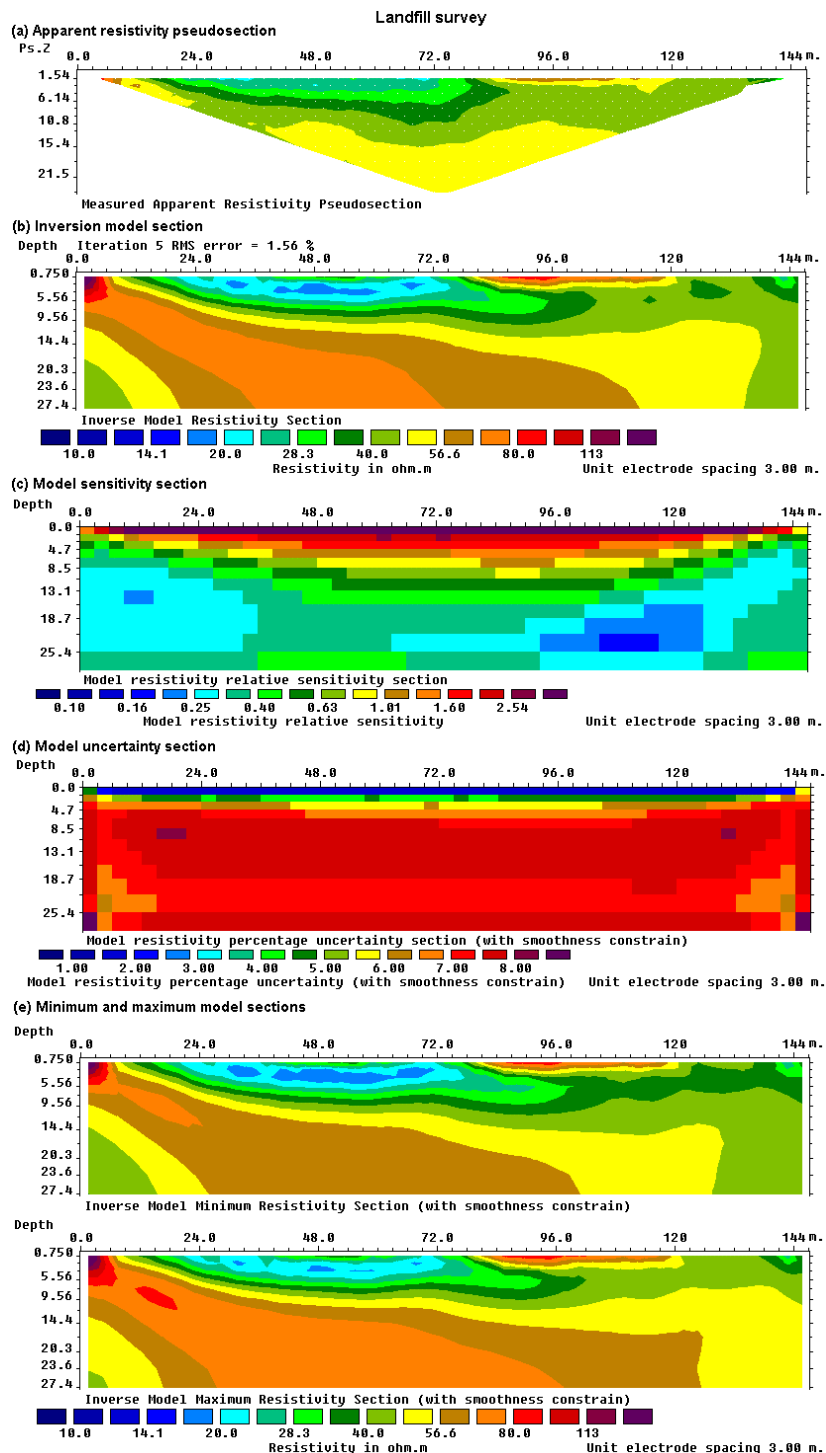


Figure 4.11. Landfill survey example (Wenner array). (a) Apparent resistivity pseudosection , (b) model section, (c) model sensitivity section (d) model uncertainty section, (e) minimum and maximum resistivity sections.

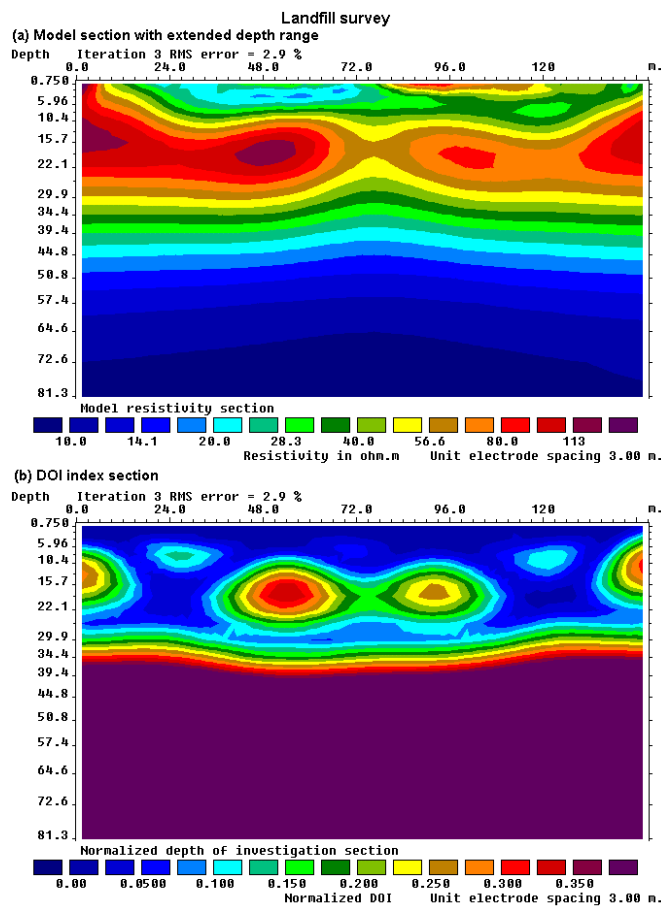


Figure 4.12. Landfill survey depth of investigation determination. (a) Model section with extended depths and (b) the normalized DOI index section.

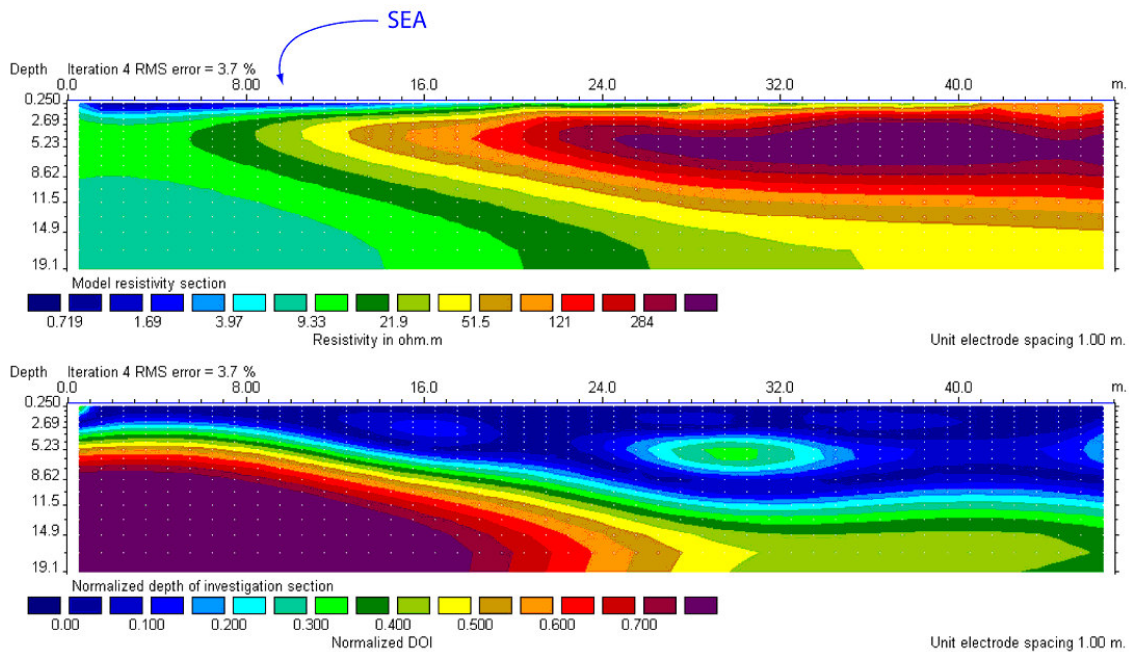


Figure 4.13. Beach survey example in Denmark. The figure shows the model section with extended depths and the normalized DOI index section.

Figure 4.13 shows the DOI plot from a survey to map the boundary between the salt and fresh water zones across a beach in Denmark (Marescot and Loke, 2003). The profile is perpendicular to the seashore and the electrodes 1 to 16 are under the seawater, while the rest of the profile is above the water. Note the strong increase in DOI values on the left part of the profile that is covered with seawater. As this section is covered with seawater, most of the current actually flows within the seawater and does not penetrate into the subsurface. Thus the depth of investigation there is much shallower.

The DOI method is useful in marking the regions where the model values are well constrained by the data set, and thus greater confidence can be placed on the model resistivity values at such regions.

The DOI method may be considered an empirical method to determine the regions where we can reasonably resolve the subsurface. Another method based on the model resolution values is discussed in section 4.8.

4.5 Methods to handle topography

In surveys over areas with significant changes in the elevation of the ground surface, the effect of the topography must be taken into account when carrying out an inversion of the data set. It is now generally recognized that the traditional method of using the “correction factors” for a homogeneous earth model (Fox *et al.* 1980) does not give sufficiently accurate results if there are large resistivity variations near the surface (Tong and Yang 1990). Instead of trying to “correct” for the effect of the topography on the measurements, the preferred method now is to incorporate the topography into the inversion model. The RES2DINV program has three different methods that can be used to incorporate the topography into the inversion model (Loke 2000).

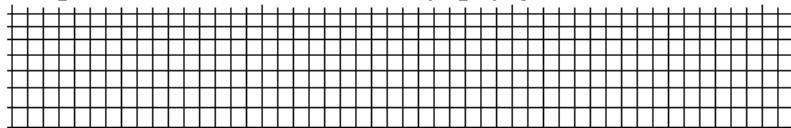
The three methods are similar in that they use a distorted finite-element mesh. In all these methods, the surface nodes of the mesh are shifted up or down so that they match the actual topography. In this case, the topography becomes part of the mesh and is automatically incorporated into the inversion model. The difference between these three methods is the way the subsurface nodes are shifted. The simplest approach, used by the first finite-element method, is to shift all the subsurface nodes by the same amount as the surface node along the same vertical mesh line. This is probably acceptable for cases with a small to moderate topographic variation (Figure 4.14b).

In the second approach, the amount the subsurface nodes are shifted is reduced in an exponential manner with depth (Figure 4.14c) such that at a sufficiently great depth the nodes are not shifted. This comes from the expectation that the effect of the topography is reduced or damped with depth. This produces a more pleasing section than the first finite-element method in that every kink in the surface topography is not reproduced in all the layers. For data sets where the topography has moderate curvature, this is probably a good and simple method. One possible disadvantage of this method is that it sometimes produces a model with unusually thick layers below sections where the topography curves upwards. Thus in Figure 4.14d, the model is probably slightly too thick near the middle of the line where the topography curves upwards and too thin towards the right end of the line where the topography curves downwards. The resulting model is partly dependent on the degree of damping chosen by the user. A value of 0.5 to 1.0 is usually used for the topography damping factor in the RES2DINV program. One main advantage of this method is that it can be easily implemented, particularly for 3-D models (Holcombe and Jirack 1984).

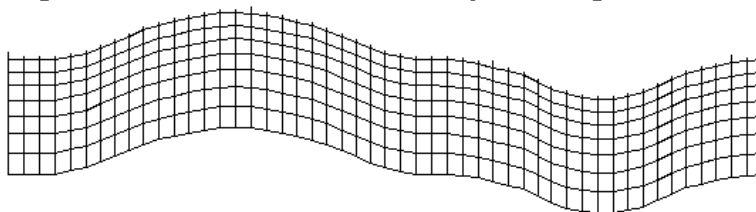
In the third method, the inverse Schwartz-Christoffel transformation method (Spiegel *et al.* 1980) is used to calculate the amount to shift the subsurface nodes (Loke 2000). Since this method takes into account the curvature of the surface topography it can, for certain

cases, avoid some of the pitfalls of the second finite-element method and produces a more “natural” looking model section (Figure 4.14e). For this data set, this method avoids the bulge near the middle of the line produced by the second finite-element method with a damped distorted mesh. However, in the middle part of the line, the model produced by this method is slightly thicker than that produced by the first finite-element method with a uniform distorted mesh.

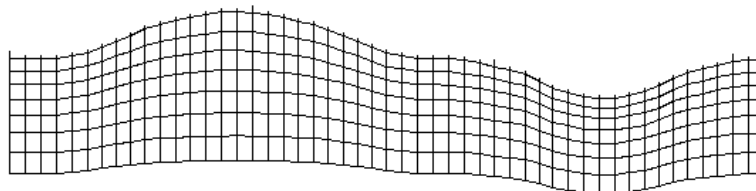
a). Arrangement of model blocks without topography



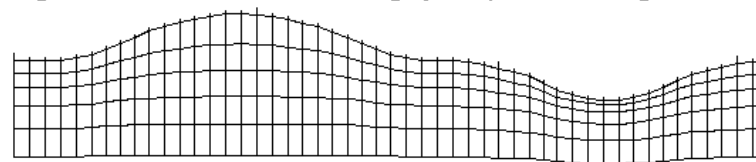
b). Arrangement of model blocks with a uniformly distorted grid



c). Arrangement of model blocks with a moderately damped distorted grid



d). Arrangement of model blocks with a highly damped distorted grid



e). Arrangement of model blocks with the inverse Schwartz-Christoffel transformation

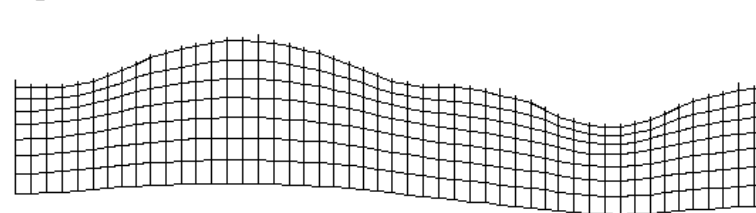


Figure 4.14. Different methods to incorporate topography into a 2-D inversion model. (a) Schematic diagram of a typical 2-D inversion model with no topography. A finite-element mesh with four nodes in the horizontal direction between adjacent electrodes is normally used. The near surface layers are also subdivided vertically by several mesh lines. Models with a distorted grid to match the actual topography where (b) the subsurface nodes are shifted vertically by the same amount as the surface nodes, (c) the shift in the subsurface nodes are gradually reduced with depth or (d) rapidly reduced with depth, and (e) the model obtained with the inverse Schwartz-Christoffel transformation method.

Exercise 4.3 : Tests with different topographic modeling options

Data set and purpose	Things to try
<p>RATCHRO.DAT – An example field data with significant topography. This survey was conducted over a possible ancient burial mound in Ireland (Waddell and Barton 1995).</p>	<p>(1). After reading the data file, select the robust inversion option as the burial chamber probably has a sharp contrast with the soil. After that, click the ‘Display topography’ option under the ‘Topography Options’ in the Main Menu bar.</p> <p>(2). Next click the ‘Type of topographic modeling’ option. Select the uniformly distorted grid method. Run the inversion, and then switch to the ‘Display’ window to take a look at the results. In the ‘Display’ window, choose the ‘Display sections’ followed by ‘Include topography in model display’ options.</p> <p>(3). Now, select the damped distorted grid option in the ‘Type of topographic modeling’ dialog box. Run the inversion again, and then take a look at the model section with the topography. Now we will reduce the width of the side cells as well. Select the ‘Make sure model blocks have same widths’ option, and check out the arrangement of the cells. Next run the inversion again.</p> <p>(4). Next select the inverse Schwartz-Christoffel transformation method in the ‘Type of topographic modeling’ dialog box. Run the inversion again, and take a look at the model with the topography.</p> <p>Which topographic modeling method do you prefer?</p>
<p>GLADOE2.DAT – A data set taken to check for leakage from a dam (Dahlin pers. comm.). The survey area has topography.</p>	<p>(1). If you have the time, run the same tests as you did earlier for the RATHCRO.DAT data set. This is another example where the option to reduce the effect of the side cells makes a significant difference when the robust inversion option is used.</p>

4.6 Incorporating information from borehole logs and seismic surveys

In some areas, information from borehole logs is available concerning the resistivity of part of the subsurface. This program allows you to fix the resistivity of up to 1000 sections of the subsurface. The shape of the section to be fixed must be rectangular or triangular. Borehole logs give the resistivity of the formations along the borehole. However, some caution must be used when incorporating the borehole log information into an inversion model for surface measurements. Borehole measurements usually only give the resistivity of a very limited zone near the borehole. Depending on the type of instrument used, the borehole log generally samples the subsurface within about 1 meter from the borehole. In contrast, the inversion model gives the average resistivity of a much larger region of the subsurface. Thus the RES2DINV program uses a flexible method to incorporate the borehole log information.

The format used by the input data file for RES2DINV to fix the model resistivity values is described in detail in the RES2DINV manual. Here, we will only look at a fragment of it to illustrate the general ideas involved. As an example, part of the example data file MODELFIX.DAT with the resistivity fixing option is listed below.

2		Number of regions to fix, put 0 if none
R		Type of first region, R for rectangular
24,0.7		X and Z coordinates of top-left corner of rectangle
28,2.3		X and Z coordinates of bottom-right corner of rectangle
2.0		Resistivity value of rectangular region
2.0		Damping factor weight
T		Type of second region, T for triangular
30,0.0		X and Z coordinates of first corner of triangle
30,3.0		X and Z coordinates of second corner of triangle
45,3.0		Coordinates of third corner of triangle
10.0		Resistivity value of triangular region
2.0		Damping factor weight

The first item is the number of regions where the resistivity is to be specified. In the example above, 2 regions are specified. If a value of 0 is given (default value), then there is no region where the resistivity is specified by the user. Next, the shape of the region is given, R for rectangular or T for triangular. If a rectangular region is specified, then the X and Z coordinates of the top-left and bottom-right corners of the rectangle are given, as shown in the Figure 4.15. If a triangular region is chosen, the X and Z coordinates of the 3 vertices of the triangle must be given in an anti-clockwise order. After the coordinates of the region to be fixed are given, the next data item is the resistivity of the region. After that, the damping factor weight for the resistivity of the region is needed. This parameter allows you control the degree in which the inversion subroutine can change the resistivity of the region. There is usually some degree of uncertainty in resistivity of the region. Thus, it is advisable that the program should be allowed (within limits) to change the resistivity of the region. If a damping factor weight of 1.0 is used, the resistivity of the region is allowed to change to the same extent as other regions of the subsurface model. The larger the damping factor weight is used, the smaller is the change that is allowed in the resistivity of the "fixed" region. Normally, a value of about 1.5 to 2.5 is used. If a relatively large value is used, for example 10.0, the change in the resistivity of the region would be very small during the inversion process. Such a large value should only be used if the resistivity and shape of the region is accurately known. Figure 4.16 shows the allocation of the cells in the subsurface model together with the fixed regions for the MODELFIX.DAT data set.

Seismic refraction and seismic reflection surveys are commonly used in engineering surveys. Both methods can give accurate and detailed profiles of the subsurface interfaces. In some cases, a distinct and sharp transition between two layers can be mapped by the seismic survey. This information can be used to improve the results from the inversion of a 2-D resistivity imaging survey along the same line. The subsurface in the inversion model can be divided into two zones, one above and one below the interface calculated from the seismic survey. The resistivity values are constrained to vary in a smooth manner within each zone, but an abrupt transition across the zone boundary is allowed by removing any constrain between the resistivity values below and above the zone boundary (Smith et al. 1999).

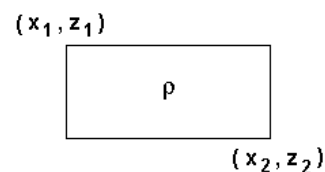
Figure 4.17 shows an example where the boundaries of a clay and a gravel layer were known from a seismic refraction survey (Scott *et al.* 2000). The known boundaries were then incorporated into the resistivity inversion model (Figure 4.17a) that allows the model resistivity to change abruptly across the boundaries. Note the sharp contrast across the gravel layer and the underlying low resistivity clay layer (marked by the bottom blue region in lower section in Figure 4.17b).

Fixing model resistivities

Data format

R
 x_1, z_1
 x_2, z_2
 ρ
 2.0

Rectangular regions



Data format

T
 x_1, z_1
 x_2, z_2
 x_3, z_3
 ρ
 2.0

Triangular regions

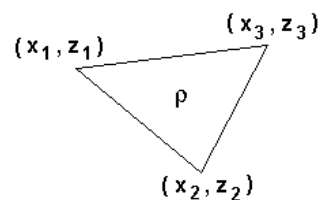


Figure 4.15. Fixing the resistivity of rectangular and triangular regions of the inversion model.

Exercise 4.4 : Tests with option to fix the model resistivity

Data set and purpose	Things to try
MODELFIX.DAT – A synthetic data file with two fixed regions.	(1). After reading the data file, select the robust inversion option as the synthetic model has sharp boundaries. Next choose the ‘Display model blocks’ option to take a look at the locations of the fixed regions. Run the inversion of the data set.
CLIF4_NORMAL.DAT – A data set from the Clifton, Birmingham area (Scott <i>et al.</i> 2000) to map layers within the unconsolidated sediments. CLIF4_LAYERS.DAT – The same data set but with the layers specified. The depths to the layers were determined from a seismic refraction survey.	(1). After reading in the CLIF4_NORMAL.DAT data file, select the robust inversion option, and then run an inversion of the data set. In this case, we have not included additional constraints on the inversion. You might have to use the option to “Reduce effect of the side blocks” to avoid distortions at the bottom-left and bottom-right corners of the inversion model. (2). Do the same for the CLIF4_LAYERS.DAT data file. In this file, the depths to two layers determined from a seismic refraction survey have been included. Take a look the distribution of the model cells, as well as the layers specified, using the ‘Display model blocks’ option. Run the inversion again, and compare the results with that obtained earlier without the layers.

4.7 Model refinement

Normally RES2DINV uses a model where the width of the interior model cells is the same as the unit electrode spacing (for example as in Figure 4.17). In some situations with large resistivity variations near the ground surface, this might not be sufficiently accurate. The model with a cell width of one unit electrode spacing has a maximum possible misfit of one-half the electrode spacing for a near-surface inhomogeneity (Figure 4.18a). In some cases, this misfit can cause significant distortions in the lower sections of the inversion model. The cell size is too coarse to accurately model the anomalies due to the small near-surface inhomogeneities. This forces the inversion program to distort the lower sections of the model in an attempt to reduce the data misfit.

A finer model with a cell width of half the electrode spacing has a maximum misfit of one-quarter the unit electrode spacing (Figure 4.18b), so the effect of the model cell boundary misfit should be much less. In theory, it is possible to reduce the cell width further, but the error due to the misfit becomes increasingly less significant. Reducing the cell increases the number of model parameters, thus increasing the computer time and memory required.

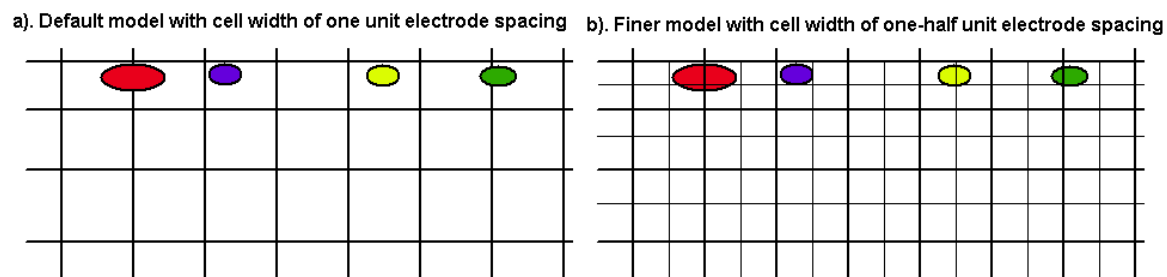


Figure 4.18. The effect of cell size on the model misfit for near surface inhomogeneities. (a) Model with a cell width of one unit electrode spacing. (b) A finer model with a cell width of half the unit electrode spacing. The near surface inhomogeneities are represented by coloured ovals.

Figure 4.19 shows a synthetic model used to illustrate the effect of the model cell misfit. The main structure is a faulted block of $100 \Omega \cdot \text{m}$ and a rectangular prism of $1 \text{ ohm} \cdot \text{m}$ in a medium of $10 \Omega \cdot \text{m}$. A series of small near-surface high resistivity blocks with widths of 1.0, 0.75, 0.50 and 0.25 m. and resistivity of $300 \Omega \cdot \text{m}$ are placed above the faulted block. A similar series of low resistivity blocks of $1.0 \Omega \cdot \text{m}$ are located to the left. The pole-dipole array has the P1-P2 dipole length (“a”) fixed at 1.0 m., but with “n” factor ranging from 1 to 16. Note the strong anomalies produced by the near-surface inhomogeneities. Note also that the Wenner array is much less affected by the near-surface inhomogeneities. The reason lies in the sensitivity patterns of the two arrays (compares Figures 2.10 and 2.17). For the pole-dipole array with large “n” values, the region with the highest positive sensitivity values is concentrated below the P1-P2 dipole pair.

Figure 4.20 shows the inversion results for the pole-dipole data set with different cell widths. The model with a cell width of 1.0 m. (i.e. one unit electrode spacing) shows significant distortions near the top of the faulted block as well as in the low resistivity rectangular block (Figure 4.20b). Most of the distortions are removed in the model with a cell width of half the unit electrode spacing (Figure 4.20c). This means the residual misfits with widths of up to one-quarter the unit electrode spacing does not have a significant effect on the calculated apparent resistivity values. The model with a cell width of one-quarter the unit electrode spacing (Figure 4.20d) does not show any major improvement over the half cell width model although in theory it should more accurately model the near surface

inhomogeneities. In fact, there is a poorer agreement with the true model in the lower part of the faulted block (Figure 4.20d). Experiments with a number of data sets show that using a cell width of one-quarter the unit electrode spacing can sometimes lead to oscillating model resistivity values. This is probably because the data does not have sufficient information to accurately resolve such small cells.

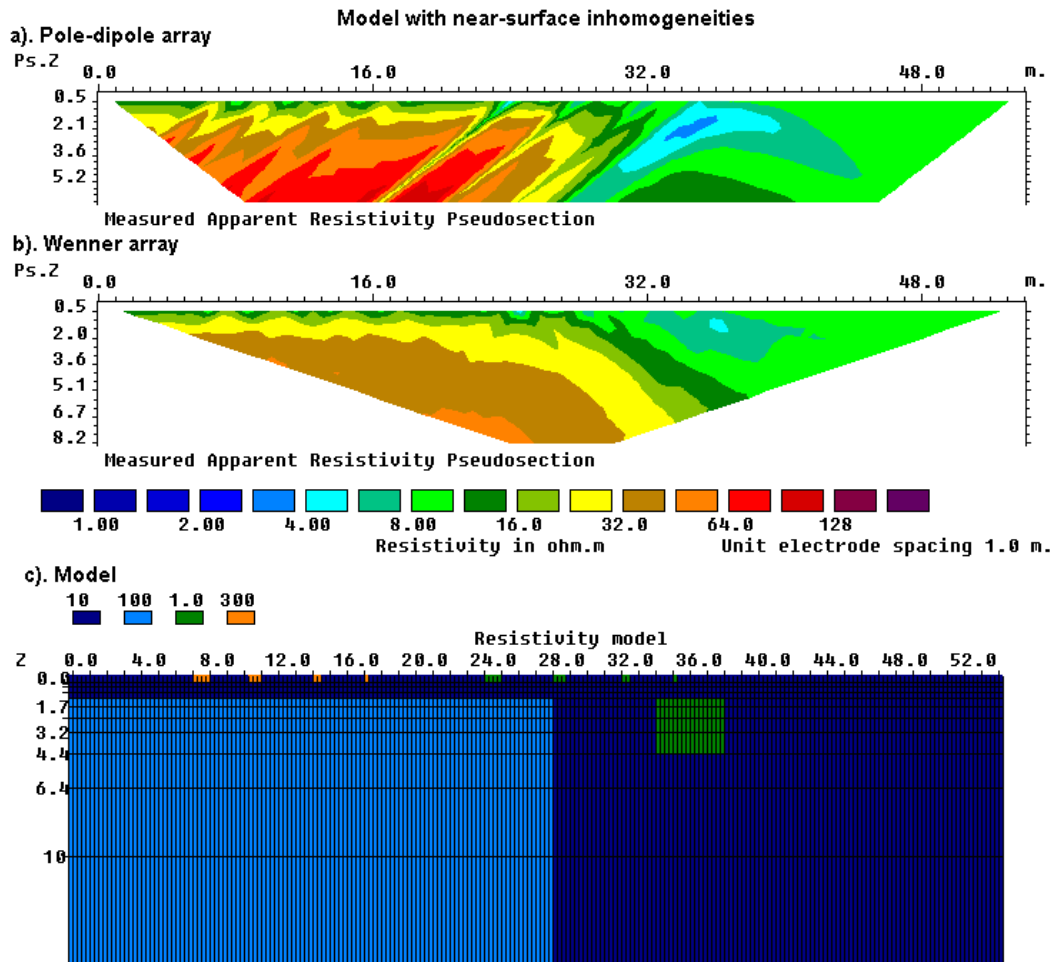


Figure 4.19. Synthetic model (c) used to generate test apparent resistivity data for the pole-dipole (a) and Wenner (b) arrays.

Figure 4.21 shows an example from a survey over an underground pipe using the Wenner-Schlumberger array. There are large resistivity variations near the surface, probably due to stones in the topmost layer of the soil. If the effect of the near surface variations are not accurately accounted for by the inversion model, it can lead to distortions in the lower portions of the model as the programs attempts to reduce the data misfit by distorting the lower part of the model. The model with a cell width of half the unit electrode spacing in Figure 4.21c shows a slightly better fit with the measured data (i.e. lower RMS error) and a more circular shape for the low resistivity anomaly below the 12 meters mark.

In conclusion, for most cases, using a cell width of half the unit electrode spacing seems to give the optimum results. Using a cell width of one-third the unit spacing seems to be beneficial only a certain cases with the pole-dipole and dipole-dipole arrays with very large 'n' values (see the following section 4.8j). A cell width of one-quarter the unit spacing sometimes leads to instability with oscillating model values, particularly in the first few

layers. Thus the use of a cell width of less than one-quarter the true unit electrode spacing is not advisable.

Note that using finer cells will lead to longer inversion times, so using a width of the half the unit electrode spacing seems to provide the best trade-off. These examples present a strong case for using a model with a cell width of half the unit electrode spacing as the default choice in the inversion of most data sets. It avoids the problem caused by model cells boundary misfits if the cell is too coarse, and the increase in computer time is tolerable.

One effect of using finer model cells for some data set is the emergence of 'ripples' in the first couple of layers in the inversion model. Figure 4.22a shows the pseudosection from a survey in the Blue Ridge region in north-east USA (Seaton and Burbey, 2000). The inversion model using the blocky model inversion norm in Figure 4.22b show some rapid near-surface alternating resistivity values between the 160 and 240 meter marks. These artifacts can be significantly reduced by using a higher damping factor for the top layer as shown in Figure 4.22c.

As a final note, it appears that the effect of using narrower model cells is less dramatic in 3-D inversion. This is probably because in the 2-D model each cell extends to infinity in the y -direction, whereas in the 3-D model the same cell is divided into a large number of much smaller cells. Thus the effect of a single near-surface cell in the 3-D model on the calculated apparent resistivity values is much smaller than in the equivalent 2-D model.

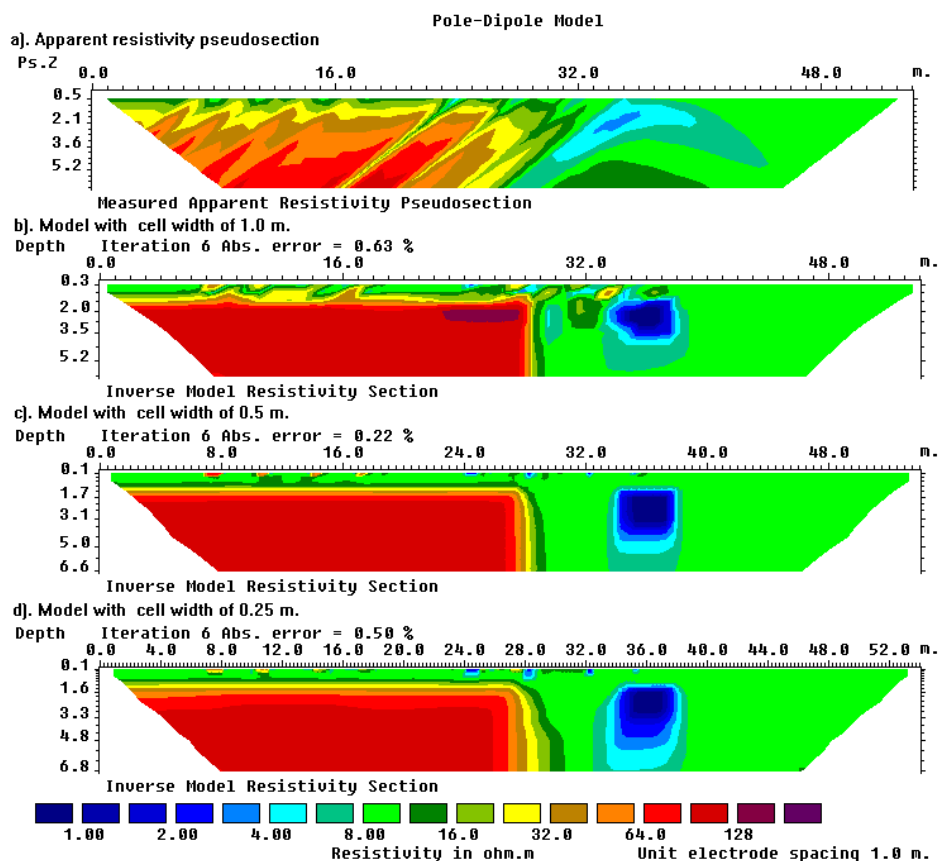


Figure 4.20. The effect of cell size on the pole-dipole array inversion model. Pole-dipole array (a) The apparent resistivity pseudosection. The inversion models obtained using cells widths of (b) one, (b) one-half and (c) one-quarter the unit electrode spacing.

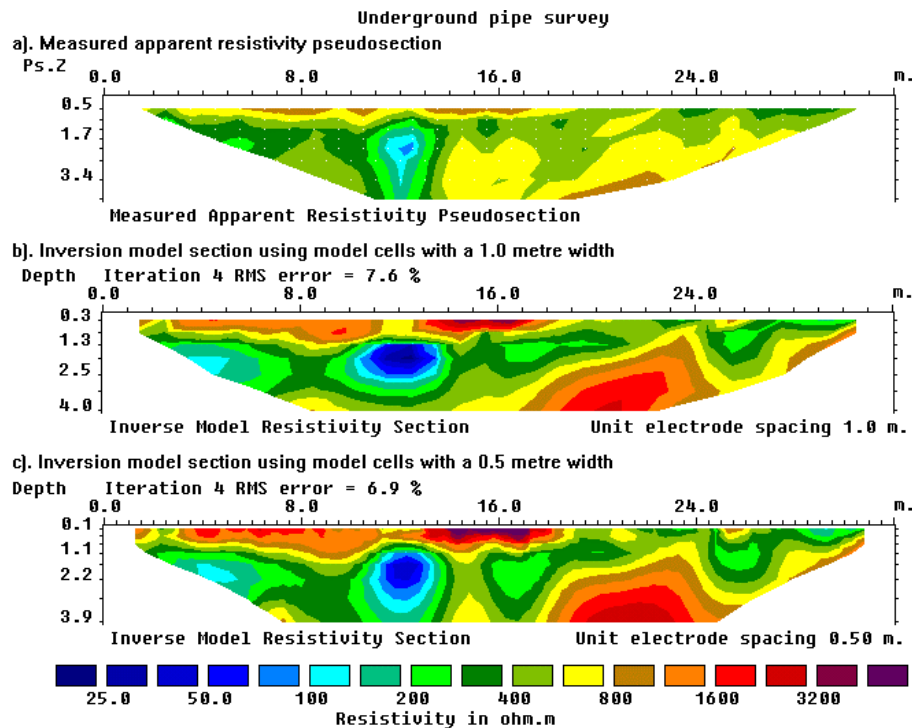


Figure 4.21. Example of the use of narrower model cells with the Wenner-Schlumberger array. (a) The apparent resistivity pseudosection for the PIPESCHL.DAT data set. The inversion models using (b) cells with a width of 1.0 meter that is the same as the actual unit electrode, and (c) using narrower cells with a width of 0.5 meter.

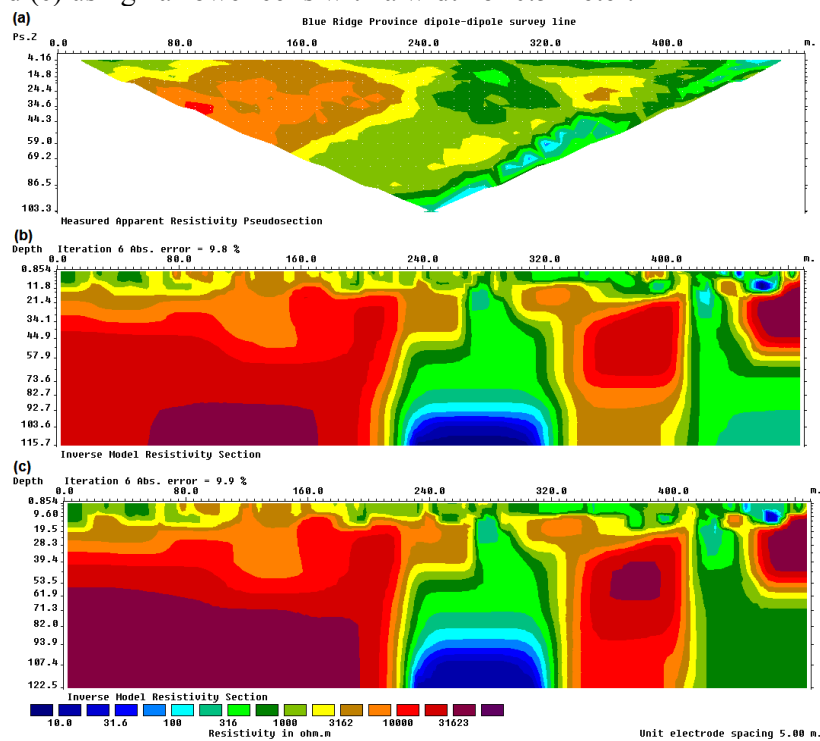


Figure 4.22. Example of reduction of near-surface 'ripples' in inversion model. (a) Apparent resistivity pseudosection for the BLUERIDGE.DAT data set. (b) Normal inversion using the robust inversion norm and model refinement. (c) Inversion using higher damping factor for first layer to reduce the 'ripple' effect in the top layer.

4.8 Model resolution and automatic array optimization methods

4.8.1 Concept of model resolution

The sensitivity functions plots are useful explaining the behavior of common arrays, but they only tell us the characteristics of each individual array. This will help in selecting an array for certain structures, eg. For predominantly horizontal or vertical structures. However, a survey will consist of many measurements with different spacings and horizontal positions along the line. The cumulative sensitivity values described in the previous section is a simple method to combine the sensitivity values from different measurements. It can be calculated rapidly but it is not mathematically rigorous. Our purpose in carrying out the survey is to detect or resolve structures below the survey line. How do we quantify the model ‘resolution’?

The model resolution equation is related to the least-squares equation used for the inversion for resistivity data described earlier in section 1.4.

$$(\mathbf{J}^T \mathbf{J} + \lambda \mathbf{F}) \Delta \mathbf{q}_k = \mathbf{J}^T \mathbf{g} - \lambda \mathbf{F} \mathbf{q}_k, \quad (1.21)$$

Using linear approximations, it can be shown that the relation between the calculated model resistivity and the true resistivity is approximately given by is given by

$$\mathbf{q}_{\text{Model}} \approx \mathbf{R} \mathbf{q}_{\text{True}},$$

where

$$\mathbf{R} = (\mathbf{J}^T \mathbf{J} + \lambda \mathbf{F})^{-1} \mathbf{J}^T \mathbf{J} \quad (2.8)$$

The model resolution matrix \mathbf{R} may be viewed as a filter through which the inversion method attempts to resolve the subsurface resistivity (Day-Lewis et al. 2005). In the ideal case with perfect resolution, the elements of the main diagonal (R_{jj}) are 1 while the off-diagonal elements are 0.

4.8.2 A heuristic explanation of model resolution – through a glass darkly

This section attempts to give an illustration of model resolution in a less mathematical manner. The effect of the model resolution matrix can be shown diagrammatically below. Consider an original optical image used in testing eyesight, such as

ABC

A person with less than perfect eyesight might see it as

ABC

Someone with very poor eyesight might see it as

ABC

The matrix \mathbf{R} might be considered as a ‘blurring’ matrix which contaminates the calculated value with values from nearby cells. To illustrate it in terms of the model used in resistivity inversion, consider a simple model with only 4 cells.

Model with 4 cells

q_1	q_2
q_3	q_4

This can be written in matrix form as

$$\begin{pmatrix} q_{M1} \\ q_{M2} \\ q_{M3} \\ q_{M4} \end{pmatrix} = \begin{pmatrix} R_{11} & R_{12} & R_{13} & R_{14} \\ R_{21} & R_{22} & R_{23} & R_{24} \\ R_{31} & R_{32} & R_{33} & R_{34} \\ R_{41} & R_{42} & R_{43} & R_{44} \end{pmatrix} \begin{pmatrix} q_{A1} \\ q_{A2} \\ q_{A3} \\ q_{A4} \end{pmatrix}$$

$$\mathbf{q}_{\text{Model}} = \mathbf{R} \mathbf{q}_{\text{Actual}}$$

If the cells are perfectly resolved, then the model resolution matrix will be the form below where the diagonal elements are 1.0 and elsewhere it is 0, so the model resolution matrix can be written as

$$\begin{pmatrix} q_{M1} \\ q_{M2} \\ q_{M3} \\ q_{M4} \end{pmatrix} = \begin{pmatrix} 1.0 & 0.0 & 0.0 & 0.0 \\ 0.0 & 1.0 & 0.0 & 0.0 \\ 0.0 & 0.0 & 1.0 & 0.0 \\ 0.0 & 0.0 & 0.0 & 1.0 \end{pmatrix} \begin{pmatrix} q_{A1} \\ q_{A2} \\ q_{A3} \\ q_{A4} \end{pmatrix}$$

This means the calculated value for each cell only depends on the true value. In the case with imperfect resolution, we might have something like

$$\begin{pmatrix} q_{M1} \\ q_{M2} \\ q_{M3} \\ q_{M4} \end{pmatrix} = \begin{pmatrix} 0.7 & 0.1 & 0.1 & 0.1 \\ 0.1 & 0.7 & 0.1 & 0.1 \\ 0.1 & 0.1 & 0.5 & 0.3 \\ 0.1 & 0.1 & 0.3 & 0.5 \end{pmatrix} \begin{pmatrix} q_{A1} \\ q_{A2} \\ q_{A3} \\ q_{A4} \end{pmatrix}$$

$$\mathbf{q}_{\text{Model}} = \mathbf{R} \mathbf{q}_{\text{Actual}}$$

The diagonal elements give the ‘degree’ of resolution, while the off diagonal elements give the degree of ‘contamination’ or cross-correlation with the neighboring model cells. One way to illustrate the resolution is to plot the values of the diagonal elements of the R matrix. This shows the degree at which the calculated model value depends on the true value. A value of about 0.05 (5%) is commonly chosen as the ‘cutoff’ value.

4.8.3 Examples of model resolution with standard arrays

The diagonal elements of the resolution matrix give a quantitative means to compare the resolving power of different arrays. In this section, plots of the model resolution values of three common arrays are shown. As a simple example, we consider the case for a multi-electrode system with 30 independent nodes and a spacing of 1.0m between adjacent electrodes. First we look at the resolution for the widely used Wenner array. Assume we make all the possible measurements, with the ‘ a ’ spacing ranging from 1.0 to 9.0 m. giving a total of 135 data points. The model resolution section (Figure 4.23a) shows that the resolution is greatest near the surface, decreases rapidly with depth, and is very small below a depth of about 2.0 meters. Next we look at the Wenner-Schlumberger array with the ‘ a ’ spacing

ranging from 1.0 to 3.0 m. and the ‘ n ’ factor ranging from 1 to 8 giving a total a 292 data points. It performs significantly better than the Wenner array (Figure 4.23b) with significant resolution values up to about 3.0 m. The third array we will look at is the dipole-dipole array with the dipole length ‘ a ’ fixed at 1.0 m. and the ‘ n ’ factor ranging from 1 to 6, giving a total of 147 data points. Its performance is surprisingly good and comparable to the Wenner-Schlumberger array with significant model resolution values to about 3.5 meters, although it only has about half the number of data points (Figure 4.23c). It is much better than the Wenner array although it only has 12 more data points.

In an attempt to improve the resolution for the dipole-dipole array, we next attempt to use overlapping data levels with it. The ‘ a ’ dipole length ranges from 1.0 to 3.0 m. while the ‘ n ’ factor ranges from 1 to 6. The region with significant resolution values increases to about 5 meters (Figure 4.23d), an improvement from the 3.5 meters limit with a single ‘ a ’ dipole length (although it is mainly concentrated near the center). It only has about 50 data points more than the Wenner-Schlumberger (342 compared to 292), but it is a significant improvement.

It is possible to further improve the resolution we can get for a limited number of independent nodes?

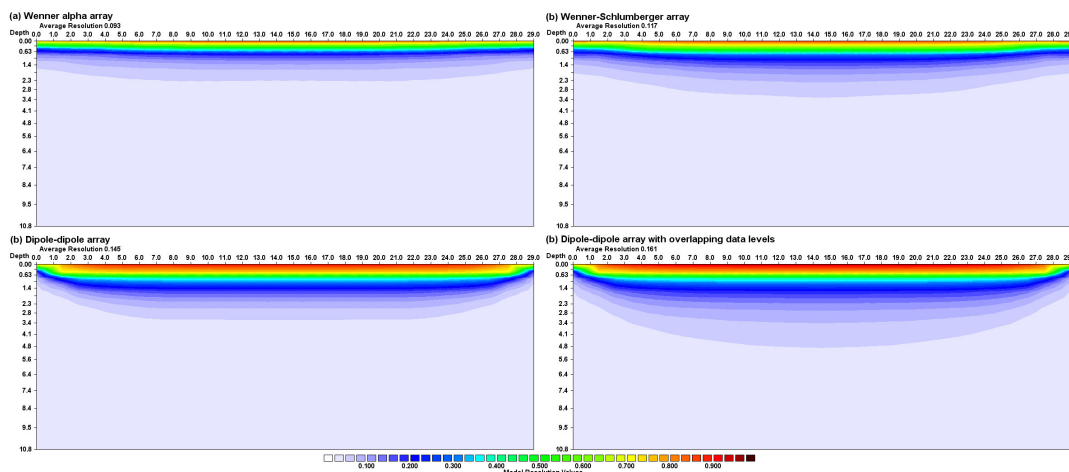


Figure 4.23. Model resolution sections for the (a) Wenner, (b) Wenner-Schlumberger and (c) simple dipole-dipole array (d) dipole-dipole array with overlapping data levels.

4.8.4 Array optimization methods

The model resolution section gives an insight on the section of the subsurface we can resolve. Is there a way to automatically select the arrays that will give the maximum resolution for a given number of electrodes? In recent years, there have been some significant developments in this effort (Stummer et al. 2004, Wilkinson et al. 2006, Loke et al. 2007, Loke and Wilkinson 2009). Consider a survey system with N independent electrodes. The number of possible array combinations (M) with 4 electrodes is

$$M = N(N-1)(N-2)(N-3)/8$$

As an example, for a system with 30 electrodes, there are 82215 possible configurations. We can reduce the number by rejecting all configurations with the Gamma arrangement (with interleaved current and potential electrodes), and those with very high geometric factors (i.e. low potentials) of greater than the dipole-dipole with $a=1$ and $n=6$. This reduces the total number of possible array configurations to 51283, which is called the ‘comprehensive’ data set (Wilkinson et al. 2006). If we make measurements with all these possible array configurations, we should get the best possible resolution. The model

resolution section for this ‘comprehensive’ data set is shown in Figure 4.24a. The region with significant resolution values extends to about 8 meters, significantly more than the dipole-dipole (5 meters) array.

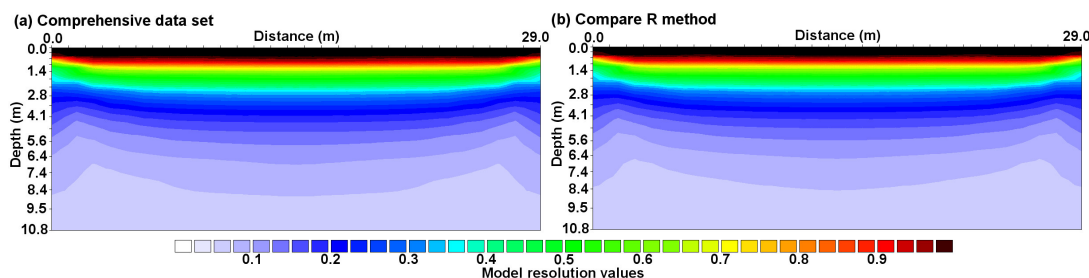


Figure 4.24. (a) Model resolution section for comprehensive data set. (b) Model resolution section for optimized data set generated by the ‘Compare R’ method.

Although taking all the 51283 possible readings will give the maximum possible resolution, this is not practical in actual field survey. We want to take a small subset of the possible readings that gives almost the same resolution. A possible algorithm (Stummer et al. 2004, Wilkinson et al. 2006) is as follows.

1. Start with a small set, the ‘base’ data set, such as the dipole-dipole readings with $a=1$ and $n=1$ to 6 (147 readings).
2. Calculate the increase in the model resolution as each new array is added to the ‘base’ set (there are several alternatives for this step with differences in speed and accuracy). Add the arrays that give the highest increase to the model resolution (and are sufficiently independent of each other) to the base set. After each iteration, increase the base set by about 9%.
3. Use the new set (base plus new arrays) as the base set, and repeat the procedure. Stop when the desired maximum number of arrays (eg. 5000) is reached.

Different Methods have been proposed to carry out step (2) in selecting the arrays that will give the maximum increase in the model resolution (Wilkinson et al. 2006). Here, only the results of one method, the ‘Compare R’ method, will be shown. It gives the most accurate results in terms of optimized arrays, but it is also taking the longest computer time to generate the arrays (Wilkinson et al. 2006). However the time needed has been reduced by about two orders of magnitude using optimized computer code and parallel programming techniques (Loke and Wilkinson 2009). On a 2.66GHz Nehalem i7 PC with a Nvidia 285GTX graphics card it takes about 30 seconds minutes to generate the optimized data set with 40 iterations for a multi-electrode system with 30 nodes, compared to 6 hours reported by Wilkinson et al. (2006). The model resolution section for optimized data set (Figure 4.24b) is almost identical with that for the ‘comprehensive’ data set (Figure 4.24a). The optimized data set has only 4462 array configurations, which is about 9% of the ‘comprehensive’ data set.

To illustrate the performance of the different array configurations in detecting subsurface structures, a test model with four rectangular blocks at different depths (Wilkinson et al. 2006) is used (Figure 4.25). Synthetic data sets were generated for the Wenner, Wenner-Schlumberger, dipole-dipole and optimized arrays. The data sets were then inverted to recover back the subsurface resistivity.

Figure 4.26a shows the resulting inversion model for the Wenner array data set. The two topmost blocks are well resolved while the third block is poorly resolved. The deepest block is completely unresolved. The Wenner-Schlumberger array data set (Figure 4.26b)

performs slight better in resolving the third block but still cannot resolve the deepest block. The simple dipole-dipole array data set with a single dipole length ($a=1.0\text{m.}$) performs significantly better than even the Wenner-Schlumberger array data set where the third block is well resolved (Figure 4.26a), even though it has fewer data points (147 compared with 292). However, it still cannot resolve the deepest block. The dipole-dipole array data set with multiple dipole lengths (all possible data points with $a=1.0$ to 3.0m. and $n=1$ to 6 , with the restriction that the geometric factor cannot exceed that for $a=1.0$ and $n=6$) shows higher resistivity values at the location of the deepest block but it is not able to resolve the block (Figure 4.26d).

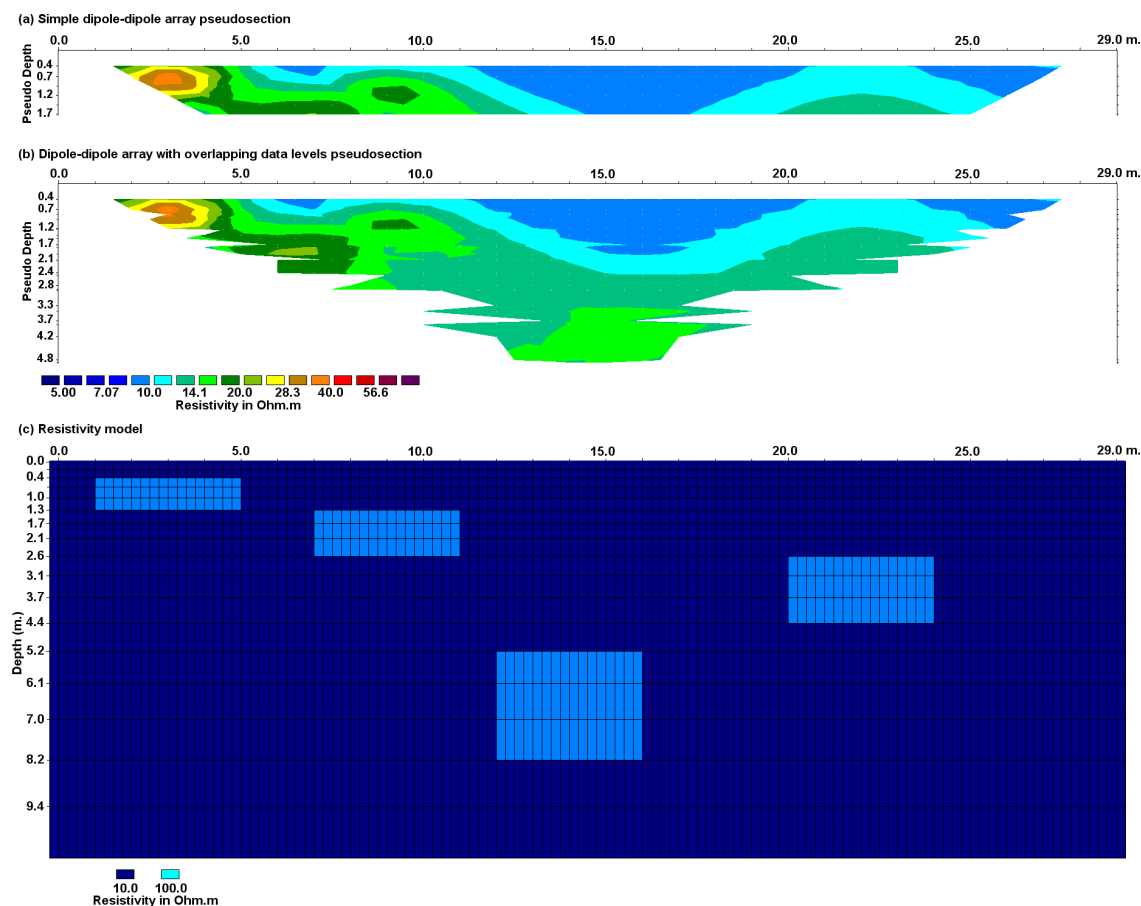


Figure 4.25. Test inversion model for the different arrays. (a) Apparent resistivity pseudosection for the simple dipole-dipole array with a dipole length ' a ' of 1.0 meter with the dipole separation factor ' n ' of 1 to 6. (b) Apparent resistivity pseudosection for the dipole-dipole array with overlapping data levels. (c) The synthetic model with 4 rectangular blocks of $100 \Omega\cdot\text{m}$ embedded in a medium of $10 \Omega\cdot\text{m}$. as used by Wilkinson *et al.* (2006).

The deepest block is fairly well resolved in the inversion model for the optimized data set with 4462 data points (Figure 4.27a) where the shape and dimensions are close to the true structure. It might be argued that the better performance of the optimized data set compared to the dipole-dipole array with multiple dipole lengths is due to the much larger number of data points (4462 compared to 342). Next we use a truncated subset of the optimized data set with only 413 data points that is comparable to the dipole-dipole array data set. The inversion model with the truncated optimized data set (Figure 4.27b) still shows significant better resolution for the deepest block compared to the dipole-dipole array model (Figure 4.26d).

While the shape of the deepest block is significantly less sharp compared to the large optimized data set, it still is better defined compared to the dipole-dipole array model. The third deepest block is also much better resolved by both optimized data sets with resistivity values of over 50 Ohm.m at the center compared to less than 30 Ohm.m for the dipole-dipole array model.

The simple example shows that there can be significant improvements in the depth resolution by using an optimized data set. An old rule of thumb in resistivity sounding is that the maximum depth of investigation is about one-sixth (17%) the line length, i.e. slightly less than 6 meters near the center of the line in the above examples. However, using an optimized data set has pushed this limit close to 8 meters or slightly more than one-fifth (about 28%) the line length.

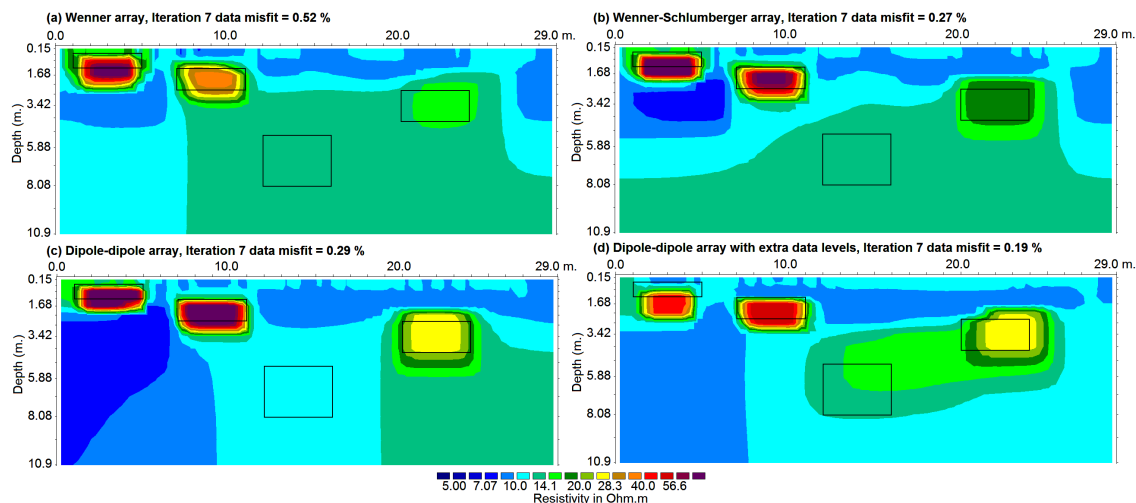


Figure 4.26. Inversion results with the (a) Wenner array, (b) Wenner-Schlumberger array, (c) simple dipole-dipole array and (d) dipole-dipole array with overlapping data levels.

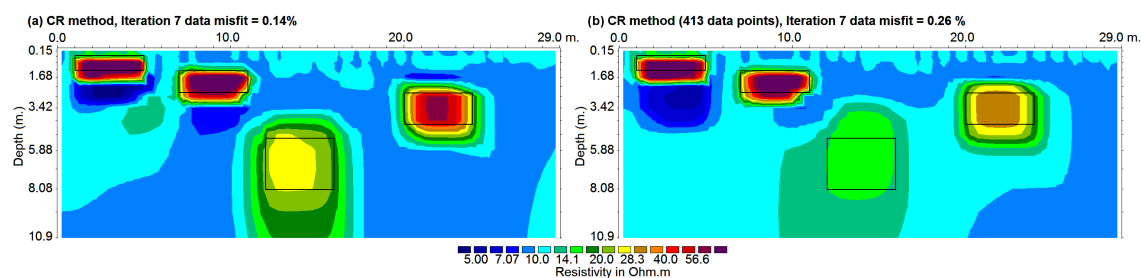


Figure 4.27. Inversions models with the (a) optimized data set with 4462 data points and (b) a truncated optimized data set with 413 data points.

4.8.5 DOI versus model resolution?

In section 4.4 we have looked at the Depth of Investigation (DOI) method to estimate the practical depth of investigation of field data sets. How does the model resolution section compare with the DOI? The model sections and DOI section for the Landfill survey data set were shown in Figures 4.11 and 4.12. Figure 4.28 shows a comparison between the model resolution and DOI sections for this data set. If we use the value of 0.05 as the cutoff point for the model resolution values, then the average maximum depth of survey is probably about 12 to 14 meters. It is slight deeper between the 72 and 120 meters marks and slightly shallower between the 24 and 72 meters marks. This is similar to that shown by the DOI index section. The model resolution shows a more gradual change with depth (and also

laterally) in the resolution values, compared to the DOI index section that has localized regions with high DOI index values. The 0.05 model resolution contour is generally at the upper boundary of the 0.1 DOI index contour.

One advantage of the model resolution section is that it avoids the localized regions with high DOI index values (that is sometimes caused by local high resistivity regions, or noise in the data). It has an theoretical appeal in that it is less empirical in nature compared to the DOI index method. One disadvantage of the model resolution method is that it requires an inversion of a matrix with a computer time that is proportional to n^3 (where n is the number of model cells). This makes it impractical for models with more than about 5000 cells that is a significant limit for 3D models with present PC technology. A significant challenge would be to reduce the computer time to about $n^{2.5}$ or even n^2 . Research is being carried out to extend the practical limit to beyond about 10000 cells.

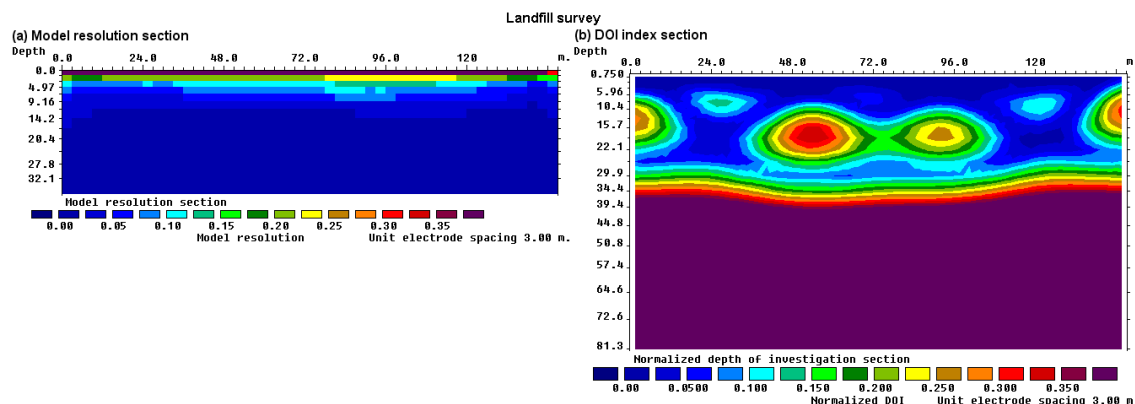


Figure 4.28. Comparison between the (a) model resolution and (b) DOI index sections for the Landfill data set.

4.9 Pitfalls in 2-D resistivity surveys and inversion

While 2-D resistivity surveys have made the mapping of many complex structures possible, caution must still be exercised in interpreting the results from the data. Below are some of the common pitfalls.

(a). Incorrect use of the dipole-dipole array. This is still a surprisingly common problem. There are two common mistakes in the use of this array. The first is to assume that the depth of investigation is at the point of intersection of the two 45° diagonals projected from the dipoles. This greatly overestimates the depth of investigation. For example, for the case where the dipole separation factor " n " is equals to 6, the point of intersection is about 3 times the median depth of investigation (see Table 2.1). The second common mistake is to monotonically increase the " n " factor, while keeping the dipole length " a " fixed, in an effort to increase the depth of investigation. This usually results in very noisy and unusable data, with negative apparent resistivity values in some cases, for " n " values of greater than 8. To solve this problem the " n " value should not exceed 6, and the method of overlapping data levels (section 2.5.6) with different " a " dipole lengths can be used.

(b). Poor electrode ground contact. This problem arises in stony or dry soils where it is not possible to plant the electrodes to a sufficient depth, and/or the soil is too dry such that it is not possible to pass enough current into the ground. In the pseudosection, this is seen as an inverted "V" shaped pattern of bad data points with the two legs originating from an electrode. This problem is more severe when the electrode is used as a current electrode. The potential electrode is less sensitive to poor ground contact, so this problem in certain situations can be overcome by swapping the current and potential electrodes.

(c). Poor current penetration. The success of the resistivity method depends on a current flowing through the areas to be mapped. If the top layer has a very high resistivity, it might be very difficult to get enough current to flow through the ground at all. The opposite problem occurs if the top layer has an extremely low resistivity. The current might be trapped in the top layer, so not much information is expected from the lower layers.

(d). Not letting the current charge decay. When an electrode is used as a current electrode, charges tend to build up around the electrode. When the current is no longer flowing through the electrode, it still takes a finite amount of time for the charges to disperse. If the same electrode is used as a potential electrode immediately after it has been used as a current electrode, this could result in an erroneous reading (Dahlin 2000).

(e). Mistakes in the field. This can arise from a variety of sources. It could be caused by instrumentation errors during the field survey, poor electrode contact in dry, sandy or stony ground, shorting of electrodes due to very wet conditions or metal objects (such as fences, pipes etc.) or mistakes such as attaching electrodes to the wrong connectors. Fortunately, it is usually very easy to pick out such bad data points by viewing the pseudosection or the data in the form of profiles. Before inverting a data set, take a look at it!

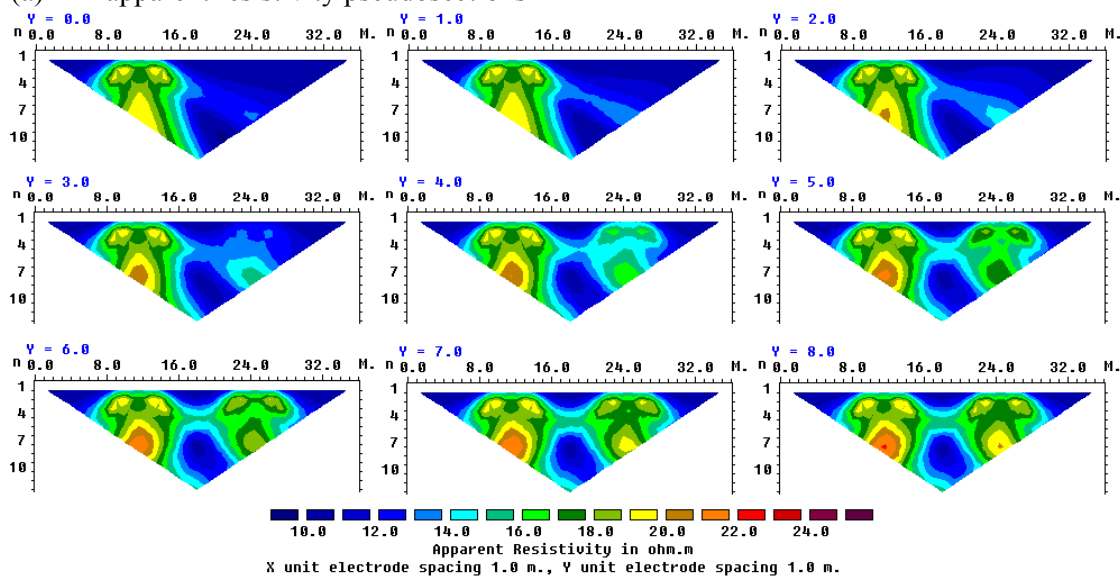
(f). 3-D geology. It is assumed that the subsurface is 2-D when interpreting the data from a single line. This assumption is valid if the survey is carried out across the strike of an elongated structure. If there are significant variations in the subsurface resistivity in a direction perpendicular to the survey line (i.e. the geology is 3-D), this could cause distortions in the lower sections of the model obtained. Measurements made with the larger electrode spacings are not only affected by the deeper sections of the subsurface, they are also affected by structures at a larger horizontal distance from the survey line. This effect is most pronounced when the survey line is placed near a steep contact with the line parallel to the contact. Figure 4.29 shows the apparent resistivity pseudosection for the Wenner array over a 3-D model that has two structures of 100 $\Omega\cdot\text{m}$ that have the same widths within a 10 $\Omega\cdot\text{m}$ medium. One structure is truly 2-D while the second is truncated near the middle of the area at the y -axis coordinate of 3 meters. At a large distance from the edge of the second structure, for example at the y -axis coordinate of 8 meters, the anomaly due to the right structure is almost as high as that due to the left structure. However, close to the edge, for example at y -axis coordinate of 5 meters, the anomaly due to the right structure is significantly weaker. If a survey was carried out along this line, and the subsurface was assumed to be 2-D, then the dimensions of the right structure obtained from an inversion of the data set would be wrong. Dahlin and Loke (1997) did a comparison of the sensitivity of different arrays to structures off the axis of a 2-D survey line. In general, it was found that the dipole-dipole array was the most sensitive (i.e. suffered the greatest distortion) due to off-axis structures. The best way to handle 3-D structures would be a full 3-D survey and data inversion. We will look at 3-D surveys in the later part of these notes.

It must be emphasized that a 2-D survey with very good quality data and very dense data coverage, and inverted with a good inversion algorithm, can still give the wrong results if the assumption of a 2-D geology on which the model is based is seriously wrong. This is a particularly a problem in mineral surveys (which commonly also involve IP measurements) where very complex geological structures and mineralization patterns are usually encountered. In such situations, the results from a 2-D resistivity and IP model should be treated with some reservations unless it is confirmed by a 3-D survey and model. There have been many cases where expensive drill-holes have passed through barren zones in areas where the 2-D model shows a strong IP anomaly.

(g). Limits of the physics of the resistivity method. While 2-D and 3-D surveys and data inversion has greatly extended the range of field problems that can be solved using the

resistivity method, there are still basic laws of physics that place certain limitations on these techniques. The resolution of the resistivity method decreases exponentially with depth. We see the subsurface “as through a glass darkly” and the image becomes increasingly fuzzier with depth. It is unlikely to be able to map a structure with a size of 1 meter at a depth of 10 meters using the resistivity method. The resistivity phenomena is based on the diffusion equations, so its resolution is inherently poorer than the seismic or ground radar method at depths greater than one wavelength.

(a) 2-D apparent resistivity pseudosections



(b) The actual 3-D model

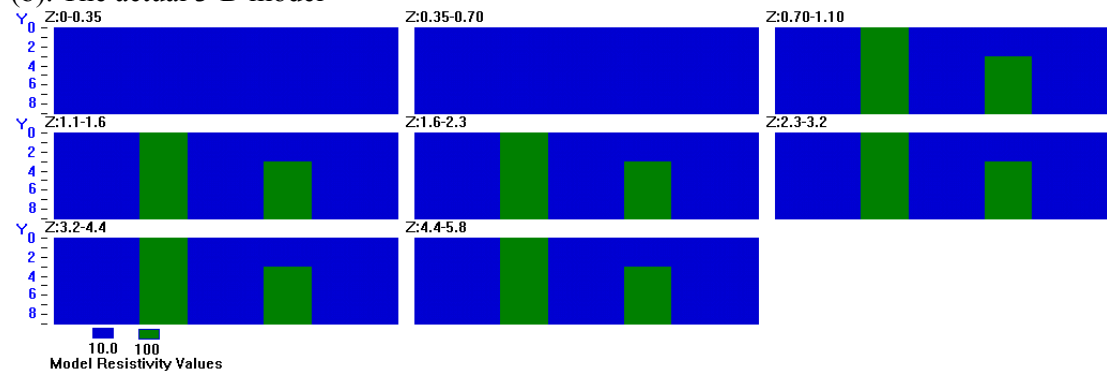


Figure 4.29. An example of 3-D effects on a 2-D survey. (a) Apparent resistivity pseudosections (Wenner array) along lines at different y -locations over (b) a 3-D structure shown in the form of horizontal slices.

(h). Non-uniqueness. It is well known that more than one model can produce the same response that agrees with the observed data within the limits of the data accuracy. In 1-D resistivity sounding modeling, the problems of equivalence and suppression are well known. The problems, in different forms, also occur in 2-D and 3-D modeling. A good example was shown in the paper by Oldenburg and Li (1999). In 2-D and 3-D modeling, constraints are used so that a stable solution can be obtained. The use of a smooth or blocky constraint results in the production of models that look more reasonable, but it is no guarantee that they are indeed correct. The accuracy of the result is only as good as the accuracy of the

assumptions made. The resulting model thus depends to a significant extent on the constraint used, and will closely approximate the true subsurface resistivity only if the constraints correspond to the real situation.

(i). Optimization versus inversion. The RES2DINV program, like most non-linear inversion programs, actually carries out an optimization (i.e. not a direct one-to-one inversion in the sense it must have only one solution) in that it tries to reduce the difference between the calculated and measured apparent resistivity values. If there is infinite data and a perfect fit between the calculated and measured values, how the data is measured should not have an effect on the results. However with real, noisy and limited data, how the data is measured does have an effect. A model with 5% rms error in the fit between the measured and calculated apparent resistivity values with one data set might not give the same model as a 5% rms error with another data set although both might be from the same place. For this reason, the dipole-dipole array gives an inversion model with much better resolution than the pole-pole array although in theory the dipole-dipole values can be extracted from the pole-pole values.

(j). Increasing the electrode separation does not always increase the survey depth. It is generally assumed that as the separation between the electrodes is increased, the region of the subsurface that is 'sensed' by the array also increases. While this is true of most arrays, there are certain important exceptions. In particular, this is not true of the pole-dipole array under certain circumstances. In some surveys with the pole-dipole array, the separation between the C1 current electrode and the P1-P2 dipole is increased in an effort to increase the depth of survey by the array. However, if this is done with the P1-P2 dipole length (the ' a ' factor in Figure 1.4) kept at a constant spacing, certain interesting effects come into play. In section 2.5.8 this practice was strongly discouraged on the basis that the potential will decrease with the square of the ' n ' factor. This problem can be overcome by a combination of using higher currents and more sensitive receivers. However, the problem caused by the change in the array sensitivity pattern as the ' n ' factor is monotonically increased is usually not taken into account. The change in the sensitivity pattern when the ' n ' factor changes from 1 to 6 was shown earlier in Figure 2.17. Figure 4.30 shows what happens when the ' n ' factor jumps from 6 to 12 to 18. Here, the dipole length is kept constant at 1 meter. When ' n ' is equal to 6 there are reasonably high sensitivity values to a depth of about 3 to 4 meters between the C1 current and the P1 potential electrode. When ' n ' is increased to 12, the zone of high sensitivity values becomes increasingly more concentrated below the P1-P2 dipole in an even shallower region. This means that the array with ' n ' equal to 12 is in fact less sensitive to deeper structures than the array with ' n ' equal to 6. This effect is even more pronounced when ' n ' is increased to 18.

Thus increasing the separation between the current electrode and the potential dipole, while keeping the dipole length fixed, does not increase the survey depth of the array. It, in fact, effectively decreases the depth of the region sensed by the array!

Figure 4.31 shows the apparent resistivity anomaly due to a small near-surface high resistivity block for the pole-dipole array for ' n ' values of up to 28. Note that the amplitude of the high resistivity anomaly due to the near-surface block increases with the ' n ' value, i.e. the array becomes increasingly more sensitive to the near-surface block as the separation between the electrodes increase. In field surveys with the pole-dipole array where the ' n ' factor is monotonically increased in the belief that this increases the survey depth, the pseudosection is frequently dominated by a series of parallel slanting high-amplitude anomalies due to near-surface inhomogeneities. The anomalies due to the near-surface structures frequently mask the anomalies due to deeper structures that are of interest.

To increase the depth of penetration with the pole-dipole array, the ' a ' dipole length

should be increased when the ‘ n ’ factor exceeds 6 to 8. This method was discussed in detail in section 2.5.9. For example, instead of fixing the ‘ a ’ dipole length to 1 meter and increasing the ‘ n ’ factor to 28 in Figure 4.31, a more prudent approach is increase the ‘ a ’ spacing from 1 to 4 meters while ensuring the ‘ n ’ factor does not exceed 8.

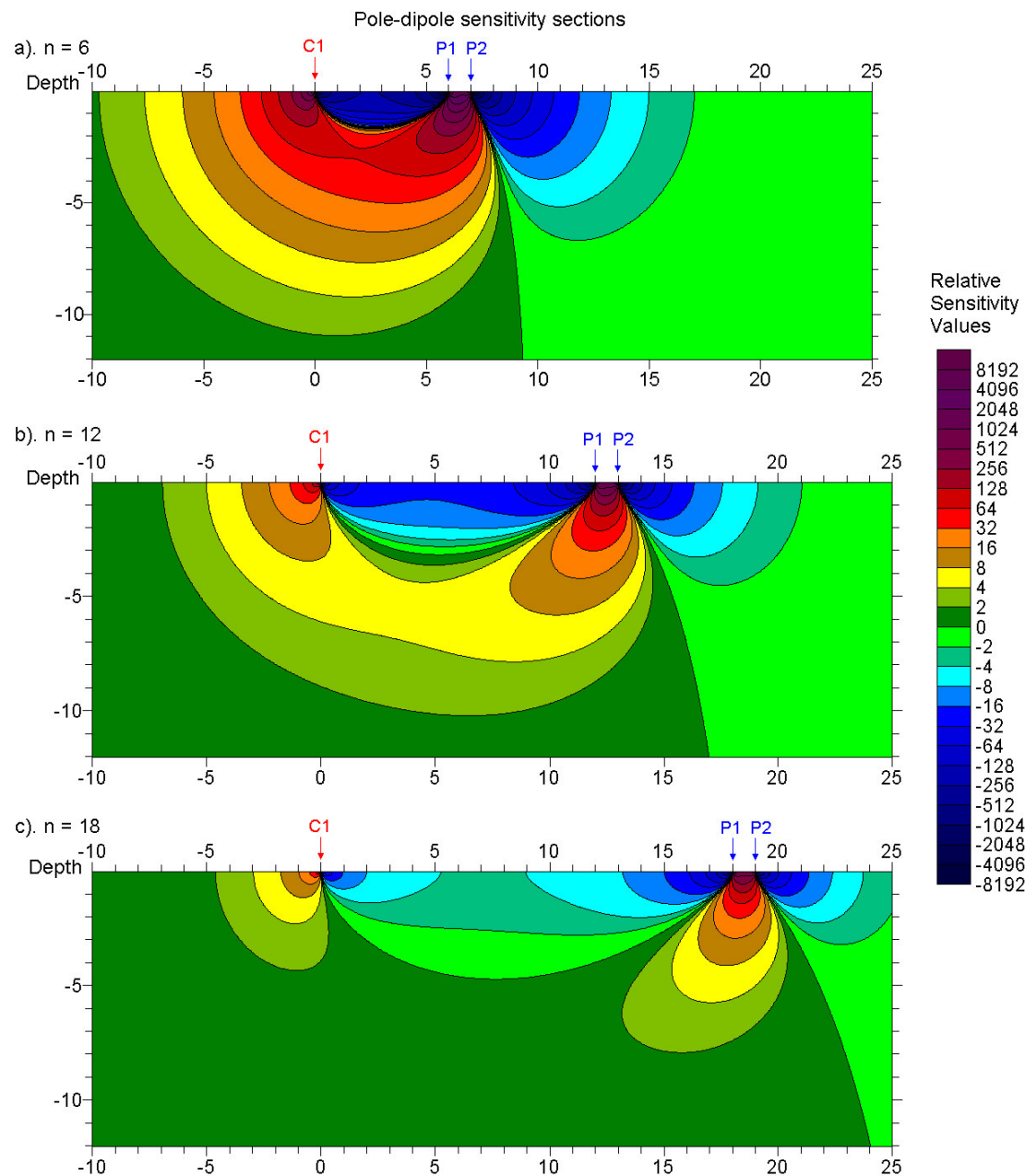


Figure 4.30. The 2-D sensitivity sections for the pole-dipole array with a dipole length of 1 meter and with (a) $n=6$, (b) $n=12$ and (c) $n=18$. Note that as the ‘ n ’ factor increases, the zone of high positive sensitive values becomes increasingly concentrated in a shallower zone below the P1-P2 dipole.

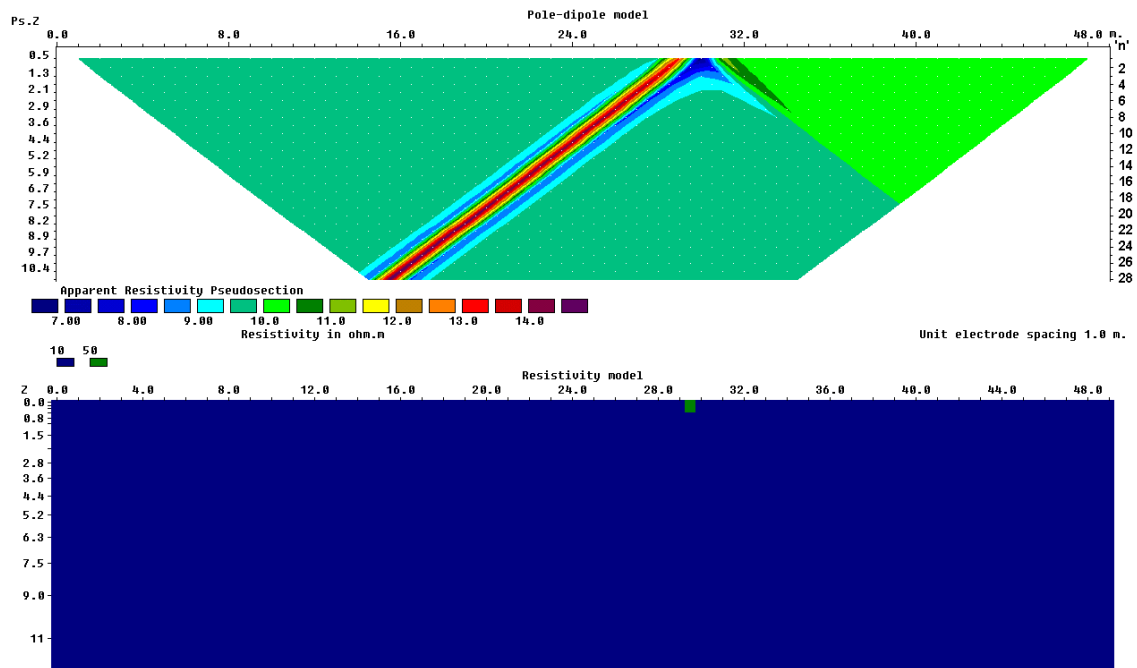


Figure 4.31. Example of apparent resistivity pseudosection with pole-dipole array with large ' n ' values. Note that the anomaly due to a small near-surface high resistivity block becomes greater as the ' n ' factor increases. This means that the sensitivity of the array to the near-surface region between the P1-P2 potential dipole becomes greater as the ' n ' factor increases.

5 IP inversion

5.1 Introduction

One of the more recent developments in the instrumentation for electrical imaging surveys has been the addition of Induced Polarization (IP) capability in the multi-electrode resistivity meter system. Many of the early 2-D surveys were resistivity and IP surveys carried out using conventional 4-electrode systems in the 1950's onwards for mineral exploration, particularly for conductive sulfide ore bodies. Quantitative interpretation of such historical data was rather limited due to the limited computing facilities available at that time. Such historical data provides an interesting source of data for testing modern 2-D and 3-D inversion software. Re-interpretation of such old data to produce quantitative models sometimes has shed new light on the geological structures.

One of the distinctive characteristics of the IP method has been the different parameters in the time and frequency domains used to represent the IP effect. The following section briefly discusses the IP phenomena and the different IP parameters. This is followed by a few exercises in the inversion of IP data with the RES2DINV program. The data format used by the RES2DINV and RES3DINV programs is described in their respective manuals. As such, we will not cover it here.

5.2 The IP effect

A very brief description of the IP effect will be given here. Further details can be found in many fine textbooks, such as by Keller and Frischknecht (1966), Summer (1976), Telford et al. (1990) and Zhdanov and Keller (1994).

The IP effect is caused by two main mechanisms, the membrane polarization and the electrode polarization effects. The membrane polarization effect is largely caused by clay minerals present in the rock or sediment. This is particularly relevant in engineering and environmental surveys. The electrode polarization effect is caused by conductive minerals in rocks such that the current flow is partly electrolytic (through groundwater) and partly electronic (through the conductive mineral). This effect is of particular interest in surveys for metallic minerals, such as disseminated sulfides.

IP measurements are made in the time-domain or frequency domain. In the time-domain, the IP effect is measured by the residual decay voltage after the current is switched off (Figure 5.2c). The time domain IP unit, the chargeability, is usually given in millivolt per volt (mV/V) or in milliseconds. Figure 5.1 shows the IP values (in terms of mV/V) for several mineralized rocks and common rocks. Note that the IP effect due to sulfide mineralization (the electrode polarization effect) is much larger than that due to clay minerals (membrane polarization) in sandstone and siltstones.

In the frequency domain (Figure 5.2b), it is measured by the change in apparent resistivity value from low to high frequencies (typically 1 to 10 Hz) where the unit used is the percent frequency effect. Another measure of the IP effect in the frequency domain is the phase shift between the potential signal and the input current, where the unit used is in milliradians.

One mathematical model that attempts to explain variation of resistivity with frequency observed in the IP method is the Cole-Cole mode (Pelton et al. 1978), which is defined by

$$\rho(\omega) = \rho_0 \left[1 - m \left(1 - \frac{1}{1 + (i\omega\tau)^\epsilon} \right) \right] \quad (5.1)$$

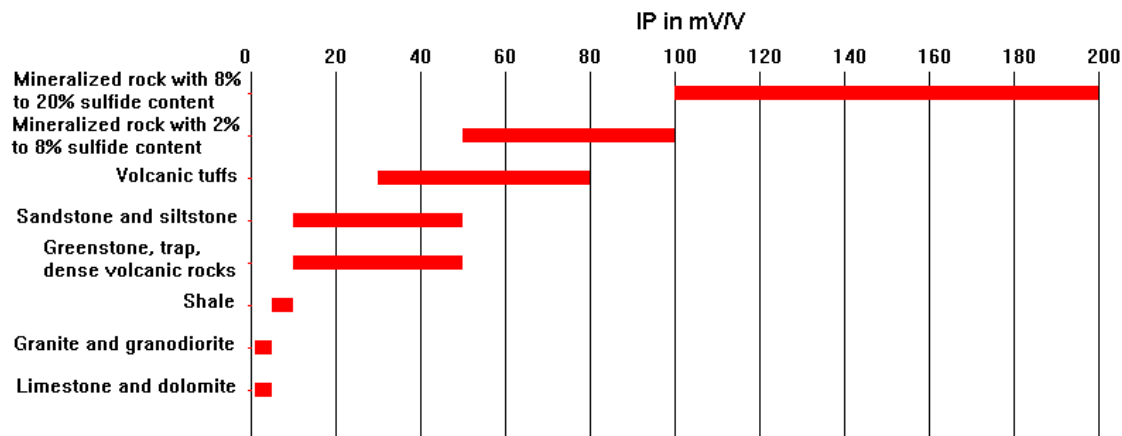
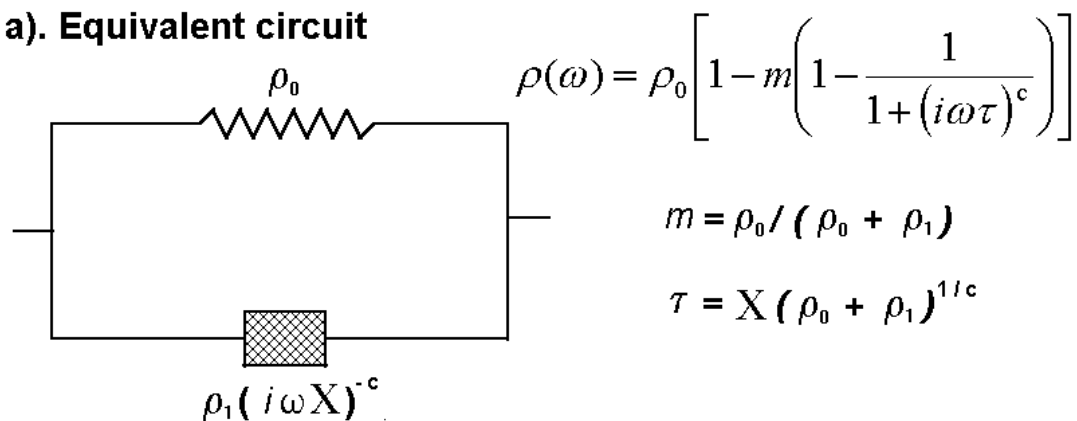
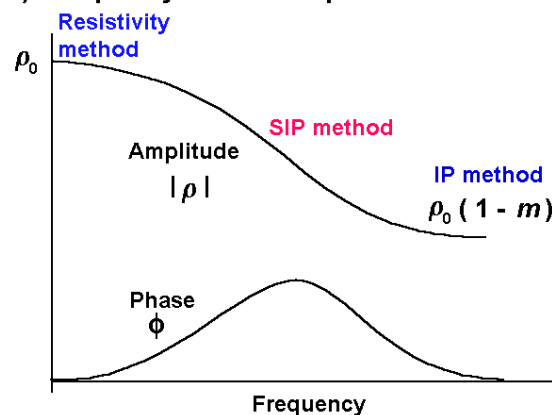


Figure 5.1. The IP values for some rocks and minerals.

a). Equivalent circuit



b). Frequency-domain response



c). Time-domain response

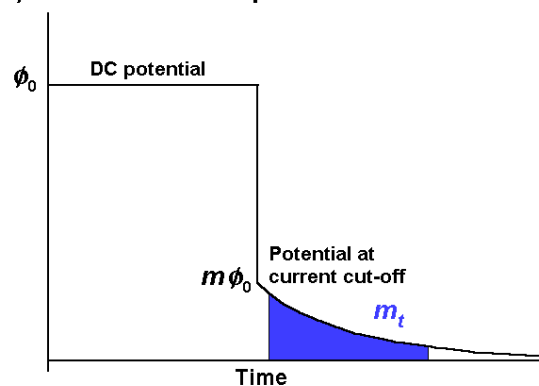


Figure 5.2. The Cole-Cole model. (a) Simplified electrical analogue circuit model (after Pelton *et al.* 1978). ρ = resistivity, m = chargeability, τ = time constant, c = relaxation constant. (b) Amplitude and phase response to sine wave excitation (frequency domain). (c) Transient response to square wave current pulse (time domain). Most IP receivers measure the integral of the decay voltage signal over a fixed interval, m_t , as a measure of the IP effect.

where ρ_0 is the DC resistivity, m is the chargeability, ω is the angular frequency ($2\pi f$), τ is a time constant and c is the exponent or relaxation constant. While the DC resistivity and chargeability determine the behavior of the material at very low and very high frequencies, the variation of the amplitude and phase curves at intermediate frequencies are also affected by the time and relaxation constants.

The time constant factor τ has a large range, from 0.01 second to several thousand seconds. The relaxation constant factor c is bounded by 0.0 to 1.0, with values frequently between 0.2 and 0.7. Much of the earlier work was on the use of spectral IP (SIP) measurements to differentiate between different types of conductive minerals for mining purposes (Van Voorhis et al. 1973, Zonge and Wynn 1975, Pelton et al. 1978, Vanhalla and Peltoniemi 1992). More recently, attempts have been made to use the SIP method for environmental surveys, such as in the detection of contaminants (Vanhalla et al. 1992). Figure 5.2 shows a simplified electrical analogue circuit for the Cole-Cole model, together with typical response curves in the frequency and time domain.

5.3 IP data types

Although the chargeability is defined as the ratio of amplitude of the residual voltage to the DC potential (Figure 5.2c) immediately after the current cut-off, this is not used in actual field measurements. Field measurements of the IP effect may be divided into two main groups, the time-domain and frequency domain methods.

(a) Time domain IP measurements

In the time-domain method, the residual voltage after the current cut-off is measured. Some instruments measure the amplitude of the residual voltage at discrete time intervals after the current cut-off. A common method is to integrate the voltage electronically for a standard time interval. In the Newmont $M_{(331)}$ standard (Van Voorhis *et al.* 1973), the chargeability, m_t , is defined as

$$m_t = 1870 \frac{\int_{0.15}^{1.1} V_s dt}{V_{DC}}, \quad (5.2)$$

where the integration is carried out from 0.15 to 1.1 seconds after the current cut-off. The chargeability value is given in milliseconds. The chargeability value obtained by this method is calibrated (Summer 1976) so that the chargeability value in msec. has the same numerical value as the chargeability given in mV/V. In theory, the chargeability in mV/V has a maximum possible value of 1000.

IP surveys have traditionally been used in the mineral exploration industry, particularly for metal sulfides, where heavy electrical generators producing high currents of the order of 10 Amperes are used. The apparent IP values from such surveys are usually less than 100 msec. (or mV/V). One recent development is the addition of IP capability to battery based systems used in engineering and environmental surveys where currents of 1 Ampere or less are normally used. An accompanying phenomenon is the observation of IP values of over 1000 msec. (or less than -1000 msec.) in some data sets. Such values are almost certainly caused by noise due to a very weak IP signal. To check whether such high IP values are real, first check the apparent resistivity pseudosection. If it shows unusually high and low values that vary in an erratic manner, the data is noisy. If the apparent resistivity values are noisy, then the apparent IP values are almost certainly unreliable. Next check the apparent IP pseudosection. If the apparent IP values show an erratic pattern (frequently with anomalous values lined up diagonally with an apex at a doubtful electrode), then the IP values are too noisy to be interpretable.

(b) Frequency domain IP measurements

In the frequency-domain methods, the apparent resistivity is measured at least two frequencies, for example at 1 Hz. and 10 Hz. The higher frequency is usually set at 10 times time the lower frequency. One commonly used frequency domain IP unit is the percent frequency effect, PFE, which is defined by

$$PFE = \frac{\rho(\omega_L) - \rho(\omega_H)}{\rho(\omega_H)} \cdot 100 \quad (5.3)$$

Another closely related unit that is also commonly used is the metal factor MF which is defined by

$$MF = \frac{\rho(\omega_L) - \rho(\omega_H)}{\rho(\omega_L) \cdot \rho(\omega_H)} \cdot 2\pi \cdot 10^5 \quad (5.4)$$

Another common frequency domain IP unit is the phase angle, ϕ . It is the phase shift between the transmitter current and the measured voltage, and the unit commonly used is milliradians.

(c) Relationship between the time and frequency domain IP units

From the measurement of the amplitude and phase spectrum of porphyry copper mineralization, Van Voorhis et al. (1973) proposed the following equation to described the observed spectra.

$$\rho(\omega) = K(j\omega)^{-b} \quad (5.5)$$

K is constant and b is a measure of the IP effect. It is a positive number of more than 0 and less than 0.1. This is also known as the constant phase model (Weller *et al.* 1996). By using the above model, the following relationship between the different IP units and the b parameter were derived.

$$\begin{aligned} PFE &= (10^b - 1)100 \\ \phi &= 1571 b \\ m_t &= 1320b \end{aligned} \quad (5.6)$$

These relationships provide a numerical link between the different IP units (Van Voorhis *et al.* 1973, Nelson and Van Voorhis 1973).

An alternative relationship is given in the paper by Kemna et al. (1997).

There have been a large number of 2-D IP surveys published over the years, so there is certainly no lack of data to test the IP inversion with the RES2DINV program. Most of the newer multi-electrode systems now come with an IP option. However, the data from many of these systems is rather noisy due to the limited current that can be injected into the ground. For reasonable IP data quality, a current of at least 0.5 Amperes is probably necessary. For environmental and engineering surveys, the most useful application of the IP data is probably in differentiating between sand and clay sediments.

Exercise 5.1 : Tests with 2-D IP inversion

Data set and purpose	Things to try
IPMODEL.DAT – A time-domain synthetic data set.	(1). After reading the data file, run the inversion with the default inversion options. (2). Next try with the robust inversion option. (3). The program also has an option to carry out the IP inversion sequentially after the resistivity inversion (under the “Type of IP inversion method” option in the “Inversion” menu). Try this and see if there are any differences in the results.
IPSHAN_PFE.DAT – A field data set from Burma (Edwards 1977) with measurements in PFE.	(1). After reading the data file, carry out the inversion with the default inversion options. Try again using the option to ‘Limit the range of model resistivity’ option. (2). Try reducing the unit electrode spacing in the data file with a text editor to half the given value. Does it improve the inversion results?
IPMAGUSI_MF.DAT – A field data set from Canada (Edwards 1977) with measurements in metal factor values.	(1). After reading the data file, carry out the inversion with the default inversion options. Try again using the option to ‘Limit the range of model resistivity’ option. (2). Run the inversion again with the ‘Select robust inversion’ option. This should make a significant difference in the results. (3). Try reducing the unit electrode spacing in the data file with a text editor to half the given value. Does it improve the inversion results?
IPKENN_PA.DAT – A field data set with the IP values in phase angles (Hollof 1990).	(1). After reading the data file, carry out the inversion with the default inversion options.

6 Cross-borehole imaging

6.1 Introduction

One of the most severe limitations of 2-D imaging surveys carried out along the ground surface is the reduction in the resolution with depth. This is a fundamental physical limitation that no amount of reconfiguration of the surface arrays or computer modeling can overcome. In theory, the only way to improve the resolution at depth is to place the sensors (i.e. the electrodes) closer to the structures of interest. This is not always possible, but when such boreholes are present, cross-borehole surveys can give more accurate results than is possible with surface surveys alone.

That has been many fine publications on such surveys; such as by Zhao *et al.* (1986), Daily and Owen (1991), Sasaki (1992), LaBrecque *et al.* (1996), Slater *et al.* (1997, 2000) and Zhou and Greenhalgh (1997, 2000). In the following section, I will attempt to summarize the main results with regards to the choice of array configurations for cross-borehole surveys. However, please refer to the original papers for the details.

6.2 Electrode configurations for cross-borehole surveys

In theory, any array that is used for normal surface surveys can be adapted for cross-borehole surveys. Thus, we can have arrays with two electrodes, three electrodes and four electrodes.

6.2.1 Two electrodes array – the pole-pole

There are two possible configurations, both electrodes can be in the same borehole (Figure 6.1a), or the electrodes can be in different boreholes (Figure 6.1b). Figure 6.1c considers a third possibility that is frequently not considered, with one electrode on the surface. In all cases, the areas of highest sensitivities are concentrated near the electrodes, particularly if the two electrodes are far apart in different boreholes as in Figure 6.1c. Note that the electrodes do not actually scan the area between them, as would be expected for a seismic survey with the source and receiver in different boreholes. Note that the region between the two electrodes generally has negative sensitivity values.

If there are n electrodes (including surface electrodes, if any), there are a total of $n(n-1)/2$ possible independent measurements. Most authors recommend measuring all the possible readings at the other electrodes for a current electrode, i.e. measure all the possible combinations. One problem with this array is the physical location of the two remote electrodes, C2 and P2. They must be sufficiently far so that the pole-pole approximation is sufficiently accurate. This means they must be located at a distance of at least 20 times the maximum separation used by the active C1 and P1 electrodes in the boreholes. The large distance between the P1 and P2 electrodes leads to the problem of contamination by telluric noise. These problems are exactly the same as that faced with the pole-pole array for normal surface arrays.

While many earlier researchers have used this array for cross-borehole surveys (Dailey and Owen 1991, Shima 1992, Spies and Ellis 1995), more recent work tends to be less enthusiastic about it. Sasaki (1992) and Zhou and Greenhalgh (2000) found that this array has a significantly poorer resolution than the bipole-bipole and pole-bipole arrays.

The subsurface pole-pole array gives a useful illustration of the change in the geometric factor for subsurface arrays. We have seen that for a pole-pole array with both electrodes located on the surface of a half-space, the geometric factor k is given by

$$k = 2\pi a$$

where a is the spacing between the electrodes. For the case where both electrodes are within an infinite medium, the geometric factor is given by

$$k = 4\pi a$$

where r is the distance between the current and potential electrodes. For the case where both electrodes are below the surface of a half-space, the geometric factor is given by

$$k = 4\pi \left(\frac{rr'}{r+r'} \right)$$

where r' is the distance of the reflected image of the current (Figure 6.2) from the potential electrode.

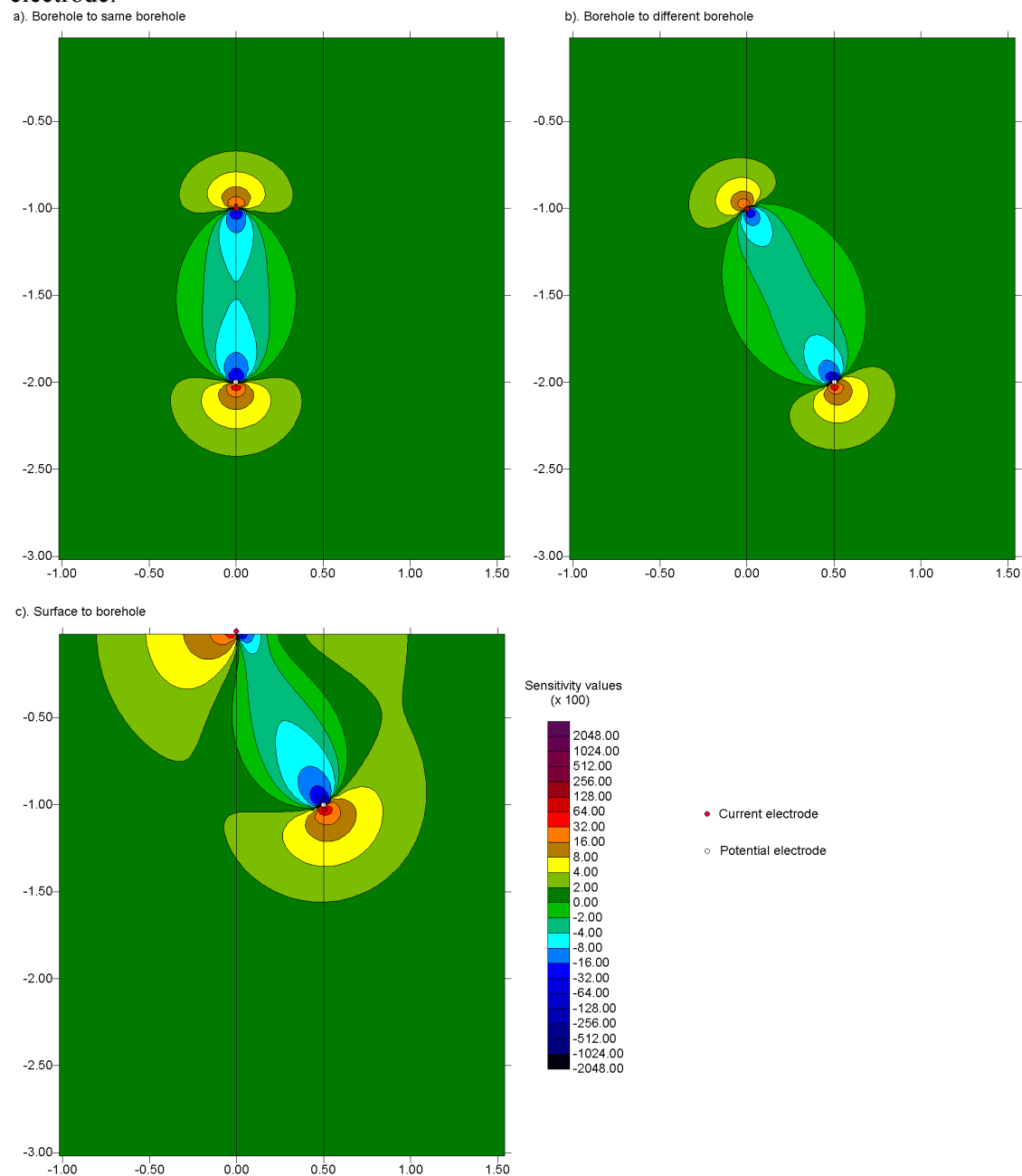


Figure 6.1. The possible arrangements of the electrodes for the pole-pole array in the cross-borehole survey and the 2-D sensitivity sections. The locations of the two boreholes are shown by the vertical black lines.

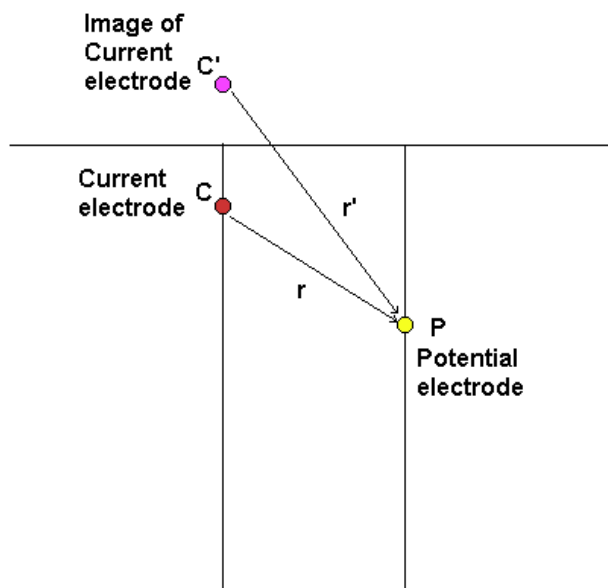


Figure 6.2. A schematic diagram of two electrodes below the surface. The potential measured at P can be considered as the sum of the contribution from the current source C and its image C' above the ground surface.

6.2.2 Three electrodes array – the pole-bipole

According to Zhou and Greenhalgh (1997), there are six possible independent configurations for the pole-bipole type of array (ignoring the surface electrodes). Of these six configurations there are two basic combinations, with the current electrode and one potential electrode in one borehole and the other potential electrode in the second borehole (Figure 6.3a), and with the current electrode in one borehole and both potential electrodes in the other borehole (Figure 6.3b). Zhou and Greenhalgh (1997) recommend the configuration with one current and potential electrode in the same borehole, and the second potential electrode in the other borehole (the C1P1-P2 or AM-N configuration). In Figure 6.3a, it can be seen that this configuration has high positive sensitivity values in between the two boreholes. This means that it provides significant information about the resistivity of the material between the two boreholes. The zones with the negative sensitivity values are confined to between the C1 and P1 electrodes in the first borehole and to the left of the P2 electrode in the second borehole.

The second configuration, with the current electrode in one borehole and both potential electrodes in the other borehole, has large negative sensitivity values between the C1 and P1 electrode and large positive values between the C1 and P2 electrodes. In between these two bands, there is a zone with small sensitivity values, i.e. the array does not give significant information about the resistivity in this zone. Another possible disadvantage of this array is that for some positions of the P1-P2 bipole, the potential value measured is very small or zero. This causes the signal to noise ratio to be small.

Figure 6.3c shows the sensitivity pattern when all three electrodes are in the same borehole. There are very high negative and positive sensitivity values in the vicinity of the borehole. Sugimoto (1999) recommends that such measurements also be made as they give valuable information about the dip of structures between the boreholes. Figure 6.3d shows the sensitivity pattern when the current electrode is on the surface. The sensitivity values between the C1 and P1 electrodes are relatively small (probably due to the large distance between these two electrodes), while the sensitivity values between the P1 and P2 electrodes have moderate positive values.

Overall, many authors have positive remarks about this array. It provides better resolution and is less sensitive to telluric noise (since the two potential electrodes are kept within the survey area) compared to the pole-pole array. While in theory the resolution of the array is slightly poorer than the bipole-bipole array, the potential values measured are significantly higher.

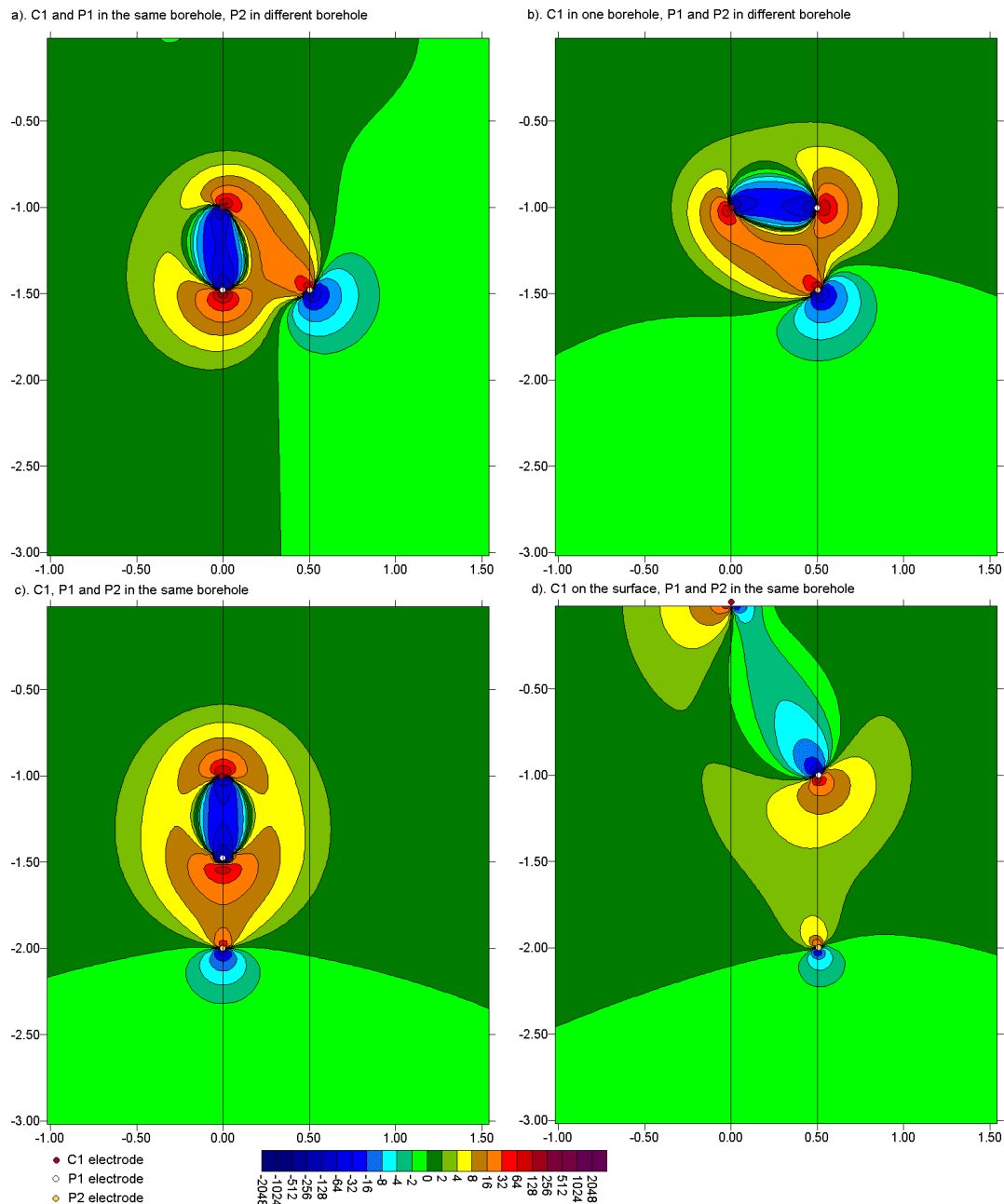


Figure 6.3. The 2-D sensitivity patterns for various arrangements with the pole-bipole array. The arrangement with (a) C1 and P1 in first borehole and P2 in second borehole, (b) C1 in the first borehole and both P1 and P2 in the second borehole, (c) all three electrodes in the first borehole and (d) the current electrode on the ground surface.

6.2.3 Four electrodes array – the bipole-bipole

Zhou and Greenhalgh (1997) list four possible independent configurations for this array, of which there two basic combinations. In the first arrangement, the positive current and potential electrodes C1 and P1 are located in one borehole, while the negative current and potential electrodes C2 and P2 are located in the second borehole (Figure 6.4a).

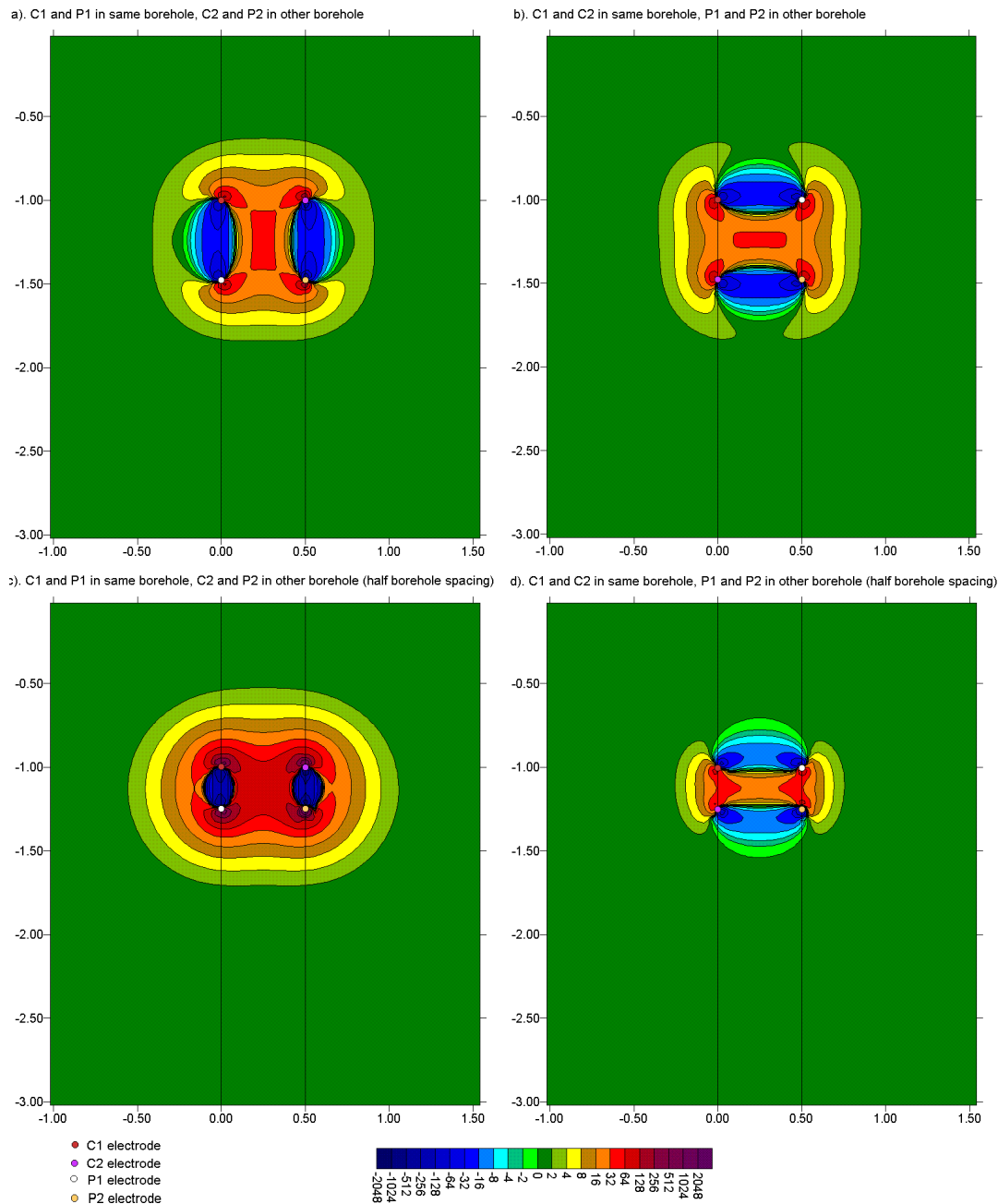


Figure 6.4. The 2-D sensitivity patterns for various arrangements of the bipole-bipole array. (a) C1 and P1 are in the first borehole, and C2 and P2 are in second borehole. (b) C1 and C2 are in the first borehole, and P1 and P2 are in second borehole. In both cases, the distance between the electrodes in the same borehole is equal to the separation between the boreholes. The arrangements in (c) and (d) are similar to (a) and (b) except that the distance between the electrodes in the same borehole is half the spacing between the boreholes.

In this arrangement, the C1P1-C2P2 configuration (i.e. the AM-BN arrangement of Zhou and Greenhalgh (1997)), there are large positive sensitivity values in the area between the two boreholes. This is a desirable property for a cross-borehole array since the intention is to map the material between the two boreholes. The large negative sensitivity values are confined to the region along the boreholes between the C1 and P1 (and C2 and P2 electrodes). Figure 6.4c shows a similar arrangement, but with the spacing between the electrodes in the same borehole reduced to half the spacing between the boreholes. Not again the large positive sensitivity values between the two boreholes.

In the second basic configuration (Figure 6.4b), the C1C2 current bipole is located in one borehole while the P1P2 potential bipole is located in the other borehole. There is also a large region with positive sensitivity values between the two boreholes. However it is flanked by two zones with large negative sensitivity values. Thus the response of this C1C2-P1P2 arrangement to inhomogeneities between the boreholes is more complicated than the first arrangement. When the bipole length is reduced, the positive region is significantly reduced. These features make this arrangement less desirable for cross-borehole surveys. Another disadvantage is that the potential signal strength is weaker in the C1C2-P1P2 arrangement compared to C1P1-C2P2 configuration.

Overall, Zhou and Greenhalgh (1997, 2000) recommend the C1P1-C2P2 configuration. Sasaki (1992) has found the bipole-bipole array to have better resolution compared to the pole-pole and pole-dipole arrays. Figure 6.5 shows one possible field survey measurement sequence. A series of measurements is first made with a short spacing (for example half the distance between the boreholes) starting from the top. Next, measurements are repeated with a larger spacing between the electrodes. Due to the symmetry in the arrangements shown in Figures 6.5 and 6.5b, measurements should also be made with other less symmetrical arrangements. Figures 6.5c and 6.5d show two other possible measurement sequences.

Note that the length of the boreholes must be comparable to the distance between the boreholes. Otherwise, if the spacing between the electrodes in the same borehole is much smaller than the distance between the boreholes, the readings are likely to be more influenced by the materials in the immediate vicinity of the boreholes, rather than the material in between the boreholes. In such a situation, the only alternative is probably to include the surface-surface and surface-borehole measurements.

Some more recent research in cross-borehole imaging may be found in the papers by Oldenborger et al. (2005), Chambers et al (2007), Wilkinson et al (2008) and Nimmer et al (2008).

Exercise 6.1 : A few borehole inversion tests.

Data set and purpose	Things to try
BOREHOLE.DAT – A synthetic data set with the pole-bipole array.	(1). Read in the file, and try an inversion with the default inversion parameters. (2). Next you can try with the robust inversion option.
BORELUND.DAT – A pole-pole array field data set from Lund University, Sweden. The survey was conducted to map fractures in a limestone-marl formation (Dahlin pers. comm.).	(1). Read in the file, and try an inversion with the default inversion parameters. (2). Next you can try different settings, such as the robust inversion option. (3). The program also has an option to reduce the size of the model cells by half, which you might like to try.
BORELANC.DAT – A bipole-bipole array field data set from Lancaster University, U.K (Slater et al. 1997). The survey was conducted to map the flow of a saline tracer from the ground surface through the unsaturated zone.	(1). Read in the file, and run the inversion. The path of the saline tracer is represented by regions with low resistivity values. Can you identify the tracer in the model sections?

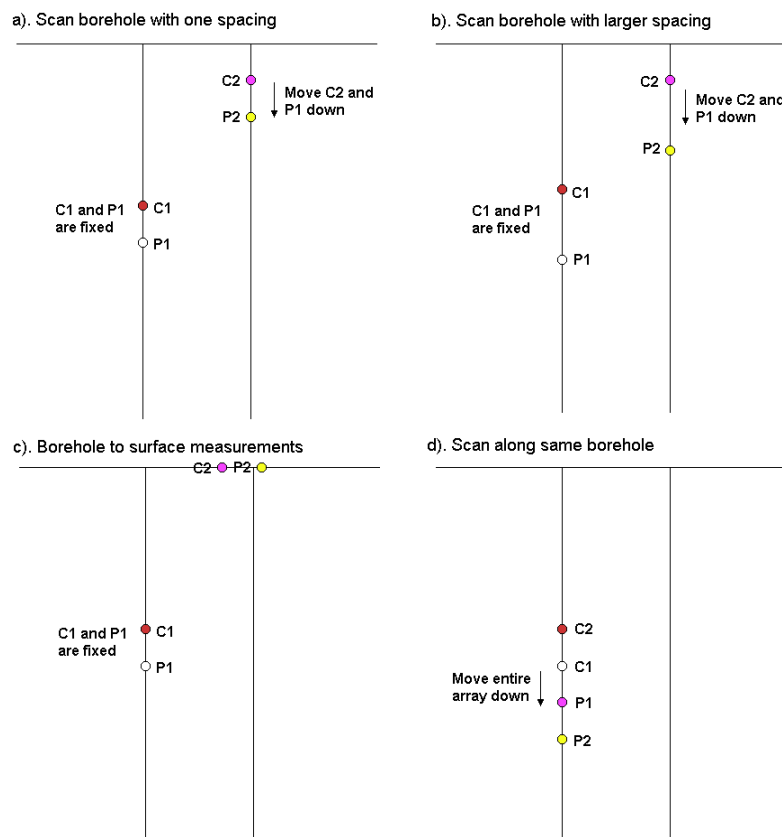


Figure 6.5. Possible measurement sequences using the bipole-bipole array. Other possible measurements sequences are described in the paper by Zhou and Greenhalgh (1997).

6.3 Single borehole surveys

When only a single borehole is available, only the borehole to surface measurements are possible. Figures 6.6a and 6.6b shows two possible arrangements with two electrodes in the borehole and two electrodes on the surface. The first arrangement (Figure 6a) has the C1-C2 current bipole in the borehole while the P1-P2 bipole is on the surface. This arrangement has large positive sensitivity values between the C1-C2 bipole, and also between the P1-P2 bipole. The region of the subsurface between the two bipoles have moderate positive sensitivity values, while an approximately parallel zone stretching from the C2 current electrode (which is higher in the borehole) to the left of the P2 potential electrode has moderate negative sensitivity values. Figure 6b shows the alternative arrangement with the C1 and P1 electrodes in the borehole and the C2 and P2 pair on the surface. There is a small region of large negative sensitivity values along the borehole between the C1 and P1 electrodes. There is also a small near-surface zone between the C2 and P2 electrodes with large negative sensitivity values. However, note that most of the region between the two pairs of electrodes has relatively high positive sensitivity values. Since the intention of the survey is to map the subsurface between the two pairs of electrodes, this might be a better arrangement than the one given in Figure 6.6a.

In some situations, it might only be possible to have only one subsurface electrode, for example at the end of a drill bit or penetrometer (Sorensen 1994). Figures 6.6c and 6.6d shows the arrangements where the upper electrode that was formerly in the borehole (in Figures 6.6a and 6.6b) is now placed on the surface near the borehole. The arrangement with the C1 electrode in the borehole and the C2 electrode on the surface (Figure 6.6c) has a near-surface zone of large negative sensitive values between the C2 electrode and the P2 electrode. However, there are moderately high positive sensitivity values in the region between the C1 electrode in the borehole and the P1-P2 bipole on the surface. The alternative arrangement with the C1 electrode in the borehole and the P1 electrode near the top of the borehole has a zone of large negative sensitivity values along the borehole. The region between the borehole and the C2-P2 electrodes has generally high positive sensitivity values, so this arrangement again might be better.

Figure 6.7 shows a pole-bipole configuration with the C1 current electrode in the borehole and the P1-P2 potential bipole on the surface. The sensitivity pattern is fairly similar to that obtained in Figure 6.6a. There is a region with moderate positive sensitivity values between the C1 electrode and the P1-P2 bipole, together with an approximately parallel zone of moderate negative sensitivity values between the C1 electrode and the region to the left of the P1 electrode. Overall, the arrangement shown in Figure 6.6d appears to be best due to the large zone of high positive sensitivity values between the borehole and the surface electrode pair. For all the possible arrangements, it is assumed that the normal surface-to-surface measurements are also made to fill in the gaps not covered by the borehole to surface measurements. The surface-to-surface measurements are particularly important to accurately map the resistivity distribution in the near-surface zone.

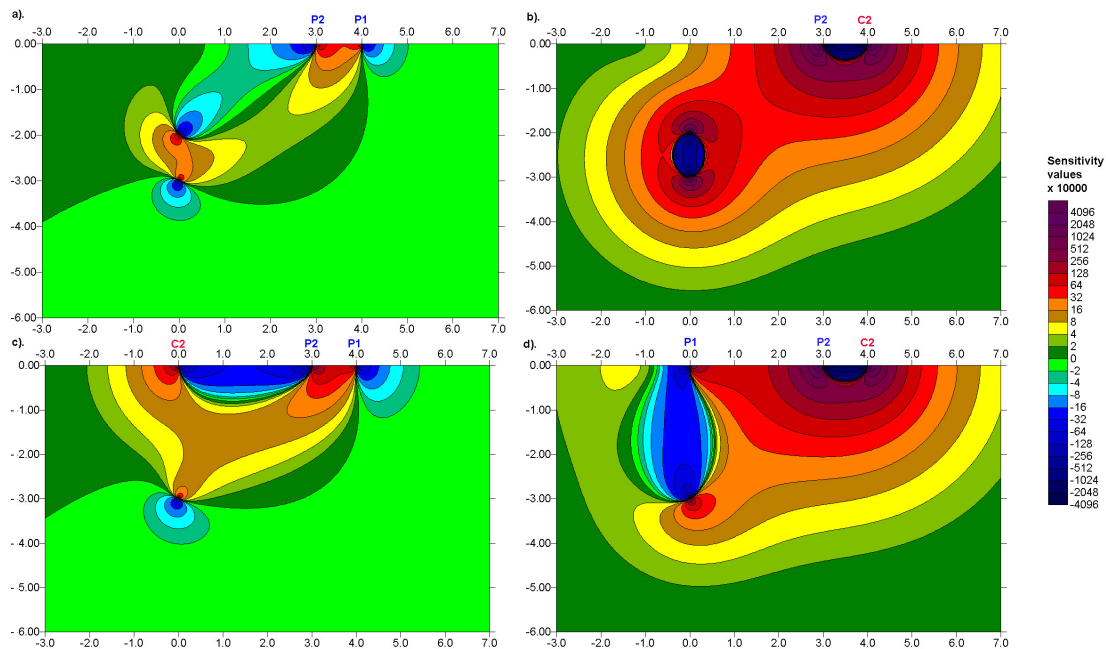


Figure 6.6. Several possible bipole-bipole configurations with a single borehole. (a) The C1 and C2 electrodes at depths of 3 and 2 meters respectively below the 0 meter mark. (b) The C1 and P1 electrodes at depths of 3 and 2 meters respectively below the 0 meter mark. (c). The C1 electrode is at a depth of 3 meters below the 0 meter mark while the C2 electrode is on the surface. (d). The C1 electrode is at a depth of 3 meters below the 0 meter mark while the P1 electrode is on the surface.

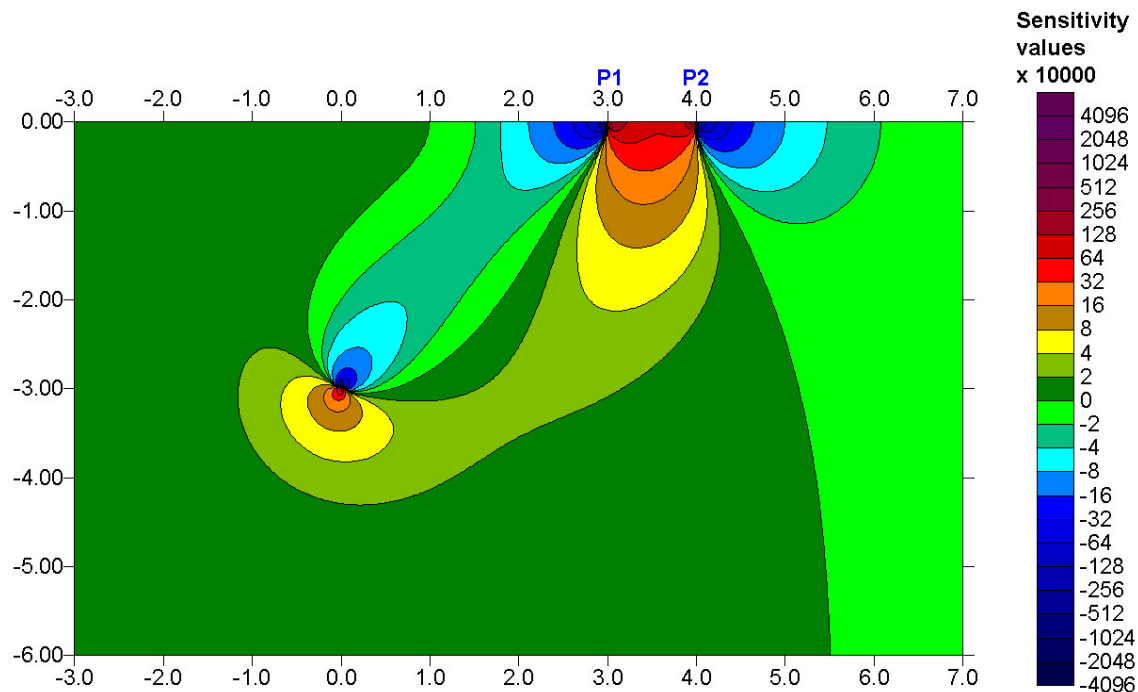


Figure 6.7. A pole-bipole survey with a single borehole. The C1 electrode is at a depth of 3 meters below the 0 meter mark.

7 2-D field examples

7.1 Introduction

Here we will look at a number of examples from various parts of the world to give you an idea of the range of practical survey problems in which the electrical imaging method has been successfully used.

7.2 Landslide - Cangkat Jering, Malaysia

A recent problem faced in Malaysia is landslides on hill slopes. The landslides are often triggered by water accumulation within part of the slope that leads to weakening of a section of the slope. Figure 7.1 shows the results from a survey conducted on the upper part of a slope where a landslide had occurred in the lower section. Weathering of the granite bedrock produces a clayey sandy soil mixed with core boulders and other partially weathered material. The image obtained from this survey shows a prominent low resistivity zone below the center of the survey line. This is probably caused by water accumulation in this region that reduces the resistivity to less than 600 Ω -m. To stabilize the slope, it would be necessary to pump the excess water from this zone. Thus, it is important to accurately map the zone of ground water accumulation. This data set also shows an example with topography in the model section.

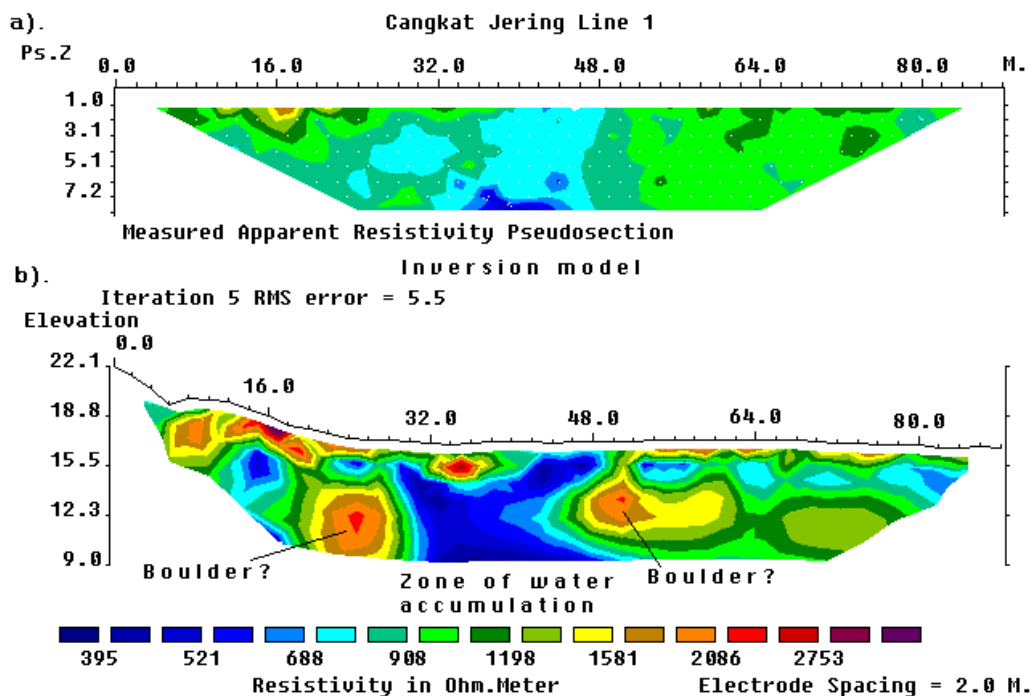


Figure 7.1. Landslide field example, Malaysia. (a) The apparent resistivity pseudosection for a survey across a landslide in Cangkat Jering and (b) the interpretation model for the subsurface.

7.3 Old Tar Works - U.K.

A common environmental problem in industrial countries is derelict industrial land. Before such land can be rehabilitated, it is necessary to map old industrial materials (such as metals and concrete blocks) that are left buried in the ground. Another problem in such areas

is chemical wastes that had been stored within the factory grounds. Due to the nature of such sites, the subsurface is often very complex and is a challenging target for most geophysical methods. The survey for this example was carried out on a derelict industrial site where leachate was known, from a small number of exploratory wells, to be moving from a surface waste lagoon into the underlying sandstones (Barker 1996). Eventually the leachate was seen seeping into a nearby stream. However, the extent of the subsurface contamination was not known.

An electrical imaging survey was carried out along an old railway bed between the lagoon and the stream. The metal railway lines had been removed except for short lengths embedded in asphalt below a large metal loading bay. In the apparent resistivity pseudosection (Figure 7.2a), the area with contaminated ground water shows up as a low resistivity zone to the right of the 140 metres mark. The metal loading bay causes a prominent inverted V shaped low resistivity anomaly at about the 90 metres mark. In the inversion model (Figure 7.2b), the computer program has managed to reconstruct the correct shape of the metal loading bay near the ground surface. There is an area of low resistivity at the right half of the section that agrees with what is known from wells about the occurrence of the contaminated ground water. The plume is clearly defined with a sharp boundary at 140 metres along the profile. The contaminated zone appears to extend to a depth of about 30 metres.

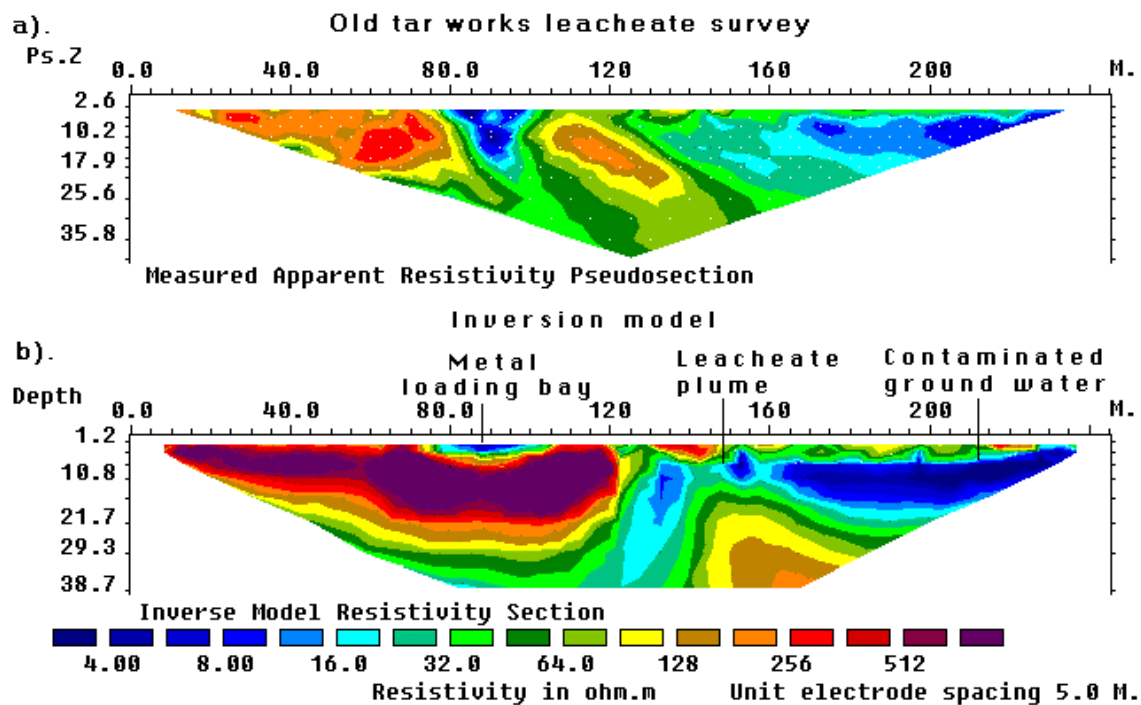


Figure 7.2. Industrial pollution example, U.K. (a) The apparent resistivity pseudosection from a survey over a derelict industrial site, and the (b) computer model for the subsurface.

7.4 Holes in clay layer - U.S.A.

This survey was carried out for the purpose of mapping holes in a clay layer that underlies 8 to 20 feet of clean sand (Cromwell pers. comm.). The results from the electrical imaging survey were subsequently confirmed by boreholes.

The pseudosection from one line from this survey is shown in Figure 7.3a. The data in the pseudosection was built up using data from horizontally overlapping survey lines. One

interesting feature of this survey is that it demonstrates the misleading nature of the pseudosection, particularly for the dipole-dipole array. In the inversion model, a high resistivity anomaly is detected below the 200 ft. mark, which is probably a hole in the lower clay layer (Figure 7.3b). This feature falls in an area in the pseudosection where there is an apparent gap in the data.

However, a plot of the sensitivity value of the cells used in the inversion model shows that the model cells in the area of the high resistivity body have higher sensitivity values (i.e. more reliable model resistivity values) than adjacent areas at the same depth with more data points in the pseudosection plot (Figure 7.3c). This phenomenon is due to the shape of the contours in the sensitivity function of the dipole-dipole array (Figure 2.11), where the areas with the highest sensitivity values are beneath the C1C2 and P1P2 dipoles, and not at the plotting point below the center of the array. This example illustrates the danger of only using the distribution of the data points in the pseudosection to constrain the position of the model cells (Barker 1992, Loke and Barker 1996a). If the model cells are placed only at the location of the data points, the high resistivity body will be missing from the inversion model, and an important subsurface feature would not be detected!

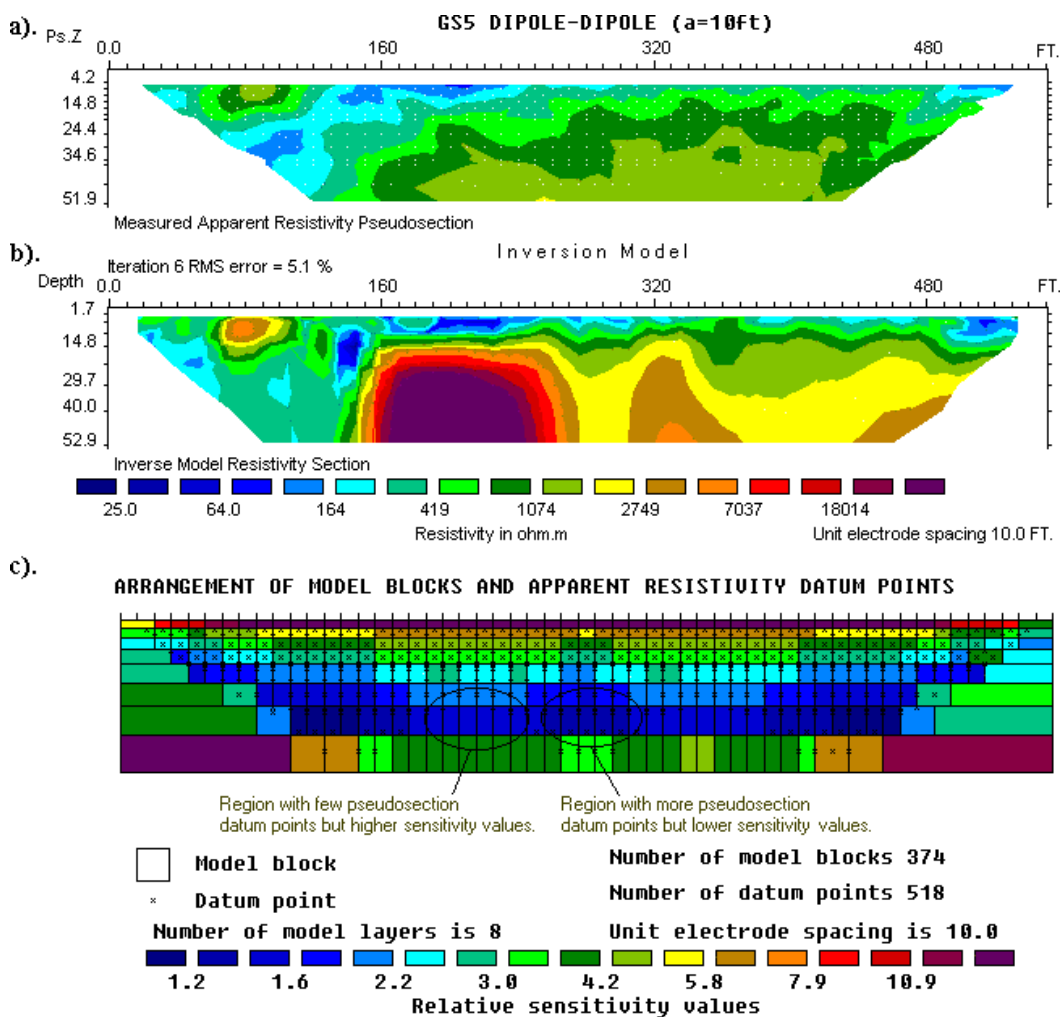


Figure 7.3. Mapping of holes in a clay layer, U.S.A. (a) Apparent resistivity pseudosection for the survey to map holes in the lower clay layer. (b) Inversion model and (c) sensitivity values of the model cells used by the inversion program.

7.5 Time-lapse water infiltration survey - U.K.

Resistivity imaging surveys have not only been carried out in space, but also in time! In some studies, the change of the subsurface resistivity with time has important applications. Such studies include the flow of water through the vadose (unsaturated) zone, changes in the water table due to water extraction (Barker and Moore 1998), flow of chemical pollutants and leakage from dams (Johansson and Dahlin 1996).

A simple, but very interesting, experiment to map the flow of water from the ground surface downwards through the unsaturated zone and into the water table was described by Barker and Moore (1998). In this section, only some of the highlights of this experiment are described as an illustration of a time-lapse survey. This experiment was carried out in the Birmingham (England) area where forty thousand litres of water was poured on the ground surface using a garden hose over a period of 10 hours. Measurements were made before and during the irrigation of the ground surface, and after that for a period of about two weeks. Figure 7.4 (a and b) shows the results of a survey carried out at the beginning of the experiment before the irrigation started. The inversion model (Figure 7.4b) shows that the subsurface, that consists of sand and gravel, is highly inhomogeneous. The water was poured out near the 24 meters mark on this line, and Figure 7.4c shows the inversion model for the data set collected after 10 hours of continuous irrigation. While the model resistivity values in the vicinity of the 24 meters mark are generally lower than the initial data set model in Figure 7.4b, the subsurface distribution of the water is not very clear from a direct comparison of the inversion models alone.

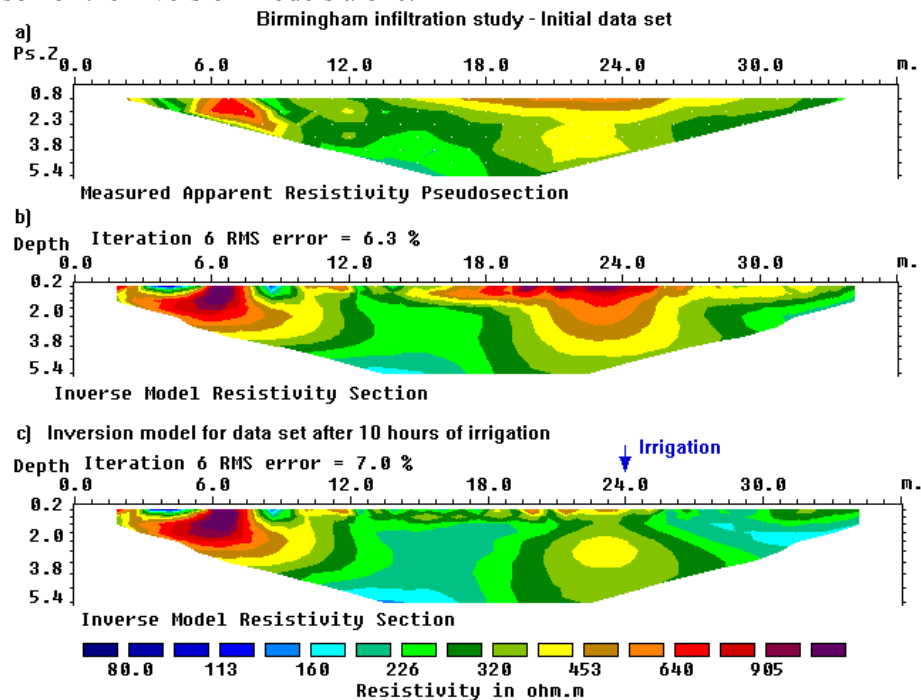


Figure 7.4. Water infiltration mapping, U.K. (a) The apparent resistivity and (b) inversion model sections from the survey conducted at the beginning of the Birmingham infiltration study. This shows the results from the initial data set that forms the base model in the joint inversion with the later time data sets. As a comparison, the model obtained from the inversion of the data set collected after 10 hours of irrigation is shown in (c).

The water distribution is more easily determined by plotting the percentage change in the subsurface resistivity of the inversion models for the data sets taken at different times (Figure 7.5) when compared with the initial data set model. The inversion of the data sets was

carried using a joint inversion technique where the model obtained from the initial data set was used to constrain the inversion of the later time data sets (Loke 1999). The data set collected at 5 hours after the pumping began shows a reduction in the resistivity (of up to over 50 percent) near the ground surface in the vicinity of the 24 meters mark. The near-surface low resistivity zone reaches its maximum amplitude after about 10 hours when the pumping was stopped (Figure 7.5b). Twelve hours after the pumping was stopped, the low resistivity plume has spread downwards and slightly outwards due to infiltration of the water through the unsaturated zone. There is a decrease in the maximum percentage reduction in the resistivity values near the surface due to migration of the water from the near surface zone. This effect of the spreading of the plume becomes increasingly more pronounced after 24 hours (Figure 7.5d) and 36 hours (Figure 7.5e) due to further migration of the water. Note that the bottom boundary of the zone with approximately 20 percent reduction in the resistivity values tends to flatten out at a depth of about 3 meters (Figure 7.5e) where the plume from the surface meets the water table.

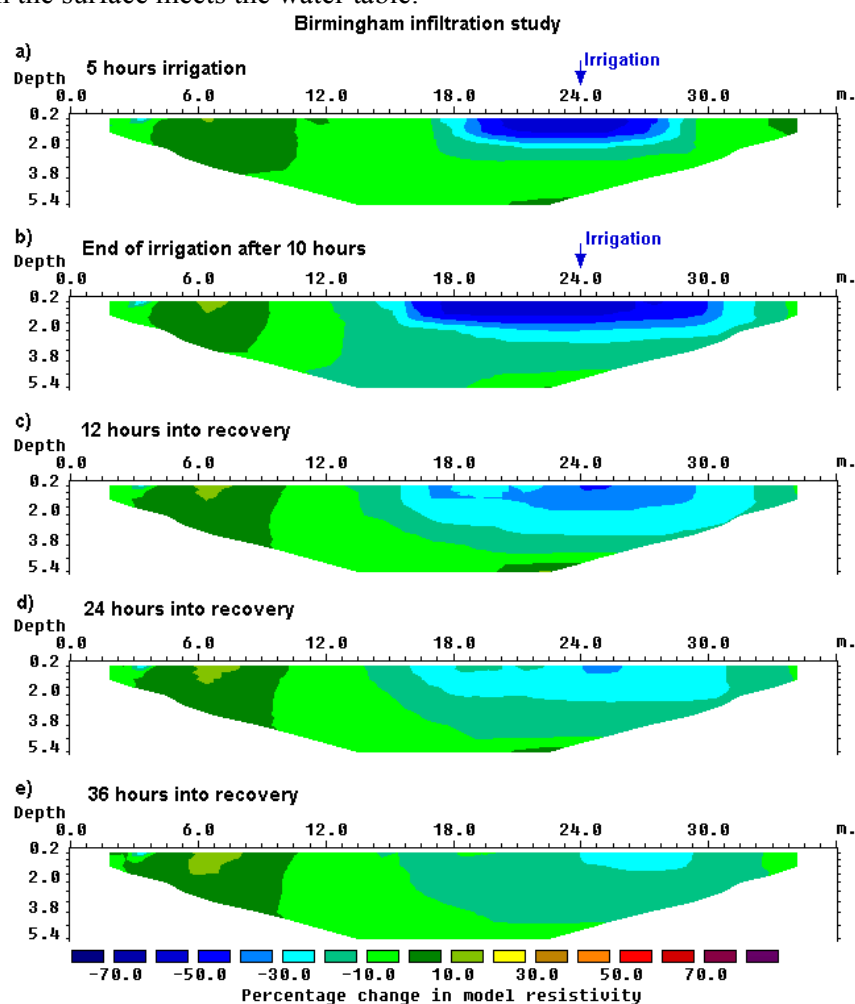


Figure 7.5. Time-lapse sections from the infiltration study. The sections show the change in the subsurface resistivity values with time obtained from the inversion of the data sets collected during the irrigation and recovery phases of the study.

7.6 Pumping test, U.K.

Resistivity imaging measurements were made during a pumping test in the Hoveringham area of East Central England. The aquifer is a sand and gravel layer overlying mudstone. Figure 7.6 shows the initial apparent resistivity pseudosection, and model sections before pumping and after 220 minutes of pumping. Figure 7.7 that shows the relative change in the resistivity at 40, 120 and 220 minutes after the start of the pumping test.

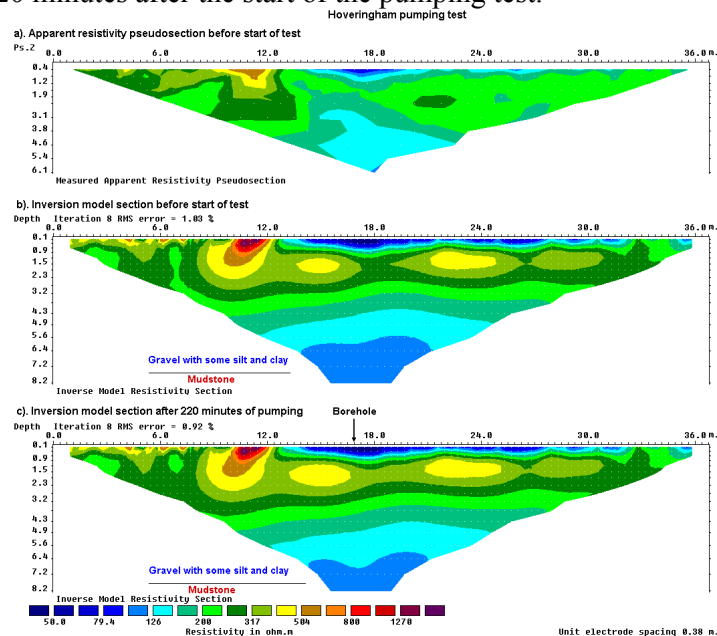


Figure 7.6. Hoveringham pumping test, U.K. (a) The apparent resistivity pseudosection at the beginning of the test. The inversion model sections at the (b) beginning and (v) after 220 minutes of pumping.

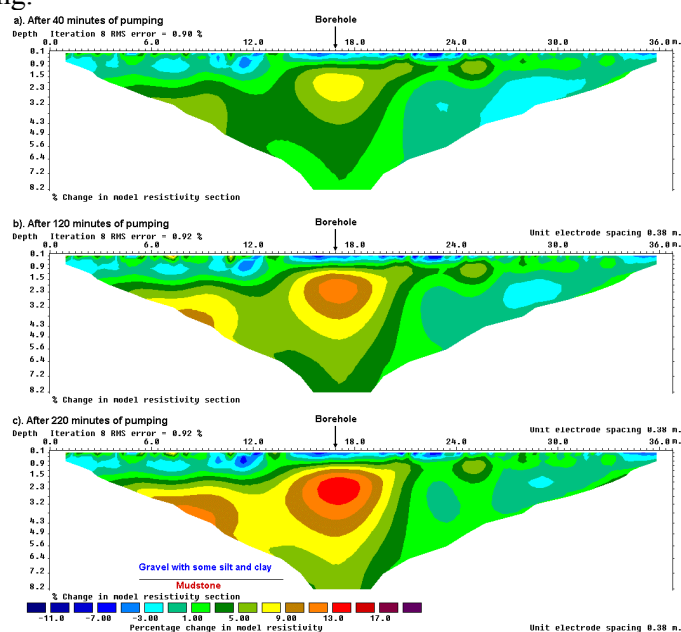


Figure 7.7. Percentage relative change in the subsurface resistivity values for the Hoveringham pumping test. To highlight the changes in the subsurface resistivity, the changes in the model resistivity are shown. Note the increase in the model resistivity below the borehole with time.

Figure 7.7 clearly shows the increase in the zone with higher resistivity values with time due to the extraction of the water. By using Archie's Law, and assuming the water resistivity does not change with time, we can estimate the change in the water saturation values. The decrease in the water saturation level within the aquifer, or desaturation values, is shown in Figure 7.8. As Archie's Law assumes that the conduction is due to the water content alone, the desaturation values are likely to be lower than the true values if there is significant clay content.

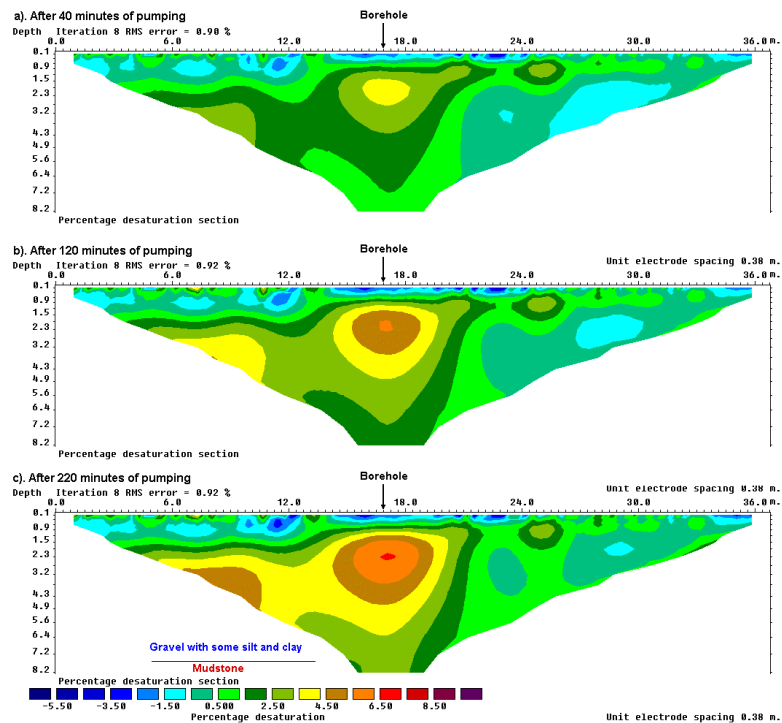


Figure 7.8. Use of Archie's Law for the Hoveringham pumping test. Sections showing the relative desaturation values obtained from the inversion models of the data sets collected during the different stages of the Hoveringham pumping test. Archie's Law probably gives a lower limit for the actual change in the aquifer saturation.

7.7 Wenner Gamma array survey - Nigeria

The Wenner Gamma array (Figure 1.4c) has a relatively unusual arrangement where the current and potential electrodes are interleaved. Compared to the Wenner Alpha and Beta arrays, the Wenner Gamma array is much less frequently used in field surveys. However, in some situations, there might be some advantage in using this array. The depth of investigation is significantly deeper than the Wenner Alpha array (0.59a compared to 0.52a, see Table 2.1), but the potential measured between the potential electrodes is only about 33% less than the Alpha array. In comparison, the voltage that would be measured by the Wenner Beta array is one-third that of the Alpha array which could be a serious disadvantage in noisy environments.

Figure 7.9a shows the Wenner Gamma array pseudosection from a groundwater survey in the Bauchi area of Nigeria (Acworth 1981). In this region, groundwater is frequently found in the weathered layer above the crystalline bedrock. The weathered layer is thicker in areas with fractures in the bedrock, and thus such fractures are good targets for groundwater. In this area, the surveys were carried out with the Wenner Alpha, Beta and Gamma arrays, together with electromagnetic profiling measurements using a Geonics

EM34-3 system (Acworth 1987). Here, only the result from the Wenner Gamma array data set is shown as an example.

To emphasize the boundary between the soil layer and the bedrock, the robust inversion option was used (section 4.3). The inversion model is shown in Figure 7.9b. The thickness of the lower resistivity weathered layer is generally about 10 to 20 meters. There is a narrow vertical low resistivity zone with a width of less than 20 meters below the 190 meters mark that is probably a fracture zone in the bedrock. A borehole well that was placed at the 175 meters mark that lies just at the edge of the fracture zone. It had yields that were somewhat lower than expected (Acworth 1987). In such a situation, the 2D resistivity model would be useful to pinpoint the exact location of the centre of the fracture zone to improve the yield from the borehole. The placement of the well was largely based on resistivity and EM profiling data, and many years before 2D resistivity inversion software and fast microcomputers were widely available.

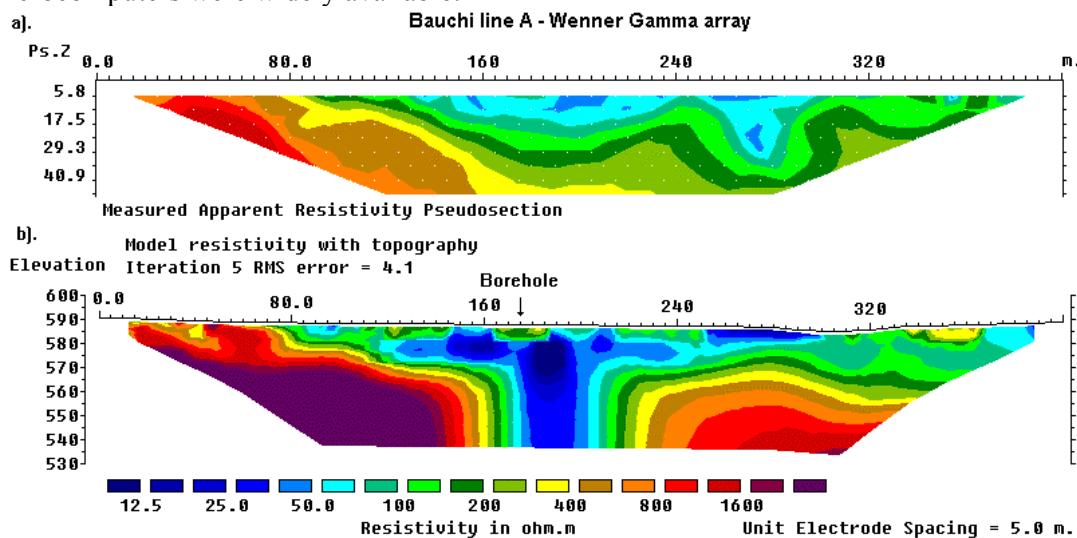


Figure 7.9. Groundwater survey, Nigeria. (a). Apparent resistivity pseudosection. (b) The inversion model with topography. Note the location of the borehole at the 175 meters mark.

As a final note, it is possible to invert data collected with the Wenner Alpha, Beta and Gamma arrays along the same line simultaneously with the RES2DINV program as a single data set. This can be done by using the "non-conventional array" option in the program where the positions of all the four electrodes in an array are explicitly specified. This might be an interesting method to combine the advantages of the different variations of the Wenner array.

7.8 Mobile underwater survey - Belgium

Contrary to popular belief, it is actually possible to carry out resistivity surveys underwater, even in marine environments. This example is one of the most unusual data sets that I have come across, and a worthy challenge for any resistivity imaging inversion software. It is not only the longest in physical length and number of electrode positions, but also uses an unusual highly asymmetrical non-conventional electrode arrangement collected by an underwater mobile surveying system. Mobile surveying systems have an advantage of faster surveying speed, but on land they suffer from the problem of poor ground contact (for the direct contact type) or low signal strength (for the electrostatic type). Please refer to section 2.3 for the details. An underwater environment provides an almost ideal situation for

a direct contact type of mobile system since there is no problem in obtaining good electrode contact!

Figure 7.10a shows the data from an eight kilometers survey line along a river. This survey was carried out by Sage Engineering of Belgium. The purpose of the survey was to map the near surface lithology of the riverbed where there were plans to lay a cable. The data set has a total of 7479 electrode positions and 6636 data points, whereas the inversion model used has 19936 cells. On a 3.2 Ghz Pentium 4 computer, it took slightly less than 2 hours to process this data set!

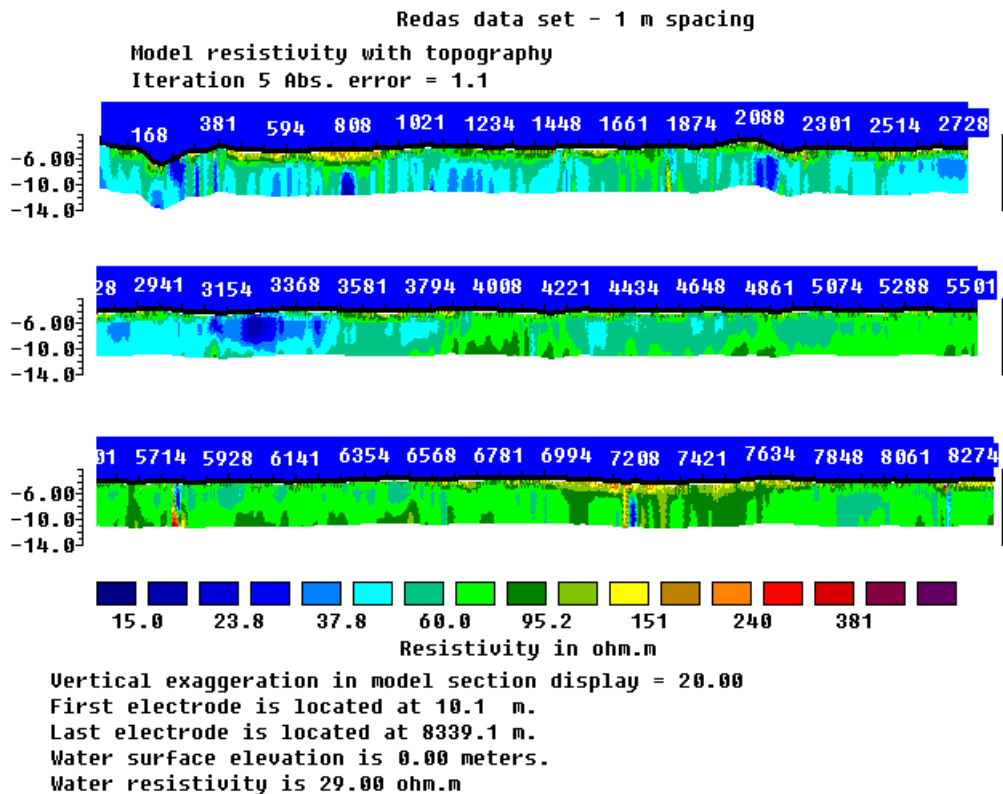


Figure 7.10. The inversion model after 4 iterations from an underwater riverbed survey by Sage Engineering, Belgium.

In the inversion model (Figure 7.10b), most of the riverbed materials have a resistivity of less than 120 Ω -m. There are several areas where the near-surface materials have significantly higher resistivities of over 150 Ω -m. Unfortunately, geological information in this area is rather limited. In the high resistivity areas, the divers faced problems in obtaining sediment samples. The lower resistivity materials are possibly more coherent sediments (possibly sand with silt/clay), whereas the higher resistivity areas might be coarser and less coherent materials.

7.9 Floating electrodes survey – U.S.A.

This survey was carried out along the Thames River in Connecticut, USA using a steamer floating on the water surface that was towed behind a boat. The steamer has 2 fixed current electrodes and 9 potential electrodes. Measurements were made with an 8-channel resistivity meter system. The water depth and conductivity were also measured during the survey. A dipole-dipole type of array configuration was used but some of the measurements used a non-symmetrical arrangement where the potential dipole length was different from the current

dipole length. The apparent resistivity pseudosection from a survey line is shown in Figure 7.11a. The inversion model (Figure 7.11b) obtained when no special constraints were placed on the part of the model that falls within the water layer shows artefacts near the surface due to noise in the data. This model is fairly accurate when the material just below the river bottom has a high resistivity, but poor in areas with low resistivities. These problems do not occur in the model where the water layer resistivity was fixed during the inversion process (Figure 7.11c).

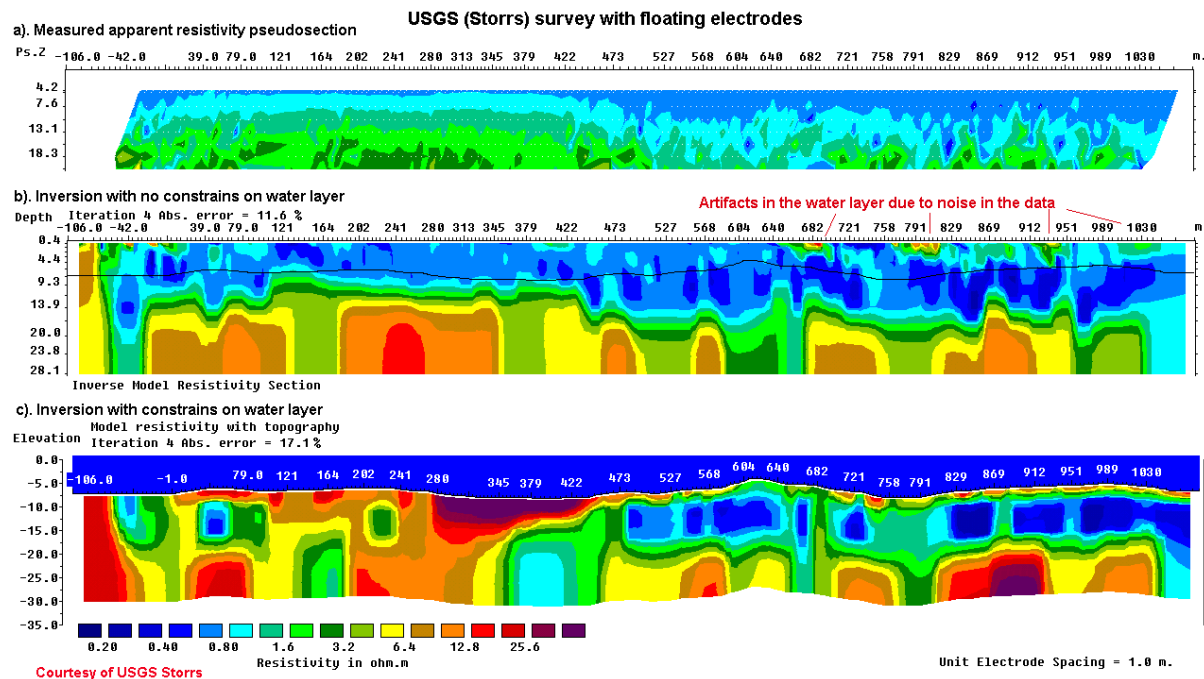


Figure 7.11. Thames River (CT, USA) survey with floating electrodes. (a) The measured apparent resistivity pseudosection. Inversion models obtained (b) without constraints on the water layer, and (c) with a fixed water layer.

7.10 Oil Sands, Canada

A new application for electrical and electromagnetic exploration methods is in the direct detection of hydrocarbons. It is well known that hydrocarbons have much higher resistivity values as compared to the surrounding sediments or sedimentary rocks, and thus ideal targets for electrical and EM based methods. One special form of hydrocarbon deposit that is ideal for the electrical imaging method is the oil sands in Canada (Kellest and Bauman, 1999). It is estimated that Canada has over 400 billion cubic metres (2.5 trillion barrels) of oil sands and heavy oil deposits. Commercial oil sands deposits are located at depths much shallower than conventional hydrocarbon reservoirs, so they can often be accurately mapped by conventional multi-electrode systems.

Figure 7.12a shows the location of three major deposits in the Province of Alberta. The largest deposits are the Athabasca Oil Sands with over 200 Gm³ of reserves. The resistivity log across one of the oil sands bodies (Figure 7.12b) shows high resistivity values approaching 1000 ohm-m for the tar sands as compared to less than 30 ohm-m for the sediments, making the resistivity method a potentially good exploration approach. An example of a resistivity section obtained from a 2D survey (Figure 7.12c) shows prominent high resistivity zones associated with the oil sands.

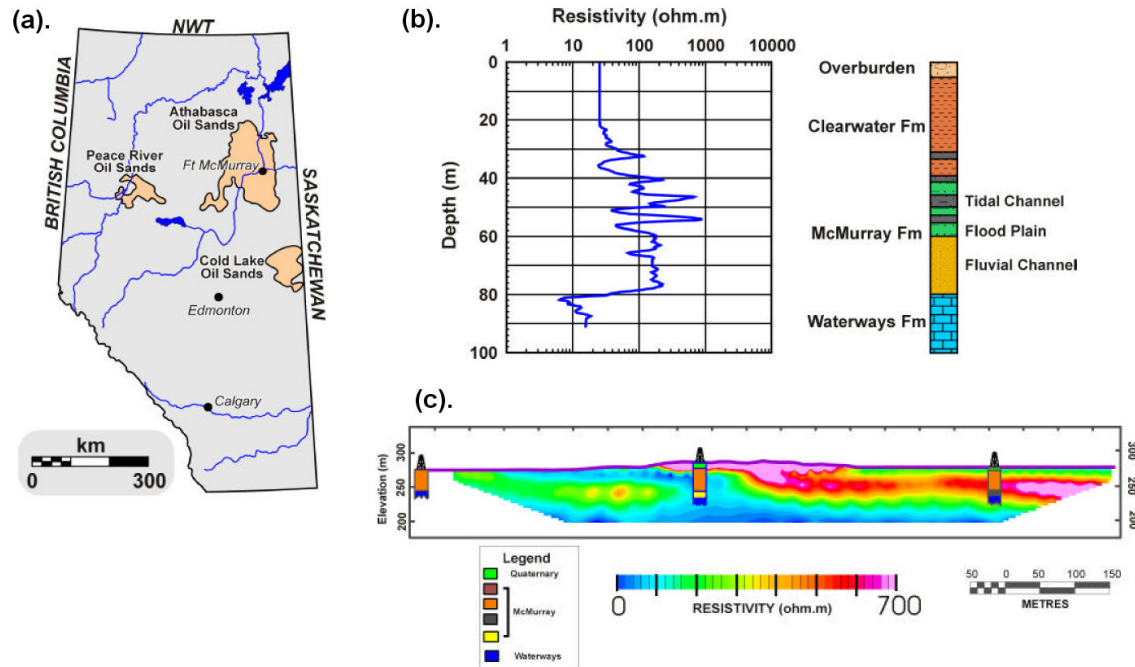


Figure 7.12. Survey to map oil sands, Alberta, Canada. (a) Location of major tar sands deposits in Alberta, Canada. (b) Example of resistivity log and geologic column of Athabasca oil sands. (c) 2-D resistivity model from imaging survey (Kellett and Bauman, 1999).

Besides these examples, 2-D imaging surveys have been carried for many other purposes such as the detection of leakage of pollutants from landfill sites, areas with undulating limestone bedrock, mapping of the overburden thickness over bedrock (Ritz *et al.* 1999), leakage of water from dams, saline water intrusion in coastal aquifers, freshwater aquifers (Dahlin and Owen, 1998), monitoring of groundwater tracers (Nyquist *et al.*, 1999) and mapping of unconsolidated sediments (Christensen and Sorensen, 1994). The resistivity imaging method has also been used in underwater surveys in lakes and dams.

8 3-D electrical imaging surveys

8.1 Introduction to 3-D surveys

Since all geological structures are 3-D in nature, a fully 3-D resistivity survey using a 3-D interpretation model (Figure 1.6c) should in theory give the most accurate results. At the present time 3-D surveys is a subject of active research. However it has not reached the level where, like 2-D surveys, it is routinely used. The main reason is that the survey cost is comparatively higher for a 3-D survey of an area that is sufficiently large. There are two current developments that should make 3-D surveys a more cost-effective option in the near future. One is the development of multi-channel resistivity meters that enables more than one reading to be taken at a single time. This is important to reduce the survey time. The second development is faster microcomputers to enable the inversion of very large data sets (with more than 8,000 data points and survey grids of greater than 30 by 30) to be completed within a reasonable time.

8.2 Array types for 3-D surveys

The pole-pole, pole-dipole and dipole-dipole arrays are frequently used for 3-D surveys. This is because other arrays have poorer data coverage near the edges of the survey grid. The advantages and disadvantages of the pole-pole, pole-dipole and dipole-dipole arrays that were discussed in section 2.5 with regards to 2-D surveys are also valid for 3-D surveys.

8.2.1 The pole-pole array

Figure 8.1 shows one possible arrangement of the electrodes for a 3-D survey using a multi-electrode system with 25 nodes. For convenience the electrodes are usually arranged in a square grid with the same unit electrode spacing in the x and y directions. To map slightly elongated bodies, a rectangular grid with different numbers of electrodes and spacings in the x and y directions could be used. The pole-pole electrode configuration is commonly used for 3-D surveys, such as the E-SCAN method (Li and Oldenburg 1992, Ellis and Oldenburg 1994b). The maximum number of independent measurements, n_{max} , that can be made with n_e electrodes is given by

$$n_{max} = n_e(n_e - 1) / 2$$

In this case, each electrode is in turn used as a current electrode and the potential at all the other electrodes are measured. Note that because of reciprocity, it is only necessary to measure the potentials at the electrodes with a higher index number than the current electrode in Figure 8.2a. For a 5 by 5 electrodes grid, there are 300 possible measurements. For 7 by 7 and 10 by 10 electrodes grids, a survey to measure the complete data set would have 1176 and 4500 data points respectively. For commercial surveys, grids of less than 10 by 10 are probably not practical as the area covered would be too small.

It is can be very time-consuming (at least several hours) to make such a large number of measurements, particularly with typical single-channel resistivity meters commonly used for 2-D surveys. To reduce the number of measurements required without seriously degrading the quality of the model obtained, an alternative measurement sequence is shown in Figure 8.2b. In this proposed "cross-diagonal survey" method, the potential measurements are only made at the electrodes along the x -direction, the y -direction and the 45 degrees diagonal lines passing through the current electrode. The number of data points with this arrangement for a 7 by 7 grid is reduced to 476 which is about one-third of that required by a complete data set survey (Loke and Barker 1996b).

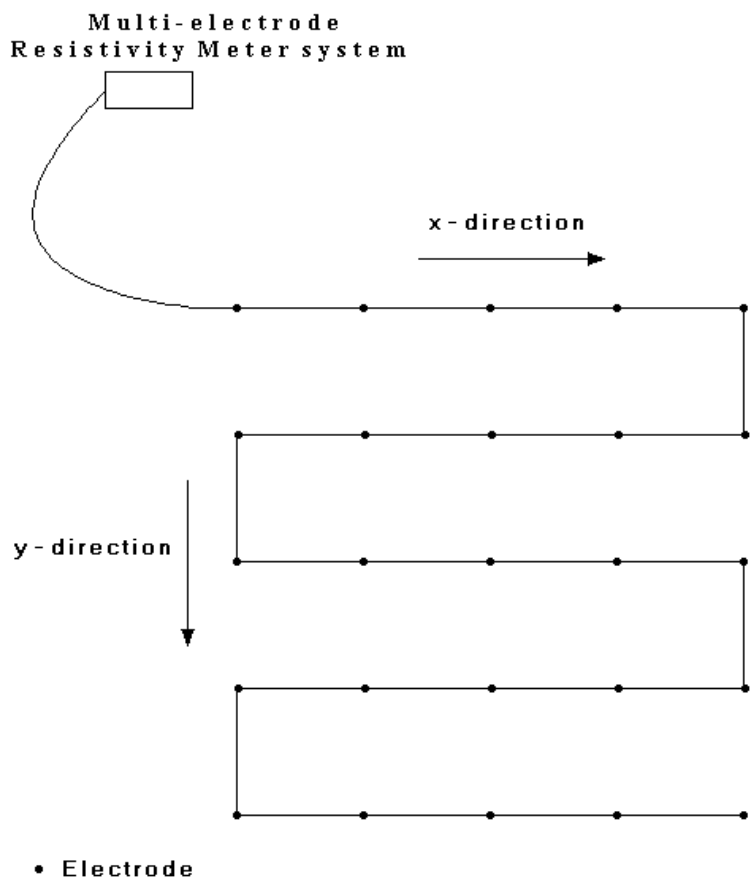


Figure 8.1. The arrangement of the electrodes for a 3-D survey.

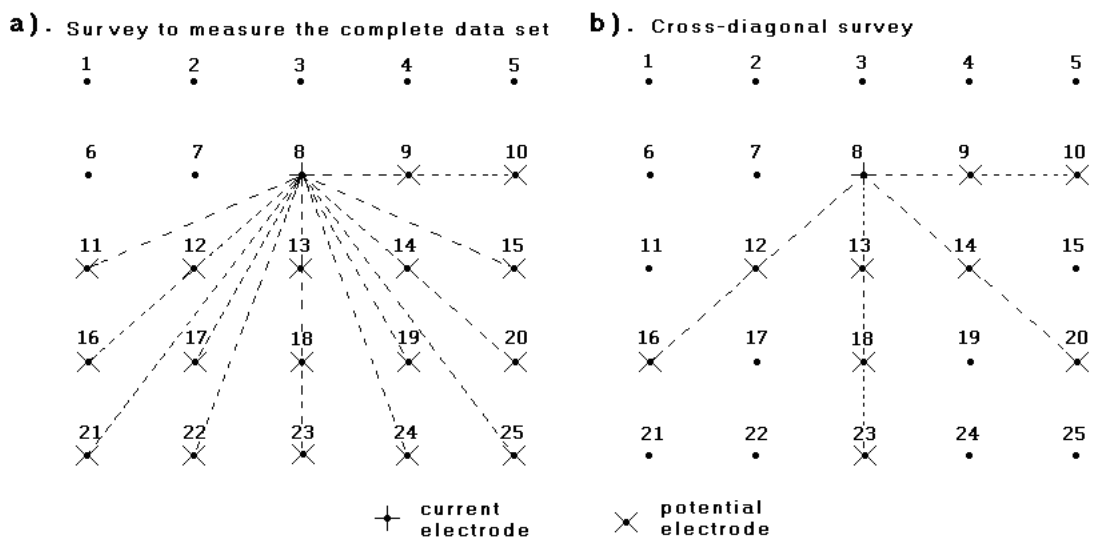


Figure 8.2. Two possible measurement sequences for a 3-D survey. The location of potential electrodes corresponding to a single current electrode in the arrangement used by (a) a survey to measure the complete data set and (b) a cross-diagonal survey.

In some cases, 3-D data sets are constructed from a number of parallel 2-D survey lines (section 8.3). Ideally there should be a set of survey lines with measurements in the x -direction, followed by another series of lines in the y -direction. The use of measurements in two perpendicular directions helps to reduce any directional bias in the data.

However, in some cases, only the data from a series of survey lines in one direction is available. This is particularly common if the surveys were originally conducted to provide 2-D images. Sometimes the spacing between the “in-line” electrodes is significantly smaller than the spacing between the lines. One important question is the maximum spacing between the lines that can be used for the data to be still considered “3-D”. A useful guide is the 3-D sensitivity plot. Figure 8.3 shows the sensitivity values on horizontal slices through the earth. The electrodes are arranged along the 0 and 1 meter marks along the x -axis. Near the surface, there is an approximately circular region with negative sensitivity values in the top two slices at depths of 0.07 and 0.25 meter. The zone with the largest sensitivity (using the 4 units sensitivity contour line as a guide) extends in the y -direction to slightly over half the electrode spacing. This means to get a complete 3-D coverage, if the measurements are only made in the x -direction, the spacing between the lines should not be much more than the smallest electrode spacing used.

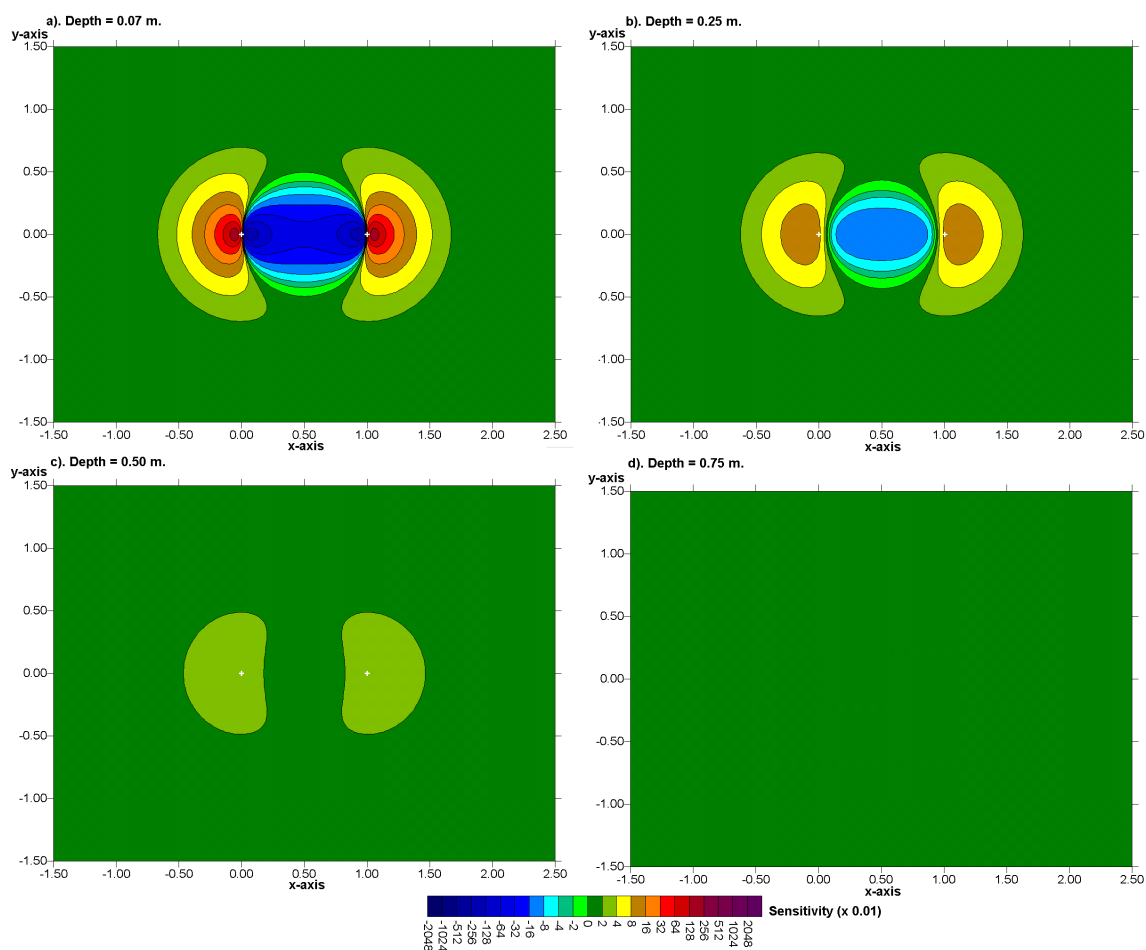


Figure 8.3. 3-D sensitivity plots for the pole-pole array. The plots are in the form of horizontal slices through the earth at different depths.

The pole-pole array has two main disadvantages. Firstly it has a much poorer

resolution compared to other arrays. Subsurface structures tend to be smeared out in the final inversion model. The second disadvantage, particularly for large electrode spacings, is that the second current electrode and potential electrode must be placed at a sufficiently large distance from the survey grid. Both disadvantages have been discussed in detail in Section 2.5.7. Park and Van (1991) who used this array for a field experiment found that about 15% of the measurements did not satisfy reciprocity because the contribution for the remote electrodes were significant. In general, this probably affects the readings with the larger spacings.

8.2.2 The pole-dipole array

This array is an attractive alternative to the pole-pole array for surveys with medium and large survey grids (12 by 12 and above). It has a better resolving power than the pole-pole array (Sasaki 1992), and is less susceptible to telluric noise since both potential electrodes are kept within the survey grid. Compared to the dipole-dipole array, it has a much stronger signal strength. Although it has one “remote” electrode (the C2 electrode), the effect of this electrode on the measurements is much smaller compared to the pole-pole array (section 2.5.8). As the pole-dipole array is an asymmetrical array, measurements should be made with the “forward” and “reverse” arrangements of the electrodes (Figure 2.16). To overcome the problem of low signal strength for large values of the “**n**” factor (exceeding 8), the “**a**” spacing between the P1-P2 dipole pair should be increased to get a deeper depth of investigation with a smaller “**n**” factor. The use of redundant measurements with overlapping data levels to increase the data density can in some cases help to improve the resolution of the resulting inversion model (section 2.5.9).

Figures 8.4 and 8.5 show the sensitivity patterns for this array with the dipole separation factor “**n**” equal to 1 and 4 respectively. There is prominent area with negative sensitivity values between the C1 and P1 electrodes (located at 0.0 and 0.5 meter along the *x*-axis). The plots are arranged such that the array length (in this case the distance between the C1 and P2 electrodes) is set at 1.0 meter for both “**n**” factors. For a larger “**n**” factor, the area of negative sensitivities between the C1 and P1 electrodes becomes larger and extends to a greater depth. The array is more sensitive to structures off the array axis (i.e. in the *y*-direction) when “**n**” is equals to 1. The area with the higher sensitivity values extends to about 0.8 times the array length (Figure 8.4), or 1.6 times the unit electrode spacing. When the “**n**” factor is larger (Figure 8.5), the array is more sensitive to off-axis structures near the P1-P2 dipole. Note also the negative sensitivity values to the right of the P2 electrode.

If the 3-D survey is carried out with a series of parallel lines, and the cross-line measurements are not made, the distance between the lines should preferably be within two to three times the inline unit electrode spacing. This is to ensure that the subsurface material between the lines is adequately mapped by the in-line measurements.

8.2.3 The dipole-dipole, Wenner and Schlumberger arrays

This array can be recommended only for grids that are larger than 12 by 12 due to the poorer horizontal data coverage at the sides. The main problem that is likely to be faced with this array is the comparatively low signal strength. Similar to 2-D surveys, this problem can be overcome by increasing the “**a**” spacing between the P1-P2 dipole to get a deeper depth of investigation as the distance between the C1-C2 and P1-P2 dipoles is increased. Also, the use of overlapping data levels is recommended (section 2.5.9).

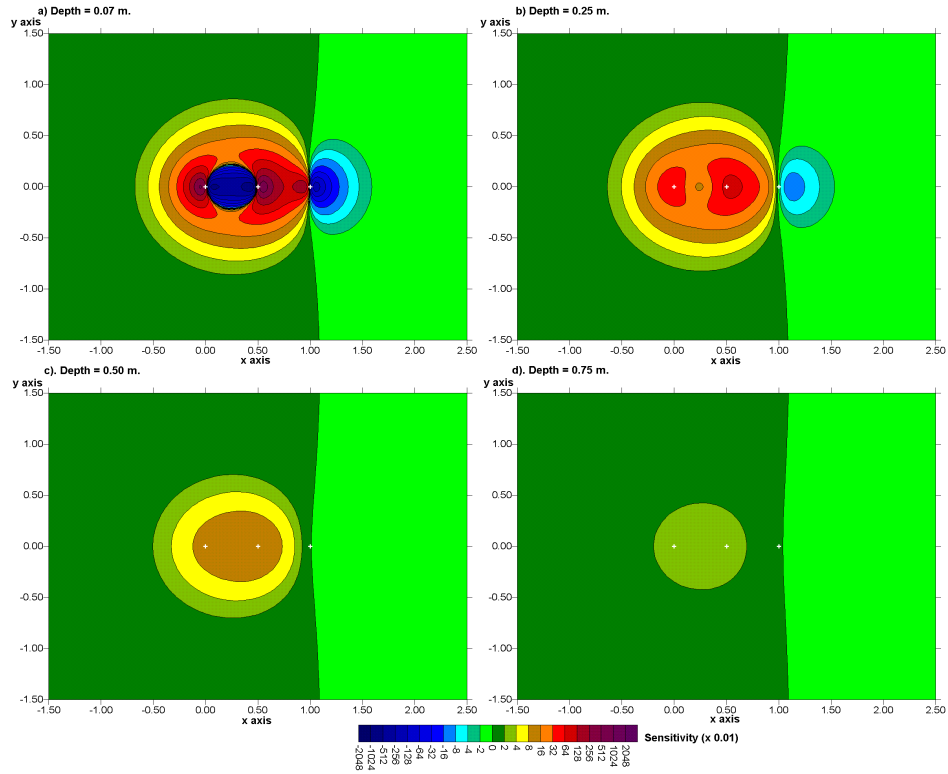


Figure 8.4. 3-D sensitivity plots for the pole-dipole array with $n=1$ in the form of horizontal slices through the earth at different depths. The C1 electrode is the leftmost white cross.

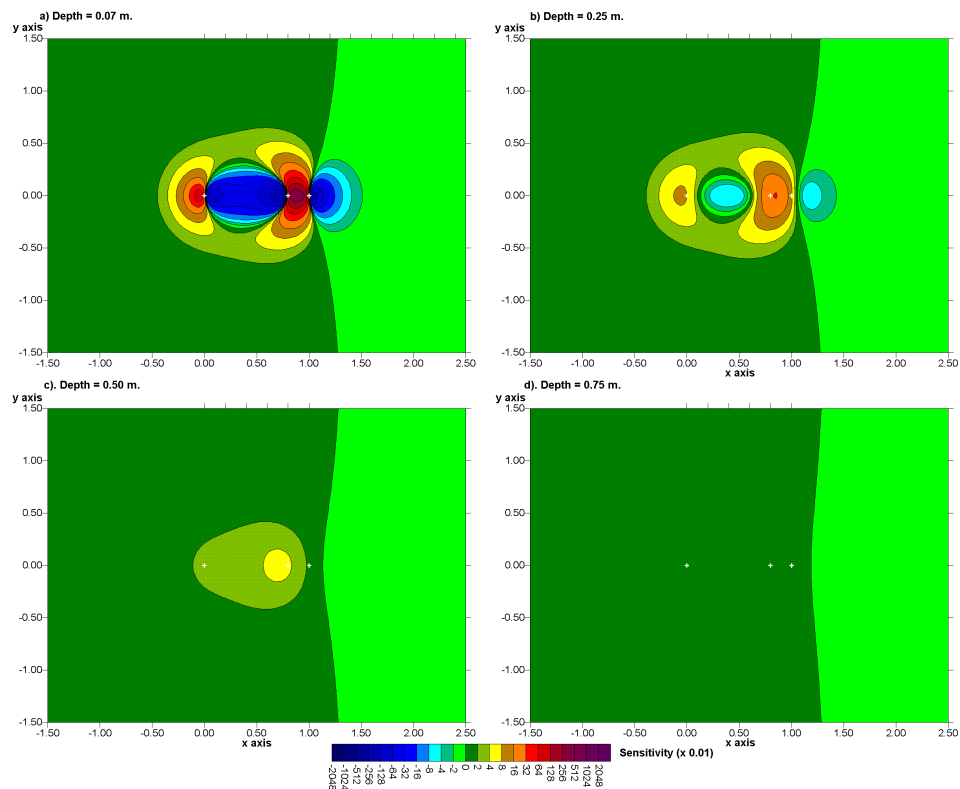


Figure 8.5. 3-D sensitivity plots for the pole-dipole array with $n=4$ in the form of horizontal slices through the earth at different depths.

Figure 8.6 and 8.7 shows the sensitivity patterns for the dipole-dipole array when the “**n**” factor is equal to 1 and 4 respectively. The sensitivity values have small but negative values outside the immediate vicinity of the array. Another interesting feature is that the sensitivity contours tend to be elongated in the *y*-direction, particularly for the larger “**n**” value. The 4 units sensitivity contour extends to about 0.6 times the array length in the *y*-direction, or about 1.8 times the unit electrode spacing. This means that the array is more sensitive to structures off the array axis compared to the pole-pole and pole-dipole arrays. This feature is troublesome in 2-D surveys, but might be advantageous in 3-D surveys.

The off-axis elongation of the sensitivity contours agrees with the observation by Dahlin and Loke (1997) that the dipole-dipole array is more sensitive to 3-D effects compared to the other common arrays. This factor is important when the dipole-dipole array is used in 2-D imaging surveys where it is assumed that the subsurface geology is 2-D.

In many cases, 3-D data sets for the dipole-dipole arrays are constructed from a number of parallel 2-D survey lines, particularly from previous surveys. Due to the elongated sensitivity pattern, the dipole-dipole array can probably tolerate a larger spacing between the survey lines (to about three times the inline unit electrode spacing) and still contain significant 3-D information.

In closing this section on four electrodes arrays, Figures 8.8, 8.9 and 8.10 show the sensitivity patterns for the Wenner alpha, Schlumberger and Wenner gamma arrays (the Wenner beta is the dipole-dipole with a “**n**” value of 1 as shown in Figure 8.6). The sensitivity contours for the Wenner alpha array, outside of the immediate vicinity of the electrodes, are elongated in the direction of the line of electrodes. This means that the Wenner alpha array is less sensitive to off-line structures than the dipole-dipole array, i.e. it is less sensitive to 3-D. This agrees with empirical observations by Dahlin and Loke (1997). The sensitivity pattern for the Wenner-Schlumberger array (Figure 8.9) is similar to that for the Wenner alpha array except for a slight bulge near the center of the array.

The sensitivity patterns for the Wenner gamma array (Figure 8.10) show characteristic bulges near the C1 and C2 electrodes that were observed earlier in the 2-D sensitivity sections (Figure 2.10). Thus it is expected to be more sensitive to 3-D structures near the C1 and C2 electrodes.

8.2.4 Summary of array types

For relatively small grids of less than 12 by 12 electrodes, the pole-pole array has a substantially larger number of possible independent measurements compared to other arrays. The loss of data points near the sides of the grid is kept to a minimum, and it provides better horizontal data coverage compared to other arrays. This is an attractive array for small survey grids with relatively small spacings (less than 5 meters) between the electrodes. However, it has the disadvantage of requiring two “remote” electrodes that must be placed at a sufficiently large distance from the survey grid. Due to the large distance between the two potential electrodes, this array is more sensitive to telluric noise. The pole-dipole array is an attractive option for medium size grids. It has a higher resolution than the pole-pole array, it requires only one remote electrode and is much less sensitive to telluric noise. For surveys with large grids, particularly when there is no convenient location for a remote electrode, the dipole-dipole array can be used. For the pole-dipole and dipole-dipole arrays, measurements with overlapping data levels using different “**a**” and “**n**” combinations should be used to improve the quality of the results. The electrodes for 3-D surveys are normally arranged in a rectangular grid with a constant spacing between the electrodes (Figure 8.1). However, the RES3DINV resistivity and IP inversion program can also handle grids with a non-uniform spacing between the rows or columns of electrodes.

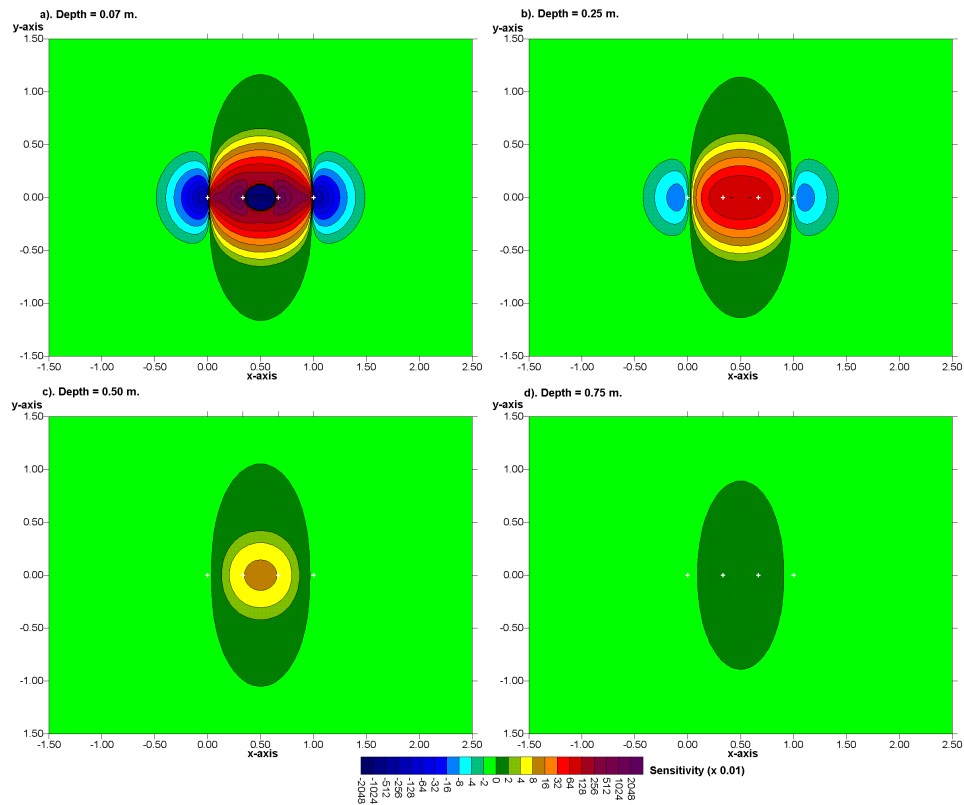


Figure 8.6. 3-D sensitivity plots for the dipole-dipole array with $n=1$ in the form of horizontal slices through the earth at different depths. The C2 electrode is the leftmost white cross.

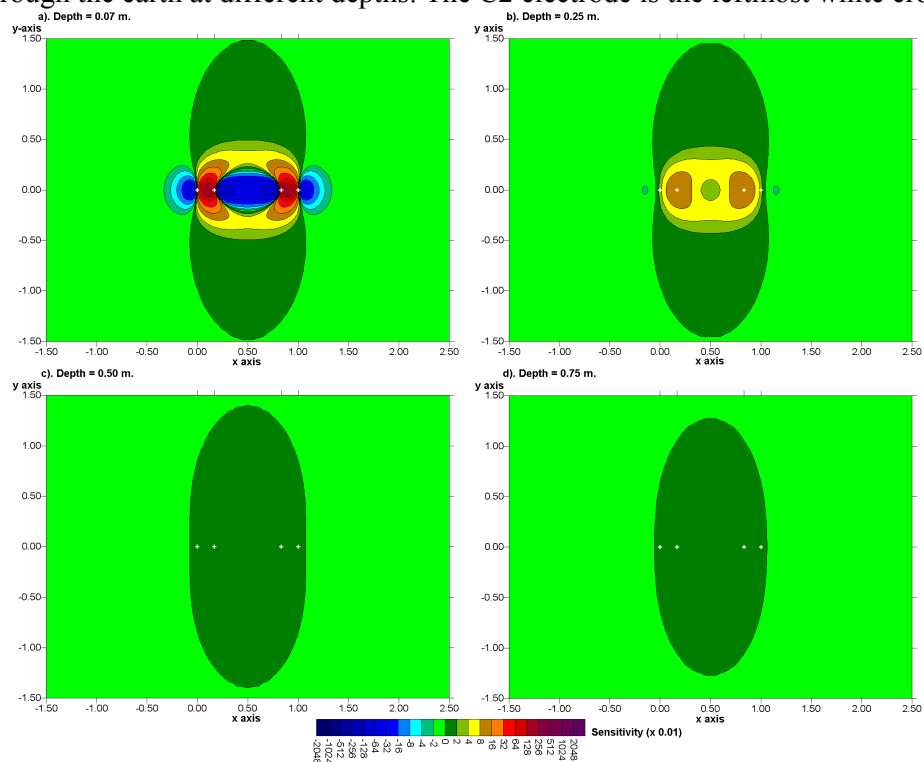


Figure 8.7. 3-D sensitivity plots for the dipole-dipole array with $n=4$ in the form of horizontal slices through the earth at different depths. The C2 electrode is the leftmost white cross.

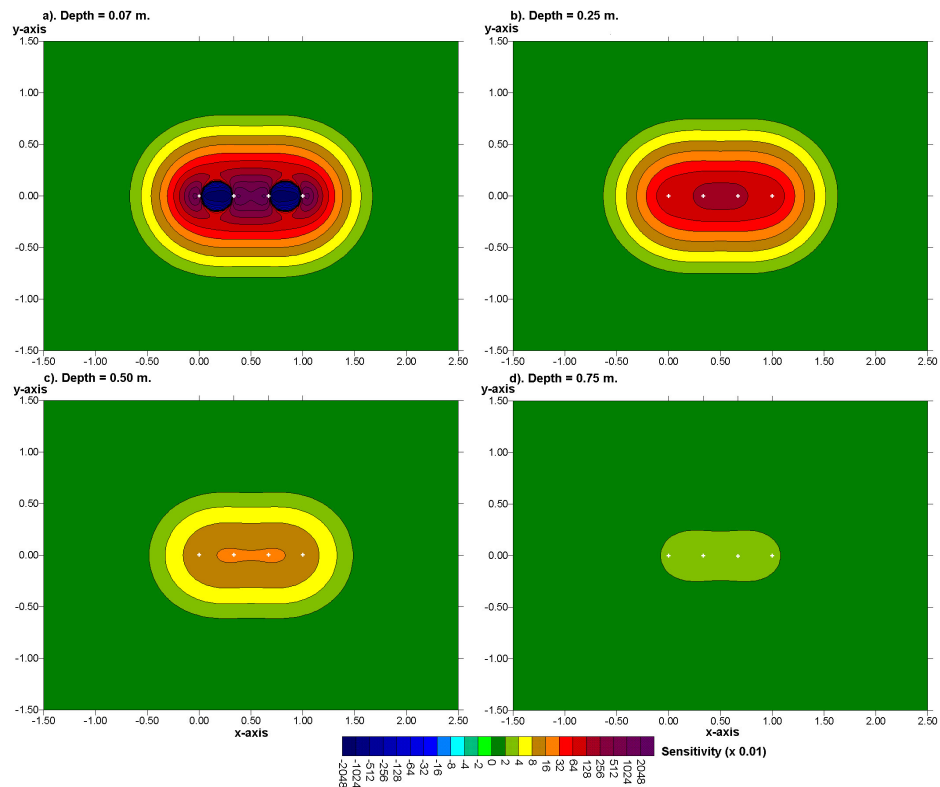


Figure 8.8. The 3-D sensitivity plots for the Wenner alpha array at different depths.

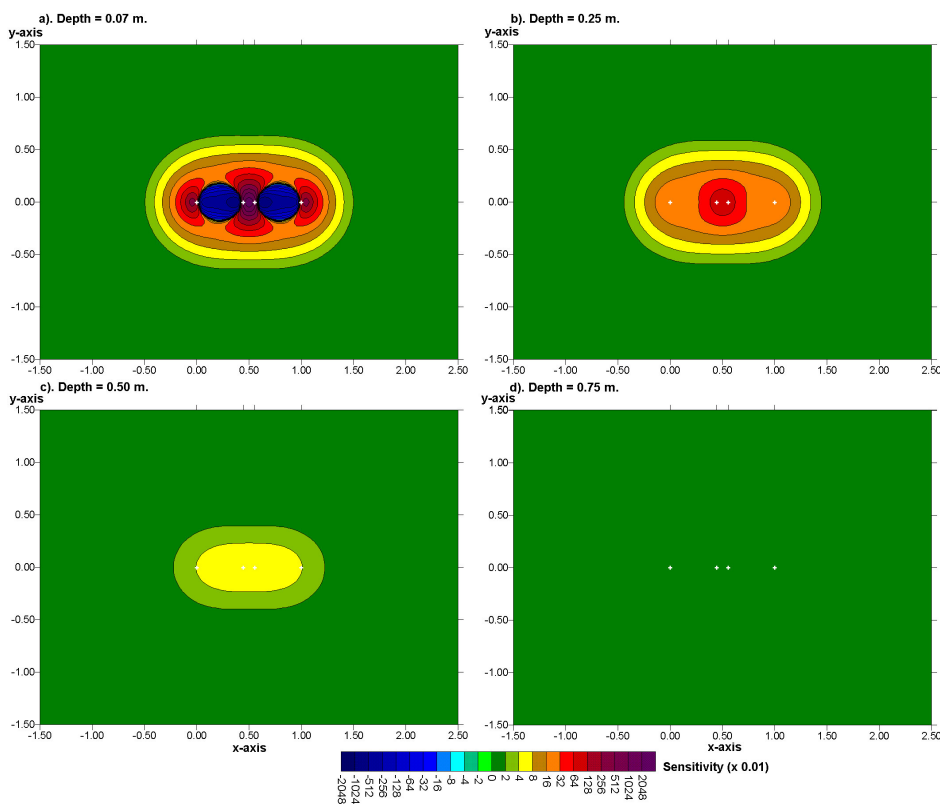


Figure 8.9. The 3-D sensitivity plots for the Wenner-Schlumberger array with the $n=4$ at different depths.

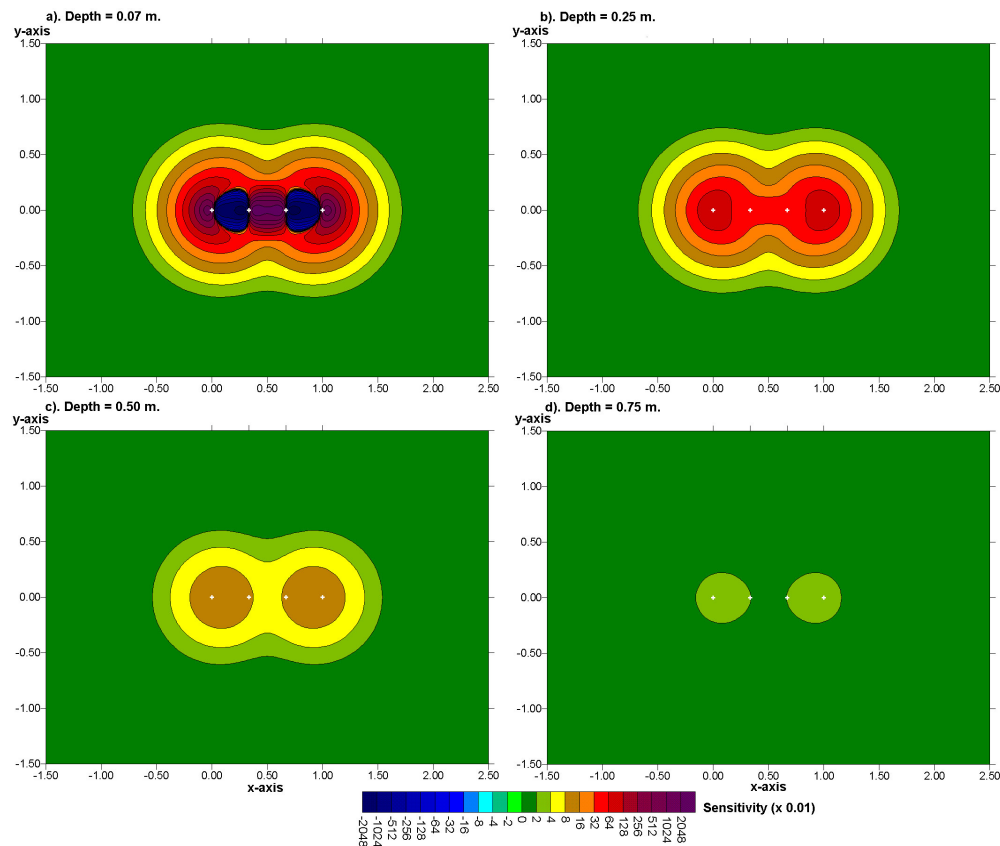


Figure 8.10. The 3-D sensitivity plots for the Wenner gamma array at different depths.

8.3 3-D roll-along techniques

Most commercial 3-D surveys will probably involve grids of at least 16 by 16 in order to cover a reasonably large area. A 16 by 16 grid will require 256 electrodes which is more than that available on many multi-electrode resistivity meter systems. One method to survey such large grids with a limited number of electrodes is to extend the roll-along technique used in 2-D surveys to 3-D surveys (Dahlin and Bernstone 1997). Figure 8.11 shows an example of a survey using a multi-electrode resistivity-meter system with 50 electrodes to survey a 10 by 10 grid. Initially the electrodes are arranged in a 10 by 5 grid with the longer lines orientated in the x -direction (Figure 8.10a). Measurements are made primary in the x -direction, with some possible measurements in the diagonal directions. Next the entire grid is moved in the y -direction so that the 10 by 5 grid now covers the second half of the 10 by 10 grid area. The 10 by 5 grid of electrodes is next orientated in the y -direction (Figure 8.11b).

The example data file PIPE3D.DAT was obtained from a survey using such a roll-along technique. It was carried out with a resistivity-meter system with only 25 nodes with the electrodes arranged in an 8 by 3 grid. The long axis of this grid was orientated perpendicularly to two known subsurface pipes. The measurements were made using three such 8 by 3 sub-grids so that the entire survey covers an 8 by 9 grid. For each 8 by 3 sub-grid, all the possible measurements (including a limited number in the y -direction) for the pole-pole array were made. In this survey, the second set of measurements in the y -direction (as in Figure 8.11b) was not carried out to reduce the survey time, and also because the pipes have an almost two-dimensional structure.

For practical reasons, the number of field measurements in some surveys might be even less than the cross-diagonal technique. Another common approach is to just make the

measurements in the x - and y - directions only, without the diagonal measurements. This is particularly common if the survey is made with a system with a limited number of independent electrodes, but a relatively large grid is needed.

In some cases, measurements are made only in one direction. The 3-D data set consists of a number of parallel 2-D lines. The data from each 2-D survey line is initially inverted independently to give a series of 2-D cross-sections. The measured apparent resistivity values from all the lines can also be combined into a 3-D data set and inverted with RES3DINV to give a 3-D picture. While the quality of the 3-D model is expected to be poorer than that produced with a complete 3-D survey, such a “poor man’s” 3-D data set could reveal major resistivity variations across the survey lines (see also section 8.5). Until multi-channel resistivity instruments are widely used, this might be the most cost-effective solution to extract some 3-D information from 2-D surveys. This arrangement might be particularly useful for surveys with the dipole-dipole array that can tolerate larger spacings between the survey lines.

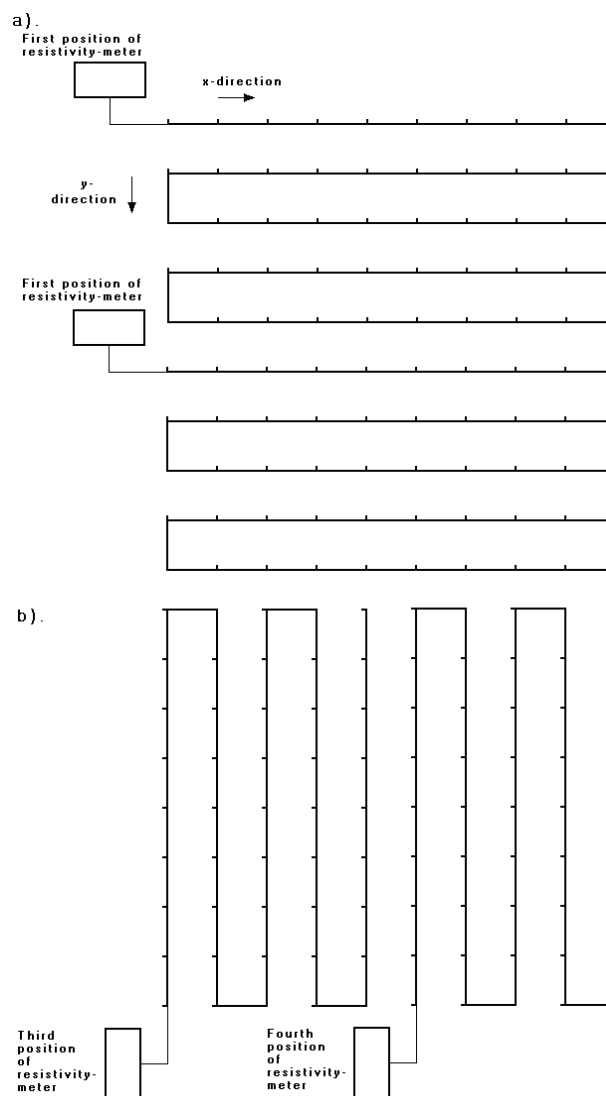


Figure 8.11. Using the roll-along method to survey a 10 by 10 grid with a multi-electrode system with 50 nodes. (a) Surveys using a 10 by 5 grid with the lines orientated in the x -direction. (b) Surveys with the lines orientated in the y -direction.

8.4 A 3-D forward modeling program

In the interpretation of data from 2-D resistivity imaging surveys, it is assumed that the subsurface geology does not change significantly in the direction that is perpendicular to the survey line. In areas with very complex geology, there are could be significant variations in the subsurface resistivity in this direction (i.e. the geology is 3-D), which could cause distortions in the lower sections of the 2-D model obtained (please refer to section 4.7).

The free 3-D resistivity forward modeling program, RES3DMOD.EXE, enables you to calculate the apparent resistivity values for a survey with a rectangular grid of electrodes over a 3-D structure. This is a Windows based program that can be used from within Windows 95/98/Me/2000/NT. To take a look the operation of the program, use the “File” option followed by “Read model data” to read in the file BLOCK11.MOD, which has a 11 by 11 survey grid. After that, click the “Edit/Display” option.

To modify the 3-D model, click the “Edit resistivity model” option. In this option, you can change the resistivity of the 3-D cells in the mesh used by the finite-difference method (Dey and Morrison 1979b) to calculate the apparent resistivity values. To quit from the “Edit” mode, press the Q or the Esc key. To calculate the apparent resistivity values, click the “Calculate” option. To take a look at the apparent resistivity pseudosections, click the “Display apparent resistivity” option. You can choose to display the apparent resistivity values in the form of horizontal pseudosections, or as vertical pseudosections as used in 2-D surveys. Displaying the vertical pseudosections will give you an idea of the effect of a 3-D structure on the measurements in a 2-D survey. In a study made by Dahlin and Loke (1997), the dipole-dipole array was found to be the most sensitive to 3-D effects while the Wenner array was the least sensitive.

The RES3DMOD program also has an option to save the apparent resistivity values into a format that can be accepted by the RES3DINV inversion program. As an exercise, save the apparent resistivity values as a RES3DINV data file for one of the models, and later carry out an inversion of this synthetic data set.

Exercise 8.1 : 3-D forward modeling examples

Data set and purpose	Things to try
PRISM2.MOD – This is a 3-D model used to generate the pseudosections shown in Figure 8.12 to illustrate 3-D effects in 2-D surveys.	<ol style="list-style-type: none"> (1). Read in the file, and then run the “Calculate” step to calculate the potential values. This is a relatively large model file, so you might to collect some coffee while the computer is running. (2). Next choose the “Display apparent resistivity” option under the “Edit/Display” menu. Try first with pole-pole array, and take a look at the pseudosections. (3).Next try with other arrays.
BLOCK15.MOD – A 15 by 15 grid model with several rectangular prisms.	<ol style="list-style-type: none"> (1). Read in the file, and then run the “Calculate” step to calculate the potential values. (2). Next choose the “Display apparent resistivity” option under the “Edit/Display” menu. Take a look at the pseudosections for a few arrays. (3). Try using the “Edit model” option to change the model, and then recalculate the potential values. Check out the effect of your changes on the apparent resistivity pseudosections.

Figure 8.12a shows an example of a 3-D model with a 15 by 15 survey grid (i.e. 255

electrodes). The model, which consists of four rectangular prisms embedded in a medium with a resistivity of $50 \Omega\text{-m}$, is shown in the form of horizontal slices through the earth. The apparent resistivity values for the pole-pole array (with the electrodes aligned in the x -direction) are shown in the form of horizontal pseudosections in Figure 8.12b. Note the low resistivity block with a resistivity of $10 \Omega\text{-m}$ near the centre of the grid that extends from a depth of 1.0 to 3.2 meters. For measurements with the shorter electrode spacings of less than 4 meters this block causes a low resistivity anomaly. However, for electrode spacings of greater than 6 meters, this low resistivity prism causes a high resistivity anomaly! This is an example of “anomaly inversion” which is caused by the near-surface zone of negative sensitivity values between the C1 and P1 electrodes (Figure 8.3).

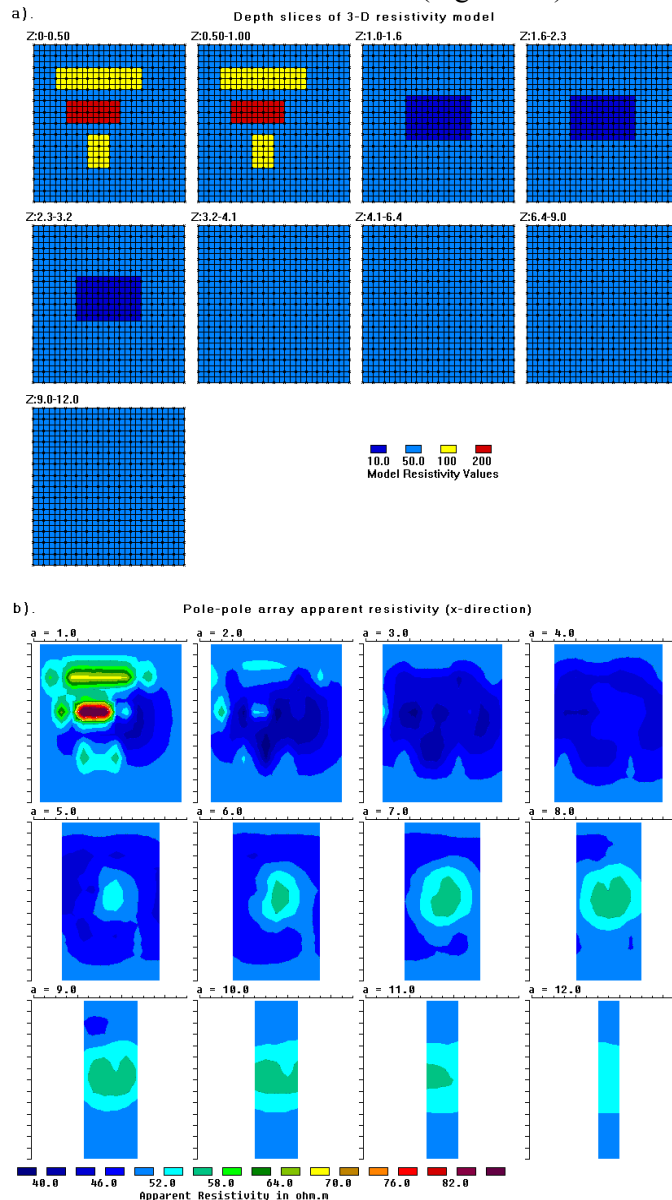


Figure 8.12. A 3-D model with 4 rectangular prisms in a 15 by 15 survey grid. (a) The finite-difference grid. (b) Horizontal apparent resistivity pseudosections for the pole-pole array with the electrodes aligned in the x -direction.

8.5 3-D inversion algorithms and 3-D data sets

Two interesting questions that sometimes arise, particularly in non-academic circles, is the definition of a 3-D inversion algorithm and what constitutes a 3-D data set. The first question can be easily answered, but the second is less clear.

A defining feature of a 3-D algorithm inversion algorithm is that it allows the model resistivity values to vary in all three directions, i.e. in the x -, y - and z -directions. This is in contrast to 2-D inversion where the subsurface resistivity is assumed to vary only in the x - and z -directions but constant in the y -direction; and in 1-D inversion where the resistivity is only allowed to be changed in the z -direction. The inversion model used by the RES3DINV program consists of independent rectangular cells (Figure 8.13) where the model values are allowed to vary in all three directions simultaneously, so it uses a true 3-D inversion algorithm. Note that a model constructed from a series of 2-D inversions along parallel lines is not a true 3-D inversion model.

Another defining characteristic of a 3-D inversion algorithm is the use of a 3-D forward modeling subroutine, such as the 3-D finite-difference and finite-element methods (Dey and Morrison 1979b, Silvester and Ferrari 1990), to calculate the model apparent resistivity and Jacobian matrix values.

A more difficult question is what constitutes a “3-D” data set. At present there is no generally accepted definition of a 3-D data set. While the inversion algorithm used to invert the data set is 3-D, whether the data set contains significant 3-D information is another matter. It was stated in section 2.2 that to get a good 2-D model for the subsurface the data coverage must be 2-D as well. For a 2-D survey, measurements are made with different electrode spacings and at different horizontal locations to obtain such a 2-D coverage. However, the degree of data coverage needed before a data set can be considered “3-D” is less clear. Using the pole-pole survey as an example, the following classification system is proposed for 3-D data sets. They are listed in decreasing order of 3-D information content.

Category 1 - An ideal 3-D survey with the electrodes arranged in a rectangular grid, and with measurements in all possible directions (such as in Figure 8.2a), i.e. along the grid lines as well as at different angles to the grid lines. The SEPTIC.DAT data file is such an example of a “complete” 3-D data set. In this survey, 56 electrodes were arranged in an 8 by 7 grid and all the possible 1540 ($56 \times 55/2$) measurements were made.

Category 2 – The electrodes are arranged in a rectangular grid. All the measurements along the grid lines (i.e. in the x - and y -directions) but only a limited number of measurements at an angle to the grid lines (such as along the 45 degree diagonals for square grids as shown in Figure 8.2b) are made. The ROOTS7.DAT data file is such an example of a survey with limited measurements in the angular directions. In this case, the survey was carried out 49 electrodes in a 7 by 7 grid and 468 measurements were made. A “complete” 3-D data set would have 1176 measurements.

Category 3 – Measurements are only made in the two directions along the grid lines, i.e. in the x - and y -directions, and no measurements at an angle to the grid lines are made. This measurement sequence is frequently used when there are insufficient nodes in the multi-electrode system to cover the entire survey area at a single time. One possible measurement sequence is shown in Figure 8.11. The data for the sludge deposit field example (Dahlin and Bernstone 1997) in section 8.7.2 falls under this category.

Category 4 – Measurements in only one direction (for example the x -direction) along a series of parallel 2-D survey lines. This situation is common for data from old surveys, particularly IP surveys for mineral deposits. For this type of data set, a series of 2-D inversions is usually first carried out. The 3-D inversion is then used on a combined data set with the data from all the survey lines in an attempt to glean new information out of old data, and to see whether 3-

D effects are significant (i.e. whether the results from the 2-D inversions are valid). The success of the 3-D inversion partly depends on the spacing between the lines and the type of array used (section 8.2). As a general rule, the spacing between the lines should not be more than twice the unit electrode spacing along the lines.

While ideally the data should be of Category 1 or at least Category 2 so that some angular data is available, the RES3DINV program will also accept data that falls under Categories 3 and 4. The accuracy of the 3-D models obtained from the Categories 3 and 4 data types will be lower than the Categories 1 and 2 data types, and will greatly depend on the spacing between the lines and the type of array used. However, even for the Category 4 data type, the results from the 3-D inversion should provide a useful indicator on whether 3-D effects are significant. This can provide a check on the validity of the results obtained from independent 2-D inversions of the different survey lines.

8.6 A 3-D inversion program

3-D inversion of field data set can be carried out in a similar way using the smoothness-constrained least-squares method used for the 2-D inversion. One model used to interpret the 3-D data set is shown in Figure 8.13a. The subsurface is divided into several layers and each layer is further subdivided into a number of rectangular cells. A 3-D resistivity inversion program, RES3DINV, is used to interpret the data from 3-D surveys. This program attempts to determine the resistivity of the cells in the inversion model that will most closely reproduce the measured apparent resistivity values from the field survey. Within the RES3DINV program, the thickness of the layers can be modified by the user. An alternative model that can be used with the RES3DINV program is shown in Figure 8.13b. The second inversion model subdivides the top few layers by half in the horizontal directions. Since the resolution of the resistivity method decreases rapidly with depth, it has been found that subdividing the blocks is only beneficial for the top two layers only. In many cases, subdividing the top layer only is enough. By subdividing the cells, the number of model parameters and thus the computer time required to invert the data set can increase dramatically.

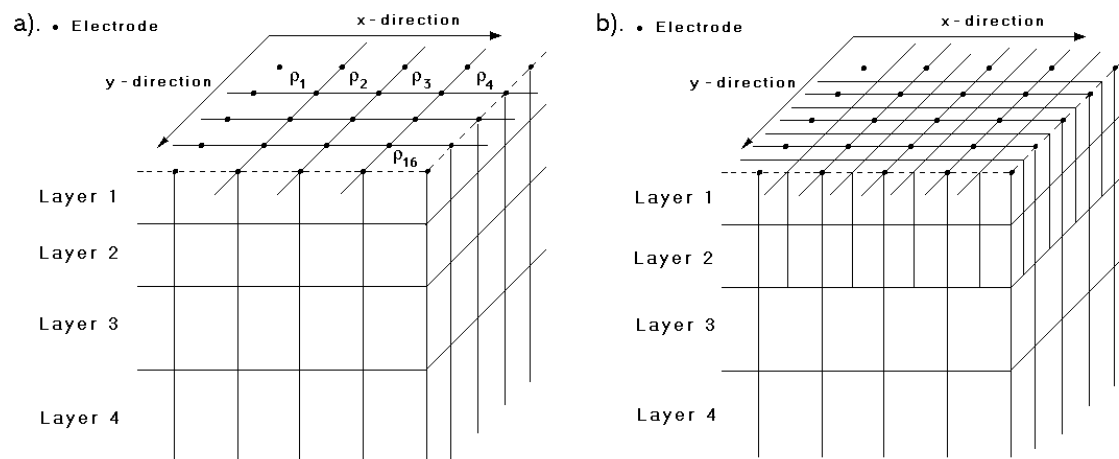


Figure 8.13. The models used in 3-D inversion. (a) Standard model where the widths of the rectangular cells are equal to the unit electrode spacings in the x - and y -directions. (b) A model where the model cells are divided in the horizontal direction.

Please refer to the instruction manual (RES3DINV.PDF) for the RES3DINV program for the data format. The set of files that comes with the RES3DINV program package has a number of field and synthetic data files. You can carry out an inversion of some of these files to get a feel of how the program works.

Exercise 8.2 : 3-D inversion examples

Data set and purpose	Things to try
PIPE3D.DAT – A field survey data file where a roll-along technique was used. The total grid size is 9 by 8.	(1). Read in the file, and then run the “Carry out inversion” step. (2). After that, take a look at the results using the “Display” window.
ROOTS7.DAT – A “cross-diagonal survey” data set using a 7 by 7 survey. ROOT7_REMOTE.DAT – The same data set with the location of the C2 and P2 electrodes included.	(1). Read in the file, and then invert the data set. (2). Try using the “Robust inversion” option, and see whether there is a significant change in the results. Try inverting this data file and see whether the remote electrodes have a significant effect of the results.
BLOCKS11T.DAT – A synthetic data set with topography. It has a 11 by 11 grid.	(1). Read in the file, and then invert the data set. (2). Invert again using the “Robust inversion” option.

8.7 Banding effects in 3-D inversion models

Many 3D field data sets are constructed by combining a series of parallel 2D survey lines. Ideally the distance between the lines should be about the same as the distance between adjacent electrodes in each line. However, in most cases, the distance between the lines can be two or more times larger than the inter-electrode spacing along the lines. This can lead to a ‘banding’ or ‘herring-bone’ effect with the structures aligned along the two axes of the survey grid, particularly if the l_1 -norm or blocky inversion method is used. Figure 8.14 shows several alternative models for a survey over the Vetlanda landfill site in Sweden that consists of 11 parallel 2D lines with 63 electrodes positions along each line (Rosqvist et al. 2009). The pole-dipole array was used. The spacing between the lines is twice the unit electrode spacing along the lines. Only the first 6 layers (that are most affected by the banding effect) of the inversion models are shown. The model using the standard inversion settings (Figure 8.14a) shows severe banding effects, particularly in the low resistivity zone in the top two layers. This is reduced, particularly in the topmost layer, by using a higher damping factor for the topmost layer (Figure 8.14b).

The normal horizontal roughness filter used has components in the x and y directions only (Figure 8.15a). Thus it has a tendency to produce structures aligned along the x and y directions. Since the model cells have sides that are aligned in the same direction as the survey grid lines, the structures in the inversion models tend to have edges that are aligned in the same directions as the survey lines. To reduce this effect, the roughness filter used is modified so that it has components in the diagonal directions (Farquharson 2008) as well in the x-y plane (Figure 8.15b). Figure 8.14c shows the inversion model produced when this modification is made to the horizontal roughness filter, while the vertical roughness filter is still only applied between the model cell and the cells immediately above and below it. The prominent banding effect in the low resistivity region in the top two layers of the model (Figure 8.14c) is greatly reduced using this horizontal diagonal filter.

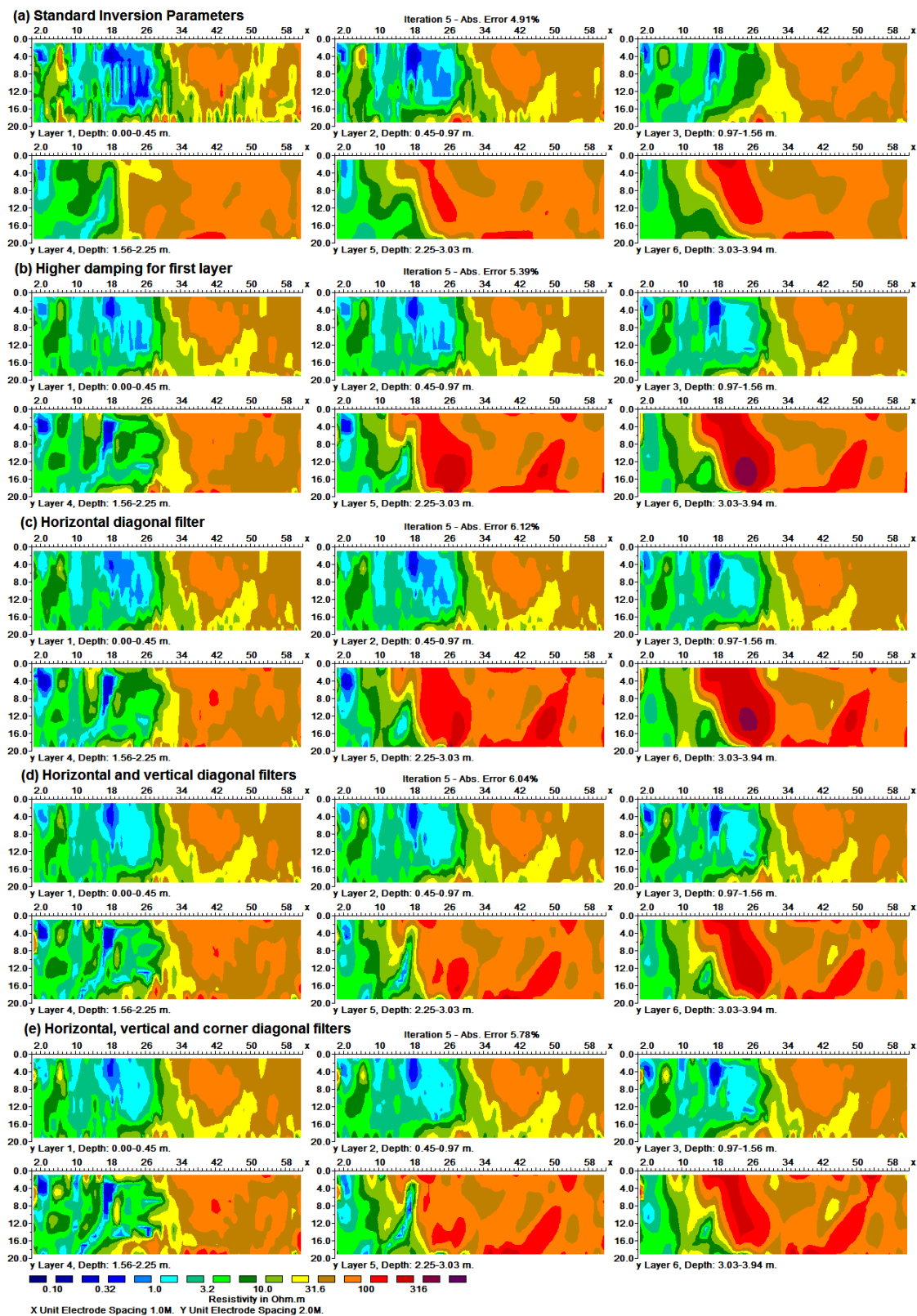


Figure 8.14. Inversion models for the Vetlanda landfill survey data set. (a) Using standard inversion settings. (b) With a higher damping factor for the topmost layer. (c) Using diagonal roughness filter in the horizontal (x - y) directions. (d) Using diagonal roughness filters in the vertical (x - z and y - z) directions as well. (e) Using the roughness filter in all directions.

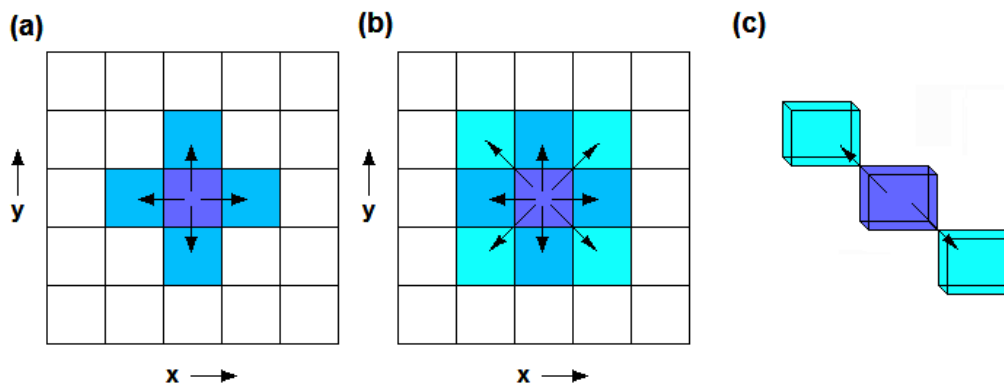


Figure 8.15. Types of 3-D roughness filters. (a) With components in the x - and y - directions only for the horizontal filter. (b) With components in the diagonal directions in the x - y plane for the horizontal filter. (c) Applying the roughness filter with the corner model cells as well. Only two (out of eight) corner cells are shown.

Applying the diagonal filter components in the horizontal direction but not in the vertical direction can lead to a bias (in the horizontal direction) in the shape of the structures produced. To remove this bias, the diagonal components are also applied to the vertical roughness filter as well in the x - z and y - z planes. The model produced with the diagonal components in the horizontal and vertical directions is shown in Figure 8.14d. The banding effect is no longer discernable in this model.

In the final model, the diagonal components for the roughness filter is also applied between the model cell and the cells adjacent to the corners of the cell (Figure 8.15c). Except for the cells at the surface, bottom and sides of the model grid, there are eight such corner neighboring cells surrounding each cell. The roughness filter is now applied between each interior model cell and all the 26 cells surrounding it. The resulting inversion model shown is in Figure 8.14e. In theory, this should reduce any bias in shape of the structures from the alignment of model cells grid (Farquharson 2008).

The model in Figure 8.14 has model cells with widths of 1 meter in the x direction and 2 meters in the y direction, i.e. elongated in the y direction. This is because the model discretization follows the spacing between the electrode positions. It is possible the banding in the y direction is partly caused by the model cells being elongated in the y direction. A possible alternative method to reduce the banding is to use model cells that are of the same widths in both directions, i.e. a selective model refinement in the y -direction. This doubles the number of model cells as well as the number of nodes in the finite-difference grid. Figure 8.16 shows the inversion models using cells of 1 meter length in both the x and y directions. The inversion model with the standard inversion settings (Figure 8.16a) does not exhibit the prominent banding in the y direction (Figure 8.14a). Instead there is a slight banding in the x direction in the top two layers with clustering of very low or high resistivity values along the survey lines. This feature is removed when a higher damping factor is used for the first layer (Figure 8.16b). The boundary of the low resistivity zone (marked by the light blue color) between x distances of 15 to 27 meters in the top three layers in this model shows a 'stepped' pattern aligned in the x or y direction. This is probably due to the use of a roughness filter with components in these directions (Figure 8.15a). This feature is removed when the roughness filter with diagonal components is used (Figure 8.15b) that does not bias the structure in the x and y directions (Figure 8.16c). The inversion model with the diagonal filter components in the z direction as well (Figure 8.16d) is also free of the 'stepped' boundary pattern.

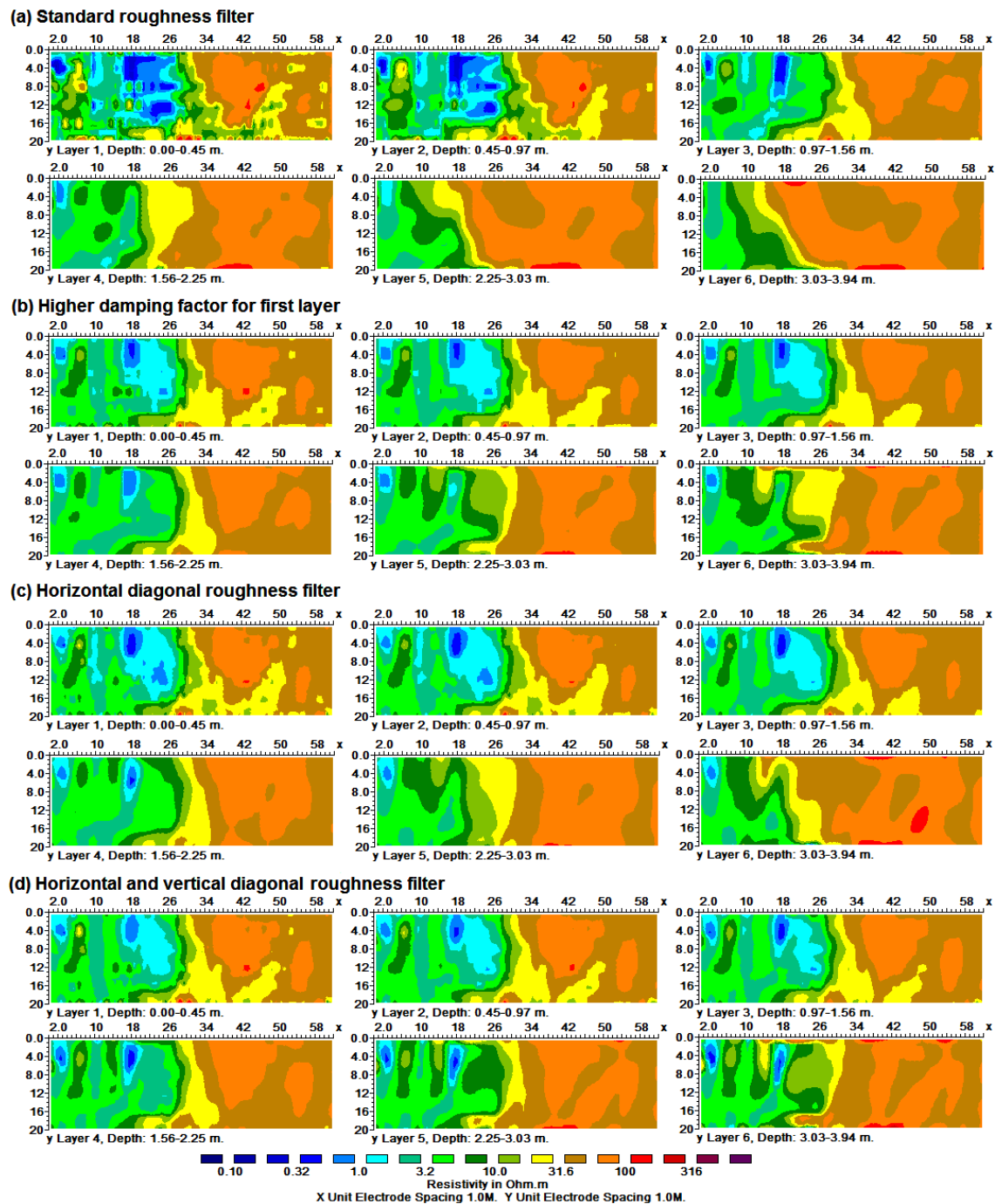


Figure 8.16. Inversion models for the Vetlanda landfill survey data set using model cells of equal lengths in the x - and y - directions. (a) Using standard inversion settings. (b) With a higher damping factor for the topmost layer. (c) Using diagonal roughness filter in the horizontal (x - y) directions. (d) Using diagonal roughness filters in the vertical (x - z and y - z) directions as well.

8.8 The use of long electrodes in 3-D surveys

It is normally assumed that the dimensions of the electrodes used are much smaller than the spacing between them so that they can be considered as ‘point’ electrodes. In some situations, the length of the electrode is sufficiently long such that it has to be taken into

account. One situation where this arises is when a metallic well casing is used as an electrode. The resistivity of the metal well casing is much lower than the surrounding medium, so the potential on the surface of the casing is essentially constant. The use of such ‘long’ electrodes has been the subject of several papers (Schenkel and Morrison, 1994; Singer and Strack, 1998; Ramirez et al., 2003; Daily et al., 2004). Many of these studies involve deep surveys where the measurements are made using the metal cased wells as electrodes. One situation of interest for environmental and engineering surveys is the use of both point and long electrodes in a survey where existing metal wells can be used as the long electrodes (Rucker et al., 2007). It is well known that well-to-well measurements involving vertical ‘long’ electrodes only have no vertical resolution. However, measurements between a ‘point’ and a ‘long’ electrode have some vertical resolution. It might even help when the long electrode extends below the target of interest.

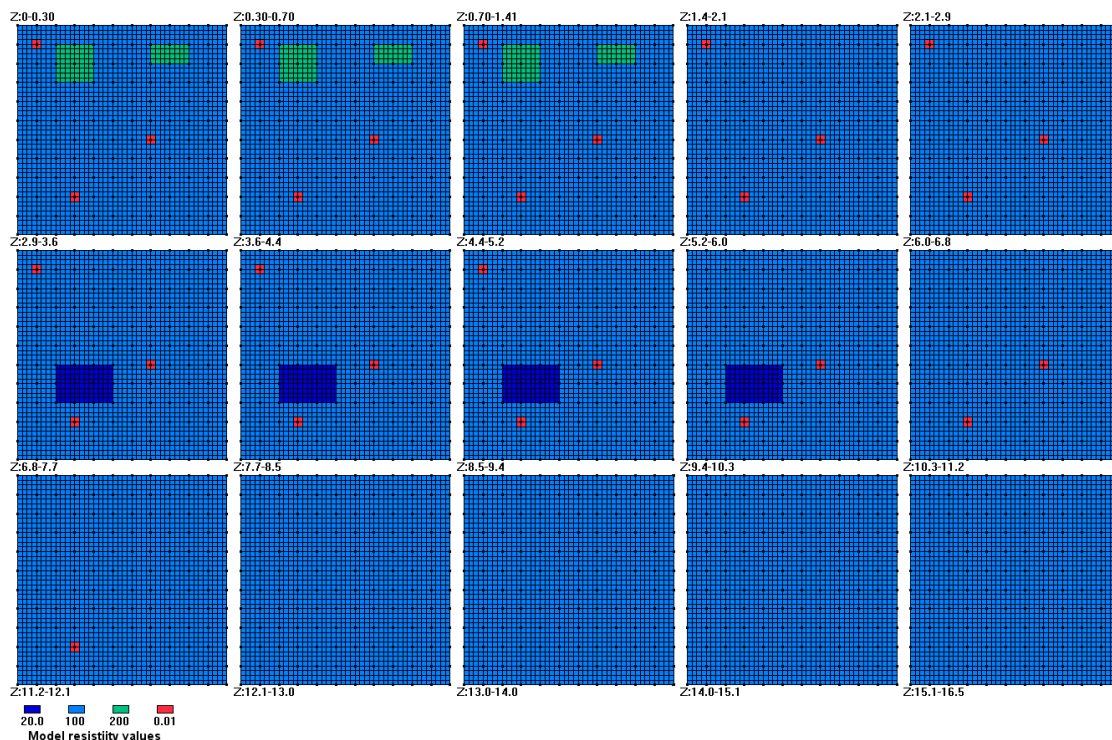


Figure 8.17. Synthetic model for long electrodes survey. 3-D model using cells of low resistivity ($0.01 \Omega\cdot\text{m}$) that are marked in red to simulate cased wells.

Figure 8.17 shows a model with a low resistivity block of $20 \Omega\cdot\text{m}$ at a depth of 2.9 to 6.0 meters. The maximum length of the block is 3 meter that is less than its average depth, thus it will be a difficult target for normal surveys with point electrodes on the surface. Figure 8.18a shows the inversion model for a pole-pole survey data set using the cross-diagonal measurement sequence (Figure 8.2b) using only point electrodes on the surface. Another data set was generated for the same model with three of the point electrodes converted into long electrodes. This was done by assigning a very low resistivity value to the cells around the point electrode, as marked by the red cells in Figure 8.17. Two of the long electrodes extend below the low resistivity block. The inversion model for the data set using the combination of point and long electrodes (Figure 8.18b) shows slightly better resolution for the low resistivity block. The lowest resistivity achieved in model is about $77 \Omega\cdot\text{m}$ (Figure 8.18a) which is lower than the value of $83 \Omega\cdot\text{m}$ achieved by the model for the data

set using only surface point electrodes (Figure 8.18a).

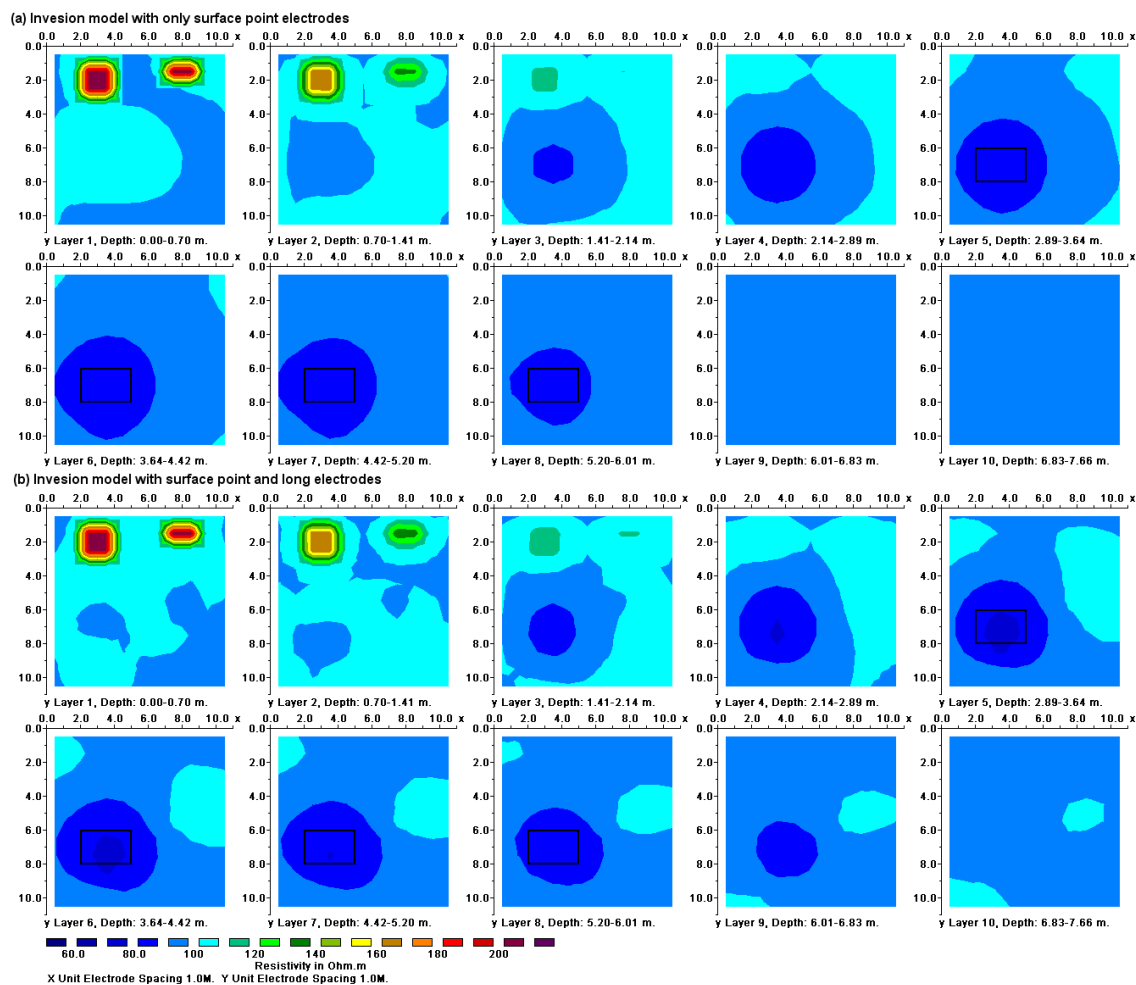


Figure 8.18. Comparison of inversion models using point electrodes with and without long electrodes. (a) Inversion model for pole-pole data set using only surface point electrodes. (b) Inversion model for pole-pole data set using 121 point and 3 long electrodes.

8.9 Examples of 3-D field surveys

In this section, we will take a look at the results from a couple of 3-D field surveys over areas with complex geology.

8.9.1 Birmingham field test survey - U.K.

This field test was carried out using a multi-electrode system with 50 electrodes commonly used for 2-D resistivity surveys. The electrodes are arranged in a 7 by 7 grid with a unit spacing of 0.5 meter between adjacent electrodes (Figure 8.19a). The two remote electrodes were placed at more than 25 meters from the grid to reduce their effects on the measured apparent resistivity values. To reduce the survey time, the cross-diagonal survey technique was used. The subsurface is known to be highly inhomogenous consisting of sands and gravels. Figure 8.19b shows the horizontal sections of the model obtained at the 6th iteration. The two high resistivity zones in the upper left quadrant and the lower right corner of Layer 2 are probably gravel beds. The two low resistivity linear features at the lower edge of Layer 1 are due to roots from a large sycamore tree just outside the survey area. The

vertical extent of the gravel bed is more clearly shown in the vertical cross-sections across the model (Figure 8.19c). The inverse model shows that the subsurface resistivity distribution in this area is highly inhomogeneous and can change rapidly within a short distance. In such a situation a simpler 2-D resistivity model (and certainly a 1-D model from conventional sounding surveys) would probably not be sufficiently accurate.

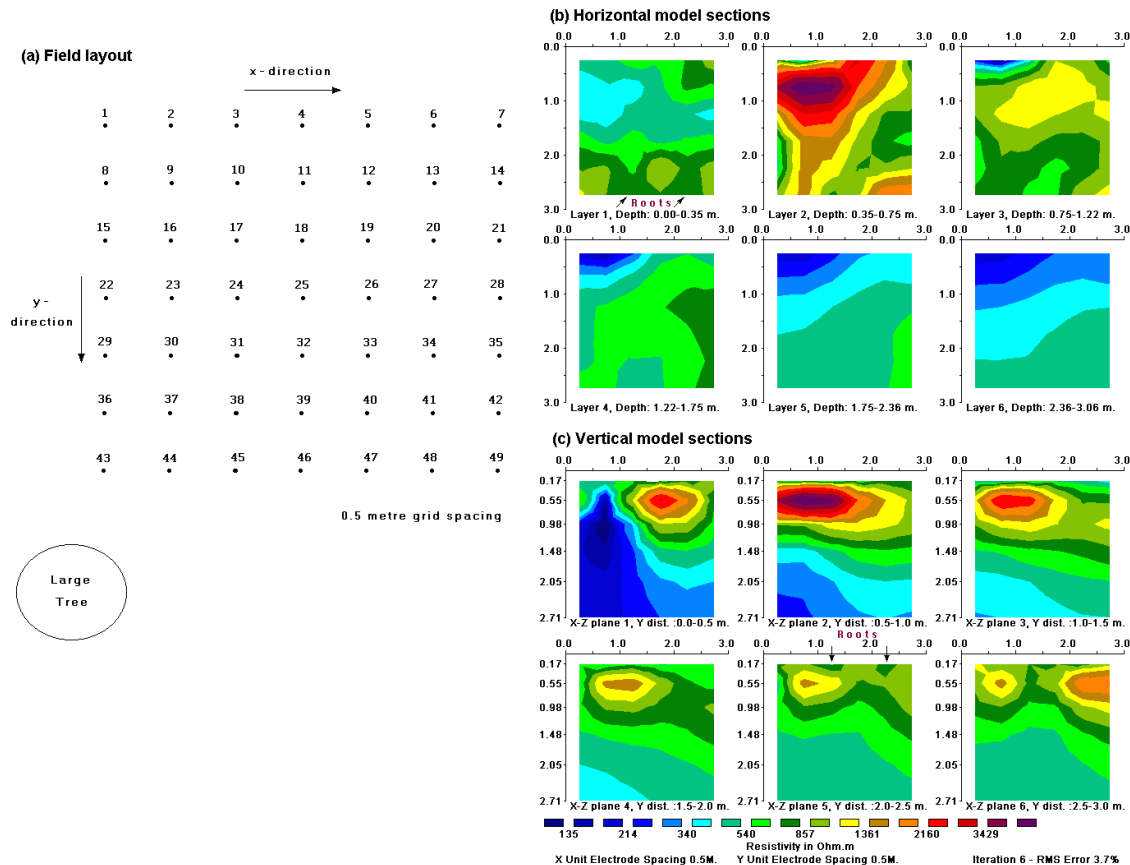


Figure 8.19. (a) Arrangement of electrodes in the Birmingham 3-D field survey. (b) Horizontal and (c) vertical cross-sections of the model obtained from the inversion of the Birmingham field survey data set. The location of observed tree roots on the ground surface are also shown.

8.9.2 Sludge deposit - Sweden

This survey covers a relatively large 21 by 17 grid by using a 3-D roll-along method (Dahlin and Bernstone 1997). To reduce the survey time, a number of parallel multi-electrode cables were used. This survey was carried out at Lernacken in Southern Sweden over a closed sludge deposit. Seven parallel multi-electrode cables were used to cover a 21 by 17 grid with a 5 meters spacing between adjacent electrodes. There were a total number of 3840 data points in this data set. In this survey, the cables were initially laid out in the x -direction, and measurements were made in the x -direction. After each set of measurements, the cables were shifted step by step in the y -direction until the end of the grid. In surveys with large grids, such as in this example, it is common to limit the maximum spacing for the measurements.

The maximum spacing is chosen so that the survey will map structures to the maximum depth of interest (section 2.5.2). In this case, the maximum spacing was 40 meters compared to the total length of 100 meters along a line in the x -direction. In this survey, the

cables were initially laid out in the x -direction, and measurements were made in the x -direction. After each set of measurements, the cables were shifted step by step in the y -direction until the end of the grid. In surveys with large grids, such as in this example, it is common to limit the maximum spacing for the measurements. The maximum spacing is chosen so that the survey will map structures to the maximum depth of interest (section 2.5.2). In this case, the maximum spacing was 40 meters compared to the total length of 100 meters along a line in the x -direction.

The model obtained from the inversion of this data set is shown in Figure 8.20. The former sludge ponds containing highly contaminated ground water show up as low resistivity zones in the top two layers (Dahlin and Bernstone 1997). This was confirmed by chemical analysis of samples. The low resistivity areas in the bottom two layers are due to saline water from a nearby sea. Figure 8.21 shows a 3-D view of the inversion model using the Slicer-Dicer 3-D contouring program. On a 200 MHz Pentium Pro computer, it took slightly over 4 hours to invert this data set. On newer computers with operating frequencies of 2 GHz or higher, and with multi-core 64-bit CPUs, the inversion time would probably be in minutes.

An interesting more recent 3-D survey over a landfill site is described in Chambers et al (2006).

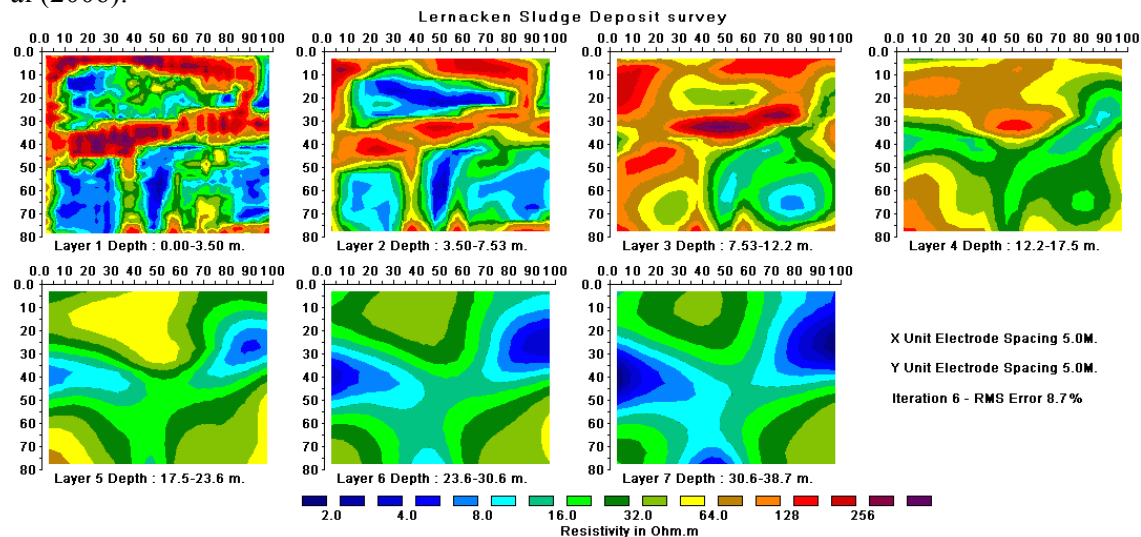


Figure 8.20. The 3-D model obtained from the inversion of the Lernacken Sludge deposit survey data set displayed as horizontal slices through the earth.

8.9.3 Copper Hill - Australia

This is an interesting example of a 3-D resistivity and IP survey provided by Arctan Services Pty. and Golden Cross Resources, Australia. Copper Hill is the oldest copper mine in NSW, Australia. An earlier survey was conducted in 1966 using mapping, rock chip sampling, an IP survey and 7 drill-holes (White et al. 2001). Copper porphyry with minor gold and palladium mineralization were found to occur in structurally controlled fractures and quartz veins. However, due to the very complex geology (Figure 8.22), large differences in ore grades were found in drill-holes that were less than 200 meters apart.

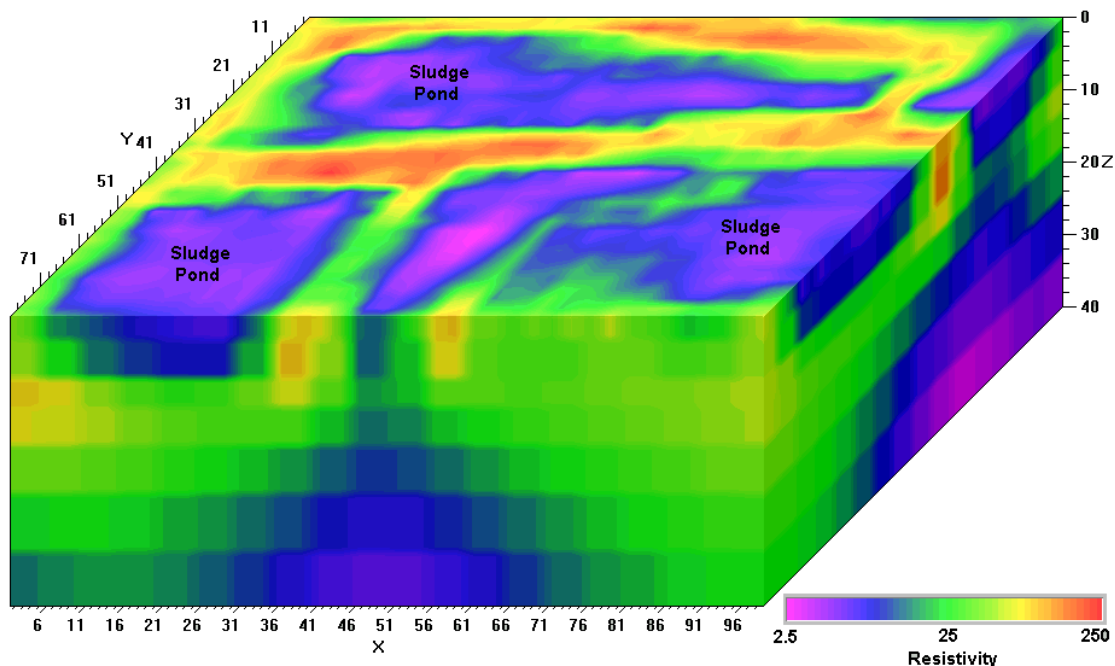


Figure 8.21. A 3-D view of the model obtained from the inversion of the Lernacken Sludge deposit survey data set displayed with the Slicer/Dicer program. A vertical exaggeration factor of 2 is used in the display to highlight the sludge ponds. Note that the color contour intervals are arranged in a logarithmic manner with respect to the resistivity.

To map the ore deposit more accurately, a new 3-D resistivity and IP survey using the pole-dipole array was used. The survey covered a large (1.6 x 1.1km) area using a series of 1.6 km lines with a spacing of 25m between adjacent electrodes. Figure 8.23 shows the arrangement of the transmitter and receiver lines. Currents of up to 7 Amps were used. The entire survey took 10 days giving a total of over 7000 measurements. Further details about the survey layout and procedures used to improve the data quality as well as to reduce the survey time are described in the paper by Denne et al. (2001). A copy of the paper can be downloaded from the www.arctan.com.au web site. Other interesting information about the mineralization at the Copper Hill area is available at the Golden Cross Resources Ltd. www.reflections.com.au/GoldenCross/ web site.

The data was inverted with the RES3DINV program that produced a 3-D resistivity as well as a 3-D IP model for the area. The 3-D IP model that shows the location of the mineralized zones more clearly is shown in Figure 8.24. The inversion model output from the RES3DINV program was rearranged into a VRML format that could be read by a 3-D visualization program (please contact Arctan Services for the details) that enables the user to display the model from any direction.

The 3D IP model in Figure 8.24 shows two en-echelon north-south trends and two approximately east-west trends forming an annular zone of high chargeability. The results from existing drill-holes that had targeted the shallower part of the western zone agree well with the resistivity and IP model. A drill-hole, CHRC58, intersected a 217m zone with 1.7 g/t gold and 0.72% copper coincided well an IP zone of greater than 35mV/V. The lower boundary of the western zone with high chargeability coincides well with low assay results from existing drill-holes. The eastern zone with high chargeability and resistivity values do not outcrop on the surface and very little drilling has penetrated it. Further surveys, including drilling, is presently being carried out.

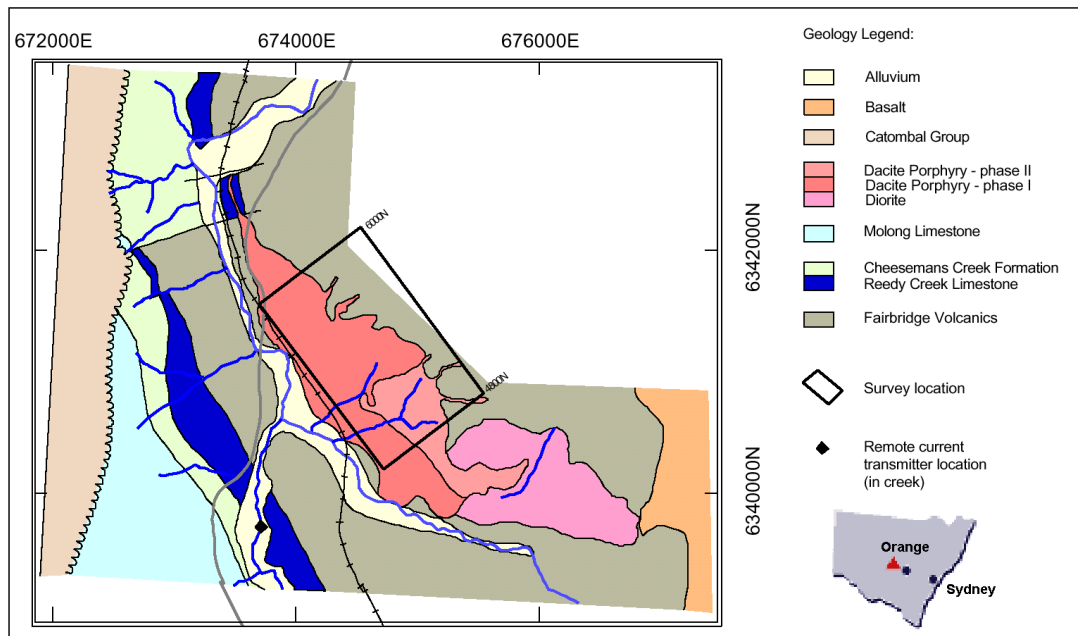


Figure 8.22. Geological map of the Copper Hill area (Chivas and Nutter 1975, White et al. 2001).

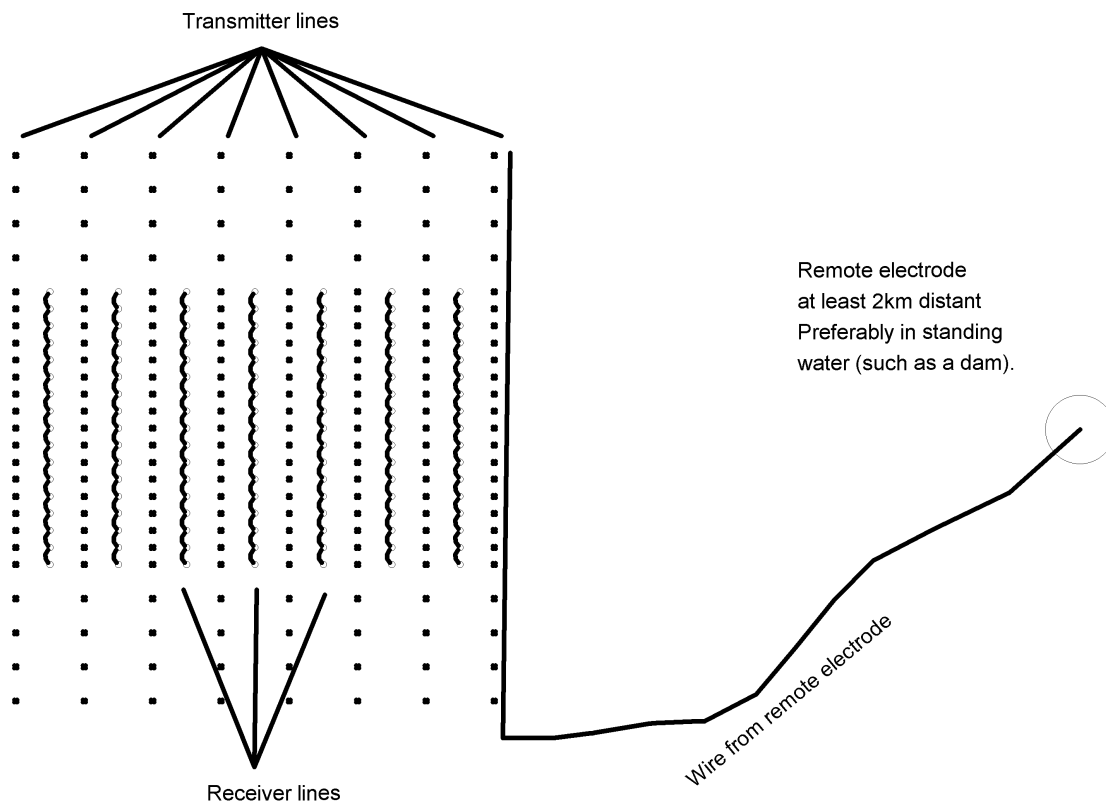


Figure 8.23. Electrodes layout used for the 3-D survey of the Copper Hill area (White et al. 2001).

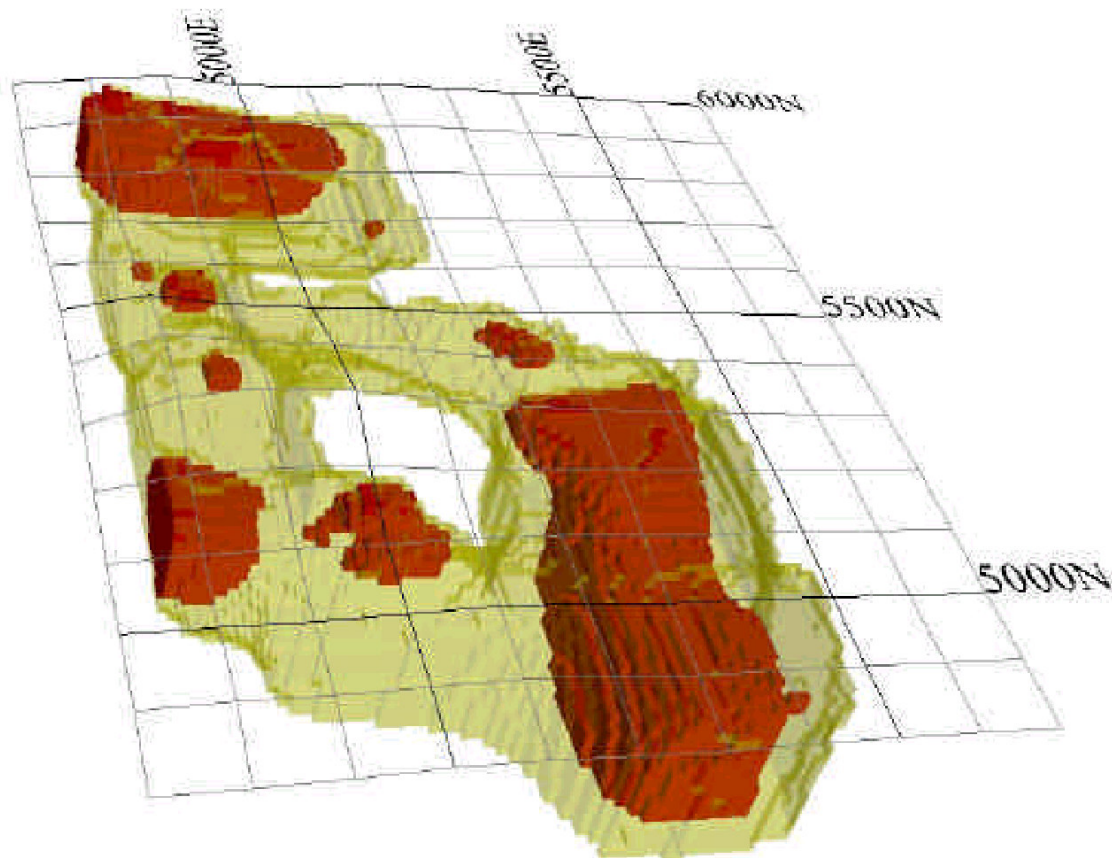


Figure 8.24. The IP model obtained from the inversion of the Copper Hill survey data set. Yellow areas have chargeability values of greater than 35 mV/V, while red areas have chargeability values of greater than 45 mV/V (White et al. 2001).

8.9.4 Athabasca Basin – Canada

With recent high oil prices, and concerns about global warming, nuclear power generation has enjoyed a small revival. This has sparked an increase in uranium ore prices, and a small boom in uranium exploration. The Athabasca basin in northern Saskatchewan (Figure 8.25) has over 30 deposits and it is the richest uranium region in the world. It produces about 21% of the world's uranium (Raemakers et al. 2006). The uranium ore is typically found in sandstones overlying metamorphic basement where it fills reactivated fault zones. The objective of the surveys is to detect the low resistivity alteration zone associated with the uranium deposit (Figure 8.26). The survey area is a challenging environment with dry surface sand with a very thin humus layer that makes good electrical contact difficult. With temperatures of minus 40°C in winter, laying out long survey lines to achieve the required depth penetration of more than 500 metres require tremendous efforts. The example in this section comes from Bingham et al. (2006) where some interesting choices were made in the survey design. The pole-pole array was used to reach the required depth of penetration with the limited survey line lengths that were available. While the pole-pole array has the poorest resolution (for depths within reach of the other arrays), here it is choice between POOR resolution or NO resolution at depths of up to 700 m. Figure 8.27 shows an example of one of the survey results for the resistivity at a depth of about 200 meters. A 3-D data set was constructed by collating data from parallel 2D survey lines. The inversion model shows a prominent narrow low resistivity zone that corresponds to the alteration zone.

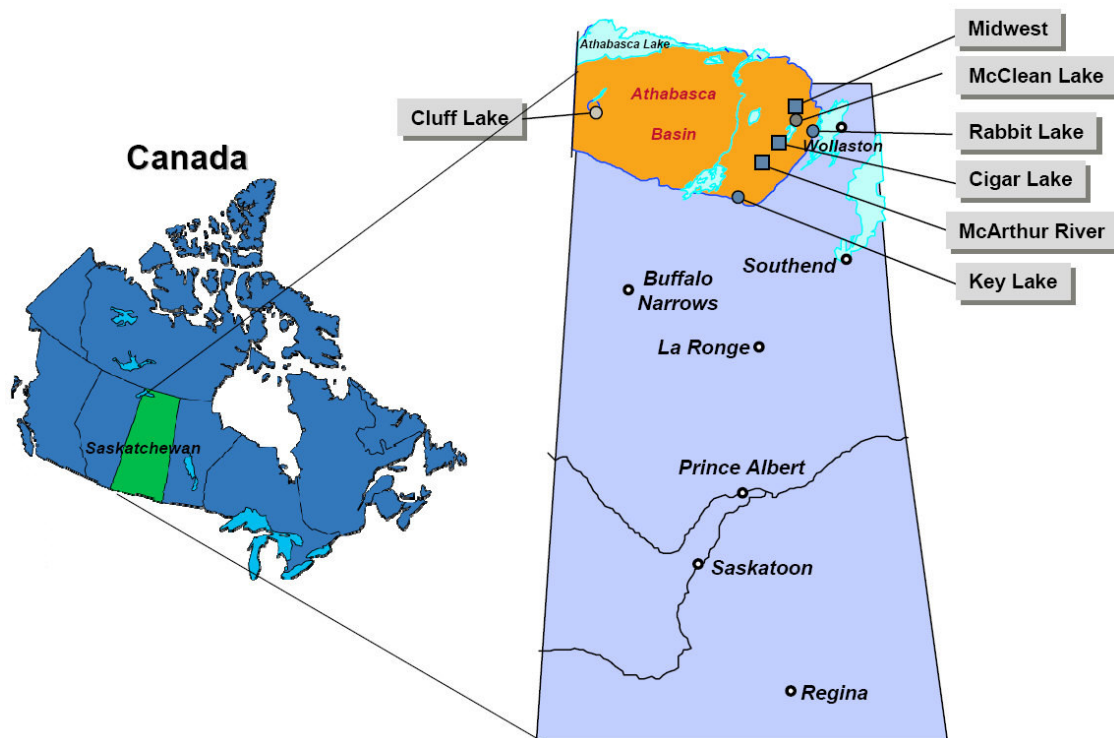


Figure 8.25. Location of uranium mines in the Athabasca basin, Saskatchewan (Bingham et al., 2006).

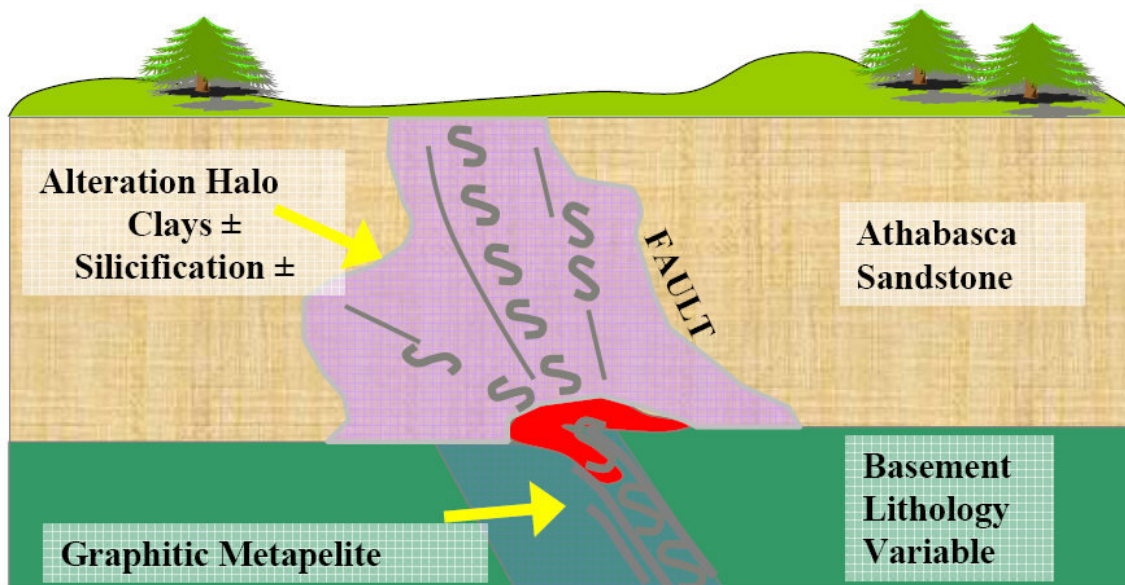


Figure 8.26. Geological model of uranium deposit (Bingham et al., 2006).

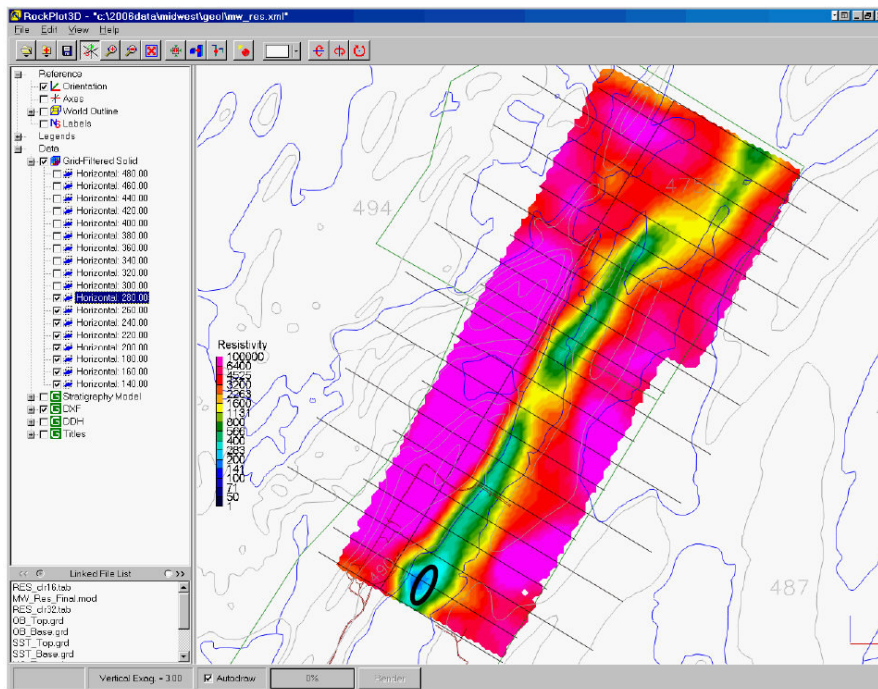


Figure 8.27. Example of inversion model from the Midwest deposit area showing the resistivity at a depth of about 200 meters (Bingham et al., 2006).

The advantages and disadvantages of the pole-pole array is a matter of some debate, particularly for deep surveys. Besides deep uranium surveys, it has also been used for other mineral surveys by some companies (see for example the www.geofisicos.com.pe web site). While there are many advocates of this array, others point out to its poor resolution compared to other arrays (assuming these arrays used a sufficient long survey line to get the same penetration depth). The pole-pole array offers field advantages of much shorter measurement arrays and the ability to penetrate deeper than any other array for the same survey line length, although there is the extra effort of maintaining two infinities (David Bingham, pers. comm., 2009). The pole-dipole array has also been used for uranium exploration in the Athabasca basin, and the 2-D and 3-D resistivity surveys played a significant role in the discovery of a very large deposit (Donald Carriere, pers. comm., 2009) at Wheeler River near the existing McArthur River deposit.

A characteristic feature of 3-D surveys is the large number of electrode positions and measurements. To achieve a sufficiently wide coverage, commercial surveys are usually carried out using a series of 2D parallel lines using multi-channel systems. For fast computer inversion of very large survey grids, a multi-core CPU with at least a few GBs of RAM is needed. Recent advances in both software and hardware have now made 3D surveys and computer modeling within reach of small service companies. The future probably lies in parallel survey techniques (using multi-channel systems) and parallel computing techniques (using multi-core CPUs). The new 64-bit versions of Windows have greatly increased the amount of usable RAM (in theory up to 128 GB, but in practice 16 to 24 GB on most modern PCs) and consequently the size of the data sets that can be processed. The limiting factor now is the computer processing time. This challenge will be met by future 8-core and 16-core CPUs (and GPUs with hundreds of cores) together with innovative programming techniques to extract the maximum performance from the available computer hardware (Loke and Wilkinson, 2009).

Acknowledgments

Dr. Torleif Dahlin of Lund University in Sweden kindly provided the Odarslov Dyke, Lernacken and Vetlanda data sets. The Grundfor data set was provided by Dr. Niels B. Christensen of the University of Aarhus in Denmark and Dr. Torleif Dahlin. The Rathcroghan data set was kindly provided by Dr. Kevin Barton and Dr. Colin Brown from data collected by the Applied Geophysics Unit of University College Galway, Ireland. Many thanks to Richard Cromwell and Rory Retzlaff of Golder Assoc. (Seattle) for the survey example to map holes in a clay layer. Dr. Andrew Binley of Lancaster University kindly provided the interesting cross-borehole data set. The Bauchi data set was provided by Dr. Ian Acworth of the University of New South Wales, Australia. The Redas river survey data set was kindly provided by Jef Bucknix of Sage Engineering, Belgium. Mr. Julian Scott and Dr. R.D. Barker of the School of Earth Sciences, University of Birmingham provided the Clifton, the Tar Works and the 3-D Birmingham survey data sets. Slicer/Dicer is a registered trademark of Visualogic Inc. I would like to thank Paul Bauman and WorleyParsons Canada for permission to use the figures for the Athabasca oil sands case history. I would like to thank David Bingham and Grant Nimeck of Areva Resources Canada Inc. for permission to use the figures for the Athabasca uranium deposit case history. Last, but not least, permission from Arctan Services Pty. and Gold Cross Resources to use the Copper Hill 3-D example is gratefully acknowledged.

References

- Acworth, R.I., 1981. The evaluation of groundwater resources in the crystalline basement of Northern Nigeria. Ph.D. thesis, Univ. of Birmingham.
- Acworth, R. I., 1987, The development of crystalline basement aquifers in a tropical environment: Quarterly Journal Engineering Geology, **20**, 265-272.
- Alumbaugh, D.L. and Newman, G.A., 2000. Image appraisal for 2-D and 3-D electromagnetic inversion. Geophysics, **65**, 1455-1467.
- Auken, E., and Christiansen, AV., 2004. Layered and laterally constrained 2D inversion of resistivity data. Geophysics, **69**, 752-761.
- Barker, R.D., 1978. The offset system of electrical resistivity sounding and its use with a multicore cable. Geophysical Prospecting, **29**, 128-143.
- Barker, R.D., 1991. Depth of investigation of collinear symmetrical four-electrode arrays. Geophysics, **54**, 1031-1037.
- Barker R.D., 1992. A simple algorithm for electrical imaging of the subsurface. First Break **10**, 53-62.
- Barker R.D., 1996. The application of electrical tomography in groundwater contamination studies. EAGE 58th Conference and Technical Exhibition Extended Abstracts, P082.
- Barker, R. and Moore, J., 1998. The application of time-lapse electrical tomography in groundwater studies. The Leading Edge, **17**, 1454-1458.
- Bauman, P., 2005. 2-D resistivity surveying for hydrocarbons – A primer. CSEG Recorder, April, 25-33.
- Bernstone, C. and Dahlin, T., 1999. Assessment of two automated electrical resistivity data acquisition systems for landfill location surveys : Two case histories. Journal of Environmental and Engineering Geophysics, **4**, 113-122.
- Bingham, D., Nimeck, G., Wood, G. and Mathieson, T., 2006. 3D resistivity in the Athabasca basin with the pole-pole array. 1 day workshop - Geophysical methods and techniques applied to uranium exploration. SEG Annual General Meeting 2006, New Orleans.
- Carpenter, E.W. and Habberjam, G.M., 1956. A tri-potential method of resistivity prospecting. Geophysical Prospecting, **29**, 128-143.
- Chambers , J.E., Kuras, O., Meldrum, P.I., Ogilvy, R.O. and Hollands, J., 2006. Electrical resistivity tomography applied to geologic, hydrogeologic, and engineering investigations at a former waste-disposal site. Geophysics, **71**, B231-B239.
- Chambers J E, Wilkinson P B, Weller A L, Ogilvy R D, Meldrum P I, and Caunt, S, 2007. Mineshaft imaging using surface and crosshole 3D electrical resistivity tomography: A case history from the East Pennine Coalfield, UK. Journal of Applied Geophysics, **62**, 324-337.
- Chivas, A.R. and Nutter, A.H., 1975. Copper Hill porphyry-copper prospect. Knight, S.L. (ed.), Economic geology of Australia and Papua New Guinea vol. I. Metals: Australasian Institute of Mining and Metallurgy Monograph No. 5, p. 716-720.
- Christensen N.B. and Sorensen K.I., 1994. Integrated use of electromagnetic methods for hydrogeological investigations. Proceedings of the Symposium on the Application of Geophysics to Engineering and Environmental Problems, March 1994, Boston, Massachusetts, 163-176.
- Claerbout, J.F. and Muir, F., 1973. Robust modeling with erratic data. Geophysics, **38**, 826-844.
- Constable, S.C., Parker, R.L. and Constable, C.G., 1987. Occam's inversion : A practical algorithm for generating smooth models from electromagnetic sounding data. Geophysics, **52**, 289-300.
- Dahlin, T., 1996. 2D resistivity surveying for environmental and engineering applications.

- First Break, **14**, 275-284.
- Dahlin, T., 2000. Short note on electrode charge-up effects in DC resistivity data acquisition using multi electrode arrays. *Geophysical Prospecting*, **48**, 181-187.
- Dahlin, T. and Bernstone, C., 1997. A roll-along technique for 3D resistivity data acquisition with multi-electrode arrays, *Procs. SAGEEP'97 (Symposium on the Application of Geophysics to Engineering and Environmental Problems)*, Reno, Nevada, March 23-26 1997, vol 2, 927-935.
- Dahlin, T. and Loke, M.H., 1997. Quasi-3D resistivity imaging-mapping of three dimensional structures using two dimensional DC resistivity techniques. *Proceedings of the 3rd Meeting of the Environmental and Engineering Geophysical Society*. 143-146.
- Dahlin, T. and Loke, M.H., 1998. Resolution of 2D Wenner resistivity imaging as assessed by numerical modelling, *Journal of Applied Geophysics*, **38**, 237-249.
- Dahlin, T. and Owen, R., 1998. Geophysical investigations of alluvial aquifers in Zimbabwe. *Proceedings of the IV Meeting of the Environmental and Engineering Geophysical Society (European Section)*, Sept. 1998, Barcelona, Spain, 151-154.
- Dahlin, T. and Zhou, B., 2004. A numerical comparison of 2D resistivity imaging with ten electrode arrays, *Geophysical prospecting*, **52**, 379-398.
- Dahlin, T. and Zhou, B., 2006. Gradient array measurements for multi-channel 2D resistivity imaging, *Near Surface Geophysics*, **4**, 113-123.
- Daily, W. and Owen, E., 1991. Cross-borehole resistivity tomography. *Geophysics*, **56**, 1228-1235.
- Daily, W., Ramirez, A., Newmark, R. and Masica, K., 2004. Low-cost reservoir tomographs of electrical resistivity. *The Leading Edge*, May 2007, 272-280.
- Daniels F. and Alberty R.A., 1966. *Physical Chemistry*. John Wiley and Sons, Inc.
- deGroot-Hedlin, C. and Constable, S., 1990. Occam's inversion to generate smooth, two-dimensional models from magnetotelluric data. *Geophysics*, **55**, 1613-1624.
- Dey A. and Morrison H.F. 1979a. Resistivity modelling for arbitrary shaped two-dimensional structures. *Geophysical Prospecting* **27**, 106-136.
- Dey A. and Morrison H.F., 1979b. Resistivity modeling for arbitrarily shaped three-dimensional shaped structures. *Geophysics* **44**, 753-780.
- Edwards L.S., 1977. A modified pseudosection for resistivity and induced-polarization. *Geophysics*, **42**, 1020-1036.
- Ellis, R.G. and Oldenburg, D.W., 1994a, *Applied geophysical inversion: Geophysical Journal International*, **116**, 5-11.
- Ellis, R.G. and Oldenburg, D.W., 1994b. The pole-pole 3-D DC-resistivity inverse problem : a conjugate gradient approach. *Geophys. J. Int.*, **119**, 187-194.
- Farquharson, C.G., 2008. Constructing piecewise-constant models in multidimensional minimum-structure inversions. *Geophysics*, **73**, K1-K9.
- Fox, R.C., Hohmann, G.W., Killpack, T.J. and Rijo, L., 1980, Topographic effects in resistivity and induced polarization surveys. *Geophysics*, **45**, 75-93.
- Griffiths, D.H. and Turnbull, J., 1985. A multi-electrode array for resistivity surveying. *First Break* **3** (No. 7), 16-20.
- Griffiths D.H., Turnbull J. and Olayinka A.I. 1990, Two-dimensional resistivity mapping with a computer- controlled array. *First Break* **8**, 121-129.
- Griffiths D.H. and Barker R.D., 1993. Two-dimensional resistivity imaging and modelling in areas of complex geology. *Journal of Applied Geophysics*, **29**, 211-226.
- Gerard, R. and Tabbagh, A., 1991. A mobile four electrodes array and its application to electrical survey of planetary grounds at shallow depths. *J. Geophys. Res.*, **96** (B-3),

- 4117-4123.
- Golub, G.H. and van Loan, C.F., 1989. Matrix computations. The John Hopkins Un. Press.
- Hallof, P.G., 1990. Reconnaissance and detailed geophysical results, Granite Mountain Area Pershing County, Nevada. in Fink, J.B., McAlister, E.O., Sternberg, B.K., Wieduwilt, W.G. and Ward, S.H. (Eds), 1990, Induced polarization : Applications and case histories : Investigations in Geophysics No. 4, SEG, 325-353.
- Holcombe, J. and Jirack, G., 1984. 3-D terrain corrections in resistivity surveys. *Geophysics*, **49**, 439-452.
- Inman, J.R., 1975. Resistivity inversion with ridge regression. *Geophysics*, **40**, 798-817.
- Johansson, S. and Dahlin, T., 1996. Seepage monitoring in an earth embankment dam by repeated resistivity measurements. *European Journal of Engineering and Geophysics*, **1**, 229-247.
- Keller G.V. and Frischknecht F.C., 1966. Electrical methods in geophysical prospecting. Pergamon Press Inc., Oxford.
- Kellett, R.L. and Bauman, P.D., 1999. Electrical resistivity imaging of oil sand horizons : A modern slant on an old technique. Komex International Ltd.
- Koefoed O., 1979. Geosounding Principles 1 : Resistivity sounding measurements. Elsevier Science Publishing Company, Amsterdam.
- LaBrecque, D.J., Miletto, M., Daily, W., Ramirez, A. and Owen, E., 1996. The effects of noise on Occam's inversion of resistivity tomography data. *Geophysics*, **61**, 538-548.
- Li Y. and Oldenburg D.W. 1992. Approximate inverse mappings in DC resistivity problems. *Geophysical Journal International* **109**, 343-362.
- Lines L.R. and Treitel S. 1984. Tutorial : A review of least-squares inversion and its application to geophysical problems. *Geophysical Prospecting*, **32**, 159-186.
- Loke, M.H., 1994. The inversion of two-dimensional resistivity data. Unpubl. PhD thesis, Un. Of Birmingham.
- Loke, M.H., 1999. Time-lapse resistivity imaging inversion. Proceedings of the 5th Meeting of the Environmental and Engineering Geophysical Society European Section, Em1.
- Loke, M.H., 2000. Topographic modelling in resistivity imaging inversion. 62nd EAGE Conference & Technical Exhibition Extended Abstracts, D-2.
- Loke, M.H. and Barker, R.D., 1995. Least-squares deconvolution of apparent resistivity pseudosections. *Geophysics*, **60**, 1682-1690.
- Loke M.H. and Barker R.D., 1996a. Rapid least-squares inversion of apparent resistivity pseudosections using a quasi-Newton method. *Geophysical Prospecting*, **44**, 131-152.
- Loke M.H. and Barker R.D., 1996b. Practical techniques for 3D resistivity surveys and data inversion. *Geophysical Prospecting*, **44**, 499-523.
- Loke, M.H. and Dahlin, T., 2002. A comparison of the Gauss-Newton and quasi-Newton methods in resistivity imaging inversion. *Journal of Applied Geophysics*, **49**, 149-162.
- Loke, M.H. and Wilkinson, P., 2009. Rapid parallel computation of optimised arrays for electrical imaging surveys. 15th European Meeting of Environmental and Engineering Geophysics, Dublin, Ireland
- Maescot, L. and Loke, M.H., 2003. Using the depth of investigation index method in 2D resistivity imaging for civil engineering surveys. SAGEEP 2003. Denver, USA.
- McGillivray, P.R. and Oldenburg, D.W., 1990. Methods for calculating Frechet derivatives and sensitivities for the non-linear inverse problem : A comparative study. *Geophysical Prospecting*, **38**, 499-524.
- Menke, W., 1984. Geophysical data analysis : Discrete inverse theory. Academic Press Inc.
- Merrick, N.P., 1997. A new resolution index for resistivity electrode arrays. *Exploration*

- Geophysics, **28**, 106-109.
- Nelson, G.D. and Van Voorhis, G.D., 1973, Letter to the editor regarding the paper "Complex resistivity spectra of porphyry copper mineralization". Geophysics, **38**, 984.
- Niederleithinger, E., 1994, Use of high resolution geomagnetics, 2D-DC-geoelectrics and induced polarisation in environmental investigations. Paper presented at SAGEEP '94, Boston, USA.
- Nimmer, R. E., Osiensky, J. L., Binley, A. M. & Williams, B. C. (2008) Three-dimensional effects causing artifacts in two-dimensional, cross-borehole, electrical imaging. *Journal of Hydrology*, 359, 59-70.
- Nyquist, J.E., Bradley, J.C. and Davis, R.K., 1999. DC resistivity monitoring of potassium permanganate injected to oxidize TCE in situ. *Journal of Environmental & Engineering Geophysics*, **4**, 135-148.
- Olivar, A., de Lime, L. and Sharma, M.M., 1990. A grain conductivity approach to shaly sandstones. *Geophysics*, **55**, 1347-1356.
- Olayinka, A.I. and Yaramanci, U., 2000, Use of block inversion in the 2-D interpretation of apparent resistivity data and its comparison with smooth inversion: *Journal of Applied Geophysics*, **45**, 63-82.
- Oldenborger, G.A., Routh, P.S. and Knoll, M.D., 2005. Sensitivity of electrical resistivity tomography data to electrode position errors. *Geophys. J. Int.*, **163**, 1-9.
- Oldenburg, D.W. and Li, Y., 1999. Estimating depth of investigation in dc resistivity and IP surveys. *Geophysics*, **64**, 403-416.
- Park, S.K. and Van, G.P. 1991. Inversion of pole-pole data for 3-D resistivity structures beneath arrays of electrodes. *Geophysics*, **56**, 951-960.
- Pazdirek, O. and Blaha, V., 1996. Examples of resistivity imaging using ME-100 resistivity field acquisition system. EAGE 58th Conference and Technical Exhibition Extended Abstracts, Amsterdam.
- Panissod, C., Dabas, M., Hesse, A., Jolivet, A., Tabbagh, J. and Tabbagh, A., 1998. Recent developments in shallow depth electrical and electrostatic prospecting using mobile arrays. *Geophysics*, **65**, 1542-1550.
- Pelton, W.H., Ward, S.H., Hallof, P.G., Sill, W.R. and Nelson, P.H., 1978. Mineral discrimination and the removal of inductive coupling with multifrequency IP. *Geophysics*, **43**, 588-609.
- Ramaekers, P., Thomas, D., Cutts, C., Gandhi, S., Delaney, G. and Olson, R., 2006. Unconformity associated uranoim deposits. 1 day workshop - Geophysical methods and techniques applied to uranium exploration. SEG Annual General Meeting 2006, New Orleans.
- Ramirez, A., Newmark, R. and Daily, W., 2003. Monitoring carbon dioxide floods using electrical resistance tomography (ERT) : Sensitivity studies. *Journal of Environmental and Engineering Geophysics*, **8**, 187-208.
- Ritz, M., Parisot, J.-C., Diouf, S., Beauvais, A. and Dione, F., 1999. Electrical imaging of lateritic weathering mantles over granitic and metamorphic basement of eastern Senegal, West Africa. *Journal of Applied Geophysics*, **41**, 335-344.
- Rosqvist, R., Leroux, V., Dahlin, T., Svensson, M., Månsson, C-H. and Lindsjö, M., 2009. Detektering av gas i deponier med resistivitet (in Swedish), Rapport SGC 208-1102-7371, ISRN SGC-R-208-SE, Svenskt Gastekniskt Center, Malmö, 66p.
- Roy, A. and Apparao, A, 1971. Depth of investigation in direct current methods. *Geophysics*, **36**, 943-959.
- Rucker, D.F., Levin, M.T. and Myers, D.A., 2007. Imaging beneath Hanford's Tank Farms

- with electrical resistivity geophysics - An innovative approach. WM '07 Conference, Feb. 25-March 1, 2007, Tuscon, AZ.
- Sasaki, Y. 1992. Resolution of resistivity tomography inferred from numerical simulation. *Geophysical Prospecting*, **40**, 453-464.
- Scott, J.B.T., Barker, R.D. Peacock, S., 2000. Combined seismic refraction and electrical imaging. *Procs. 6th Meeting of the European Association for Environmental and Engineering Geophysics*, 3-7 Sept. 1997, Bochum, Germany, EL05.
- Seaton, W.J. and Burbey, T.J., 2000. Aquifer characterization in the Blue Ridge physiographic province using resistivity profiling and borehole geophysics : Geologic analysis. *Journal of Environmental & Engineering Geophysics*, **5**, no. 3, 45-58.
- Schenkel, C.J. and Morrison, H.F., 1994. Electrical resistivity measurement through metal casing. *Geophysics*, **59**, 1072-1082.
- Shima, H., 1992. 2-D and 3-D resistivity imaging reconstruction using crosshole data. *Geophysics*, **55**, 682-694.
- Shima, H., Sakashita, S. and Kobayashi, T., 1996. Developments of non-contact data acquisition techniques in electrical and electromagnetic explorations. *Journal of Applied Geophysics*, **35**, 167-173.
- Silvester P.P. and Ferrari R.L., 1990. *Finite elements for electrical engineers* (2nd. ed.). Cambridge University Press.
- Smith, T., Hoversten, M., Gasperikova, E. and Morrison, F., 1999. Sharp boundary inversion of 2D magnetotelluric data. *Geophysical Prospecting*, **47**, 469-486.
- Singer, B.S. and Strack, K.M., 1998. New aspects of through-casing resistivity theory, *Geophysics*, **63**, 52-63.
- Slater, L., Binley, A.M., Zaidman, M.D. and West, L.J., 1997, Investigation of vadose zone flow mechanisms in unsaturated chalk using cross-borehole ERT. *Proceedings of the EEGS European Section 3rd Meeting*, Aarhus, Denmark, 17-20.
- Slater, L., Binley, A.M., Daily, W. and Johnson, R., 2000. Cross-hole electrical imaging of a controlled saline tracer injection. *Journal of Applied Geophysics*, **44**, 85-102.
- Sorensen, K.I., 1994: The Ellog auger drilling method. *Proceedings of the symposium on the application of geophysics to engineering and environmental problems*, Boston, Massachusetts. - *Environmental and Engineering Geophysical Society*, 985-994.
- Sorenson, K., 1996. Pulled Array Continuous Profiling. *First Break*, **14**, 85-90.
- Spiegel, R.J., Sturdivant, V.R. and Owen, T.E., 1980, Modeling resistivity anomalies from localized voids under irregular terrain. *Geophysics*, **45**, 1164-1183.
- Spies, B.R. and Ellis, R.G., 1995. Cross-borehole resistivity tomography of a pilot-scale, in-situ vitrification test. *Geophysics*, **60**, 1313-1325.
- Stummer, P., Maurer, H. and Green, A., 2004. Experimental design:Electrical resistivity data sets that provide optimum subsurface information. *Geophysics*, **69**, 120-129.
- Sugimoto, Y., 1999. Shallow high-resolution 2-D and 3-D electrical crosshole imaging. *The Leading Edge*, **18**, 1425-1428.
- Summer, J.S., 1976, *Principles of induced polarization for geophysical exploration*. Elsevier Scientific Publishing Company.
- Telford, W.M., Geldart, L.P. and Sheriff, R.E., 1990. *Applied Geophysics* (second edition). Cambridge University Press.
- Tong, L. and Yang, C., 1990, Incorporation of topography into two-dimensional resistivity inversion. *Geophysics*, **55**, 354-361.
- Vanhala, H., Soininen, H. and Kukkonen, I., 1992. Detecting organic chemical contaminants by spectral-induced polarization method in glacial till environment. *Geophysics*, **57**, 1014-1017.

- Vanhalla, H. and Peltoniemi, M., 1992. Spectral IP studies of Finnish ore projects. *Geophysics*, **57**, 1545-1555.
- Van Voorhis, G.D. Nelson, P.H. and Drake, T.L., 1973, Complex resistivity spectra of porphyry copper mineralization. *Geophysics*, **38**, 49-60.
- Waddell, J. and Barton, K., 1995, Seeing beneath Rathcroghan. *Archaeology Ireland*, Vol. **9**, No. 1, 38-41.
- Weller, A., Seichter, M. and Kampke, A., 1996. Induced-polarization modelling using complex electrical conductivities. *Geophys. J. Int.*, **127**, 387-398.
- White, R.M.S., Collins, S., Denne, R., Hee, R. and Brown, P., 2001. A new survey design for 3D IP modelling at Copper hill. *Exploration Geophysics*, **32**, 152-155.
- Wilkinson, P.B., Meldrum, P.I., Chambers, J.C., Kuras, O. and Ogilvy, R.D., 2006. Improved strategies for the automatic selection of optimized sets of electrical resistivity tomography measurement configurations. *Geophys. J. Int.*, **167**, 1119-1126.
- Wilkinson, P. B., Chambers, J. E., Lelliot, M., Wealthall, G. P. & Ogilvy, R. D., 2008. Extreme Sensitivity Of Crosshole Electrical Resistivity Tomography Measurements To Geometric Errors. *Geophysical Journal International*, 173, 49-62.
- Witherly, K.E. and Vyselaar, J., 1990. A geophysical case history of the Poplar Lake Copper-Molybdenum deposit, Houston Area, British Columbia. in Fink, J.B., McAlister, E.O., Sternberg, B.K., Wieduwilt, W.G. and Ward, S.H. (Eds), 1990, *Induced polarization : Applications and case histories : Investigations in Geophysics No. 4*, Soc. Expl. Geophys.
- Wolke, R. and Schwetlick, H., 1988, Iteratively reweighted least squares algorithms, convergence analysis, and numerical comparisons: *SIAM Journal of Scientific and Statistical Computations*, **9**, 907-921.
- Wynn, J.C., Grosz, A.E. and Carlson, V.L., 1990. Induced-polarization response of some titanium-bearing placer deposits in Southeastern United States. In Fink, J.B., Sternberg, B.K., McAlister, E.O., Wieduwilt, W.G. and Ward, S.H. (Eds.), *Induced polarization – Applications and case histories. Investigations in Geophysics No. 4*, SEG, 280-303.
- Zhao, J.X., Rijo, L. and Ward, S.H., 1986. Effects of geologic noise on cross-borehole electrical surveys. *Geophysics*, **51**, 1978-1991.
- Zhdanov, M.S. and Keller, G.V., 1994. *The geoelectrical methods in geophysical exploration*. Elsevier, Amsterdam.
- Zhou, B. and Greenhalgh, S.A., 1997. A synthetic study on cross-hole resistivity imaging with different electrode arrays. *Exploration Geophysics*, **28**, 1-5.
- Zhou, B. and Greenhalgh, S.A., 2000. Cross-hole resistivity tomography using different electrode configurations. *Geophysical Prospecting*, **48**, 887-912.
- Zhou B. and Dahlin, T., 2003, Properties and effects of measurement errors on 2D resistivity imaging surveying, *Near Surface Geophysics*, **1**, 105-117.
- Zonge, K.L. and Wynn, J.C., 1975. Recent advances and applications in complex resistivity measurements. *Geophysics*, **40**, 851-864.